Surface-enhanced Raman Spectroscopy for environmental and biological analysis

A Dissertation
Presented for the
Doctor of Philosophy in Nanoscience
Massey University, Manawatu, New Zealand.

Megha Mehta

September 2019

CERTIFICATE OF AUTHORSHIP AND ORIGINALITY

I certify that the work presented in this thesis is my own work and has not been previously submitted for any other course or subject at Massey University or any other institution. Any contribution that I have received to my research work and in the preparation of thesis is fully acknowledged.

I also certify that all the information written and literature used has been cited in the thesis.

MEGHA MEHTA

10 September 2019

“**Vidya Viniyoga Vikasah**”

(Sanskrit Phrase)

(Meaning: Progress comes from true application of Knowledge)

Abstract

In recent years, extended efforts have been made to protect the environment, public and animal health from toxic chemicals that create a threat to the society. Either it is rodenticides affecting the entire forest food chain or toxicity of certain drugs on animals and humans. All such outbreaks require a faster and readily available detection method as a solution. There are numerous techniques for such toxic contaminant detection, but all require specific instrumentation and tedious sample preparation procedures. Due to the growing popularity of Surface-enhanced Raman spectroscopy (SERS), detection becomes a simpler, easier, faster and inexpensive for multiplex detection of environmental, chemical or biological contaminants.

Here, we explored a variety of SERS substrates (e.g., etched silicon, silver dendrites, and silver colloidal nanoparticles) for such detection. Our results demonstrate that colloidal nanoparticles combined with an omniphobic substrate, known as slippery infused porous substrate (SLIPSERS) has the potential for detection of rodenticides and anesthetic drugs in simple and complex biological matrices. This research explores the diversity of this method as well as how it behaves differently in different environments responsible for surface enhancement by substrate characterisation.

An initial experiment was performed on Rhodamine 6G as a test analyte using SLIPSERS which give an excellent limit of detection down to picomolar level concentration. Therefore, the method was further applied for the detection of rodenticides – brodifacoum and sodium monofluoroacetate in aqueous solution and milk and lidocaine hydrochloride in aqueous and deer antler velvet. The results indicate that SLIPSERS and SERS are capable of highly sensitive detection, characterisation, and quantification of toxic analytes in the environment that pose a threat to society. Moreover, for the first time, the SLIPSERS method has been used for detection and quantification of such analytes quickly and accurately.

Acknowledgements

Firstly, I would like to thank my primary supervisor, A. Prof. Mark Waterland, for his extensive guidance, input, support and patience throughout the project, as well as to my co-supervisor A. Prof. Paul G. Plieger for his useful advice.

Dr. Mark Waterland, an amazing supervisor provided me the opportunity to carry out this research the way I want. He has given full authority to characterise my ideas and support it with a nice framework for implementation. It's an honour to work with him and learn good analytical skills – either getting trained on his homemade Raman set up or Python language. He guided me in enhancing my writing and presentation skills by providing a platform to attend national and international conferences. His assistance made me do this research in elaborate and effective way. I am highly thankful for his input whenever required.

I would also like to thank Dr. Paul Plieger for providing me labs for supervision, amount of work that can be easily managed and balanced with study to cover up my Graduate assistant responsibilities.

Big thanks to Institute of Fundamental Science, Massey University, MMIC (Manawatu Microscopy and Imaging Centre) and in particular Niki Miniards for all the time she spent in SEM for imaging nanoparticles. This research project would not be successful without the provision of materials, instruments and research workspace.

I would also like to thank Dr. Carla Meledandri, University of Otago and her team for helping me out to work in their lab for preparation of positively charged nanoparticles. Also, would like to thank University of Otago Professor Keith Gordon for providing an opportunity to work with his team and Dr. Sarah Fraser, his post-doctoral fellow for all the hours she put in collecting line scan data for my samples.

I would also like to thank Callum and Harry Deare for their efforts in refining the SLIPSERS protocols, Sam Brooke for helping out with alignment in my final data

collections phase and Robert McEwen for his guidance in understanding Python coding. Also would like to thank Josiah for his advise and input on chemometrics and baseline correction methods.

Finally, my husband Ricky, thank you for all the sacrifices you have made to make this happen and motivating me all the time to target my goal. This thesis is not just the testament of my hard work it's same as yours. I have no words to thank you, without your support I couldn't have done this research in three years. Taking the entire responsibility of home and our son made things easier for me. I also would like to thank my family without their motivation I wouldn't have gone that long way. Thanks to my newborn baby for making me concentrate while writing this dissertation.

Contents

Glossary of Terms

This thesis uses the following terms.

Term	Definition
Aggregation	Attractive interactions between nanoparticles lead to irreversible binding between nanoparticles and the formation of aggregates.
Blinking	Frequent SERS fluctuations either due to photobleaching or thermal effects
Diffraction-limited spot	The smallest possible illuminated area in an optical system. The spot dimensions are ultimately limited by diffraction of the beam by the smallest aperture in the system. The diffraction-limited spot diameter determines the spatial resolution of the optical system.
Drop casting	Dropping a drop of solution mixture onto the substrate results in spreading the liquid and forming a thin film after evaporation. The solid-liquid (or liquid-liquid in the case of SLIPS) interfacial energy determines the extent of the spreading.
Emission continuum	The combination of a large number of weak scattering processes, that occur across a wide spectral range and are amplified by plasmon enhancement effect. The emission continuum appears as a broad, unstructured background of varying intensity under the sharp Raman bands.
Enhancement Factor	Ratio of intensities of SERS and normal Raman spectrum of analyte molecule.
Fractals	A class of structures that possess the property of self-similarity which can be described as a branch on a tree with each branch divided again, and again, giving a repeated structure at a smaller scale during each division.
Focal volume	The volume within a sample that is efficiently detected by a laser.
FERGIE	FERGIE is a Raman integrated spectrograph from Princeton Instruments, USA.
Geometric Dilution	Geometric dilution is a process that thoroughly mixes a small amount of the analyte with an appropriate amount of another solid substance that binds the analyte. The total analyte is added in the first step. Because binder is added in each step the concentration of the analyte at each step is multiplied by a dilution factor at each step. The final concentration is then calculated using a geometric series (analogous to calculating compound interest), hence the name, geometric dilution.

Hot spot	Highly localised regions within the metal nanostructures where intense field enhancement of SERS signal is observed also called as 'SERS-active sites'.
Kitaev Nanoparticles	Borohydride reduced silver nanoparticles synthesis performed by Kitaev et al.
Marangoni Effect	If droplets are allowed to dry on flat surfaces, the Marangoni OR coffee ring effect is often observed which results in the analyte being deposited in rings as the droplet slowly evaporates.
Numerical aperture	In optical systems, this dimensionless quantity is used to measure the angle over which the system can accept or emit light.
Normal modes	A set of independent vibrational modes that completely describe the vibrational motion of a molecule
Pareto Distribution	Pareto principle to SERS says that 80% of the signal will come from 20% of the SERS sites. For a high concentration means there are large number of molecules on the surface, then the observed SERS signal have little fluctuations. It means many hot-spots are located on the surface. The fluctuations are then reasonably small but still present.
PCA	Principal Components Analysis (PCA) is an unsupervised method that means it makes no a priori assumptions about the number of components or factors that are required to distinguish the samples.
Photobleaching	Irreversible chemical changes to molecules from photochemical processes. Results in a change in the Raman cross section producing fluctuations in signal. Most likely to occur at hot-spots and with high laser power.
Plasmon	Collective electron oscillations to enhance Raman scattering, allowing sensitive detection
Principal component	A linear combination of the independent variables of a system that is an eigenvector of the covariance matrix.
Raman Line-scan	Technique where spectra are recorded at successive points along a line defined over the SERS substrate to look at the location and number of hotspots with analyte that can alter SERS fingerprint.
Raster scan	A process of acquiring Raman scattering from a sample on a surface where the incident laser beam scans along a sequence of horizontal strips called lines which are further divided into collections of dots (pixels). The scan sweeps across a defined area row-by-row.
SERS	Enhanced Raman scattering of molecules that are adsorbed on, or near, SERS-active surfaces such as nanostructured gold or silver. Dried SERS means drop casting the silver nanoparticle analyte mixture on the substrate.
SLIPS	Slippery infused porous surface is an omniphobic surface inspired by the surface of the Asian pitcher plant, Nepthenes.

Susceptibility ($\vec{\chi}$).	The property of the material that determines the magnitude of the polarisation under an applied electric field.
Symmetry species	The normal modes of vibration can be classified by their behaviour under the symmetry operations of a molecule. Each mode will belong to one of the symmetry species of the molecular point group.
Sub-sampling regime	Below a critical concentration the probability of finding a molecule or possibly a small aggregate of analyte molecules in the focal volume *and at a hot-spot* becomes quite low. This is the sub-sampling regime, and a certain coincidence is required to find a signal.
Substrate	Surface that the nanoparticles and analyte are deposited on.
Scattering cross-section	A scattering cross section, σ, is determined by the rate of the energy removed from the incident beam due to scattering relative to the rate of energy of the incident beam passing through a unit area perpendicular to the direction of propagation
Spot	Area on the substrate surface illuminated by laser.
Tensor	The mathematical object that acts on a vector and changes its orientation is a tensor (which looks like a two-dimensional matrix, that is, tensors have a rank equal to two.). Susceptibility is a tensor quantity.
Zetasizer	High performance instrument used for measuring the size of nanoparticles for enhanced detection of aggregation.

List of Abbreviations

AEF	Analytical enhancement factor
$AgNO_3$	Silver nitrate
AgNP	Silver nanoparticle
AuNP	Gold nanoparticle
CARS	Coherent anti-stokes Raman scattering
CCD	Charge Couple Device
CT	Charge-transfer
CTAB	Cethyltrimethylammonium bromide
CV	Coefficient of variance
DVA	Deer velvet antler
EDX	Energy dispersive X-ray spectrophotometer
EM	Electromagnetic

ENR	Enrofloxacin
GC	Gas chromatography
HF	Hydrofluoric acid
HPLC	High performance liquid chromatography
IR	Infrared spectroscopy
KCl	Potassium Chloride
LHC	Lidocaine hydrochloride
LOD	Limit of detection
LOD	Limit of quantification
LSPR	Localized surface plasmon resonances
$MgSO_4$	Magnesium Sulphate
MS	Mass spectrometry
NaCl	Sodium chloride
PAHs	Polycyclic aromatic hydrocarbons
PCA	Principal Component Analysis
PCA	Perchloric acid
PCBs	Polychlorinated biphenyls
PLS	Partial Least Squares
Polymethyl methacrylate	PMMA
R6G	Rhodamine 6G
RSD	Relative standard deviation
SEF	Substrate enhancement factor
SEM	Scanning Electron microscopy
SERS	Surface-enhanced Raman spectroscopy
SLIPS	Slippery infused porous substrate
SM	Single molecules
SMEF	Single molecule enhancement factor
UV-Vis	Ultraviolet-visible spectroscopy

List of Figures

List of Tables

Chapter 1. Introduction

For more than 50 years, chemical and biological analysis of various analytes have progressed from traditional 'wet chemistry' laboratory methods to highly advanced analytical techniques like chromatography and spectroscopy. (McGorrin 2009). Gas chromatography (GC), high-performance liquid chromatography (HPLC), mass spectrometry (MS), ultraviolet-visible (UV-Vis) spectroscopy were considered as "gold standard" developed from 1955 to1970s. (Horvath and others 1967), (James and Martin 1952a, 1952b). But these popular and established methods had advantages and disadvantages. **[1]**

For instance, food contamination is a significant problem in terms of food safety throughout the world. People are easily affected by foodborne illnesses, which may be severe leading to death. There is an increasing number of cases every year where people get sick with contaminated food caused by a variety of bacteria, parasites or due to the addition of some harmful chemicals like pesticides during harvesting **[2]**. Centre of Disease Control and Prevention, U.S.A estimated that every year 48 million people get sick from a foodborne illness out of which 128,000 are hospitalized and 3,000 die **[3]**. Hence, an effective method is required for the detection of such toxins or food borne pathogens to save people from life-threatening diseases and even death.

Traditional methods used for such detection such as cell culture which are quite tedious and difficult to differentiate whereas modern detection techniques like immunoassays or spectroscopic techniques are also quite time consuming, expensive and need a significant number of samples for detection and overall require experienced personnel for analysis.

Hence, we need an urgent and rapid method of detection with high sensitivity and specificity, which can easily detect concentrations of the sample. Raman spectroscopy, infrared and fluorescence spectroscopy have emerged as promising techniques for identification of molecules by spectral information. Fluorescence spectroscopy is used as a simple measure to determine the concentration of a known compound from its fluorescent properties. Fluorescence lacks spectral specificity which gives an opportunity to other spectroscopy techniques. Infrared (IR) and Raman spectroscopy are considered to generate a "fingerprint" spectrum of the sample which can easily

be compared between target analytes for differentiation. (Alvarezordóñez and Prieto, 2012) **[4]**. But every technique has some advantages and disadvantages. The problem with IR is the interference from water giving intense absorption which makes it unsuitable for detecting analyte in aqueous solutions. IR has some applicability if pathlengths are kept small to minimise the absorption of IR by the water solvent. Raman, however, has an advantage over this as water is a weak Raman scatterer but has high interference due to fluorescence and typically takes longer acquisition time than IR. (Craig et al., 2013) Surface-enhanced Raman (SER) methods (*vide infra*) can overcome limitations with a weak signal, however.

Therefore, the best must be chosen from the current modern analytical techniques that overcomes all these limitations and provide us with quick and sensitive information for detection of analytes. Below (Table 1.1) is the list of pros and cons of a few analytical techniques **[5]** compared with surface-enhanced Raman spectroscopy (SERS).

Table 1. 1: Pros and cons of a few modern analytical methods compared with SERS

Technique	Pros	Cons
Chromatography based methods (LC-MS/MS GC-MS/MS)	Superior sensitivity considered the best standard; Multiplexing capabilities, i.e., running multiple LC systems into a single mass spectrometer; No interferences Less cross-reactivity between metabolites	Expensive, time-consuming, variability in interlaboratory results, highly qualified personnel required, sample clean-up is necessary, a considerable number of samples is required.
Immunoassay-based method (ELISA, EMIT, CMIA, etc.)	Need a small amount of sample (<100 μL), no sample clean up required, work on highly automated systems, Multiplexing capabilities	Interference from complex matrices like antibodies, protein, lipid content in the samples, need Several steps for quantification of the analyte; less specific and sensitive.

SERS based methods	Rapid measurements with no/minimal sample preparation, Multiplexing capabilities, and advanced portable Raman spectrometer for on-site detection capability.	Require good contact between the enhancing surface and analyte; selection of right substrate for the analyte of interest is challenging; homogeneity and reproducibility issue of SERS substrate.

Therefore, surface-enhanced Raman spectroscopy is widely used and developed for a wide range of applications. This technique, an advanced form of Raman spectroscopy not only improves sensitivity up to several orders of magnitude ($10^{-7} – 10^{10}$) but also suppresses the fluorescence due to its metallic nanostructure surface, which was a major problem faced using Raman spectroscopy. (Sengupta et al., 2006). In SERS, molecules adsorb at a roughened metal surface (e.g. Ag, Au), which generate hot spots, or SERS active site that greatly enhances the Raman signal. (Najafi et al., 2014)

Figure 1. 1: Nepthenes Asian Pitcher Plant

Despite the advantages of SERS over normal Raman methods, there are still some drawbacks, one that has received recent attention is how to ensure close contact between the metal nanostructure

surface and the analyte, as enhancement requires the analyte to be within a few nanometers of the surface.

To develop a SERS platform that can detect simple chemical to complex biological analytes with high sensitivity and specificity, Wong et al. prepared an omniphobic surface inspired by the surface of the Asian pitcher plant (Figure 1.1), also called Nepthenes (as they belong to the Nepthenes genus). These plants are carnivorous by nature and have evolved a surface more slippery than Teflon. The Pitcher plant is named for their pitcher-like tubes that form at the end of tendrils. The slippery water-lubricated surface inside the pitcher causes the insect prey to slip and drown in the fluid at the bottom. The plant has an exceptional feature of controlling the level of lubricant to create a slippery surface the lubricant, so it can create a slippery surface. Wong et al. developed synthetic versions of this liquid-repellent surface called slippery liquid-infused porous surfaces (SLIPS). Wong and his group used a lubricant to create 'omniphobic surface' that repels simple liquids like water and complex solutions like blood and oil.

When combined with SERS this sensing platform is called Slippery liquid-infused porous surface-enhanced Raman scattering (SLIPSERS) method and has been used for ultra-sensitive detection and has shown a great potential to meet many analytical levels of merit. This SERS platform **[9]** delivers near 100% analyte concentration by constant contact angle drying in both aqueous and non-aqueous solvents. The metallic nanoparticles are suspended in a droplet of the analyte and drying process on the SLIPS surface also produces a high density of SERS active "hot-spots". This methodology is still in its infancy stage, and this research explores the diversity of this method as well as how it behaves differently in different environments responsible for surface enhancement.

1.1. Fundamentals of Raman spectroscopy

Raman spectroscopy is a vibrational spectroscopy that can be used for non-invasive probing of chemical and biological samples **[10]**. The diagram below depicts the scattering process that involves an initial, intermediate (virtual) state and final state, and always involves pairs of photons (incident and scattered) that cause transitions between the states (which are simultaneous).

In general, in a scattering process, the incident photon causes a transition from the initial state to the virtual state and a simultaneous transition from the virtual state to the final state. In Rayleigh scattering the initial state and final state are the same (Figure 1.2). In Raman scattering, the initial and final states are different. There are two Raman processes, Stokes Raman where the final state is at higher energy than the initial state and Anti-Stokes where the initial state is at higher energy **[11]**.

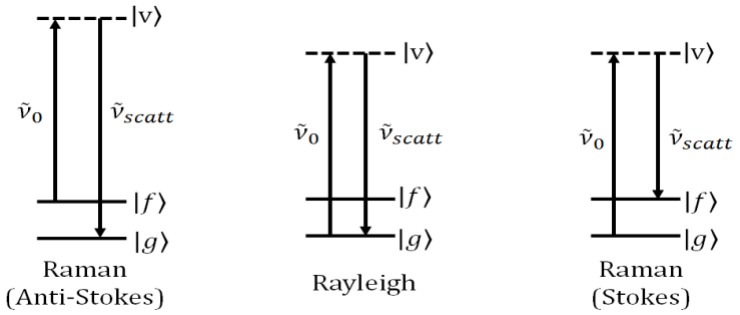

Figure 1. 2. Energy conservation for Rayleigh and Raman scattering

Energy ($E = h\nu$) is conserved during the scattering process:

$$h\nu_0 - h\nu_{scattered} \pm h\nu_{\text{vib}} = 0 \qquad (1.1)$$

where $h\nu_{\text{vib}}$ is the energy difference between the initial and final states.

At normal room temperature, the magnitude of intensity of Stokes Raman scattering is larger than that of anti-Stokes due to smaller number of molecules in an excited vibrational state than in the ground state.

The equations below provide a simple description of Rayleigh and Raman scattering using expressions from the theory of classical electromagnetism.

Consider the scattering material to be completely uniform. The polarisation is the induced dipole (per unit volume) in the material. Electromagnetic theory states that an oscillating dipole (polarisation) radiates energy, the magnitude of the dipole determines the intensity of the radiation (intensity is proportional to the square of the electric field).

The property of the material that determines the magnitude of the polarisation is the susceptibility ($\overleftrightarrow{\chi}$). This is a tensor quantity (noted with a double-headed arrow ↔).

In Eq. 1.2 the incident electric field is a vector with a specific magnitude and orientation. The polarisation is also polarised and it can be at a different orientation to the incident field.

The mathematical object that acts on a vector and changes its orientation is a tensor (which looks like a two-dimensional matrix). In other words, the susceptibility must be a tensor, to account for the observation that the orientation of the polarisation of the scattered light can be different to the orientation of polarised scattered light.

A classical description of the scattering process provides a simple explanation for the relative intensities. Consider light as an electromagnetic wave with frequency, ν_0 and electric field vector, $\vec{\boldsymbol{E}}$. If the light is incident on a material with an optical susceptibility, $\overleftrightarrow{\boldsymbol{\chi}}$, the electric field of the incident light induces a dipole $\left(\vec{\boldsymbol{P}}\right)$ in the material

$$\vec{\boldsymbol{P}}(\nu_0) = \varepsilon_0 \overleftrightarrow{\boldsymbol{\chi}} \vec{\boldsymbol{E}}(\nu_0) \quad \text{or} \quad P_i = \varepsilon_0 \sum_j \chi_{ij} E_j(\nu_0) \tag{1.2}$$

(ε_0 is the permittivity of free space).

The frequency dependence of the incident light is:

$$\vec{E}(\nu_0) = \vec{E}_0 \cos \nu_0 t \tag{1.3}$$

where E_0 is the amplitude of the electric field and ν_0 is the frequency of the laser.

The susceptibility is dependent on the positions of the atoms; there is a (large) static component and a smaller component due to the vibrational motion of the nuclei, determined by the ***change in susceptibility*** with atomic displacement (x).

$$\overleftrightarrow{\chi}(\nu) = \overleftrightarrow{\chi}_0 + \frac{d\overleftrightarrow{\chi}}{dx} x_0 \cos \nu t \tag{1.4}$$

Substituting the electric field, susceptibility and nuclear displacement into the electric dipole moment equation (1.2), below was obtained:

$$\vec{P}(\nu; \nu_0) = \varepsilon_0 \vec{E}_0 \overleftrightarrow{\chi}_0 \cos \nu_0 t + \vec{E}_0 x_0 \frac{d\overleftrightarrow{\chi}}{dx} \cos(\nu_0 + \nu) t + \vec{E}_0 x_0 \frac{d\overleftrightarrow{\chi}}{dx} \cos(\nu_0 - \nu) t \tag{1.5}$$

Using the trigonometric relation:

$$\cos x \cos y = \frac{1}{2}[\cos(x+y) + \cos(x-y)]$$

The polarization now has three components:

$\varepsilon_0 \vec{E}_0 \overleftrightarrow{\chi}_0 \cos \nu_0 t$	Rayleigh scattering
$\vec{E}_0 x_0 \frac{d\overleftrightarrow{\chi}}{dx} \cos(\nu_0 + \nu)t$	Raman (Anti-Stokes)
$\vec{E}_0 x_0 \frac{d\overleftrightarrow{\chi}}{dx} \cos(\nu_0 - \nu)t$	Raman (Stokes)

which correspond to the processes shown in Figure 1.2.

Hence, to be Raman active, the rate of change of susceptibility with the vibration (Q) must be non-zero.

$$\frac{d\overleftrightarrow{\chi}}{dQ} > 0$$

The greater the susceptibility, the greater the ability of a material to polarize in response to the field. This condition means that the vibrational displacement of atoms corresponding to a vibrational mode results in a change in the polarizability **[111]**.

These expressions are important because they show the origin of the relative intensity of Rayleigh and Raman scattering **[14]**. Noting that the incident field strength is the same in all three processes, it is the susceptibility that determines the strength of Rayleigh scattering and the so-called derived susceptibility that determines the strength of Raman scattering.

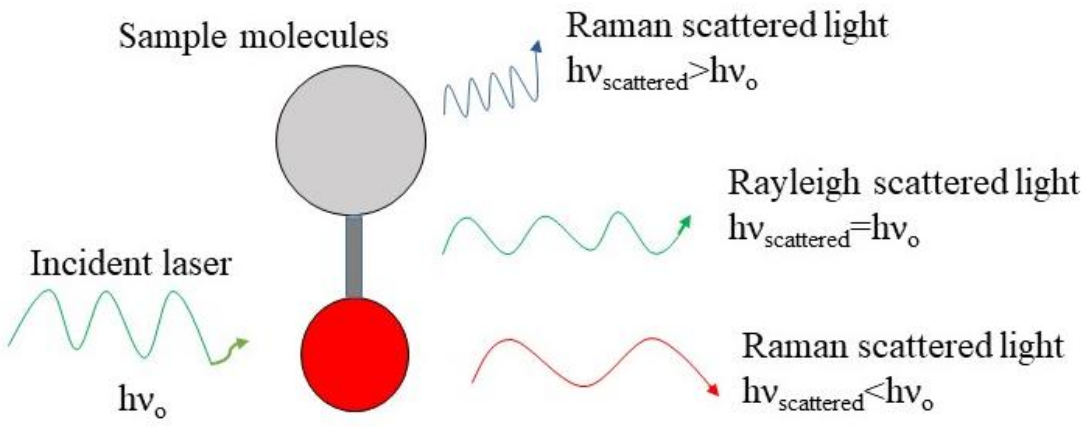

Figure 1. 3. Raman scattering process

The Raman effect is the inelastic scattering of photons while interacting with vibrational modes of molecules (Figure 1.3.). Chandrashekhra Venkata Raman first experimentally observed this inelastic scattering in 1928.

For Raman scattering:

$$\text{"Raman Shift"} = \tilde{\nu}_0 - \tilde{\nu}_{scattered} = \tilde{\nu}_{\text{vib}}$$

And so, Raman shift is directly related to the frequency of vibration of the molecule and helps in deducing molecular structure and the chemical constitution **[15, 16]**. Hence, it is considered as a valuable tool of detection and quantification of chemical and biological agents in a sample of interest.

The Raman technique can work remarkably well with solids, liquids, solutions, and even gases without spending much time on experimental set-up. This flexibility also allows for speed of analysis, prevention of sample contamination and preservation of evidential material (e.g., historical artifacts) **[17]**. Water has a very weak Raman signal and so Raman spectra can be readily obtained from aqueous solutions.

Despite these advantages, Raman spectroscopy suffers from the *drawback* of poor efficiency. Raman instrumentation has been traditionally confined to the research laboratory due to the need for high power laser sources and sensitive detectors required to analyse the inherently weak scattering process.

Raman spectroscopy needs special enhancement methods for analyte detection at trace concentration levels due to the intrinsically small Raman scattering cross-section, typically between $10^{-28} - 10^{-32}$ cm^2 per molecule which is several orders of magnitude smaller than fluorescence scattering cross-sections (for comparison).

Raman cross section

The Raman scattering intensity, I [J s^{-1}], is

$$I = \mathcal{I} \times N \times \sigma \qquad \left[\frac{\mathrm{J}}{\mathrm{s}}\right]$$

where N is the number of molecules in the scattering volume and $\mathcal{I}$ is the laser irradiance (J m^{-2}s^{-1}).

The total scattering cross section, σ, is a determined by the rate of the energy removed from the incident beam due to scattering relative to the rate of energy of the incident beam passing through a unit area perpendicular to the direction of propagation **[111]**. The scattering cross section has units of area, so any light passing through this area will be scattered.

The *differential* cross section, $\frac{\partial \sigma_{RS}}{\partial \Omega}$, may be defined using the power scattered into an element of solid angle $\partial\Omega$ [sr]. The units of differential cross-section are then [m^2 sr^{-1}]. Both total and differential cross section are usually related to a single molecule. **[112]**

Differential Raman cross section measures the Raman signal in a single direction (or at least around a small solid angle along a single direction) whereas Raman photons are generated in all directions which can be measured by total Raman cross section. Raman scattering cross section provides is used to relate scattered to incident irradiance, along with molecular number density. It serves as an important parameter to gauge likelihood of success for the proposed measurement, as it determines the scattering activity of an analyte and can be used to compare different Raman techniques for measuring that analyte (via measurement of so-called enhancement factors).

Computational chemistry methods are often used for calculating Raman cross sections for comparison with experiment.

Using only the intrinsic Raman cross-section limits detection levels to approximately $\mathrm{mmol\ L^{-1}}$ concentration levels in solution, under safe and convenient operation conditions (i.e., approximately 100 mW of incident laser power and a few minutes of data acquisition time).

For such situations, signal enhancement techniques like resonance Raman scattering or coherent anti-stokes Raman scattering (CARS) can be used but again they have other requirements to be fulfilled like high power and multiple wavelength excitation sources (CARS) which makes it challenge to implement sometimes **[18]**, or interference from fluorescence which occurs under identical conditions to resonance Raman scattering.

Surface-enhanced Raman spectroscopy (SERS), uses collective electron oscillations known as surface plasmons to enhance Raman scattering, allowing detection down to attomolar level concentrations. Metallic nanoparticles are often used as a source of surface plasmons (in which case they are known as localized surface plasmons). Localized surface plasmons generate large electric fields at the surface (by effectively focusing the incident radiation field at the nanoparticle surface), and Equation 1.2 shows that enhanced electric fields will generate stronger polarization, and so, more intense Raman scattering. The enhancement effect only extends a few nanometers from the surface, so this requires the analyte to be in close contact with the surface for effective enhancement.

Typical metals that support surface plasmons are silver, gold, copper, platinum, titanium, and chromium. **[28, 29]** For silver and gold, the plasmon frequency lies in the visible region of the electromagnetic spectrum, so plasmon resonance is obtained with visible light for these metals. Enhancement of Raman scattering through resonance with plasmon modes can enhance Raman intensities up to 5 or 6 orders of magnitude via plasmon resonance.

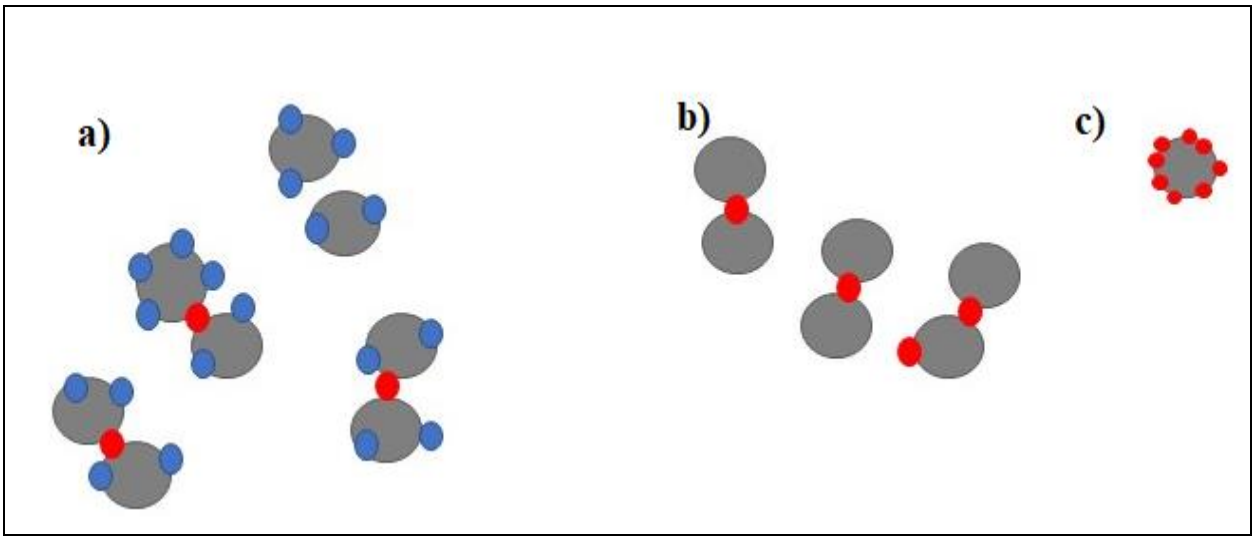

Figure 1. 4. a) A typical SERS substrate with a hot-spot in the gap between the nanoparticles. Dots represent molecules, either SERS active (red) at hot-spots and SERS-inactive (blue). b) the main objective is to get large number of SERS active regions to achieve single molecule level detection c) Aggregate of nanoparticle with lots of hot-spots

Detailed modelling of the plasmon modes show that their amplitudes are greatest at junctions between nanoparticles called "hot-spots" (Figure 1.4(a)). This leads to highly inhomogeneous intensity distributions that need to be accounted for when using SERS to determine the analytical concentration of an analyte. The main objective is to locate every analyte molecule at a hot-spot. This could be achieved by using some specific binding condition to locate the particles at the hotspots (e.g. block the areas of the nanoparticles that aren't hotspots), as shown in Figure 1.4(b), or, increase the number of hot-spots in the focal volume. The challenge is to produce a large number of SERS-active hot-spots, so that at low analyte concentration, every molecule can adsorb at a hot-spot and give highest SERS enhancement as shown in Figure 1.4(c).

Stronger Raman signals are obtained by collecting over a wide collection angle (θ), and this requires collection optics with a high numerical aperture (NA) (see diagram below):

$$\frac{f}{D} \approx \frac{1}{2NA}$$

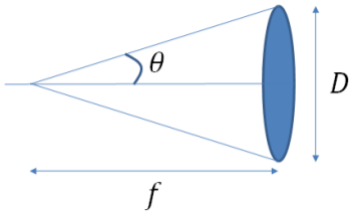

(f is the focal length and D is the diameter of the simple lens). The focal volume (that is, the region in the sample where most of the scattering is collected from) is determined by the numerical aperture and is proportional to $1/NA^3$. So, as collection efficiency increases, the focal volume decreases.

To get highly intense Raman signal from the sample, high NA optics are used so then the challenge is to get as many molecules into the (small) focal volume as possible. The solution to this problem will be discussed in the later section of this chapter under SLIPSERS.

1.2. Theory of surface-enhanced Raman spectroscopy (SERS)

SERS is a process that describes the increase in the Raman cross-section of molecules adsorbed on the surface of metallic nanostructures. SERS relies on the coupling between the electronic transitions in the system and the molecular vibrational motions that generate Raman scattering. If the coupling between the vibrational motion and electronic transitions leads to an increase in the change of the polarizability with vibrational motion then the Raman scattering intensity will increase. A key idea is that enhancement is a resonance phenomenon, so the frequency of the laser radiation that is generating the Raman scattering must be in resonance with the frequency of the electronic motions that are enhancing the Raman scattering. **[24-27]**

Identifying the enhancement mechanism in SERS is then a matter of identifying the nature of the electronic transitions in the system. For a molecule adsorbed on the surface of a metallic nanostructure (e.g. metal nanoparticle), there are three important electronic transitions:

1). The electronic transitions of the nanoparticle

2). The electronic transitions of the molecule

3). The electronic transitions between the molecule and the nanoparticle

The electronic transitions of the nanoparticle are the localized surface plasmon resonances. The plasmon resonance has a characteristic frequency known as the plasmon frequency.

Electronic transitions of the molecule itself can also enhance the Raman scattering. This effect is known as resonant Raman scattering. The conditions for strong resonant Raman scattering are

similar to those for plasmon enhancement, that is, the molecular electronic transition must be resonant with the frequency of the incident light source. This is the same condition that leads to photon absorption and this provides a simple method for optimizing the resonant Raman scattering – match the wavelength of the incident light source with the absorption maximum of the resonant molecule. For many molecules, this condition often leads to fluorescence.

An added advantage of the SERS experiment is the close contact between the molecule and the metal surface which provides very efficient quenching of fluorescence and so the problems typically associated with resonant Raman scattering of molecules in solution due to competing fluorescence scattering are avoided with SERS. The enhancement via resonant Raman scattering is similar to the plasmon enhancement mechanism and the two effects multiply together, so under ideal conditions up to 10 orders of magnitude enhancement can be obtained if the plasmon and molecular transitions are resonant with the incident light source.

For normal Raman the polarizability is represented in quantum mechanics as the sum over all the electronic states of the molecule of the product of the transition dipole moments for the one-photon "up" and "down" transitions shown in Figure 1.2. Under resonant conditions, a single *resonant* electronic state dominates the scattering. The probability of each one-photon process is proportional to the transition dipole moment of each process and the polarizability is the product of the transition dipole moments so the probability of resonant Raman scattering is proportional to the *square* of the transition dipole moment for the resonant electronic state. The transition dipole moment, in turn, is proportional to the area under the electronic absorption band. So, strongly absorbing molecules give the strongest resonant Raman enhancement, and systems with delocalized π-systems such as porphyrins, cyanine and azo dyes and "laser dyes" such as rhodamine and fluorescein all have very strong electronic transitions and have all been observed to give single-molecule Raman scattering using SERS. **[30]**

For some species there may be strong chemical interactions with the metal surface. This is the case for the very first observation of SERS reported by McQuillan, Hendra and Fleischman **[31]**, where pyridine was chemisorbed onto a roughened silver electrode. Covalent bond formation may take place and metal/ligand complex forms on the surface. The metal/ligand complex may then exhibit transitions that are associated only with the complex, such as charge-transfer from the occupied metal bands to low energy unoccupied ligand orbitals. This transition is then entirely equivalent to

the molecular transition discussed above and becomes a source of enhancement for Raman scattering. **[31]** This mechanism has been associated with the "chemical enhancement" mechanism due to it relying on the specific chemical interactions between the molecule and the surface. Charge-transfer transitions have strong electronic transitions, but not as strong as the molecular transitions discussed above.

For all three processes there are two factors that determine the strength of the enhancement:

(1) The magnitude of the electronic transition dipole and

(2) the frequency mismatch between the electronic transition frequency and the incident light frequency.

SERS can be optimized by understanding the resonant electronic states of the system and the excitation energy profiles of these states. The interaction between nanoparticle plasmonic states and molecular electronic states is also important for SERS enhancement. **[32]**

It is important to note that the plasmon transition or induced dipole is several orders of magnitude larger than the strongest molecular transitions (simply due to the large number of atoms in the nanoparticle), and so the plasmon resonance tends to dominate in most applications of SERS. As given by Kelley **[25]**, if the transition strength of a single dye molecule is 1 (arbitrary units) then the nanoparticle transition strength is 3300, and the relative enhancement factor will be approximately 10_7 which shows the very intense nanoparticle transition provides nearly all the enhancement in a nanoparticle-dye system. Proximity to the resonance condition must also be considered, this rough 10_7 factor assumes that the excitation is equally resonant with both the nanoparticle and molecule transitions. Kelley's simulations also show that in the case of strong resonance with the molecular transition but very weak resonance with the nanoparticle transition (as measured by the frequency difference, $\tilde{\nu}_{laser} - \tilde{\nu}_0$) then the molecular resonance can dominate.

Hence, SERS spectra are strongly ruled by nanoparticle transitions with minor contributions from molecular transitions. Even weak coupling between nanoparticle and dye provides a significant increase in dipole strength of molecular transition due to very large and strong nanoparticle electronic transition. **[26]** It is important to note that optimum SERS should be obtained if both plasmon and molecular states are on-resonance with excitation frequency.

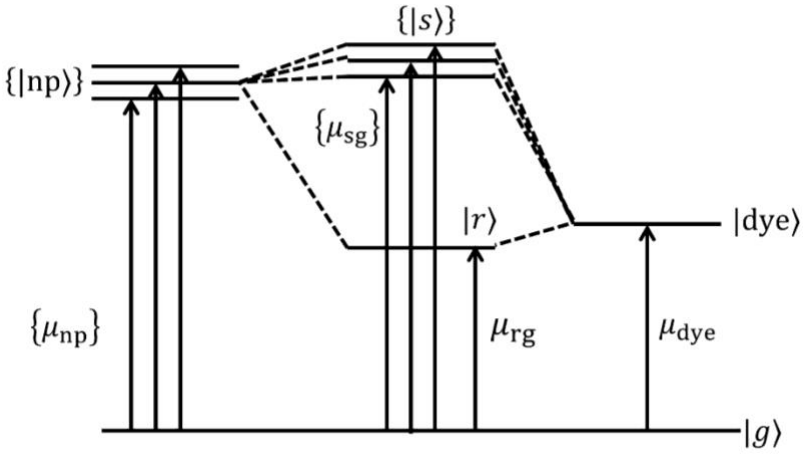

Figure 1. 5. Energy levels and transitions in a nanoparticle-dye system.

Figure 1.5 shows the energy levels and transitions in a model nanoparticle-dye system. Horizontal lines are states of the system. The nanoparticle and dye states are shown on the left and right respectively. If strong interactions between the nanoparticle and dye are present ("chemical enhancement") then new states are generated, shown here as $|r\rangle$ and $|s\rangle$ states. Vertical lines show transitions between states, labeled with the transition dipole moment,μ, for each transition **[110]**.

In older literature, there are two primary theories that explain SERS mechanisms, the "electromagnetic (EM) model" and the "charge-transfer (CT) model" **[24,26]**. These theories persist in current literature and it is worth placing them in the context of Kelley's model. The EM model accounts for the nanoparticle transitions and CT model accounts for the molecule transitions in the Kelley model. However, they both have a quantum mechanical basis and Kelley's work demonstrates that both nanoparticle and molecular resonances contribute to SERS via the same "mechanism" (i.e. resonant enhancement). Furthermore, molecular resonances include but are not limited to charge-transfer transitions. Charge-transfer enhancement, or lack of, is simply a feature of the chemical structure of the molecule itself.

1.2.1. The SERS Effect

The SERS effect is achieved by carefully controlling both nanoparticle and molecular effects, by designing the best substrates (maximise plasmon transition strength), and the ensuring the analyte is strongly adsorbed onto the surface (the resonant frequency of the analyte is clearly fixed by the analyte's molecular structure) **[33-35]**. This is an active field of research and there is no universal way to prepare one best SERS substrate for all analytes. There are several factors to consider when optimizing the SERS effect:

1). the optical resonance conditions

2). optimisation of plasmon amplitude

3). Proximity of the analyte to the nanoparticle surface, and if possible, to the sites of maximum plasmon amplitude

Optical resonance condition

As discussed, the incident laser wavelength should match the absorption maxima of the nanoparticle and molecular absorption. For the cases where the molecule does not absorb visible light then only the nanoparticle absorption is important. There is a slight complication because most commonly used colloidal metal nanoparticles have an absorption maximum at relatively short wavelength (e.g. 420 nm), but the most efficient SERS is observed at much longer wavelengths. This is due to the strong coupling between nanoparticle resonances at hotspots leading to a shift in the plasmon resonance to lower frequency. For typical silver nanoparticles the strongest resonance is observed with green laser excitation (500 – 530 nm).

Optimisation of plasmon amplitude

Interparticle interaction and stability of colloids depends on the forces between surfaces present in the system according to DLVO theory (Derjaguin–Landau–Verwey–Overbeek theory**). [36-40].** There is a relationship between ionic strength and dielectric constant - dielectric constant decreases as ionic strength increases. The decrease in dielectric constant then reduces the repulsive Coulomb force, **[123]** so the result is that aggregating agents screen the electrostatic repulsion forces and

with decreased repulsion (and van der Waals attraction largely unaffected), aggregation occurs. Aggregation generates hotspots and hence, strong SERS **[106]**.

Finding the most stable SERS responses as per the experimental design is the key point. For colloidal substrates, aggregating agent dramatically enhances the signal to 10-fold or more but one aggregating agent again cannot work for all. The most widely used aggregating agent sodium chloride (NaCl) when replaced with lithium chloride, increased SERS signals than by using NaCl **[41,42]**.

Proximity of the analyte to the nanoparticle surface

SERS enhancement depends on the distance between the analyte of interest and SERS surface as reported by Haes *et al*. **[123**]. The distance should be within 1- 30 nm from SERS surface to get strong SERS enhancement **[43-46]**. Specific surface chemistry effects and the structure of the electrical double-layer around the nanoparticle can influence the interaction between the analyte and the nanoparticle.

Le Ru *et al* have reported significant work of detecting every molecule of analyte by directing the analyte towards SERS hotspots using surfactant, cethyltrimethylammonium bromide (CTAB) **[47-49].** The principle is to chemically block access of analyte to the surface coated with surfactant layer, except at the nanoparticle surface tips, which act as hot-spots and highest enhancement factor is expected. Such technique has the capability of trace level detection with every molecule to be detected at single molecule level **[50-52]**.

1.2.2. "Normal" and SERS spectra

With SERS, one thing to be kept in mind is that SERS will give somewhat different spectra than what is obtained from normal Raman. As explained above, it is the derived *polarizability* that determines the "normal" Raman intensity. Normal Raman intensities are observed in the absence of any of the resonance effects described above. In practice this means the incident laser frequency must be well separated from any plasmon or molecular resonances in the system. Because molecular and plasmon resonances are typically in the visible or UV region, normal Raman intensities are obtained with long wavelength excitation e.g. 785 nm or 1064 nm. The derived

polarizability is a tensor quantity and there is a strong directional dependence with Raman scattering. In solution, the directional dependence averages out due to the random orientation of the analyte molecule relative to the orientation of the polarization of the incident laser source. Molecules adsorbed on nanoparticle surfaces receive enhancement from the electric field of the plasmon oscillation **[106]**. If the molecules adsorbed with a geometrical preference tend to form vertically oriented aggregates on the nanoparticle surface e.g. planar molecules such as rhodamine6G or brodifacoum, then there is limited orientational averaging relative to the plasmon field and vibrational modes with strong derived polarizability components with the same orientation as the plasmon electric field will receive preferential enhancement.

As there is a different kind of interaction between the analyte and nanoparticles adsorbed onto the surface this will result in different spectral intensities. If the interaction between the molecule and the surface is sufficiently strong then the vibrational frequency of the molecule might also be perturbed. Thus, differences in peak position, height of peaks or shape can be observed in a SERS spectrum relative to a "normal" Raman spectrum.

Resonance Raman effects can also alter peak heights (band intensities). The theory of resonance Raman scattering shows that modes that translate the molecule from its ground state geometry to the relaxed excited state geometry receive the strongest resonance Raman enhancement **[10]**.

Consider the description of ***resonant*** Raman scattering shown in Figure 1.6.

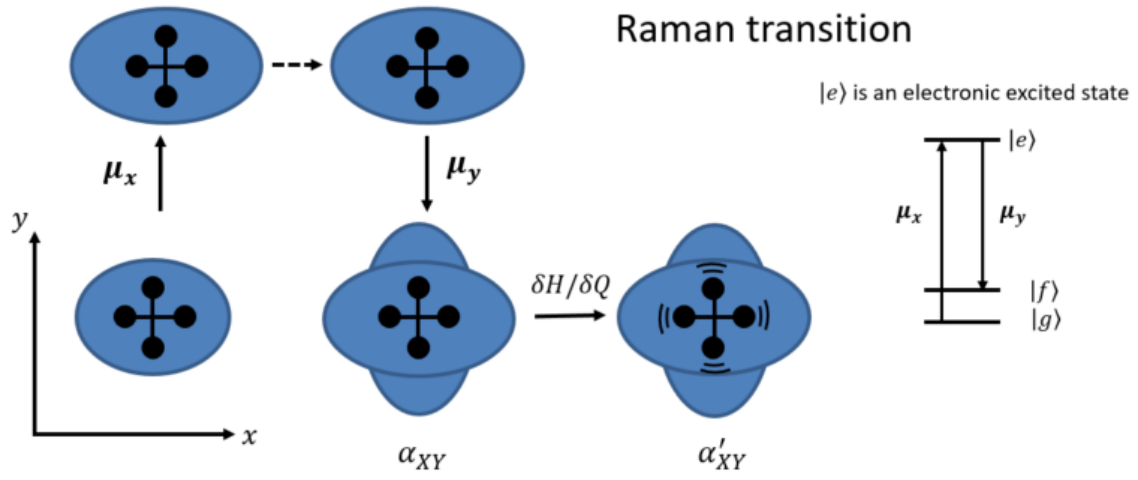

Figure 1. 6. Scheme of resonant Raman scattering

the blue regions represent the electron distribution and the balls and sticks are the nuclei and bonds in the molecule (bottom left). For example, for rhodamine6G the molecule is planar in its ground state.

In this model, resonant Raman scattering consists of an electronic transition from the ground state to a ***specific excited state***, $|e\rangle$ and a transition back to the ground state.The electronic transitions are polarised along a specific direction, in this example, along x and y. When the system returns to the ground state the molecule is now polarised, shown as a distortion of the electron distribution along the x and y axes in the example. The polarisability component, α_{XY} describes the extent of the polarisation. Note that α_{XY} is a single component of the polarisability tensor, $\overleftrightarrow{\alpha}$.

As the electronic distribution is now distorted the nuclei will adjust their positions to find the equilibrium positions in the polarised state. The only allowed motions of the nuclei that can achieve the required distortion are the molecular vibrations, that is, the normal modes, Q. The step shown with $\delta H/\delta Q$ represents the displacement of the nuclei towards their new equilibrium positions. $\delta H/\delta Q$ itself is the gradient of the total energy along the normal coordinate – or, in other words, the force acting on the nuclei along the normal coordinates due to the polarised electron distribution.

Only vibrations that distort the molecule to match the shape of the distorted electronic distribution are allowed. The shape of the electronic distribution determines the symmetry of the molecule, or in other words, the shape of the electronic distribution determines which symmetry elements the molecule possesses. To maintain the correct symmetry, the active vibration must possess ***all*** of the same symmetry elements, and a vibration that possesses all of the symmetry elements of a group is, by definition, the totally symmetric vibration. **[118]** Thus, only totally symmetric modes are expected to be enhanced in resonant Raman scattering with a single electronic state.

Comparison with "normal" Raman scattering

This analysis doesn't necessarily work for normal Raman scattering because for normal Raman there is no resonance with a ***specific excited-state***, usually because the excitation energy is below the energy of the lowest excited state energy. Polarisation still occurs but because there is no resonance with one excited-state, quantum mechanics states that for the Raman process, ***all*** of the excited states should be involved.

So the description explained above using the symmetry of a single component of the polarisability tensor must be replaced with a description that considers the symmetry of the entire polarisability tensor **[119]**, as the polarisability tensor contains all possible combinations of $\sigma \times \rho$ where σ and ρ are "translations" i.e. x, y or z.

$$\vec{\vec{\alpha}} \equiv \begin{pmatrix} \alpha_{xx} & \alpha_{xy} & \alpha_{xz} \\ \alpha_{yx} & \alpha_{yy} & \alpha_{yz} \\ \alpha_{zx} & \alpha_{zy} & \alpha_{zz} \end{pmatrix}$$

Group theory methods are most commonly used for this purpose **[120]**. A simple rule is derived from the group theoretical analysis:

> Raman active vibrations have the same symmetry as the "quadratic polynomials".

Character tables give the symmetry species for all the quadratic polynomials so Raman activity can be easily read from a character table. Only totally symmetric vibrations (a normal mode with all characters = 1 in the character table) give rise to polarized lines. **[114]**

1.2.3. Incident laser power

The laser power must be carefully optimized for SERS measurements, to maximize the signal intensity (and detection limits) but without causing sample damage. Higher laser powers are desirable but high laser power can damage the sample, which introduces errors when attempting to quantify the amount of sample present. Sample damage is more likely in SERS measurements where the solvent is removed (by drying) as the solvent provides a convenient bath to dissipate the energy supplied by the laser. All resonant Raman measurements are prone to sample damage by absorption of the laser light (because resonance is a necessary condition for photon absorption). Due to the dependence on the nanoparticle morphology, or formation of hotspots, the plasmon resonance effect is highly localized and the plasmons effectively focus the light into highly confined volumes within the sample. This focusing effect is compounded using high numerical aperture microscopy lenses, which can produce a diffraction-limited focal diameter that is less than 1 micron for visible excitation **[53-55]** This produces very high irradiance (photons per unit area per unit time) and the plasmon effect increases the effective irradiance even further. Without

solvent to dissipate the photon energy, power levels as low as a few mW can cause irreversible sample damage. For comparison, a sample in solution with no resonance effects (and using long working distance lenses) can tolerate hundreds of mW without showing any signs of damage.

1.2.4. SERS enhancement factors

Le Ru et al. have introduced definitions of SERS enhancement factors, such as SMEF and SERS substrate enhancement factor (SSEF). Both explain the intrinsic behavior of the substrate. **[20,21]**

SMEF is the ratio of SERS intensity of single molecule, I_{SERS}^{SM}, to Raman intensity of single molecule without any metallic substrate, I_{RS}^{SM},

$$SMEF = \frac{I_{SERS}^{SM}}{\langle I_{RS}^{SM} \rangle}$$

Where the angle brackets indicate the average (over an orientation in solution) Raman intensity per molecule. Such comparison of SERS intensity with Raman intensity of a free molecule will produce variations in SERS enhancement factor as I_{SERS}^{SM} depends on substrate position, geometry, orientation of the molecule and it is difficult to control these factors experimentally.

On the other hand, SSEF is defined as the ratio of SERS intensity (per molecule adsorbed on the SERS substrate, N_{SERS}) to normal Raman intensity of analyte molecule in solution. SSEF is obtained from the SMEF by averaging over all possible orientations of the molecule on the substrate and then averaging over all spatial locations. This is a good estimation for evaluating SERS activity, but it can be difficult to calculate N_{SERS}. It has been observed during drying the drop of analyte solution on SERS substrate that multiple layers are created with an increased thickness on the edges due to the 'coffee ring' effect (explained in detail in section 1.7.1.) compared to the molecules adsorbed at the centre. Such variation in the uniformity of pattern formed on SERS substrate creates complexity in estimating the number of SERS adsorbed molecules. **[21-23]**

$$SSE\ Factor\ = \frac{I_{SERS}}{I_{RS}} \frac{N_{RS}}{N_{SERS}}$$

To overcome both above mentioned SERS enhancement factors, Le Ru et al. proposed an Analytical Enhancement Factor (AEF) which is useful for colloidal nanoparticles and evaluating SERS efficiency with respect to the concentration of the analyte used. The AEF **[56-58]** is defined as

$$AEF\ = \frac{I_{SERS}}{I_{RS}} \frac{C_{RS}}{C_{SERS}}$$

Where I_{RS} is the Raman signal of an analyte at concentration C_{RS}. Similarly, I_{SERS} is the SERS signal measured for the same analyte at concentration C_{SERS}.

SERS for the detection of single molecules (SM) adsorbed on nanostructured surfaces is referred as SMSERS. Single molecule SERS efficiency (SMSERS), η , also called adsorption efficiency, can be measured to roughly estimate the number of analyte molecules adsorbed in the hot-spot region using single molecule enhancement factor (SMEF), which is the ratio of SERS intensity of a specific single molecule to the normal Raman intensity for the same molecule under consideration and Analytical enhancement factor (AEF= $I_{SERS}C_{RAMAN}$/ $I_{RAMAN}C_{SERS}$; where I_{SERS}, I_{RAMAN} represents peak intensity with and without Ag nanoparticles and C_{SERS}, C_{RAMAN} are the concentration of analyte with and without Ag nanoparticles.) ;

$$\eta = AEF/SMEF$$

In an ideal case, where every analyte molecule is responsible for enhancement, then it has the highest enhancement factor, η=1. However, for the best experimental case where average AEF, that is, every molecule experience specific adsorption enhancement close to SMEF then it should be within the theoretical range of $0.1 \leq \eta \leq 1$. It depends on the system of study whether it is a colloid or solution, molecular orientation with respect to polarization at the hot-spots will change leading to the SM detection level.

1.3. SERS-active substrates

In this section, a few terms are used to explain the common SERS active substrates. A substrate is the surface that the nanoparticles and analyte are deposited on and a nanoparticle refers to the silver nanoparticles. Nanoparticle surface is then the interface where the analyte adsorbs.

Scattering from SERS hotspots dominates over SERS scattering from other locations. Hotspots are generated randomly in silver nanoparticle (AgNP) aggregates. Hence, reproducibility is the main issue with analytical applications of SERS **[51]**.

There are various types of SERS-active substrates including silver colloids **[55]**, silver nanowires (Tao and others 2003), silver/gold fractal aggregates (Qiu and others 2008b), silver dendrites (Song and others 2006), roughened gold film electrode (Sauer and others 2004), gold-coated silicon plate (Alexander and Le 2007b) etc.

Most SERS substrates are fabricated by "**bottom-up**" techniques that largely utilize controlled or random self-assembly of nanoparticles that can provide tremendously enhanced Raman signals. **[52-54]**

Other substrates are fabricated by "**top-down**" techniques (e.g. electron-beam lithography) (Alexander and Le 2007b); however, they often produce weaker signals although reproducible signals can be obtained. Additionally, most "top-down" techniques involve the use of costly equipment and complex methods.

Therefore, a better method is needed to fabricate substrates that are reproducible, stable, easy-to-make, economic, and can provide satisfactory signal enhancement. **[56-59]**

One of the problems limiting the use of SERS as a conventional lab technique is the absence of reliable substrates **[60-61].** Despite the high number of publications and licenses where new active materials are proposed, commercial substrates are still rare, often expensive and quite unstable. The SERS active substrates obtained by either 'bottom-up' or 'top-down' approaches give ideally a reliable and cost-effective substrate and experimental results show higher enhancement signal

than that obtained with expensive commercial substrates **[62, 64].** Therefore, parameters to be considered for best enhancement postulated by Natan et al. are below **[74]**:

1. Spot-to-spot reproducibility: spot-to-spot variations should be less than 20% to ensure uniformity and to obtained good statistics.
2. Substrate-to-substrate reproducibility: Less than 20% variations within different substrates to ensure repeatability.
3. High enhancement factors of more than 10^5.
4. Shelf-life stability of at least a few months.
5. Effective adsorption of analyte at the surface.
6. SERS cross section should be higher than any interferents.
7. Low cost of production.
8. Tian et al. **[75]** added one more factor to consider that the substrate should be clean enough to avoid any signal from the surface of the substrate itself which might interfere with SERS signal of an analyte, leading to false interpretations.

This last point is important if the analyte has weak interactions with the nanoparticles, then interference from the contaminants cannot be ignored. Therefore, measures should be taken to obtain clean SERS substrates. It can be by either centrifuging the nanoparticles a few times or by use of competitive chemical adsorbates that react with the nanoparticles to eliminate the interference. The background signal and SERS spectrum of the analyte should be carefully compared to identify competing adsorbates.

The most commonly used SERS substrates, included in this dissertation, are colloidal metal solutions either silver (Ag) or gold (Au). AuNP's have longer shelf time and are compatible with various biomolecules like antigen, antibody, and DNA whereas AgNP's delivers better performance in SERS due to their stronger localised field **[65]**. Silver is a much better and efficient optical material giving 10 to 100-fold higher SERS signal than gold **[108]**. Also, silver can easily excite from the UV region to the IR while gold is restricted to the red visible and IR region damped by interband transitions **[109]**. Colloidal metal substrates are nanoparticles suspended in solutions ranging in size from 30 to 100 nm in diameter, and with a variety of particle shapes. Silver nanostructures are the most common substrates for achieving strong SERS signals.

There are numerous methods in the literature for the preparation of silver nanoparticles **[66]** with ideal methods offering some control over particle size and shape.

Reduction by citrate ion, most commonly known as the Lee and Meisel method [**67]**, produce AgNP's in water, but with no attempt made to control particle size and shape. There is difficulty in controlling the reduction of silver ions that lead to the broad size distribution of nanoparticles which creates a problem in stabilizing the particle shape. Therefore, several researchers investigated the parameters to improve the reproducibility from these silver nanoparticles using a modified Lee Meisel method.

Kitaev et al**. [68]** reported such a synthesis for controlling the particle size and shape within the range of 10-70 nm. Sodium borohydride was used as the reducing agent. Citrate acts as a stabilizer and forms complexes with the Ag nanoparticles creating negatively charged surfaces which prevents aggregation. These two reagents are commonly used in silver nanoparticle synthesis. Kitaev also used potassium bromide to alter the shape of silver nanoparticles by acting as a shape-modifying agent and giving different plasmon frequencies (plasmon frequency is more sensitive to particle shape than average particle size). Hydrogen peroxide works as an etching agent to rapidly digest unstable nanoparticles and create a stable, and therefore uniform, distribution of nanoparticles (with shape controlled by addition of the bromide ions). These chemical approaches are quite simple and effective in controlling the morphology of particles. The Kitaev method is used in this work and nanoparticles produced via this method will be referred to as "Kitaev nanoparticles".

Like various methods for the preparation of silver nanoparticles in literature, there are several substrate materials for SERS characterization (where substrate means the surface on which the silver nanoparticles are deposited). In the case of solid analytes, there is no specific need for substrate preparation just cleaning the surface of the substrate can work (and typical substrates are simple glass microscope slides). On the other hand, for the liquid sample where drop casting is done **[116]**, i.e. placing a drop of analyte and silver nanoparticles on the surface of the substrate and acquiring the spectrum after the drop has dried, the substrate properties need to be carefully controlled to control drying process in order to collect as many nanoparticles and analyte molecules into the focal volume of collection optics.

There are many options like using a silicon wafer as silicon gives stable peak that is a good reference point for calibration purpose or microscope glass slides **[69]**. For the liquid samples, one should use a substrate that will not impact the results based on, for example, chemical reactions between the substrate and the liquid sample or by introducing Raman features that may cause confusion in terms of interpreting the Raman spectra. For instance; glass slides will contribute interfering bands in the Raman spectrum which can be fixed by background subtraction **[70].** Slippery liquid-infused porous surfaces are another method for preparing thin film sample from liquids on a substrate using a spin coating process. This method is explained in a later section of this chapter. **[9]**

1.4. Advantages of SERS techniques

Some of the SERS advantages are:

1. SERS is very sensitive. It can reach the lowest detection level by optimising the surface concentration of active sites (hot-spots) of analytes which are more easily enhanced in signal intensity than the signal from other sites. Therefore, SERS is suitable for trace detection of analytes in different matrices. **[71]**
2. SERS technique requires minimum sample preparation before measurement.
3. SERS can achieve the rapid diagnosis of diseases and detecting the differences in various stages by analysing spectral features.
4. Extraction methods can be simplified compared to time-consuming methods employed for HPLC or LC/MS, and large particles do not affect the results significantly.
5. SERS equipment is cheaper and smaller than mass spectroscopy if LC/MS or GC/MS is used. With the development of SERS substrates and the use of a portable Raman, it is possible to have cost-efficient SERS methods for on-site investigation.

1.5. Challenging issues

Some challenges for implementing SERS include:

1. Picking a suitable substrate for the sample to be investigated.
2. Other components in complex matrices may influence the SERS signals of target samples. The SERS signals of the target analyte may be much weaker than other components.
3. Proper match of substrate plasmon resonance frequency and laser frequency to get the best SERS enhancement. Matching can be difficult because a large proportion of the Raman signal can come from a small portion of nanoparticles with a dramatically shifted plasmon resonance from the nanoparticle population that contributes most to the absorption maximum.
4. Currently, there are only a few SERS substrates commercially available, and they are costly.
5. Nanoparticle preparation. When making metal nanoparticles, it is necessary to clean glassware properly, and prepare fresh solutions so desired nanoparticle size and shape is achieved. Aggregating agent selection is also of utmost importance, as aggregation affects the formation and density of hotspots.
6. Variation in hot-spot density will lead to larger uncertainty, or spread, in the measured intensities and therefore concentrations. This affects precision of SERS.

1.6. Some Applications of SERS

This section of the dissertation provides an overview of applications of SERS currently employed or new areas of research that may benefit from SERS high sensitivity, specificity, and simplified technique. There are several reviews **[73-79, 82-89]** that are available in this context to find more in-depth details.

Few applications of SERS with relevant examples as per this study are listed below:

1.6.1. SERS in bioanalytics

SERS is a promising technique in bioanalytics, which combines specificity with ultrasensitive detection. For example, for ultrasensitive detection of Enkephalin, an endogenous substance in the human brain using SERS, Kneipp et al. **[72]** employed a SERS tag to functionalise nanoparticles to detect that specific biomolecule **[73-75]**.

The biggest challenge of SERS biosensing is to achieve selectivity of the analyte of interest and to keep the unwanted analytes from the complex matrix away from adsorption. This can be achieved by making some modification in the silver nanoparticles colloids and surface of the substrate. Immunoassay techniques are widely used for biomolecular detection, but due to low sensitivity, there is a need for advanced and sensitive analytical techniques. Hence, the immunoassay platform coupled with SERS labels (molecules of highly intense and distinguishable Raman signal such as dyes) is employed for sensitive detection. **[76-77]**

The most important targets are proteins **[78-79, 95]**, DNA or nucleotides [**80-82**], detection and identification of bacteria **[83-85]** and small molecule metabolites **[86-87].**

1.6.2. Environmental Pollutants and Pesticides

Environmental monitoring is another significant challenge. Small trace pollutants like polyatomic anions and organic compounds are present in the atmosphere, soils, rivers, and lakes. SERS is a very promising technique for the detection of such pollutants in the environment. A few novel SERS sensors have been made for sensitive detection of soil and water contaminants that are creating an impact on the environment and non-target animals. For example, polycyclic aromatic hydrocarbons (PAHs), a toxic pollutant in the atmosphere was determined by Huang et al. group by combining SERS with magnetic extraction. PAH shows high performance because of its structure which is quite similar to other compounds that gives excellent SERS such as porphyrins, rhodamine, fluorescein, crystal violet, nile red. All these molecules (and PAHs) have conjugated aromatic rings. Therefore, SERS has always shown very good results in PAH detection compared to other techniques as it can easily generate SERS spectra of different components in PAH. Limit of detection (LOD) of PAH's from Huang et al.'s work was 10^{-10} mol/L and for polychlorinated biphenyls (PCBs) detection was 10^{-7} mol/L **[88-90]**. Compared to the SERS detection limit with SLIPSERS, Yang et al. has further enhanced LOD to a nanomolar level that gives a subject of future investigation on various simple and complex chemical contaminants with just a proof- of - concept done previously.

Another work of Liu and co-workers **[91]** developed a SERS-based method to detect three different pesticides - Carbaryl, phosmet, and azinphosmethyl extracted from the surfaces of apples and

tomatoes. Using multivariate statistical techniques including Partial Least Squares (PLS) and Principal Component Analysis (PCA), both quantitative and qualitative analysis of the data was carried out. It involved a few steps of sample preparation, extraction, and detection with a detection limit within the range of 4.51 ppm for carbaryl, 6.51 for phosmet and 6.6 ppm for azinphosmethyl for apples and 5.5 ppm for carbaryl, 2.91 for phosmet and 2.94 ppm for azinphosmethyl on tomatoes. Chromatographic methods are currently employed for such detection which again as described before are time-consuming, complex and lengthy extraction procedures and requires highly trained staff for analysis. **[92-93]**

1.6.3. Pharmaceuticals

Several pieces of work have been done in this field of pharmaceutical applications of SERS**.** Pavel et al. **[121]** in their work have included SERS data on therapeutic drug categories like antibiotics, antimalarial, antipyretic, anticarcinogenic drugs, and other such classes. From these, antibiotics are the most common drugs used to treat human infections. These are also used for the treatment of animals and aquatic life. Any toxicity or residues remaining in these species and passed onto the food products is a serious concern. Liver and kidney are highly susceptible to residues given their biological function. Enrofloxacin (ENR) and chloramphenicol are commonly used antibiotics in chickens for the treatment of infections of the respiratory system and various other bacterial diseases **[94]**. However, antibiotic residues in food products are of great concern because of the potential to develop antibacterial resistance to these drugs in humans. SERS has the potential to detect such antibiotics by functionalising the substrate with an active group which helps in rapid detection of trace amounts.

1.7. Focus on analytical applications of SERS

As already discussed before, the sensitivity of SERS is demonstrated by the observation of scattering from single-molecule. Single-molecule SERS only confirms that there is at least one molecule generating Raman scattering but not the total number of molecules (or concentration) in the sample and so the conditions used for single-molecule SERS are not entirely appropriate for

analytical applications. Some approaches have been suggested for improving the analytical performance of SERS, such as ensuring the analyte adheres firmly to the nanoparticle surface **[122]**, and attempts to either localise the analyte to a small region of the substrate, or reduce the volume of the sample to increase the local concentration and thereby generate scattering from a more significant fraction of the sample (as discussed at the end of Section 1.1).

1.7.1. Increasing local concentration by controlled drying

One approach to increasing the local concentration is by controlled drying of a small volume (droplet) of the analyte solution. Controlled drying refers to the ability to control the shape of the analyte droplet by control over the interfacial energy between the analyte solution and the substrate.

One approach is to place a small droplet on the tip of a nanostructure with a very small cross-sectional area **[96]**. The surface tension of the solution holds the droplet on the tip, and the droplet evaporates leaving the analyte concentrated at the end of the nanostructure tip, which is then placed at the focal point of the Raman collection optics.

If droplets are allowed to dry on flat surfaces, the Marangoni ("coffee ring") effect is often observed which results in the analyte being deposited in rings as the droplet slowly evaporates. The effect is a combination of many factors, one that is relevant to controlling drying of a droplet is known as "contact line pinning," which occurs when the contact line between the liquid and solid becomes fixed. If the contact line is fixed, then the droplet evaporates from the centre of the droplet, outwards, towards the contact line. This results in a build-up of an analyte at the contact line (and, eventually, the formation of a "coffee ring") as shown in Figure 1.7(a).
Under these conditions, the analyte is spread over the circumference of the ring (which will be roughly the same size as the diameter of the droplet) and only a small fraction of the analyte will be in the focal volume of the focused laser beam. Contact line pinning can be reduced by lowering the interfacial energy between the solid and liquid and hydrophobic, superhydrophobic, and ultimately, omniphobic substrates all reduce contact line pinning compared to high energy solid surfaces (e.g., glass). If contact line pinning can be reduced, or ideally, removed, then evaporation occurs uniformly over the approximately spherical surface of the droplet, leading to the minimum possible volume of dried sample (a few microns in ideal conditions, depending on the mass of

analyte present). Typical focal volumes for microscope objectives have dimensions of a few microns so it would be possible to acquire Raman scattering from every molecule in the sample if the sample is dried without contact angle pinning.

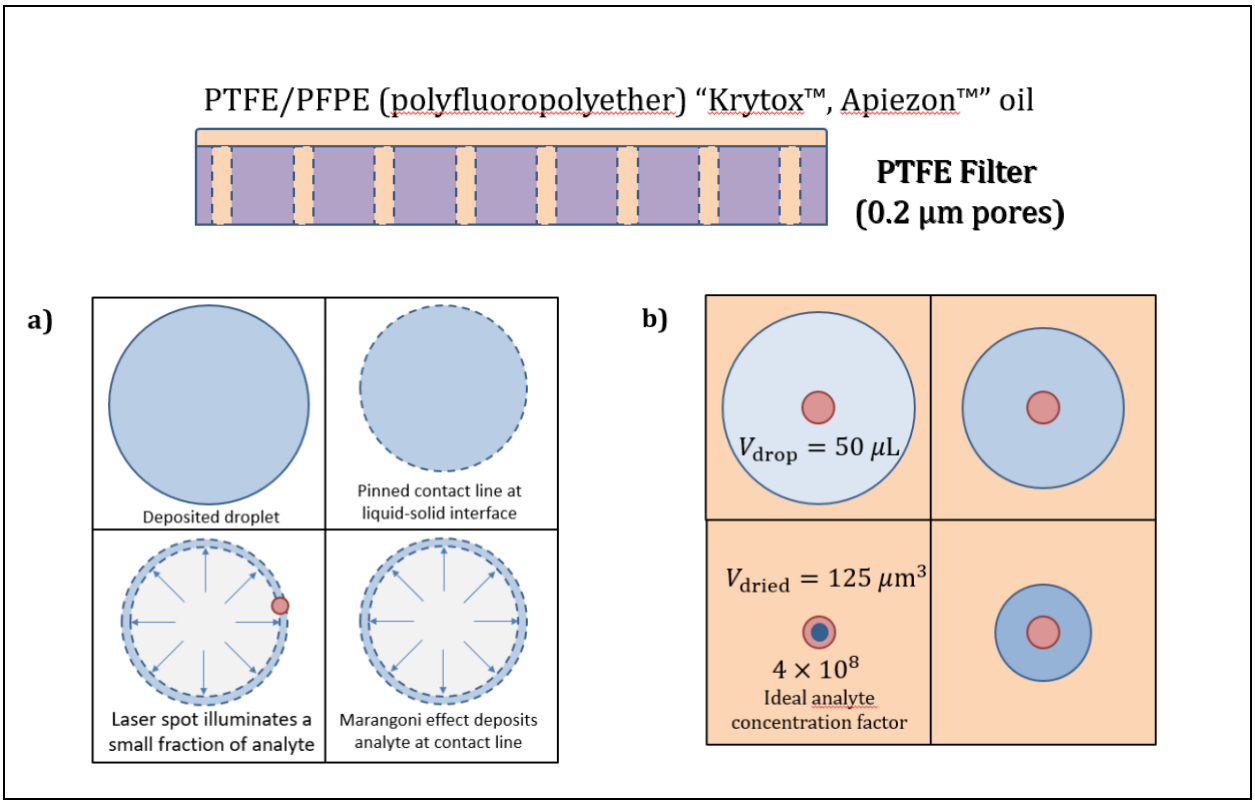

Figure 1. 7. Top. The SLIPS surface (polyfluoropolyether oil on porous PFTE). Bottom left. Drying process on high surface energy substrate. The diameter of the Marangoni ring would be approximately 900 µm for a 50 µL droplet. Laser spot (not to scale) diameter is approximately 2µm. Bottom Right. Drying process on omniphobic SLIPS substrate, without contact line pinning.

1.7.2. Omniphobic substrates

The need for substrates that can control droplet drying, and in particular avoid contact line pinning has been described above. Contact line pinning can be avoided by using smooth interfaces with low interfacial energy. Surfaces can obtain superhydrophobic properties by creating a Cassie-Baxter wetting regime using nanoscale surface structures (e.g. lotus leaf). However, the nanoscale structures eventually lead to contact line pinning as the interfacial energy starts to dominate surface tension at very small liquid volumes, and capillary action draws the liquid into the nanoscale cavities on the surface.

Thus, surface with very low interfacial energy and atomically smooth interfaces are required to avoid contact line pinning. A very effective method for creating atomically smooth interfaces is to use a thin layer of a low energy liquid on a suitable substrate.

The Pitcher Plant has provided the inspiration for such surfaces by demonstrating that liquids over porous surfaces provide the required properties. Wong et al. reported these surfaces as slippery liquid-infused porous surface (SLIPS) inspired by Nepthenes pitcher plant **[99]**. These SLIPS surfaces can repel both aqueous and non-aqueous solvent and are classified as omniphobic surfaces. SLIPS surface also allow prevent contact line pinning and give rise to a drying process as described in Figure 1.7 (bottom right) where the droplet dries to the smallest possible volume, leading to not only a significant increase in effective concentration but a very high hot-spot density when silver nanoparticles are included in the droplet along with the analyte. Thus, SLIPS substrates provide two significant advantages for SERS applications.

There are various methods for generating omniphobic surfaces by using different lubricants on the hydrophobic surface. Lynn et al. prepared an omniphobic surface by lubricating the hydrophobic surface and then placed for repeated chemical bath treatment for fabricating robust surface to get a nice smooth layer **[100]**. Tesler et al. prepared SLIPS surfaces by coupling of electrodepositions of tungstite films on steel and finally lubricating with Krytox which is polyfluoropolyether oil **[101]**. Wang et al. prepared a roughened surface on aluminium after fluorinating the surface and then lubricating **[102]**. Zhang et al. prepared the first superhydrophobic surface by depositing fluorinated silicone nanofilaments on glass surfaces and then fabricating by lubricant **[103]**.Yang et al. prepared a SLIPS surface by lubricating a Teflon membrane with Krytox 103**[9]** as shown in Figure 1. 7.

1.7.3. Omniphobic substrate - SLIPSERS

The SLIPS surface provides an ideal SERS substrate. SLIPS coupled with SERS is commonly called as SLIPSERS.

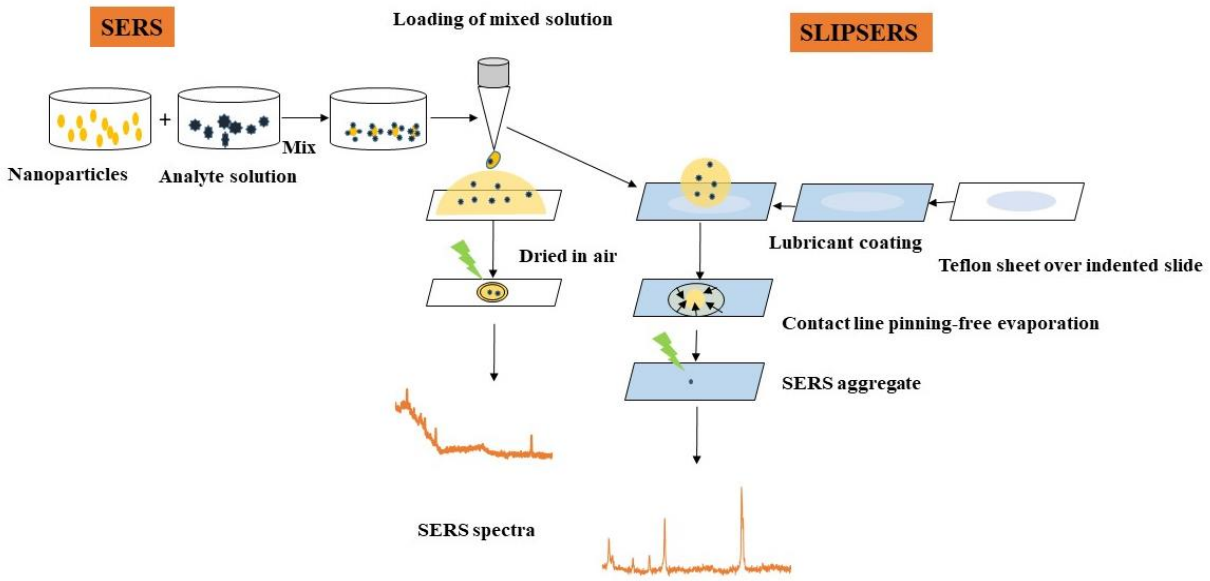

Figure 1. 8. Conventional SERS and concept of SLIPSERS

SLIPS surface is formed by a hydrophobic liquid filling the pores of a Teflon filter. The teflon filter is a standard polytetrafluoroethylene (PTFE) membrane filter, then a polyfluoropolyether liquid is dropped onto the surface, capillary action draws the liquid and the result is a slippery surface to which nothing adheres. The intention was to develop a substrate that gradually and uniformly shrinks the size of liquid volume on drying which leads to small densely packed silver nanoparticle aggregates, so a better signal can be obtained. Other surfaces are unable to perform in a similar way whereas SLIPS can do it.

It has been observed that if a droplet of liquid is placed on any normal surface, when the liquid evaporates, the target molecules are left in random deposits with weak signals. But if all the molecules can be clustered among the silver nanoparticles, they will produce a very strong Raman signal. Although there are several pieces of work **[115,116]** that allow researchers to concentrate molecules on a surface, those techniques mostly work with water as the medium whereas SLIPS can be used with any organic liquid.

Figure 1.8. represents the concept of SLIPSERS of how lubricating fluid, Krytox GPL-K10321 is fabricated onto a Teflon membrane, a nanoporous polymer, to obtain smooth film over it creating free of pinning surface.

The strategy in this work is to develop this substrate and test this with a simple matrix (analytes in aqueous solutions) and then more complex matrices. Hence, this can be called as a universal platform that allows enrichment and delivery of targets into the SERS-sensitive sites called 'hot spots' for detection in both aqueous and non-aqueous fluids (Yang et al. 2016) by controlled drying of analyte solutions into a small volume. Working on this technique helped to understand how the superhydrophobic interaction of surfaces vary with different analytes and how different structures can improve SERS from single molecule detection of simple analytes of environmental concern to biomolecule detection **[104]**. SLIPSERS technique has opened doors for a wide variety of applications including medical diagnostics, environmental monitoring, and analytical chemistry, and allows analysis of solid, liquid and even gaseous samples.

It is quite challenging to apply this SLIPSERS technique to biological samples and suffers from a few limitations like:

1. Poor adhesion between biological matrix and lubricating fluid results to wetting and dispersed the drop over the substrate. This means weak bonding between the substrate and various matrices adsorbed on the surface.
2. The lubricant is lost after evaporation **[99,101]**.
3. For nanostructures, mechanical robustness is required for high contact angle which reduces smoothness **[124]**.
4. Biological samples prevent close-packed structures from forming will decrease the hotspot density.

Figure 1.8 shows the SERS and SLIPSERS methods for comparison. Both methods require adhesion of the analyte to the silver nanoparticle surface. With SERS detection a droplet of the silver nanoparticle suspension (loaded with analyte) can dry on a standard substrate (e.g., glass), with strong wetting and contacting line pinning during drying resulting in the nanoparticles being dispersed over the substrate. **[105]** Subsampling may occur during collection of Raman scattering (i.e., some positions may show very little, or no signal, other positions, which contain high hotspot density in silver nanoparticle aggregates will show strong signal).

The controlled drying on the SLIPS surface concentrates the silver nanoparticles into a small aggregate with a consistently high hotspot density and a strong signal can be observed from a much higher proportion of the sample. An advantage of SLIPSERS in this situation is that the small sample volume and therefore high analyte concentration favours adhesion of the analyte to the nanoparticle surface. Hence, it can act as a universal platform for multiple analytes in highly diluted aqueous and non-aqueous solutions.

The following chapters will discuss applications of SLIPSERS for detection in simple aqueous media (Chapter 3: Ultra-sensitive SERS detection of brodifacoum and sodium monofluoroacetate in aqueous solution) and complex biological matrices (Chapter - 6 highly sensitive SERS detection and quantification of lidocaine hydrochloride in deer antler velvet).

1.8. Dissertation Organization

The unique ability to detect molecules of an analyte at very low concentration in a chemical and biological environment using surface-enhanced Raman scattering (SERS) makes the spectroscopy of considerable interest. The primary goal of this study is to continue this development and to look for new applications in fields such as food security, environmental applications and biomedical applications **[6, 8]**

This dissertation is organised into six sections.

Chapter 1 discussed above includes the literature review which led to the motivation of this dissertation. Also outlining the strengths and weaknesses of each approach focussing on minimal sample preparation time, faster speed of analysis, prevention of sample contamination and preservation of evidential material which makes SERS as the best technique.

Chapter 2 describes the investigation of a range of potential SERS substrates.

Following four research chapters are presented as a separate manuscript.

Chapter 3 explains about SERS using omniphobic substrate, SLIPS that overcomes the drawback faced by SERS regarding a collection of hot-spots and delivering ultra -sensitive and enhanced Raman signal of brodifacoum and 1080. Both these compounds are under the category of rodenticides, but both behave quite differently in the collection by SERS extending to the lowest detection concentration to picomolar level. This has demonstrated the versatility in terms of types of an analyte.

Chapter 4 investigates the application of SLIPSERS substrate for the detection of brodifacoum and 1080 in a complex matrix, milk, with the objective of attaining highly sensitive and specific detection.

Chapter 5 investigates the performance of line-scan Raman spectroscopy for detection and imaging of lidocaine hydrochloride. This analysis is useful in finding out the spectral variations and the most significant modes which are contributing these variations using Principal Component Analysis (PCA).

Chapter 6 extends the LHC drug detection from dog plasma to deer antler velvet. Several analytical methods have been published for detection of LHC in various biological fluids like serum, urine, plasma but detection of LHC residues in antler velvet is still novel. This work compares the reproducibility and sensitivity of SLIPSERS with other bioanalytical techniques

All other techniques are quite time-consuming, difficult and involve a lot of costs but SLIPSERS solved this problem and created a unique place through this work. This dissertation concludes with a general summary of all the work done and highlights the future work for this exciting approach of detection using SERS.

References:

1. Witkowska, E., Korsak, D., Kowalska, A., Księżopolska-Gocalska, M., Niedziółka-Jönsson, J., Roźniecka, E., Michałowicz, W., Albrycht, P., Podrażka, M. & Hołyst, R. 2017, 'Surface-enhanced Raman spectroscopy introduced into the International Standard Organization (ISO) regulations as an alternative method for detection and identification of pathogens in the food industry', *Analytical and bioanalytical chemistry*, vol. 409, no. 6, pp. 1555-67.
2. Simonne, A., Nille, A., Evans, K. & Marshall Jr, M. 2004, 'Ethnic food safety trends in the United States based on CDC foodborne illness data', *Food Protection Trends*, vol. 24, no. 8, pp. 590-604.
3. Jaworska, A., Fornasaro, S., Sergo, V. & Bonifacio, A. 2016, 'Potential of surface enhanced raman spectroscopy (SERS) in therapeutic drug monitoring (TDM). A critical review', *Biosensors*, vol. 6, no. 3, p. 47.
4. Álvarez-Ordóñez, A., Prieto, M., Bernardo, A., Hill, C. & López, M. 2012, 'The acid tolerance response of Salmonella spp.: an adaptive strategy to survive in stressful environments prevailing in foods and the host', *Food Research International*, vol. 45, no. 2, pp. 482-92.
5. Doering WE, Nie S. 2002. Single-molecule and single-nanoparticle SERS: examining the roles of surface active sites and chemical enhancement. *J Phys Chem B* 106(2): 311-7.
6. Kim, H., Kosuda, K.M., Van Duyne, R.P. & Stair, P.C. 2010, 'Resonance Raman and surface-and tip-enhanced Raman spectroscopy methods to study solid catalysts and heterogeneous catalytic reactions', *Chemical Society Reviews*, vol. 39, no. 12, pp. 4820-44.
7. Alvarez-Puebla, R.A. & Liz-Marzan, L.M. 2012, 'Traps and cages for universal SERS detection', *Chemical Society Reviews*, vol. 41, no. 1, pp. 43-51.
8. Wang, Y., Yan, B. & Chen, L. 2012, 'SERS tags: novel optical nanoprobes for bioanalysis', *Chemical reviews*, vol. 113, no. 3, pp. 1391-428.
9. Yang, S., Dai, X., Stogin, B., & Wong, T. (2016) Ultrasensitive surface-enhanced Raman scattering detection common fluids. *Proceedings of the National Academy of Science,*113(2),268-273.
10. Albrecht, A.C. 1961, 'On the theory of Raman intensities', *The Journal of Chemical Physics*,

vol. 34, no. 5, pp. 1476-84.

11. Srivatsan, T. 2014. Practical Raman Spectroscopy: An Introduction: Peter Vandenabeele, *Wiley, John & Sons, Incorporated*, 2013, 192 Pp., ISBN: 9780470683187. Taylor & Francis.
12. Myers, A.B. 1997, '"Time-Dependent"Resonance Raman Theory', *Journal of Raman spectroscopy*, vol. 28, no. 6, pp. 389-401.
13. Haynes CL, McFarland AD, Van Duyne RP. 2005a. Surface-enhanced Raman spectroscopy. *Anal Chem* 77(17): 338a-346a.
14. Fofang, N.T., Grady, N.K., Fan, Z., Govorov, A.O. & Halas, N.J. 2011, 'Plexciton dynamics: exciton− plasmon coupling in a J-aggregate− Au nanoshell complex provides a mechanism for nonlinearity', *Nano letters*, vol. 11, no. 4, pp. 1556-60.
15. Wilson, E.B., Decius, J.C. & Cross, P.C. 1980, *Molecular vibrations: the theory of infrared and Raman vibrational spectra*, Courier Corporation.
16. Rimai, L., Heyde, M. & Gill, D. 1973, 'Vibrational spectra of some carotenoids and related linear polyenes. Raman spectroscopic study', *Journal of the American Chemical Society*, vol. 95, no. 14, pp. 4493-501.
17. Haynes CL, Yonzon CR, Zhang XY, Van Duyne RP. 2005b. Surface-enhanced Raman sensors: early history and the development of sensors for quantitative biowarfare agent and glucose detection. *J Raman Spectrosc* 36(6-7): 471-84.
18. Zumbusch, A., Holtom, G.R. & Xie, X.S. 1999, 'Three-dimensional vibrational imaging by coherent anti-Stokes Raman scattering', *Physical review letters*, vol. 82, no. 20, p. 4142.
19. Le Ru, E.C., Meyer, M. & Etchegoin, P.G. 2006, 'Proof of single-molecule sensitivity in surface enhanced Raman scattering (SERS) by means of a two-analyte technique', *The journal of physical chemistry B*, vol. 110, no. 4, pp. 1944-8.
20. Le Ru, E., Blackie, E., Meyer, M. & Etchegoin, P.G. 2007, 'Surface enhanced Raman scattering enhancement factors: a comprehensive study', *The Journal of Physical Chemistry C*, vol. 111, no. 37, pp. 13794-803.
21. Etchegoin, P.G. & Le Ru, E. 2008, 'A perspective on single molecule SERS: current status and future challenges', *Physical Chemistry Chemical Physics*, vol. 10, no. 40, pp. 6079-89.
22. Le Ru, E.C. & Etchegoin, P.G. 2012, 'Single-molecule surface-enhanced Raman spectroscopy', *Annual Review of Physical Chemistry*, vol. 63, pp. 65-87.
23. Le Ru, E. C. & E Etchegoin, P. G. 2013. Quantifying SERS enhancements. *MRS bulletin*,

38, 631-640.

24. Kodali AK,BhargavaR. 2010. Nanostructured probes to enhance optical and vibrational spectroscopic imaging for biomedical applications. In *The Oxford Handbook of Nanoscience and Technology.* Vol. 3: Applications, ed. AV Narlikar, YY Fu, pp. 539–67. Oxford, UK: Oxford Univ. Press. 856 pp.
25. Kelley, A. M. 2007. A molecular spectroscopic description of optical spectra of J-aggregated dyes on gold nanoparticles. *Nano letters*, 7, 3235-3240.
26. Lombardi, J. R. & Birke, R. L. 2009. A unified view of surface-enhanced Raman scattering. *Accounts of chemical research,* 42**,** 734-742.
27. Kneipp, K., Moskovotis, M. & Kneipp, H. 2007. Surface-enhanced Raman scattering. *Physics Today,* 60**,** 40.
28. Koo, T.-W., Chan, S., Sun, L., SU, X., Zhang, J. & Berlin, A. A. 2004. Specific chemical effects on surface-enhanced Raman spectroscopy for ultra-sensitive detection of biological molecules. *Applied spectroscopy,* 58**,** 1401-1407.
29. McNay, G., Eustace, D., Smith, W. E., Faulds, K. & Graham, D. 2011. Surface-enhanced Raman scattering (SERS) and surface-enhanced resonance Raman scattering (SERRS): a review of applications. *Applied spectroscopy*, 65, 825-837.
30. Jensen, L. & Schatz, G.C. 2006, 'Resonance Raman scattering of rhodamine 6G as calculated using time-dependent density functional theory', *The Journal of Physical Chemistry A*, vol. 110, no. 18, pp. 5973-7.
31. Fleischmann, M., Hendra, P.J. & McQuillan, A.J. 1974, 'Raman spectra of pyridine adsorbed at a silver electrode', *Chemical Physics Letters*, vol. 26, no. 2, pp. 163-6.
32. Schatz, G.C. 1984, 'Theoretical studies of surface enhanced Raman scattering', *Accounts of Chemical Research*, vol. 17, no. 10, pp. 370-6.
33. Nguyen, H., Park, J., Kang, S. & Kim, M. 2015, 'Surface plasmon resonance: a versatile technique for biosensor applications', *Sensors*, vol. 15, no. 5, pp. 10481-510.
34. Smitha, S., Gopchandran, K., Ravindran, T. & Prasad, V. 2011, 'Gold nanorods with finely tunable longitudinal surface plasmon resonance as SERS substrates', *Nanotechnology*, vol. 22, no. 26, p. 265705.
35. Willets, K.A. & Van Duyne, R.P. 2007, 'Localized surface plasmon resonance spectroscopy and sensing', *Annu. Rev. Phys. Chem.*, vol. 58, pp. 267-97.

36. Kobayashi, M., Juillerat, F., Galletto, P., Bowen, P. & Borkovec, M. 2005, 'Aggregation and charging of colloidal silica particles: effect of particle size', *Langmuir*, vol. 21, no. 13, pp. 5761-9.
37. Kim, T., Lee, K., Gong, M.-s. & Joo, S.-W. 2005, 'Control of gold nanoparticle aggregates by manipulation of interparticle interaction', *Langmuir*, vol. 21, no. 21, pp. 9524-8.
38. Hunter, R. 1992, 'Foundations of Colloid Science, Clarendon Pres', *London, Great Britain*.
39. Lee, T.G., Kim, K. & Kim, M.S. 1991, 'Raman scattering of α-toluenethiol adsorbed on silver sol', *Journal of Raman spectroscopy*, vol. 22, no. 6, pp. 339-44.
40. Segets, D., Marczak, R., Schäfer, S., Paula, C., Gnichwitz, J.-F., Hirsch, A. & Peukert, W. 2011, 'Experimental and theoretical studies of the colloidal stability of nanoparticles− a general interpretation based on stability maps', *ACS nano*, vol. 5, no. 6, pp. 4658-69.
41. Zheng, J. & He, L. 2014, 'Surface-Enhanced Raman Spectroscopy for the Chemical Analysis of Food', *Comprehensive reviews in food science and food safety*, vol. 13, no. 3, pp. 317-28.
42. Kennedy B. J., Spaeth S., Dickey M., Carron K. T. Determination of the distance dependence and experimental effects for modified sers substrates based on self-assembled monolayers formed using alkanethiols. *The Journal of Physical Chemistry B*. 1999; 103 (18):3640–3646.
43. Singh A. K., Khan S. A., Fan Z., et al. Development of a long-range surface-enhanced Raman spectroscopy ruler. *Journal of the American Chemical Society*. 2012; 134 (20):8662–8669.
44. Kukushkin V. I., Van'kov A. B., Kukushkin I. V. Long-range manifestation of surfaceenhanced Raman scattering. *JETP Letters*. 2013;98 (2):64–69.
45. Dieringer J. A., McFarland A. D., Shah N. C., et al. Surface enhanced Raman spectroscopy: new materials, concepts, characterization tools, and applications. *Faraday Discussions*. 2006; 132:9–26.
46. Israelsen, N. D., Hanson, C. & Vargis, E. 2015. Nanoparticle properties and synthesis effects on surface-enhanced Raman scattering enhancement factor: an introduction. *The Scientific World Journal*, 2015.
47. Le Ru, E. C., Grand, J., Sow, I., Somerville, W. R., Etchegoin, P. G., Treguer-Delapierre, M., Charron, G., Felidj, N., Levi, G. & Aubard, J. 2011. A scheme for detecting every single target molecule with surface-enhanced Raman spectroscopy. *Nano letters*, 11, 5013-5019.
48. Le Ru, E. C. & E Etchegoin, P. G. 2013. Quantifying SERS enhancements. *MRS bulletin*,

38, 631-640.

49. Le Ru, E. & E Etchegoin, P. 2009. Phenomenological local field enhancement factor distributions around electromagnetic hot spots. AIP.
50. Lee, A.; Andrade, G. F. S.; Ahmed, A.; Souza, M. L.; Coombs, N.; Tumarkin, E.; Liu, K.; Gordon, R.; Brolo, A. G.; Kumacheva, E. Probing Dynamic Generation of Hot-Spots in Self-Assembled Chains of Gold Nanorods by Surface-Enhanced Raman Scattering. *J. Am. Chem. Soc*. 2011, 133, 7563–7570
51. Chen, T.; Wang, H.; Chen, G.; Wang, Y.; Feng, Y.; Teo, W. S.; Wu, T.; Chen, H. Hotspot-Induced Transformation of Surface-Enhanced Raman Scattering Fingerprints. *ACS Nano* 2010, 4, 3087–3094
52. Chen, T.; Du, C.; Tan, L. H.; Shen, Z.; Chen, H. Site-selective localization of analytes on gold nanorod surface for investigating field enhancement distribution in surface-enhanced Raman scattering. *Nanoscale* 2011, 3, 1575–1581
53. Lin M. The application of surface-enhanced Raman spectroscopy to identify and quantify chemical adulterants or contaminants in foods. In: Li-Chan E, Griffiths P, Chalmers J, editors. *Applications of vibrational spectroscopy in food science*. Chichester: John Wiley &Sons; 2010
54. Luo, S.-C., Sivashanmugan, K., Liao, J.-D., Yao, C.-K. & Peng, H.-C. 2014. Nanofabricated SERS-active substrates for single-molecule to virus detection in vitro: A review. *Biosensors and Bioelectronics*, 61, 232-240.
55. Sun, M., Fang, Y., Yang, Z. & Xu, H. 2009. Chemical and electromagnetic mechanisms of tip-enhanced Raman scattering. *Physical Chemistry Chemical Physics*, 11, 9412-9419.
56. Tao, A., Kim, F., Hess, C., Goldberger, J., He, R., Sun, Y., Xia, Y. & Yang, P. 2003. Langmuir− Blodgett silver nanowire monolayers for molecular sensing using surface-enhanced Raman spectroscopy. *Nano letters*, 3, 1229-1233.
57. Banholzer, M. J., Millstone, J. E., Qin, L. & Mirkin, C. A. 2008. Rationally designed nanostructures for surface-enhanced Raman spectroscopy. *Chemical Society Reviews*, 37, 885-897.
58. Huang, W. E., Li, M., Jarvis, R. M., Goodacre, R. & Banwart, S. A. 2010. Shining light on the microbial world: the application of Raman microspectroscopy. *Advances in applied microbiology. Elsevier*.

59. Wang, X., Song, C., Geng, K., Zeng, F. & Pan, F. 2006. Luminescence and Raman scattering properties of Ag-doped ZnO films. *Journal of Physics D: Applied Physics*, 39, 4992.
60. Gomez, M. & Lazzari, M. 2014. Reliable and cheap SERS active substrates. *Materials Today*, 7, 358-359.
61. Jaworska, A., Fornasaro, S., Sergo, V. & Bonifacio, A. 2016. Potential of surface enhanced Raman spectroscopy (SERS) in therapeutic drug monitoring (TDM). A critical review. *Biosensors*, 6, 47.
62. Alvarez-Pubela, R. A. & Liz-Marzan, L. M. 2012. SERS detection of small inorganic molecules and ions. *Angewandte Chemie International Edition*, 51, 11214-11223.
63. Deepak, F. L. 2017. *Metal Nanoparticles and Clusters: Advances in Synthesis, Properties and Applications*, Springer.
64. McNay, G., Eustace, D., Smith, W.E., Faulds, K. & Graham, D. 2011, 'Surface-enhanced Raman scattering (SERS) and surface-enhanced resonance Raman scattering (SERRS): a review of applications', *Applied spectroscopy*, vol. 65, no. 8, pp. 825-37.
65. Kumar, V. & Yadav, S.K. 2009, 'Plant-mediated synthesis of silver and gold nanoparticles and their applications', *Journal of Chemical Technology & Biotechnology*, vol. 84, no. 2, pp. 151-7.
66. Pacioni, N.L., Borsarelli, C.D., Rey, V. & Veglia, A.V. 2015, 'Synthetic routes for the preparation of silver nanoparticles', *Silver nanoparticle applications, Springer*, pp. 13-46.
67. Lee, P. & Meisel, D. 1982, 'Adsorption and surface-enhanced Raman of dyes on silver and gold sols', The Journal of Physical Chemistry, vol. 86, no. 17, pp. 3391-5.
68. Frank, A. J., Cathcart, N., Maly, K. E. & Kitaev, V. 2010. Synthesis of silver nanoprisms with variable size and investigation of their optical properties: a first-year undergraduate experiment exploring plasmonic nanoparticles. *Journal of Chemical Education*, 87, 1098-1101.
69. Smith, W. 2008. Practical understanding and use of surface enhanced Raman scattering/surface enhanced resonance Raman scattering in chemical and biological analysis. *Chemical Society Reviews*, 37, 955-964.
70. Wang, H. H., Liu, C. Y., Wu, S. B., Liu, N. W., Peng, C. Y., Chan, T. H., Hsu, C. F., Wang, J. K. & Wang, Y. L. 2006. Highly raman enhancing substrates based on silver nanoparticle arrays with tunable sub-10 nm gaps. *Advanced Materials*, 18, 491-495.

71. Santos, J.J., Toma, S.H., Corio, P. & Araki, K. 2017, 'Key role of surface concentration on reproducibility and optimization of SERS sensitivity', *Journal of Raman Spectroscopy*, vol. 48, no. 9, pp. 1190-5.
72. Kneipp, J., Kneipp, H. & Kneipp, K. 2008, 'SERS—a single-molecule and nanoscale tool for bioanalytics', *Chemical Society Reviews*, vol. 37, no. 5, pp. 1052-60.
73. Kneipp, K., Kneipp, H., Abdali, S., Berg, R.W. & Bohr, H. 2004, 'Single molecule Raman detection of enkephalin on silver colloidal particles', *Journal of Spectroscopy*, vol. 18, no. 3, pp. 433-40.
74. Natan, M.J. 2006. Concluding remarks-surface enhanced Raman scattering. *Faraday discussions,* 132, 321-328.
75. X.M. Lin, Y. Cui, Y.H. Xu, B. Ren, Z.Q. Tian 2009. Surface-enhanced Raman spectroscopy: substrate-related issues. *Analytical and bioanalytical chemistry*, 394, 1729-1745.
76. Bantz, K. C., Meyer, A. F., Wittenberg, N. J., IM, H., Kurtulus, Ö., Lee, S. H., Lindquist, N. C., Oh, S.-H. & Haynes, C. L. 2011. Recent progress in SERS biosensing. *Physical Chemistry Chemical Physics*, 13, 11551-11567.
77. Prochazka, M. 2016. Bioanalytical SERS Applications. *Surface-Enhanced Raman Spectroscopy*. Springer.
78. Cao, Y.C., Jin, R. J., Nam, M., Thaxton, C.S., Mirkin, C.A. 2003. Raman dye-labeled nanoparticle probes for proteins. *Journal of the American Chemical Society*, 125, 14676
79. Chen, Z., Tabakman, S.M., Goodwin, A.P., Kattah, M.G., Daranciang, D., Wang, X., Zhang, G., Li, X., Liu, Z. & Utz, P.J. 2008, 'Protein microarrays with carbon nanotubes as multicolor Raman labels', *Nature biotechnology*, vol. 26, no. 11, p. 1285.
80. Bell, S.E. & Sirimuthu, N.M. 2006, 'Surface-enhanced Raman spectroscopy (SERS) for sub-micromolar detection of DNA/RNA mononucleotides', *Journal of the American Chemical Society*, vol. 128, no. 49, pp. 15580-1.
81. Cao, Y.C., Jin, R. & Mirkin, C.A. 2002, 'Nanoparticles with Raman spectroscopic fingerprints for DNA and RNA detection', *Science*, vol. 297, no. 5586, pp. 1536-40.
82. Cao, Y.C., Jin, R. & Mirkin, C.A. 2002, 'Nanoparticles with Raman spectroscopic fingerprints for DNA and RNA detection', *Science*, vol. 297, no. 5586, pp. 1536-40.
83. Cotton, T.M., Kim, J.H. & Chumanov, G.D. 1991, 'Application of surface-enhanced Raman spectroscopy to biological systems', *Journal of Raman spectroscopy*, vol. 22, no. 12, pp.

729-42.

84. Fan, C., Hu, Z., Mustapha, A. & Lin, M. 2011, 'Rapid detection of food-and waterborne bacteria using surface-enhanced Raman spectroscopy coupled with silver nanosubstrates', *Applied microbiology and biotechnology*, vol. 92, no. 5, pp. 1053-61.
85. Jarvis, R.M. & Goodacre, R. 2008, 'Characterisation and identification of bacteria using SERS', *Chemical Society Reviews*, vol. 37, no. 5, pp. 931-6.
86. Faulds, K., Jarvis, R., Smith, W.E., Graham, D. & Goodacre, R. 2008, 'Multiplexed detection of six labelled oligonucleotides using surface enhanced resonance Raman scattering (SERRS)', *Analyst*, vol. 133, no. 11, pp. 1505-12.
87. Koglin, E. & Séquaris, J.-M. 1986, 'Surface enhanced Raman scattering of biomolecules', *Analytical Problems*, Springer, pp. 1-57.
88. Tang, S., Li, Y., Huang, H., Li, P., Guo, Z., Luo, Q., Wang, Z., Chu, P.K., Li, J. & Yu, X.-F. 2017, 'Efficient enrichment and self-assembly of hybrid nanoparticles into removable and magnetic SERS substrates for sensitive detection of environmental pollutants', *ACS applied materials & interfaces*, vol. 9, no. 8, pp. 7472-80.
89. Song, D., Yang, R., Long, F. & Zhu, A. 2018. Applications of magnetic nanoparticles in surface-enhanced Raman scattering (SERS) detection of environmental pollutants. *Journal of Environmental Sciences*.
90. Lai, H., Xu, F. & Wang, L. 2018. A review of the preparation and application of magnetic nanoparticles for surface-enhanced Raman scattering. *Journal of materials science*, 1-22.
91. Liu, M., Hashi, Y., Song, Y., & Lin, J.-M. (2005). Simultaneous determination of carbamate and organophosphorus pesticides in fruits and vegetables by liquid chromatography–mass spectrometry. *Journal of Chromatography A*, 1097(1–2), 183–187.
92. Sentellas, S., Saurina, J., Hernández-Cassou, S., Galceran, M. T., & Puignou, L. S. (2001). Multivariate calibration methods for quantification in strongly overlapping capillary electrophoretic peaks. *Journal of Chromatography A*, 909(2), 259–269.
93. Grimalt, S., Pozo, Ó. J., Sancho, J. V., & Hernández, F. (2007). Use of liquid chromatography coupled to quadrupole time-of-flight mass spectrometry to investigate pesticide residues in fruits. *Analytical Chemistry*, 79(7), 2833–2843.
94. Xu, Y., Du, Y., Li, Q., Wang, X., Pan, Y., Zhang, H., Wu, T. & Hu, H. 2014. Ultrasensitive detection of enrofloxacin in chicken muscles by surface-enhanced Raman spectroscopy

using amino-modified glycidyl methacrylate-ethylene dimethacrylate (GMA-EDMA) powdered porous material. *Food Analytical Methods*, 7, 1219-1228.

95. Bizzarri, A.R. & Cannistraro, S. 2007, 'SERS detection of thrombin by protein recognition using functionalized gold nanoparticles', *Nanomedicine: Nanotechnology, Biology and Medicine*, vol. 3, no. 4, pp. 306-10.
96. Stewart, A., Murray, S. & Bell, S. 2015. Simple preparation of positively charged silver nanoparticles for detection of anions by surface-enhanced Raman spectroscopy. *Analyst*, 140, 2988-2994.
97. Gao, J., Zhang, N., Ji, D., Song, H., Liu, Y., Zhou, L., Sun, Z., Jornet, J.M., Thompson, A.C. & Collins, R.L. 2018, 'Superabsorbing Metasurfaces with Hybrid Ag–Au Nanostructures for Surface-Enhanced Raman Spectroscopy Sensing of Drugs and Chemicals', *Small Methods*, p. 1800045.
98. Lu, Y., He, G., Carmalt, C. J. & Parkin, I. P. 2016. Synthesis and characterization of omniphobic surfaces with thermal, mechanical and chemical stability. *RSC Advances,* 6**,** 106491-106499.
99. Wong, T.-S., Kang, S. H., Tang, S. K., Smythe, E. J., Hatton, B. D., Grinthal, A. & Aizenberg, J. 2011. Bioinspired self-repairing slippery surfaces with pressure-stable omniphobicity. *Nature,* 477**,** 443.
100. Manna, U. & Lynn, D. M. 2015. Fabrication of Liquid-Infused Surfaces Using Reactive Polymer Multilayers: Principles for Manipulating the Behaviors and Mobilities of Aqueous Fluids on Slippery Liquid Interfaces. *Advanced Materials,* 27**,** 3007-3012.
101. Tesler, A. B., Kim, P., Kolle, S., Howell, C., Ahanotu, O. & Aizenberg, J. 2015. Extremely durable biofouling-resistant metallic surfaces based on electrodeposited nanoporous tungstite films on steel. *Nature communications,* 6**,** 8649.
102. Wang, P., Zhang, D., Lu, Z. & Sun, S. 2016. Fabrication of slippery lubricant-infused porous surface for inhibition of microbially influenced corrosion. ACS applied materials & interfaces, 8, 1120-1127.
103. Zhang, J., Wu, L., Li, B., Li, L., Seeger, S. & Wang, A. 2014. Evaporation-induced transition from Nepenthes pitcher-inspired slippery surfaces to lotus leaf-inspired superoleophobic surfaces. *Langmuir,* 30**,** 14292-14299.
104. Kleinman, S. L., Fronteira, R. R., Henry, A.-I., Dieringer, J. A. & Van Duyne, R. P. 2013.

Creating, characterizing, and controlling chemistry with SERS hot spots. *Physical Chemistry Chemical Physics,* 15**,** 21-36.

105. Ouyang, L., Ren W., Zhu, L. & Irudayaraj, J. 2017. Prosperity to challenges: recent approaches in SERS substrate fabrication. *Reviews in Analytical Chemistry,* 36.
106. Levy, A., Andelman, D. & Orland, H. 2012. Dielectric constant of ionic solutions: A field-theory approach. *Physical review letters*, 108, 227801.
107. Le Ru, E., & Etchegoin, P. (2008). Principles of Surface-Enhanced Raman Spectroscopy: and related plasmonic effects: *Elsevier*.
108. Abalde-Cela S, Aldeanueva-Potel P, Mateo-Mateo C, Rodríguez-Lorenzo L, Alvarez-Puebla RA, Liz-Marzán LM. Surface-enhanced Raman scattering biomedical applications of plasmonic colloidal particles. *Journal of the Royal Society Interface*. 2010;7(suppl_4):S435-S50.
109. Zhao J, Pinchuk AO, McMahon JM, Li S, Ausman LK, Atkinson AL, et al. Methods for describing the electromagnetic properties of silver and gold nanoparticles. *Accounts of chemical research*. 2008;41(12):1710-20.
110. Dykstra HM, Hall SB, Waterland MR. A spectroelectrochemical investigation of nanoparticle and molecular resonances in surface enhanced Raman scattering from crystal violet and malachite green. *Journal of Raman Spectroscopy*. 2017;48(3):405-12.
111. Skoog D, Leary J. *Principles of Instrumental Analysis*, Harcourt Brace College Publishers. Fort Worth. 1992.
112. Long DA. *Raman spectroscopy*. New York. 1977:1-12.
113. Adar F. Depth resolution of the Raman microscope: Optical limitations and sample characteristics. 2010.
114. Kim H, Kosuda KM, Van Duyne RP, Stair PC. Resonance Raman and surface-and tip-enhanced Raman spectroscopy methods to study solid catalysts and heterogeneous catalytic reactions. *Chemical Society Reviews*. 2010;39(12):4820-44.
115. Song W, Psaltis D, Crozier KB. Superhydrophobic bull's-eye for surface-enhanced Raman scattering. *Lab on a Chip*. 2014; 14(20):3907-11.
116. Tan JMR, Ruan JJ, Lee HK, Phang IY, Ling XY. A large-scale superhydrophobic surface-enhanced Raman scattering (SERS) platform fabricated via capillary force lithography and assembly of Ag nanocubes for ultratrace molecular sensing. *Physical Chemistry Chemical*

Physics. 2014; 16(48):26983-90.

117. Jana D, Mandal A, De G. High Raman enhancing shape-tunable Ag nanoplates in alumina: a reliable and efficient SERS technique. *ACS applied materials & interfaces*. 2012; 4(7):3330-4.
118. Peticolas WL, Nafie L, Stein P, Fanconi B. Quantum theory of the intensities of molecular vibrational spectra. *The Journal of Chemical Physics*. 1970; 52(3):1576-84.
119. Rull F. The Raman effect and the vibrational dynamics of molecules and crystalline solids. *Raman Spectroscopy applied to Earth Sciences and Cultural Heritage*. 2012:1-60.
120. Ruedenberg K. Chemical Applications of Group Theory. By FA Cotton. *Inorganic Chemistry*. 1964; 3(5):784.
121. Pınzaru SC, Pavel IE. SERS and Pharmaceuticals. *Encyclopedia of Applied Spectroscopy*. 2011.
122. Meng Y, Lai Y, Jiang X, Zhao Q, Zhan J. Silver nanoparticles decorated filter paper via self-sacrificing reduction for membrane extraction surface-enhanced Raman spectroscopy detection. *Analyst*. 2013; 138(7):2090-5.
123. Phan HT, Haes AJ. What Does Nanoparticle Stability Mean? *The Journal of Physical Chemistry C*. 2019.
124. Wong T-S, Huang AP-H, Ho C-M. Wetting behaviors of individual nanostructures. *Langmuir*. 2009; 25(12):6599-603.

Chapter 2. Substrate Development

The beginning of this research started with the idea to develop a SERS method coupled with novel nanosubstrates and to evaluate its performance in detection, characterization, and quantification of different substances with a focus on environmental and food security applications. Being new to the SERS field, several substrate fabrication techniques were explored by the thesis author. The aim of the work in this chapter is to carry out a systematic investigation of SERS substrates, to determine the positive and negative features of each type of substrate and then select which one to select for this research.

There are several techniques in the literature to develop rapid, sensitive and suitable solid SERS substrates but they also have some drawbacks which needs to be addressed before adopting one technique for developing SERS substrate. Similarly, there are several companies like Real-Time Analyzers, Sigma Aldrich, Horiba Scientific, Ocean Optics and Mesophotonics that offer commercial SERS substrates with uniformity and high sensitivity **[61]**. Despite the progress in manufacturing these substrates, it is not yet obvious what specific applications are for a reproducible SERS substrate. These substrates are getting more popular for fast on-site detection, but this thesis involves the development of SERS substrate in the laboratory understanding the role of various optimization factors to get highly reproducible and quantifiable results. The main concerns are the high cost of fabrication, complex procedures, and shelf life, sensitivity to air, the need for specialized fabrication equipment and many others which may be beyond the reach to carry out on a frequent basis. These barriers drive the need to design a simple and accessible substrate used for most of the analytes **[43]**. In this chapter, firstly the most common methods were evaluated then based on the experience gained a substrate was prepared that was suitable for most of the analytes with the aim of developing low cost, simple and sensitive method.

For identifying a simple SERS substrate, we have set a few guidelines, which must fit the fabrication method for SERS substrates:

All the equipment and reagent can be easily found in a typical lab as daily routine chemicals and readily available equipment like centrifuges, sonicator, magnetic stirrers, and oven.

1. Minimal training required for sample preparation and how to use the equipment.
2. Easily fabricated with shelf life of at least six months.
3. Easy to use on Raman system without any complicated procedures of sample handling.

Keeping these criteria as a basis of identification, three substrate fabrication "classes" were investigated in this chapter:

a. Etched-silicon method: The first work begins with a *metal-assisted etching method* for developing SERS substrate and then understanding how morphology affects SERS activity and a chosen silicon substrate. The first experiment performed in search of a suitable SERS substrate was an adaptation of work presented by Benoit et al. **[1]** of preparing silver dendritic nanostructures via metal- assisted chemical deposition method in the form of stems, branches and leaf patterns using aqueous hydrofluoric acid (HF) and silver nitrate ($AgNO_3$) solution. The experimental procedure was followed with variation in HF, $AgNO_3$ concentration and etching time parameter. The growth mechanisms are discussed in the further section. Obtained samples were investigated by scanning electron microscope combined with energy dispersive X-ray (EDX) spectrophotometer. Scanning Electron microscopy (SEM) and EDX have revealed the presence of silver nanoparticles on a silicon wafer. Silver (Ag) nanoparticles showed different morphology with different concentration and a different time**.** **[2**] This method however suffered from lack of control of Ag network shape even when controlling etching parameters such as concentration of reactants. A high concentration of HF can form some randomly-aligned pores, i.e., voids within the surface, which can be the result of the increasing strain of HF movement inside the etched structures. This method has the potential of fabricating nanodevices and delivers promising results in the field of nanotechnology, but this study was performed in search of finding a simple method of detection of chemical and biological analytes.

b. Dendritic nanoparticles: The method involves developing SERS-active Ag dendritic nanostructures which provide a rapid and practical potential for onsite detection of trace level of toxins. These Ag dendritic nanostructures were tested to detect pesticide rhodamine 6G (R6G). Scanning Electron Microscopy examined the morphology of nanostructures. This method is good in terms of detection, but dendritic nature often results in variability and deterioration of the nanoparticles. This could lead to inconsistent results and lack of

reproducibility. Hence, it is a challenge to control all the parameters for successful detection.

c. Colloidal nanoparticles, the most popular method used since decades **[44]**: Silver (Ag) colloids-based nanostructures are the most common substrates for achieving strong SERS signals with high sensitivity. The hot spots formed between the nanoparticles provide ease for sensing analyte-using Raman. Kitaev et al. **[53]** method was used for the preparation of silver nanoparticles. We have used these nanoparticles for detecting R6G in aqueous solution in this chapter.

2.1. Preparation of silver nanostructures on silicon as SERS active substrate using metal-assisted chemical etching method

The metal-assisted chemical etching method was considered as a first choice in the search for active SERS substrate due to its low-cost, simplicity and sensitivity. Several publications of nano-dendrites formed by etching of silicon have been reported **[4-6]**. The objective of performing this experiment is to understand the surface characteristics of etched silicon over time which is an important parameter for the substrate stability.

Etched silicon has a large surface area and open pore structure which can yield highly sensitive SERS substrates. The objective is to obtain a substrate of nanoporosity which can be directly used for analyte detection. The main issue faced in fabricating silicon is controlling the size of nanoparticles etched on it. Hydrofluoric acid plays a double role; it maintains the size of nanoparticles and contributes to the adhesion of AgNPs onto the pores of Si substrate. It also reduces the ability of aggregation of AgNPs and leads to nanoparticles sizes. Different concentration of hydrofluoric acid was used as an electrolyte solution for etching silicon.

In this process, silver (I) ions are reduced to silver, and in the presence of fluoride ions, silicon is oxidized to Si (IV) in the form of soluble SiF_6^{2-} So the silver is deposited as silver metal nanostructures, into the cavities produced by the dissolution of the silicon. Silicon acts as both the anode and cathode in this process.

The morphology of the deposited layer, density and the average particle size, depends according to the literature, on two main factors: (1) the structure of the underlying silicon substrate, which is determined by the etching conditions, and (2) the deposition conditions, mainly the concentration of the metallic solution used and the deposition duration. The large surface area creates suitable nucleation sites. **[1, 3]** The synthesis includes pre-nucleation of silver nanoparticles inside the pores of an etched silicon wafer as seeds and on the apex of formed silicon nanowires, and subsequently self-organized growth of silver dendritic nanostructures.

2.1.1. Experimental

Reagents and materials: HF, ethanol, silver nitrate, silicon wafers, acetone, distilled water.

Safety procedures were followed while working with hydrofluoric acid. Few were listed below:

1. Material Safety Data Sheet (MSDS) was read before conducting the experiment.
2. First aid kit and HF spill kit were kept nearby.
3. The experiment was conducted in a fume hood in the presence of laboratory technician and supervisor.
4. Laboratory coat, acid resistant coat and safety glasses were worn by team.
5. Neoprene rubber gloves on the top of nitrile gloves was worn during the experiment.
6. All solutions, samples were properly labelled and kept in the fume hood.
7. Worked in a chemical compatible containment tray so if any HF spill happens, it can be discarded in a Hazardous waste container following the hazardous waste disposal procedures.
8. Experiment containers were kept close to each other to minimise the exposure.

A polished silicon wafer of size 2cm x 2cm was cut into slices and rinsed with acetone and ethanol to remove possible contaminants and for degreasing. After rinsing with distilled water and drying in a nitrogen atmosphere, the silicon slices were immediately immersed in the mixing of silver nitrate (0.013M) and hydrofluoric acid (5M) solution for a variable time of 20 seconds, 60 seconds

and 5 minutes at room temperature (24° C) (Figure 2.1). These initial experimental conditions were changed to observe the effect of each factor **[7]**. After etching, the samples were rinsed with deionised water and ethanol for 1 minute. The concentrations were varied with a factor two (lower or higher) with variable time frames. Scanning electron microscopy was employed for the microscopic characterization of the SERS substrate. ImageJ software was used to analyse the size distributions of the fractal nanostructures, that is, described as uneven structure composed of fragments whose structural design is repeated with self-similarity like trees where each branch divides again and again giving a repeated structure on every branch. **[60]**

All the measurements were carried out at room temperature.

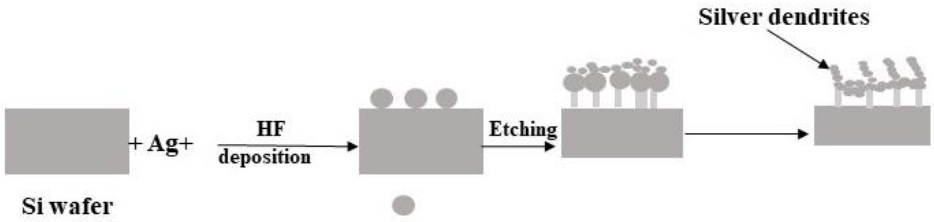

Figure 2. 1: Schematic representation of growth of silver dendrites shown as circles on silicon wafer etched with hydrofluoric acid.

2.1.2. Results and Discussion

Silver was chosen because it is the best SERS substrate. Metal assisted etching is done between an oxidizing agent and Si. **[45]**

At cathode, there is reduction of Ag+:

$Ag^{+} + e^{-} \rightarrow Ag$ $\quad E_0 = +0.79\ V$

At anode, Si substrate is dissolved on oxidation:

$Si + 2H_2O \rightarrow SiO_2 + 4H^{+} + 4e^{-}$ $\quad E_0 = +0.91\ V$

$SiO_2 + 6HF \rightarrow SiF_6^{2-} + 2H_2O + 2H^{+}$

Overall reaction:

$$SiO_2 + 4Ag^+ + 6HF \rightarrow SiF_6^{2-} + 4Ag + 6H^+$$

The mechanism of silver nanoparticle growth process on silicon surface starts immediately after immersion creating holes on the silicon surface in a few seconds. Ag nanoparticles are deposited on the Si surface and their development is restricted by Ag^+ diffusion. At the same time, few nanoparticles connect with each other and form a large network. This network due to Ag deposition results in the formation of silver dendrites clearly visible on the surface. It was observed during the process of etching; the Ag network has two layers: the bottom layer results from the oxidation of silicon while the top layer embedded over silicon is due to the reduction of Ag^+. As it grows, the silver network sinks into the silicon substrate. **[11]**

To obtain nanoparticles of desired length and diameter, the need is to optimise the etching parameters: [$AgNO_3$], [HF] and time. Three different concentration sets of HF and $AgNO_3$ were used to etch the silicon wafer for 20 seconds, 60 seconds and 5 minutes at room temperature (24°C).

i. 5 M HF+ 13mM $AgNO_3$,
ii. 2.5M HF + 88 mM $AgNO_3$,
iii. 10M HF + 5.3 mM $AgNO_3$

The experiment was conducted using 5 M HF+ 13mM $AgNO_3$ and then parameters changed to observe the effect. 5 M HF formed more densely packed silver nanoparticles covering most of the surface than deposited with the solution containing 2.5M HF.

Peng et al. proposed that different morphologies can be obtained with changing the concentration of HF. SEM was used to investigate samples for surface morphology. Figure 2.2, 2.3 and 2.4 shows that the surface of silicon layers etched for different times with different concentrations.

At low HF concentrations, SiO_2 is deposited at the surface and is only fairly solubilized by HF **[8].** At high HF concentration, complete dissolution of the silicon surface occurs as Ag collects

the electrons from silicon and allows Ag^{+} ions to be reduced at its surface. Vertical pores are created at the junction between Ag and silicon resulted in etching of the surface near the Ag nanoparticles **[9, 10]**. The unetched walls between the pore lead to fractal structures with high concentrations and increased time. (Figure 2.4)

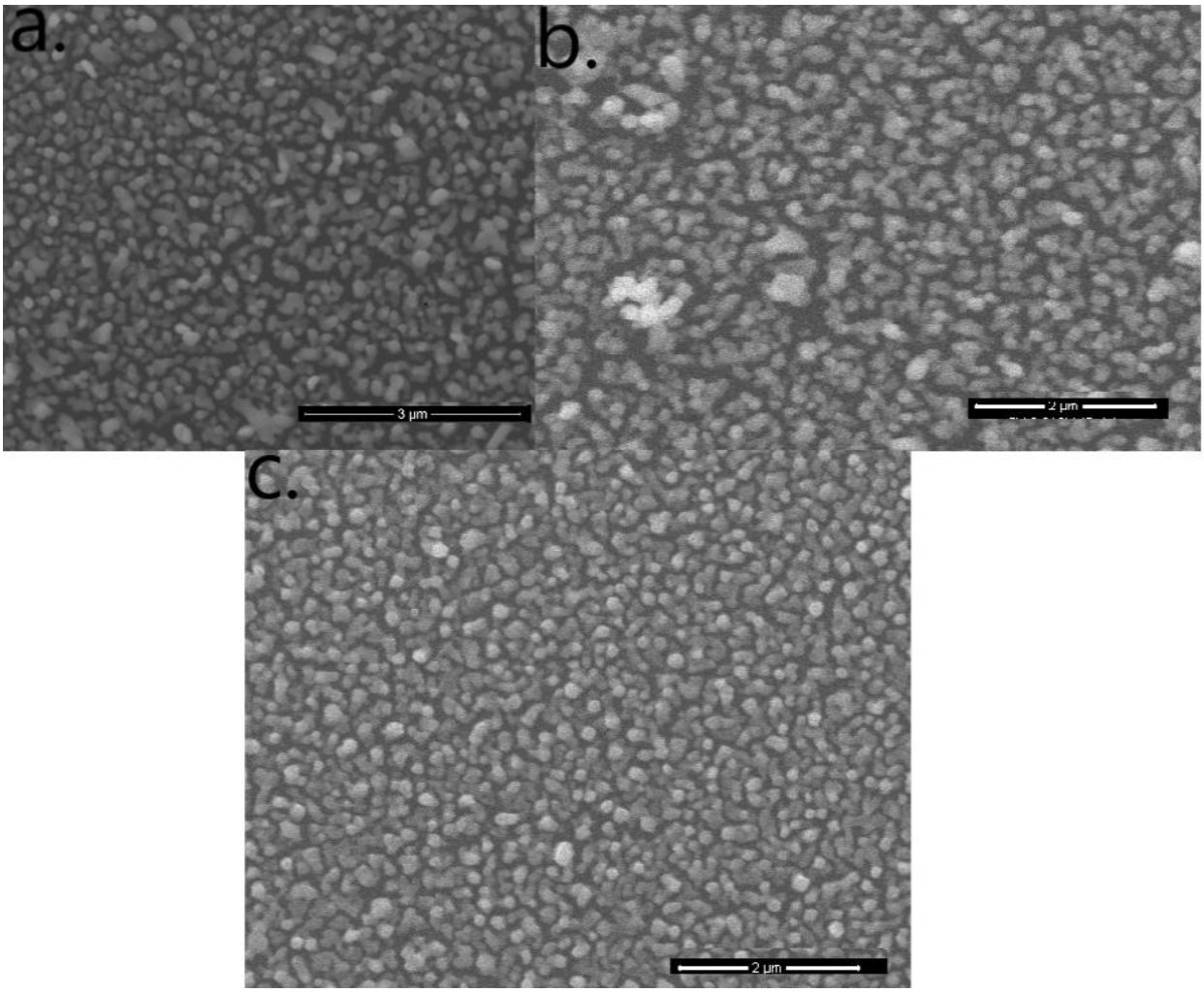

Figure 2. 2: SEM images of SERS substrates prepared by dipping Si wafer into a deposition solution of 5M HF + 13mM $AgNO_3$ for a) 20s b) 60s c) 5minutes

Figure 2.2(a-c) measured SEM images of silver nanoparticles deposited on silicon wafer using 5M HF + 13mM $AgNO_3$ for 20, 60 seconds and 5 minutes. At this high concentration of $AgNO_3$, with increased time rough surface was formed resulting non-uniform distribution. It was found that the nanostructures length depends on HF. The diameters of the nanostructures are not highly variable but are more compact and less detached for 5 M HF (Figure 2.2). Using the micrographs above, the average diameter of structure for 5M HF/13mM $AgNO_3$ went down from 27.03 nm to 11.08 nm with respect to time from 20 seconds to 5 minutes measured using Image J software masking the area of 1μm. Surprisingly; a higher $AgNO_3$ does not affect the length but reduces the substrate thickness. The diameter of the nanoparticles formed has increased with a rougher surface. It was observed even with the naked eye, as the concentration of $AgNO_3$ increases, the colour changes from brown to black **[57]**

[HF] concentration had a significant influence on the surface area. SEM images of samples etched at HF = 10 M i.e., with the longest fractal nanostructures show that the surface structures are closer to tree/leaf-like structures (Figure 2.3) than observed at lower [HF]. This indicates that the Ag/Si contact area (bottom of the Ag network) is reduced when [HF] is increased. It was hypothesised that [HF] may affect the deposition of Ag at the nucleation step and increase the extent of the Si/Ag contact area **[12]**. Because Si is dissolved only at Ag/Si contacts, different contact areas could result in different dendritic lengths, even if the dissolution rate and etching time are identical. Like Benoit et al.'s work **[1]**, in this case of silver deposition, the etched silicon wafer was always covered with a layer of thick silver film, which is slightly loose and could be easily detached from the surface of the silicon wafer.

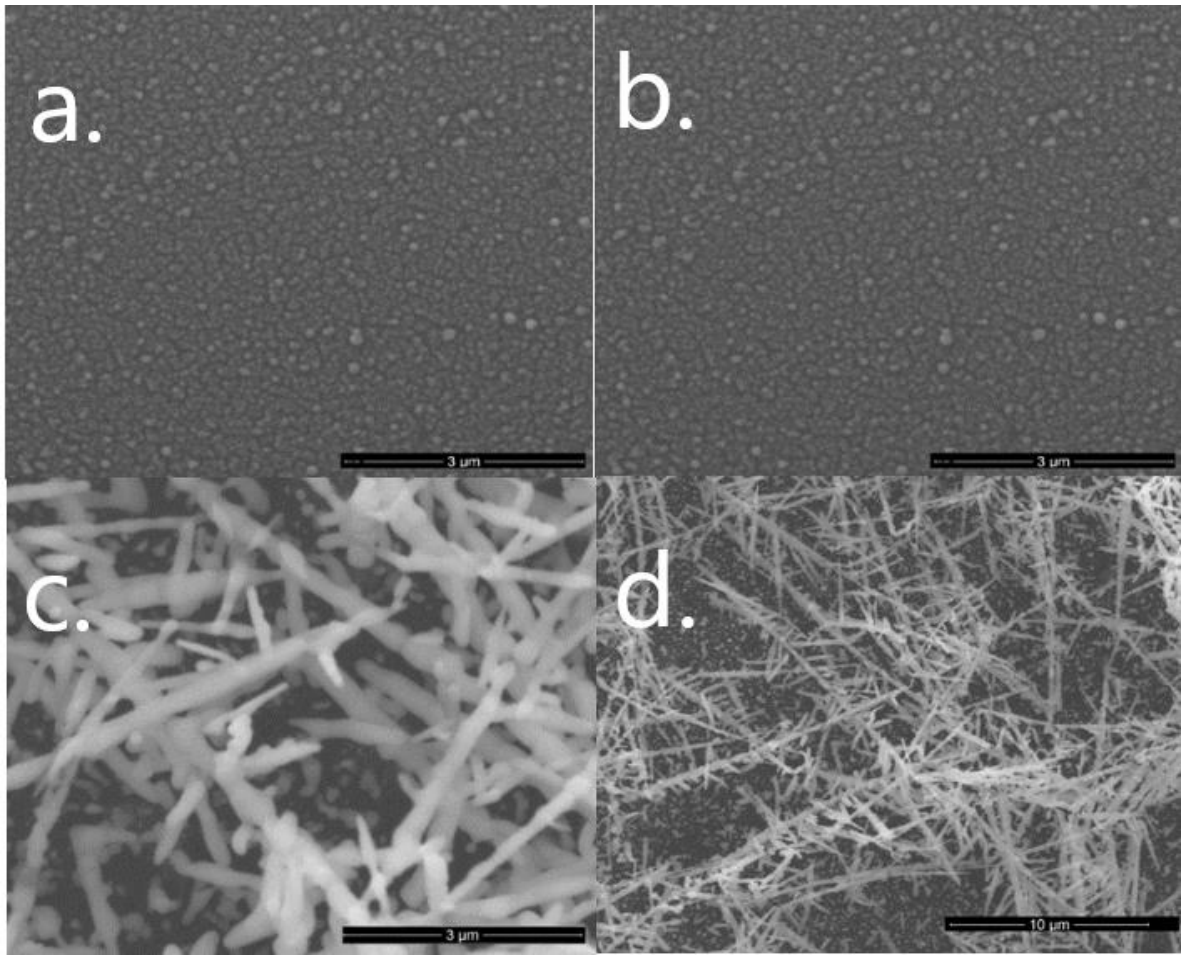

Figure 2. 3: SEM images of SERS substrates prepared by dipping Si wafer into a deposition solution of 2.5M HF + 88mM $AgNO_3$ for a) 20s b) 60s c) 5minutes (low magnification) d) 5 minutes (high magnification)

With the increase in $AgNO_3$ concentration, the etching rate increases resulted in higher dissolution rate and longer dendritic structures (Figure 2.3(a-d)). SEM observations of sample etched for 5 min, shows that the surface remains smooth after losing the thick top layer. **[13-15].** It was assumed that during etching, consumption of Ag^+ is not controlled by diffusion. The duration of this stage increases with [$AgNO_3$]. Once the surface concentration of Ag^+ is depleted, the Ag^+ diffusion regime is reached, and fractals start to grow. After 5 min etching, Si wires 200 nm in length are observed.

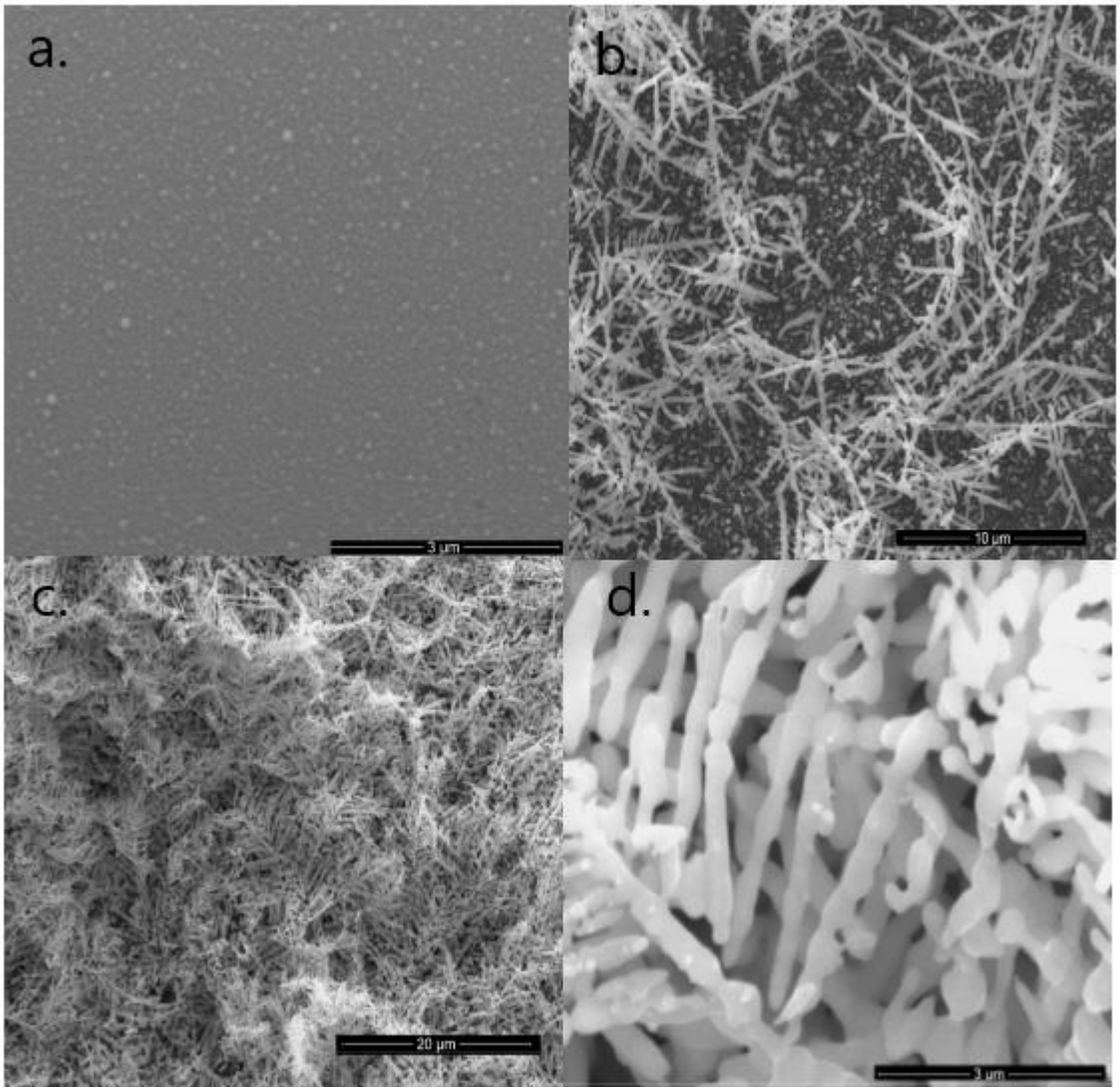

Figure 2. 4: SEM images of SERS substrates prepared by dipping Si wafer into a deposition solution of 10M HF + 5.6mM $AgNO_3$ for a) 20s b) 60s c) 5minutes (low magnification) d) 5 minutes (high magnification)

Besides fractal nanostructures, various kinds of leaf life structures are formed, irrespective of the soaking composition. The silver layer looks detached from the etched surface of silicon **[2]** and gives leaf-like silver dendrites Figure 2.4(a-d). Si nanostructures were covered with dendrite-like Ag-deposits as a top layer, which was clearly observed **[16].**

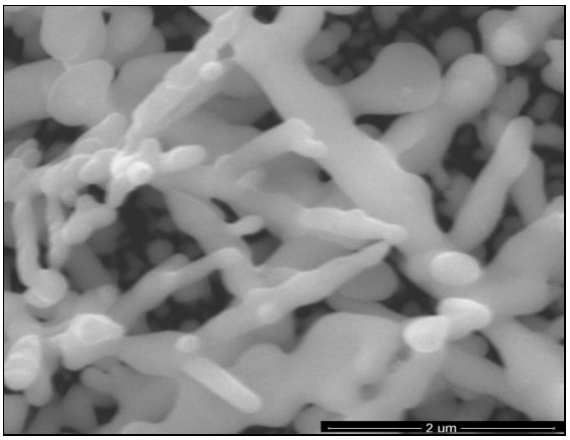

Figure 2. 5: SEM image (60,000 X magnification) of SERS substrates prepared by dipping Si wafer into a deposition solution of 10M HF + 5.6mM $AgNO_3$ for 5minutes.

A study with 10 M HF /5.6 mM $AgNO_3$ was done to examine the morphology of dendrites at higher magnification. The dendrites become thicker with a higher growth rate which resembles a network of dendrites sinking into the Si substrate. **[58]**

EDX analysis was done to prove the presence of Ag on a silicon wafer. Results of EDX for all the concentration at 60 seconds are shown in Figures 2.6, 2.7 and 2.8. It was found that as HF concentration increased (with the lowest concentration of $AgNO_3$), gives greater deposition of Ag on silicon due to favourable etching conditions. Minimum traces of silver nanoparticles were found at the lowest HF concentration and highest $AgNO_3$ concentration. Moderate concentration shows a good quantity of Ag on a silicon wafer. And with respect to time, as the dissolution rate increases, more fractals are produced with maximum HF concentration and a considerable quantity of silver on silicon. **[17, 18]** There were some traces of carbon and oxygen even which most likely comes from rinsing the silicon with acetone and ethanol. Also, trace metal peaks (other than silver) might suggest that there were some trace metal contaminants in silver.

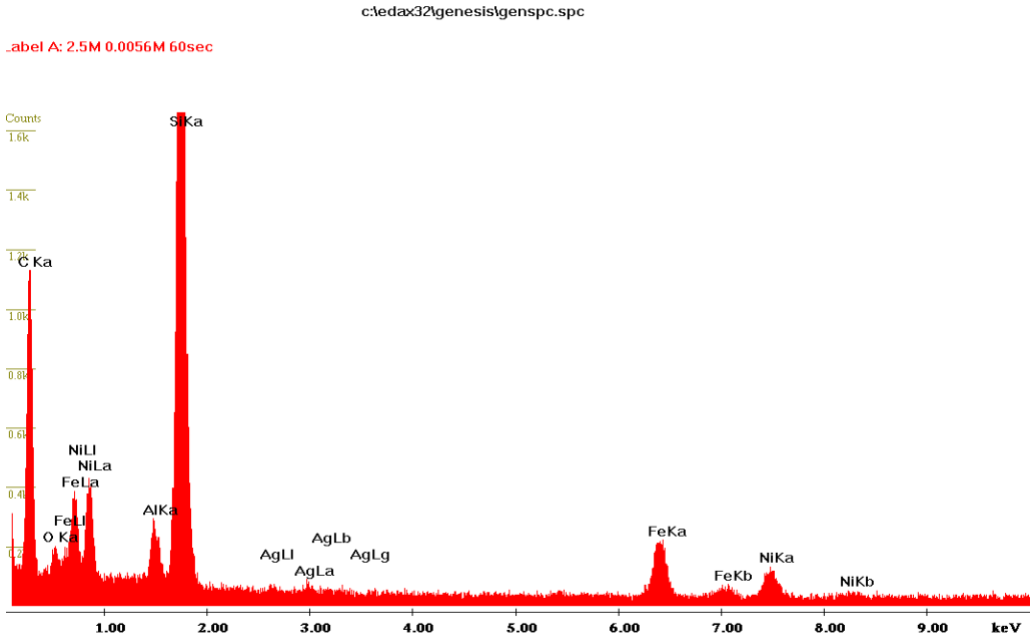

Figure 2. 6: EDX elemental results of Silicon wafers into deposition solution of 2.5M HF + 88mM $AgNO_3$ for 60s

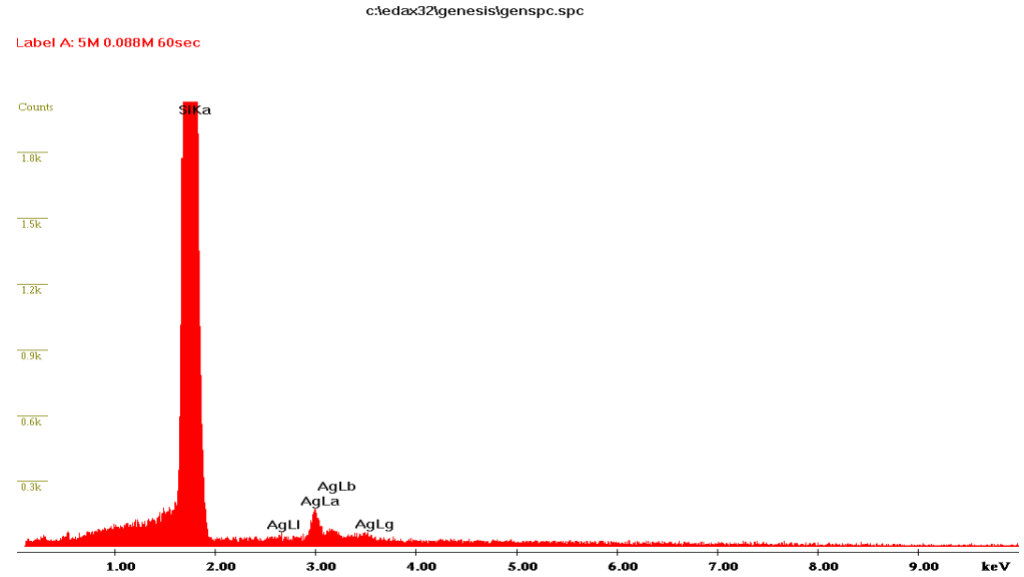

Figure 2. 7: EDX elemental results of Silicon wafers into deposition solution of 5M HF + 13mM $AgNO_3$ for 60s

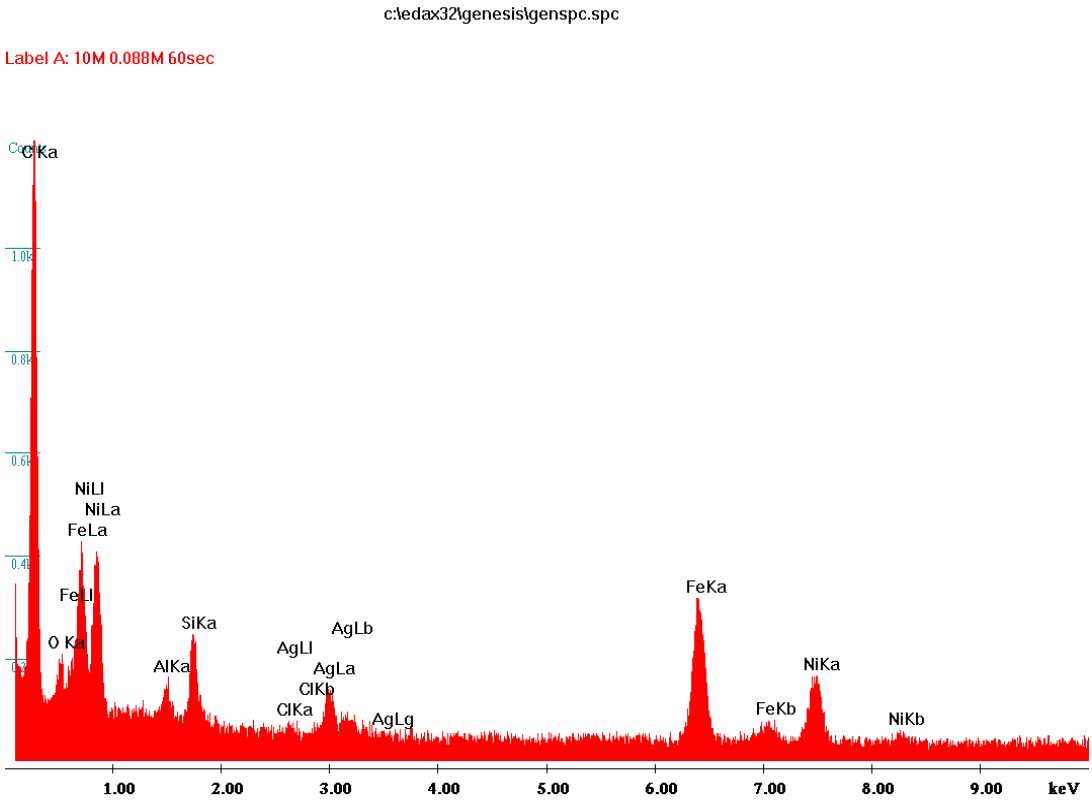

Figure 2. 8: EDX elemental results of Silicon wafers into deposition solution of 10M HF + 5.6mM AgNO3 for 60s.

2.1.3. Conclusion

The substrate in this section was produced by metal-assisted chemical etching method with silver nanoparticles precipitated on the surface. SEM analysis of the etched silicon wafers has revealed the formation of round-shaped pores at a moderate concentration with decreased diameter size whereas for lowest (13mM) silver concentration, there was considerable number of Ag NPs in 5 minutes with size reduced to 11.08 nm. It was found that length and width of pores can be controlled by selecting an appropriate etching time. SEM analysis of samples with precipitated Ag NPs has shown a non-uniform distribution of Ag NPs on the surface of silicon wafers. Ag NPs were also observed inside of pores in the silicon layer which is confirmed by EDX analysis at a later stage. On increasing the time, the small pores grow to fractal structures which has an

increasing quantity of Ag deposited on it. 10M HF and 0.088 M $AgNO_3$ revealed large fractal structure with a good quantity of Ag on silicon wafer compared to the other two concentrations. This method, however, suffers from lack of control of Ag network shape even when controlling etching parameters such as the concentration of reactants. The presence of Ag NPs was additionally proved by EDX analysis, which showed that the quantity of Ag in silicon samples amounts to almost 5% of the total percentage weight at a maximum concentration of HF.

To consider this as SERS substrate for any further work, a comprehensive study is required analysing the etching rate, the direction in which etching was done and orientation of silicon substrate. Therefore, gaining the knowledge from this experiment and understanding the shortcomings, for example, silver getting oxidised at room temperature reduced the substrate shelf-life of around a month, another method using silver dendrites was identified and carried out for a reproducible SERS substrate.

2.2. Method of forming silver dendritic nanostructures

The primary interest in silver as a SERS substrate is due to its optical properties and the fact that it has a plasmon resonance in the visible region. Silver dendritic nanoparticles are quite popular SERS substrates due to its branches and stems which have unique electromagnetic field enhancement **[27]**.

Silver dendrites can be easily formed via simple reduction method using metals like copper (Cu) **[19]**, magnesium (Mg) **[20]**, zinc (Zn) **[21]** or iron (Fe) **[22]**. These metals transfer electrons through galvanic displacement by reducing Ag^+ ions and silver is deposited on the metallic surface, copper mesh, in the form of dendrites **[23**]. The difference between this bimetallic (Ag/Cu) nanostructures method with etching of silicon by silver ions method is the different reductant, that is, copper for bimetallic and silicon for etching method.

The standard electrode potential of the Ag^+ /Ag pair (E^0= +0.799V) is higher than Cu^{2+} /Cu pair (E^0= +0.377V) whereas in the previous etching method Si^{2+}/Si has a higher electrode potential than the Ag^+ /Ag pair which allows silver to sink into silicon surface results in etching. In these

bimetallic dendritic nanostructures, copper atoms reduce silver ions to silver atoms with the simultaneous release of Cu^{2+} ions that covers the whole copper surface with dendrites in a few minutes. **[44,45]**. Therefore, it is a simple, rapid and low-cost method to synthesize silver nanostructures than using dangerous hydrofluoric acid for etching silicon with silver. These Ag dendritic nanostructures were used to detect rhodamine 6G(R6G) in this experimental work.

2.2.1. Experimental

2.2.1.1. Materials

Copper powder (<425 μm mesh), silver nitrate, rhodamine 6G and ethanol of analytical grade was used. Milli-Q water was used for the preparation of all solutions.

2.2.1.2. Preparation of silver dendrites and SERS samples

Silver (Ag) dendritic nanostructures were formed using 0.07 g copper powder (<425 μm mesh) added to 0.22g silver nitrate ($AgNO_3$) aqueous solution at 50° C without stirring. After 24 hours, Ag dendrites were formed, then washed twice with ethanol and water and the dendrites were collected in deionised water. 10 μL of R6G were pipetted onto the quartz coverslip which already had Ag dendritic nanoparticles dried on it. R6G drop was left for few minutes for air drying and then analysed using a 532 nm laser with a 9 mW power and 40× objective. The integration time was 15 seconds with four accumulations **[24]**.

2.2.1.3. Instrumentation

A home-built Raman microscope system was used which is based on an inverted fluorescence microscope, various optical components, and dedicated Raman spectrograph, FERGIE, and detectors. All SERS measurements were measured using FERGIE integrated spectrograph (Princeton Instruments). A setup of this kind is illustrated in Figure 2.9. The sample was placed on the stage placed above the microscope. The spectrometer was calibrated using standard Raman positions of Polymethyl methacrylate (PMMA). Light field software was used for collection and analysis of Raman spectra. Spectra were obtained using 532 nm excitation wavelength using a 40 × 0.65 NA objective, 9 mW laser power, 15s exposure time and 4 accumulations.

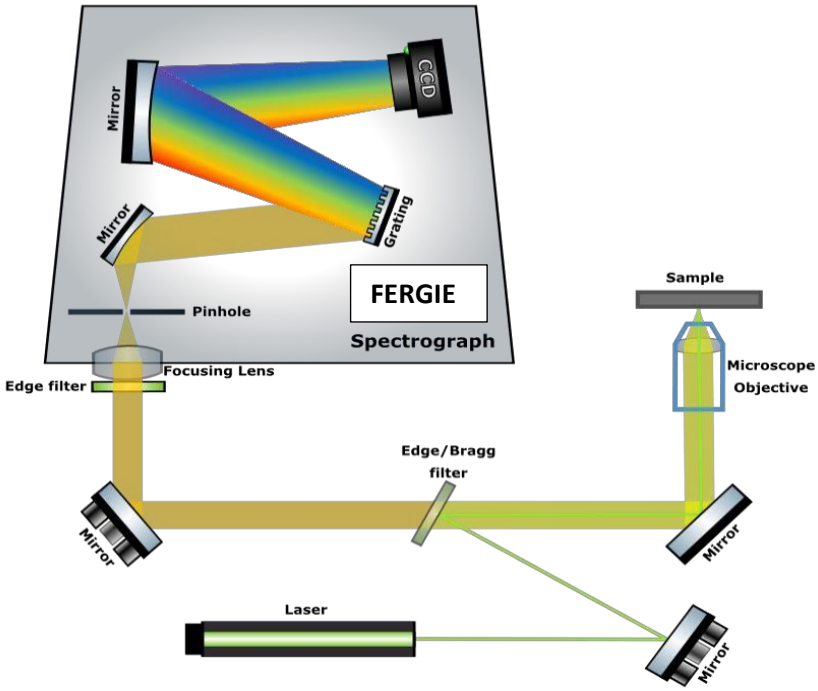

Figure 2.9. Illustration of Raman spectroscopy hardware and setup.

Scanning electron microscopy was employed to understand the morphology of silver nanoparticles. Zeta-potential and nanoparticle size was measured using Malvern Zetasizer Nano ZS. A sonicator was used to homogenise the samples at 50 watts, 10% amplitude.

2.2.2. Results and Discussion

A simple reduction method without the use of any surfactant was employed for fabrication of silver dendrites using copper powder. Copper powder was used as a reducing agent which plays an important role in the formation of silver dendrites. Copper has a high standard reduction potential and can reduce silver ions at a faster rate than any other metals **[28]**. Keeping the copper powder and silver nitrate solution undisturbed for 24 hours will promote the reaction allowing to get regular crystalline branches of silver dendrites that gives the fractal network even on decantation. It can easily control the size and shape of dendrite giving regular nanodendrites with equivalent growth on all sides **[25,46]**.

The copper powder would certainly speed things up due to the greater surface area. Without stirring will make complete use of copper powder in a timely manner giving most of the silver cemented at the bottom and when cement silver was washed well, it will remove any contamination from the left traces of copper in solution. The solution initially turned light blue after the reaction but cleared up after washing. Higher surface area of copper allows more analyte molecules to get adsorbed at the surfaces that can serve as an attractive sensing substrate for SERS analysis **[62]**.

The concentration of silver nitrate has a significant effect on the morphology of silver dendrites, changing the size and shape of dendrites. Higher Ag^+ concentration results in faster formation of nanodendrites in the form of branches and stems while low concentration can lead to irregular nanoparticles with fewer chances of forming regular dendrites **[26]**.

2.2.2.1. Morphology of silver dendrites substrate

Scanning electron microscopy (SEM) images in Figure 2.9. demonstrate a leaf-like branching pattern of Ag dendritic nanostructures with R6G deposited on it. The details of the structures were revealed at various magnifications. Length of each individual dendrite varies from 3-6 μm. Time plays an important role in morphology, size and amount of formation of dendrites, if all the reactants were added with stirring and reaction time was more than 24 hours, copper powder turns the silver dendrites to dark black. So, it requires an optimum procedure for addition of chemicals and keeping the reaction time to 20 hours. High density of nanoparticle clusters between the edge of neighbouring branches acts as SERS 'hot-spots' and responsible for an enhanced SERS signal. These dendritic nanostructures clearly differentiate from the earlier etching method.

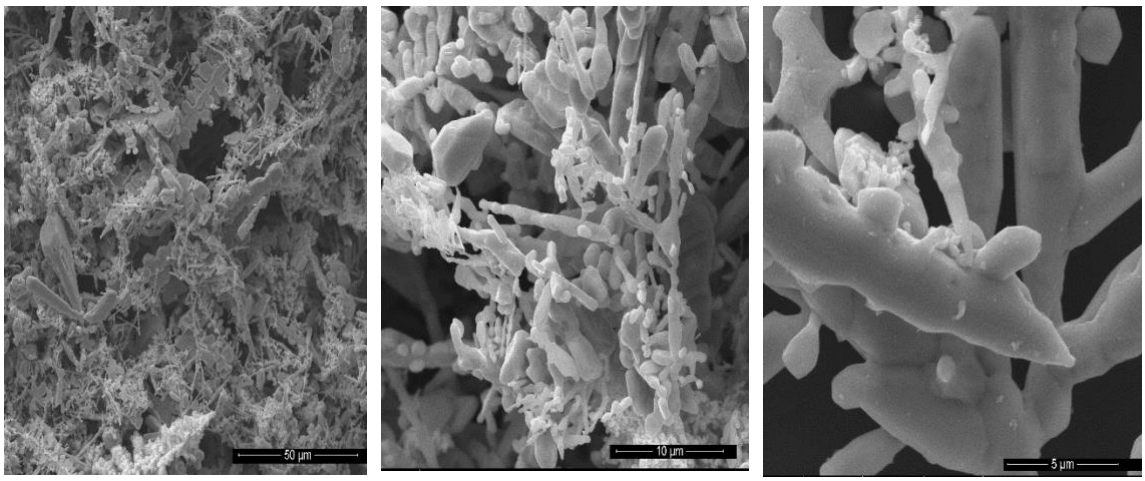

Figure 2. 10: SEM of a) R6G (10^{-4} M) on silver dendrites from low magnification (50 µm), (10 µm) to high magnification 5 µm

2.2.2.2. SERS performance in rhodamine 6G.

Rhodamine 6G, Raman active dye, was used as a standard for evaluation of SERS performance on silver dendritic nanostructures with the aim of obtaining high sensitivity. This is generally the most popular target analyte for single-molecular detection.10 µL of 10^{-5} mol/L R6G ethanolic solution was used for testing on Ag dendritic substrates. Figure 2.11 shows the spectra that demonstrates the efficiency of dendritic SERS substrates. R6G fluorescence and Raman spectra overlap in the spectral range 540-580 nm **[63]**, the Raman spectrum has a strong fluorescence background. Therefore, SERS spectra of 10^{-5} M and 10^{-7} M R6G in water was acquired as shown in Figure 2.11. The strong Raman peaks above the fluorescence background were found at 613 cm^{-1}, 777 $cm^{-1}$are associated with C-C- C ring in plane, C-H out-of-plane bending, 1188 cm^{-1} and C- C stretching vibrations 1362 cm^{-1}, 1505 cm^{-1}, and 1649 cm^{-1} assigned to totally symmetric modes of aromatic C-C stretching vibrations. **[29, 31]** The experimental results obtained from R6G concentrations using silver dendritic nanostructure matched with the literature data.

With decrease in concentration from 10^{-5} to 10^{-7} M R6G, few detectable Raman bands were lost. This illustrates that this silver dendritic SERS substrate is limited to a certain range of detection level without much potential for ultra-sensitive detection to probe single molecule regime. To

overcome this sensitivity problem which is an important feature of SERS substrate, the fate of colloidal SERS substrate was investigated and described in the next section.

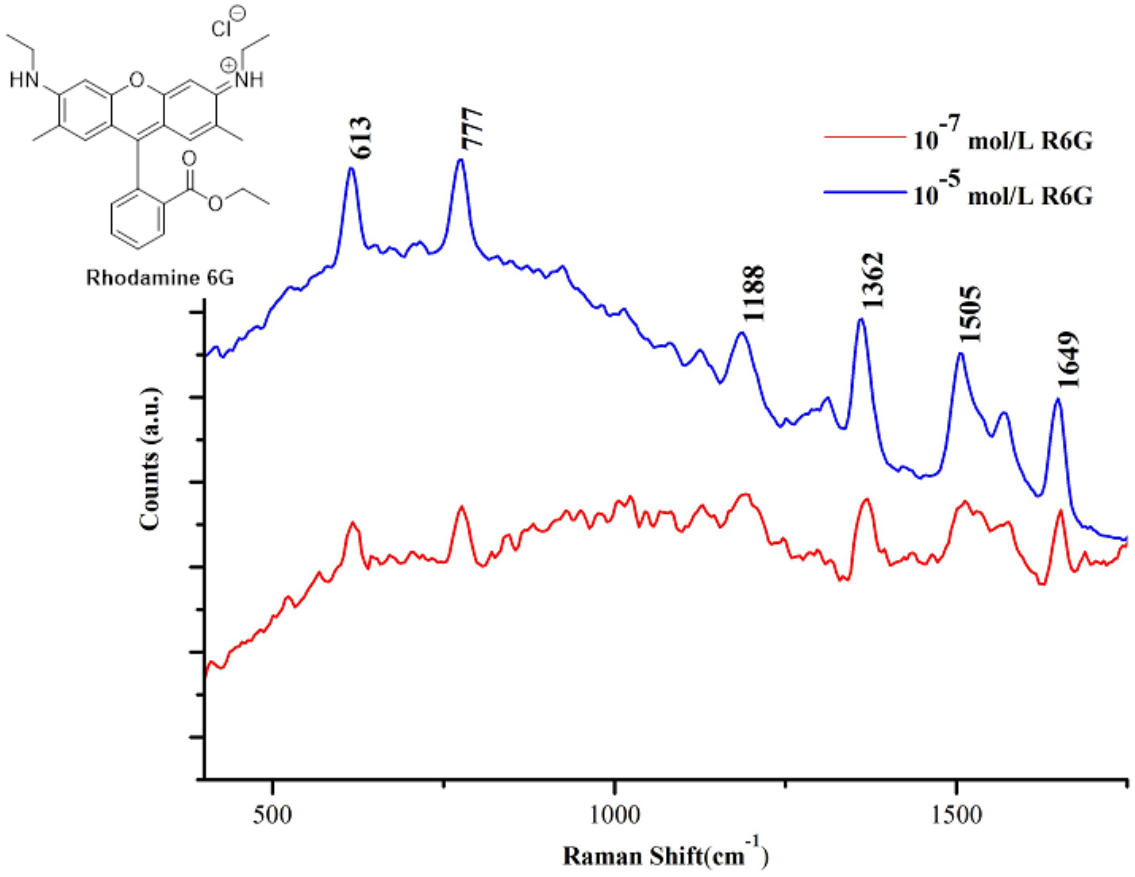

Figure 2. 11: SERS spectra of R6G 10-5and 10-7 M on Ag dendrites acquired at 532 nm laser wavelength with 40 × *objective, laser power of 9 mW and 15 s exposure time with average spectra from four accumulations.*

Despite many advantages, few shortcomings of the technique were found. At the time of deposition, suspension of dendrites creates a thin layer of nanoparticles at the centre and they dry in a ring-shape, so the particles collect at the edge of the ring. The dendrites are dispersed around the circumference of the ring, so even if the focus is on few hot-spots of the dendrite ring, there are still a lot of analytes that is not generating SERS intensity. This diverted the objective to look for some other options for SERS substrate. The fabrication process of the dendritic substrate is

very simple and inexpensive, and dendrites have stable SERS signal, and they can be used for wider applications in Raman analysis and imaging but are not particularly suited for analytical applications.

2.2.3. Conclusion

The method developed was quite simple and reproducible for detection of R6G using Ag dendritic nanostructures. Good enhanced SERS signal was found with different concentration of R6G at several 'hot-spots' found at the edge of a dendritic ring formed. Dendrites can give strong SERS, but they disperse across the substrate when drying and this creates problems. Therefore, the colloidal nanoparticles method was investigated that could overcome the dispersal problem as previous method deal with silver dendrite suspensions.

2.3. Use of SLIPS surfaces as a SERS substrate with silver colloidal nanostructures

Silver (Ag) colloid-based nanostructures are the most common method of achieving strong SERS signals as compared to any other method. These colloids are investigated for the shape, size and an extent of aggregation of colloidal nanoparticles **[46-50]**. The hot spots formed in between the nanoparticles provide ease for sensing analyte using Raman. Aggregation by salt addition can also activate surface chemistry leading to more enhanced signal for surface-enhanced Raman spectroscopy. R6G, an analyte that gives very large Raman signals, is often used as a standard probe for SERS investigation on silver colloids **[35]**. Such dyes like R6G, malachite green and crystal violet are the most popular analytes of interest for single-molecule detection because of their high scattering ability.

Many SERS studies are published for silver colloids using different reducing agents, such as borohydride, hydroxylamine **[36-38]**. Researchers have widely used silver colloids using sodium borohydride and proven to be effective substrate for SERS **[51-52]**. In this section, Kitaev et al. method was used for preparing borohydride-reduced silver colloid which provide the ultrasensitive detection of R6G to picomolar level **[39, 53]**.

2.3.1. Experimental

2.3.1.1. Preparation of silver nanoparticles

I. Silver nanoparticle preparation was performed in accordance with Kitaev et al. **[53]** method. These nanoparticles are referred to as '*Kitaev silver nanoparticles*' throughout the dissertation. To a borosilicate vial, 4 mL of 1.25×10^{-2}mol L^{-1} trisodium citrate, 1 mL of 3.75×10^{-3}mol L^{-1}silver nitrate, 9 mL of Milli-Q water and 10 mL of 5.0×10^{-2}mol L^{-1}hydrogen peroxide were mixed. Then 0.80 mL of 1.0×10^{-4}mol L^{-1} potassium bromide was added. Lastly, 5 mL of 5.0×10^{-3}mol L^{-1}sodium borohydride was added and stirred continuously for two minutes. A permanent yellow colour solution was formed immediately. 0.8 mL volume of KBr was chosen for SERS analysis as it gives the best spectra with R6G. Therefore, Kitaev silver nanoparticles prepared using 0.8mL of KBr is chosen for a 532nm laser for SERS.

II. Lee Meisel Colloid: 90 mg silver nitrate was dissolved in 500 mL of Milli-Q water and brought to boiling. 10 mL solution of 1% sodium citrate was added. The solution was kept on boiling for one hour. A greenish yellow colour solution was formed and used for SERS analysis.

2.3.1.2. SERS sample preparation

For SERS analysis, to 2 mL centrifuge tube, an aqueous solution of 750 µL of analyte, (i.e., any chemical substance that needs to be detected and measured), 750 µL of Kitaev nanoparticles and 150 µL of 0.01 mol/L magnesium sulphate ($MgSO_4$) or potassium chloride (KCl), used as an aggregating agent, were sequentially added to Raman vials. The solution was then vortexed for 1 minute, sonicated for five minutes and then used for SERS detection.

The solution finally obtained was used either as dried SERS samples by simply pipetting 2 µL of the solution mixture onto quartz coverslip, allowed to dry at room temperature, and then used for

SERS analysis. Or as it is in solution form by taking few mL's in a cuvette and then placing it in a cuvette holder for SERS analysis, termed as 'Liquid SERS' in the thesis.

2.3.1.3. SLIPS sample preparation

The lubricant used for SLIPS substrate was Krytox which is a polyfluoropolyether oil and the Teflon sheet used was Sterlitech Polytetrafluoroethylene (PTFE) unlaminated membrane filters of 0.2 micron pore size and diameter of 13mm. The white Teflon sheets were first placed at the top of concave well of the indented glass slide. 15µL lubricant was dropped onto the centre of each Teflon sheet using a pipette. The glass slides were then tilted in every direction to ensure the lubricant completely covers the Teflon sheet before being placed on the spin coater. The spin coater was spun at 1000 rpm for 1 minute to ensure excess lubricant was removed.

The lubricated membrane was placed in an oven set at temperature 64 ˚ C and a 50 µL drop of analyte solution was place on the Teflon membrane. 10 µL of Ag nanoparticles with 1 µL 0.01 mol/L $MgSO_4$ or KCl aggregating agent was injected onto the droplet. The slide was removed once the aggregate was dried. It took approximately an hour to dry the sample. To accelerate the evaporation process, the optimum temperature for drying is required. Overheating may degrade the sample. Yang et al. have shown that increasing the temperature beyond 64 ˚C could increase the evaporation but also causes the droplet to enter a "sticky" Wenzel state where droplets are pinned to the surface and have strong contact with the surface **[39]**. Therefore, optimum temperature set for SLIPS surface is 64 ˚ C that facilitates the pinning-free formation of aggregate. After evaporation, the droplet formed as a single black dot, visible to the naked eye. Finally, the aggregate was transferred to a coverslip for Raman analysis.

For Raman testing, the laser power should be as low as possible, ~1 mW, to avoid sample damage and an exposure time of 15 seconds with 4 accumulations. It was found that the Teflon sheet could be used multiple times to create the SLIPS surfaces. To carry out the multiple usages, the Teflon sheet was wiped with ethanol to remove any remaining solute and then 10µL of lubricant was reapplied to the Teflon sheet, tilted to spread evenly and spun on the spin coater.

SERS measurements were performed on aggregates which consist of close-packed nanoparticles, an aggregating agent and analyte of interest. All SERS measurements were recorded on FERGIE spectrograph at 532 nm laser wavelength as described in the above section of Instrumentation.

2.3.2. Results and Discussion

The preparation of silver nanoparticles involves the aqueous solutions of all above listed chemicals that plays an important role in getting size dependent AgNPs. Bromide has been used as a shape-modifying agent for AgNPs. It alters the size and limit the growth of silver nanoparticles, leading to different sizes of nanoparticles. Bromide strongly binds to the silver surface, forming silver bromide that restricts the growth of silver particle surfaces. Sodium citrate acts as a buffer and stabilizes the silver nanoparticles. Firstly, citrate form complex with silver, then combines with Ag^{+} of a growing nanoparticle, making the surface negatively charged and electrostatically preventing nanoparticles from aggregating. Hydrogen peroxide serves as an etching agent and facilitates formation of shape-selected nanoparticles. Sodium borohydride acts as a reducing agent that reduce silver nitrate and allow silver atoms to aggregate. Sodium borohydride used should be fresh as it decomposes over time rendering larger size nanoparticles. With proper laboratory care and handling, AgNP preparation is robust and reliable and can last for few months.

Another important addition in getting highly enhanced SERS signal for any analyte detection is the addition of suitable aggregating agent which does not compete with the analyte molecule during adsorption. Previous reports suggested that different aggregating agents have different influence on SERS enhancement. Several combinations of cations (Mg^{2+}, Na^{+}, K^{+}, Li^{+}) with anions (Cl^{-}, Br^{-}, SO_4^{2-}, I^{-}) where one combination can work for an analyte whereas other can work for another **[59]**. Aggregating agents cause metal colloids to aggregate because they compromise the electrostatic stabilisation that colloid particles have at their surface which keep them in colloidal suspension. The electric double layer thickness is compromised by the increase in electrolyte concentration so lessening the repulsive forces and allowing the natural attractive dispersion forces between the particles to dominate so favouring their agglomeration into larger particles.

Two different aggregating salts were chosen and used: 0.01 M $MgSO_4$ and 0.01 M KCl for comparison for SERS enhancement. Both are capable of aggregating silver colloids forming a

cluster of nanoparticles. These aggregates obtained were analysed under SEM. Although aggregation is essential for strong SERS, it can be difficult to control. Using these two aggregating agents, it was found that chloride based aggregating agents can cause issues with silver colloids due to the formation of insoluble AgCl blocking the adhesion of the analyte to the AgNP surface but sulfate does not act in a similar manner, it has low affinity to silver therefore occupies the AgNP surface sites and enhance the signal by aggregation.

Also, interesting to note, as per Law of Schultz and Hardy **[64]**, $MgSO_4$ with its divalent cation (Mg^{2+}) will be more effective at aggregating the colloids relative to the KCl which has monovalent cation and have the same influence at a lower concentration of aggregating agent. Even increased concentration of aggregating agent results in instability of the colloidal solution and eventually leads to precipitation of nanoparticles. Ag has the potential of aggregating themselves and adding an aggregating agent of an optimal amount can increase SERS enhancement whereas if the concentration has increased it will ultimately lead to a significant decrease. Therefore, one-fifth to the volume of sample mixture was added as an aggregating agent to optimally achieve enhancement.

2.3.2.1. Morphology of colloidal substrates

Two types of nanoparticles were initially investigated, the Kitaev nanoparticles **[53]** and the Lee & Meisel nanoparticles **[65]**. Kitaev nanoparticles are typically spherical in shape and of almost same size whereas Lee-Meisel colloids has different shape nanoparticles but size of both nanoparticles ranges from 44 nm-50 nm. (Figure 2.12)

Mark Waterland's undergraduate students - Harry Deare and Callum Hill investigated both colloids in detail for their nanoscience project and found that both produced good Raman spectra with Rhodamine 6G in the concentration range of 10^{-6} to 10^{-10} mol/L using 532nm Raman laser but below that the Lee & Meisel nanoparticles were unable to produce constant results. It was suspected that even on very low powers (~1mW) the laser is still altering the shape of the Lee & Meisel nanoparticles causing the spectra produced to change erratically. While the Kitaev nanoparticles produced good spectra till at least the 10-15 concentration. The volume

of KBr used in the reaction also plays an important role of the size of the nanoparticles formed and therefore, 0.8mL KBr nanoparticles seemed to produce the best and reproducible spectra.

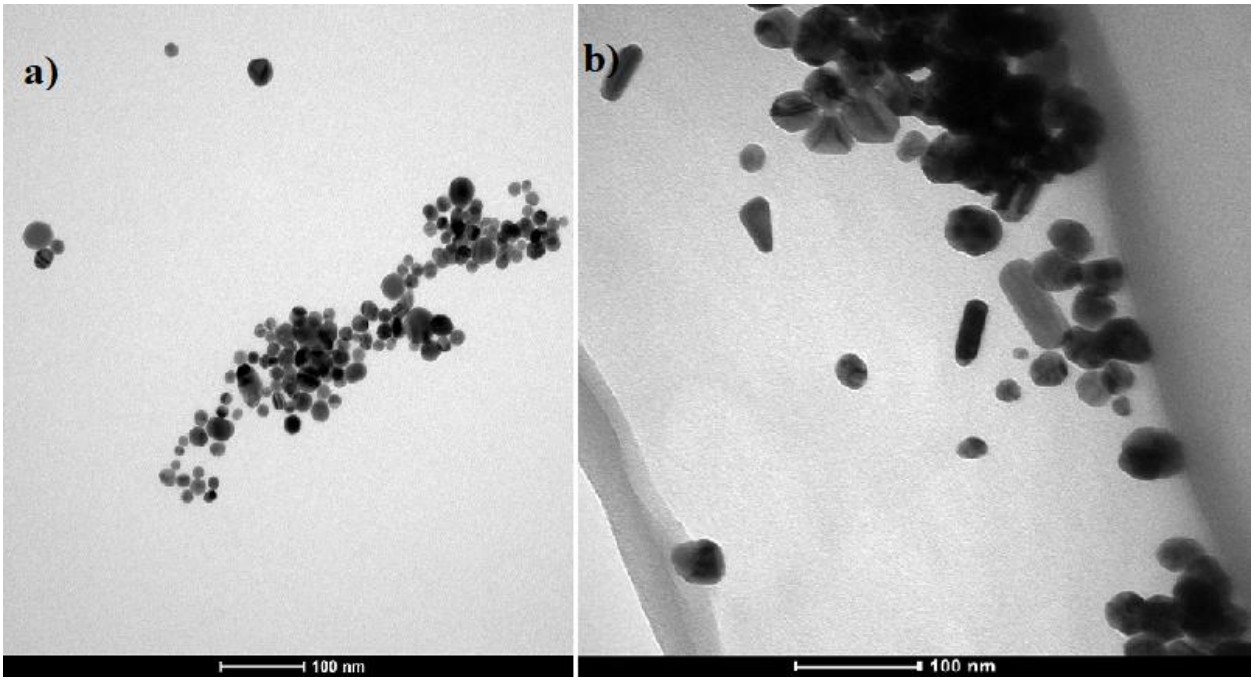

Figure 2. 12: Transmission electron microscopy images of a) Kitaev silver nanoparticles, b) Lee Meisel silver colloid.

After learning the information about the morphology and stability of these nanoparticles, Kitaev silver nanoparticles were chosen for sensitive detection and quantification of our selected analytes.

Figure 2.13 a, b and c shows the effect of an aggregating agent on Kitaev silver nanoparticles. Before aggregation, the nanoparticles are isolated and randomly distributed. The clusters shown in the figure below is the dried solution. Once the salt has been added the nanoparticles form dense structures and form large flakes, which can be easily seen with the naked eye. These flakes were made of particles of different shapes and sizes. Under SEM examination it was found that with $MgSO_4$, the shape of aggregate is more circular with some gaps found at the junction of nanoparticles whereas with KCl it's like a mesh with no space in between. It has been reported by Bell et al. **[32]** that $MgSO_4$ does not compete with the analyte at the adsorption sites allowing more analyte molecules to adsorb and finally giving strong enhancement. It is important to add analyte molecules to nanoparticles before adding aggregating salt to it. This allows the analyte molecule binds strongly to the nanoparticle surface giving large signal intensity. **[35]**

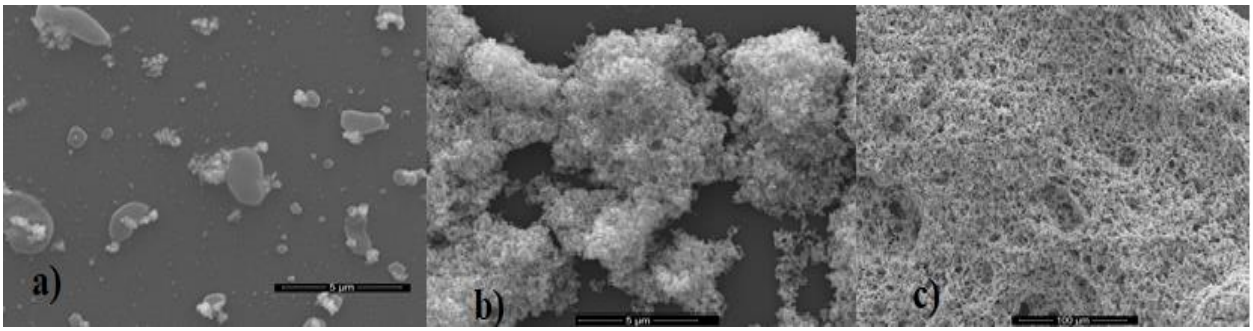

Figure 2. 13: SEM image of original Kitaev silver nanoparticles a) before aggregation (scale: 5 µm) b) after aggregation with 0.01 M MgSO4 (scale: 5µm) c) after aggregation with 0.01M KCl (scale: 100 µm)

2.3.2.2. UV-Visible Characterisation

UV-Vis spectra of Kitaev silver nanoparticles mixed with two different salts, 0.01 M $MgSO_4$ and 0.01 M KCl, were obtained as shown in Figure 2.14. The spectra were recorded immediately after adding the aggregating agents to the nanoparticles because the nanoparticles eventually aggregate and fall out of suspension. In case of $MgSO_4$, the peak was reduced as compared to Kitaev silver nanoparticles absorption peak which is due to silver nanoparticles aggregating whereas KCl absorbance is the lowest due to large aggregates settling out of solution. **[40]**. Also, it was found that $MgSO_4$ gave much better SERS intensities due to weak adhesion of the sulfate ion. This is proved by the results obtained in Chapter 4. Unaltered colloids, colloids without any aggregating agent offered weak (low SERS intensity) spectra as compared to ones with salt. Chapter - 4 demonstrates the significance of $MgSO_4$ by presenting the SERS spectra of an analyte with and without aggregating salt.

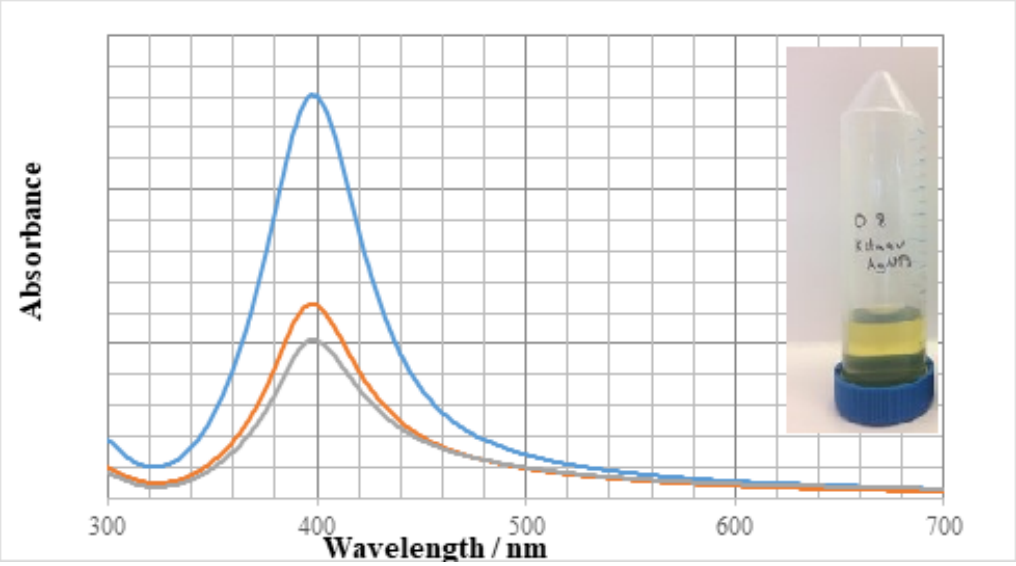

Figure 2.14: UV-Vis spectra of Kitaev silver colloid (blue), Kitaev silver colloid aggregated using $MgSO_4$ (orange) and Kitaev silver colloid aggregated using KCl (grey) (inset: Kitaev silver nanoparticles)

2.3.2.3. SERS and SLIPSERS performance of R6G with citrate-reduced silver colloid.

The performance of the colloid was evaluated by SERS and SLIPSERS activity with R6G.

Firstly, the Raman spectra of Krytox (polyfluoropolyether oil used for SLIPS substrate preparation, Figure 2.15) and Kitaev silver nanoparticles were acquired (Figure 2.16). In the preparation of SLIPS surfaces, an indented glass slide is used as opposed to a regular glass slide as gravity gives good assistance in forming a smaller aggregate. The Raman spectrum of Krytox is heavily dominated by noise and therefore, has very weak signal. The 'peak' at about 2200 cm^{-1} would be overpowered by sample spectra of higher intensity. The spectrum is considered as a reference when using samples at very low concentrations.

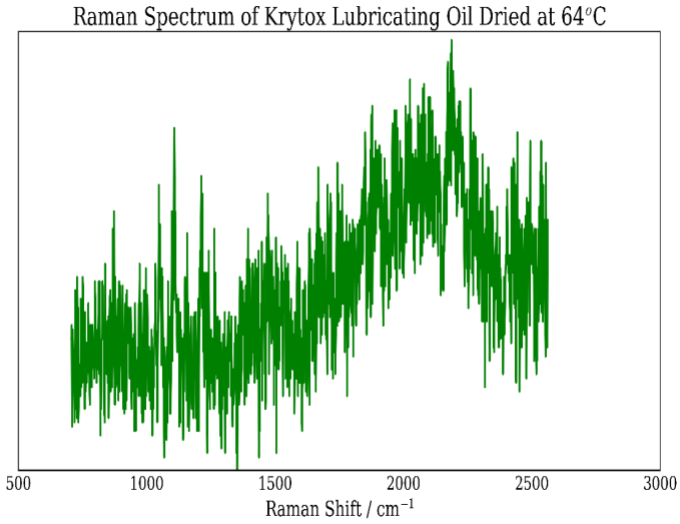

Figure 2. 15: 532nm Raman spectrum of the liquid Krytox lubricating oil.

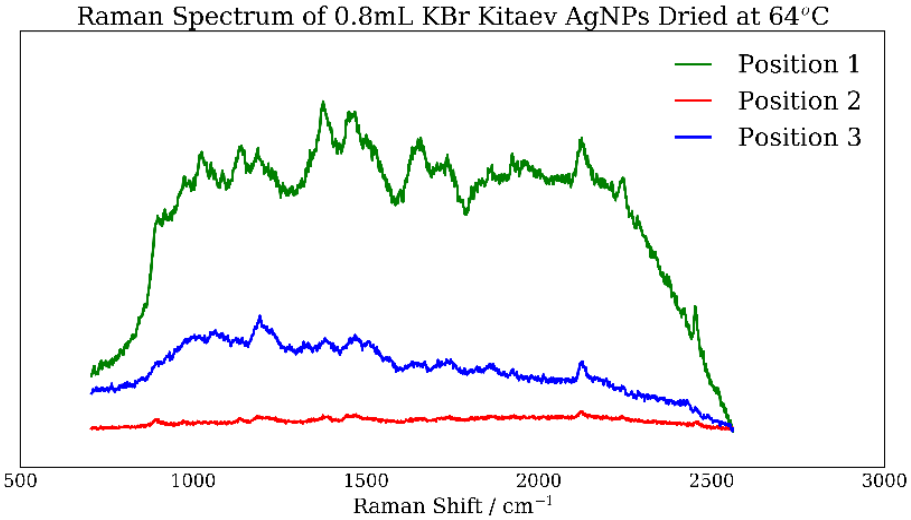

Figure 2. 16: Raman spectrum of Kitaev silver nanoparticles

There is always a maximum concentration of an analyte that gave an observable SERS signal. The molecules are either scattering or absorbing the incident laser so that very little SERS enhancement occurs for the sample with very high analyte concentration. Hence, for this study, SERS detection was initiated from10^{-7} mol/L concentration of R6G concentration. Concentrations higher than this gives a very high intensity signal resulting in unreadable spectra that results from R6G fluorescence. As the concentration increases, R6G completely covers the aggregate giving no

SERS and no spectrum obtained. Silver nanoparticles quench any fluorescence from R6G. So, if fluorescence is observed, then it is coming from molecules that are not in contact with the surface.

Rhodamine 6G is a large molecule (65 atoms including 4 conjugate ring structures) with high fluorescence quantum yield **[54]** and thus has larger Raman cross-section. The particles can completely cover the aggregate at higher concentrations and such adsorption prevents the scattering of signal. The aggregate structures are visible in the Figure 2. 9(left), but in the Figure 2. 10 (right) the aggregates are obscured by the dried analyte. Higher the concentration of analyte, higher is the surface coverage resulting to increase in the probability of accidental clustering which blocks SERS enhancement. It was observed that for higher concentrations, a crystallized R6G structure formed on top of the AgNP aggregates. To determine the appropriate concentration to detect the analyte of interest, it must be kept in mind that the nanoparticles are used to create "hot spots". If the solution is at too high concentration, the solute will form a shiny surface over the surface of the silver nanoparticles blocking the "hot spot" effect.

Figure 2.17 and 2.18 are two SEM images, show the difference in surface structure between the 10^{-2} and 10^{-10} mol/L concentrations. Higher concentration at 0.001M R6G, structure looked shiny with analyte in bulk giving no SERS spectra whereas low concentration (10^{-10} mol/L) the image has a rough, dry looking surface and gives strongly enhanced spectra.

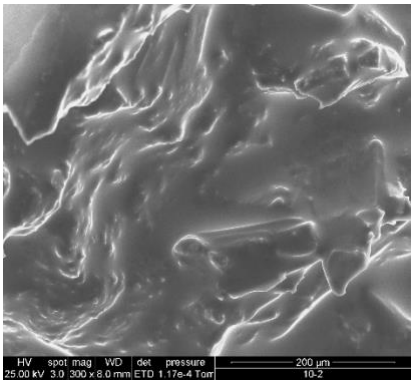

Figure 2. 17: (left) 10^{-2} R6G SEM image. Note, the smooth crystallized R6G surface

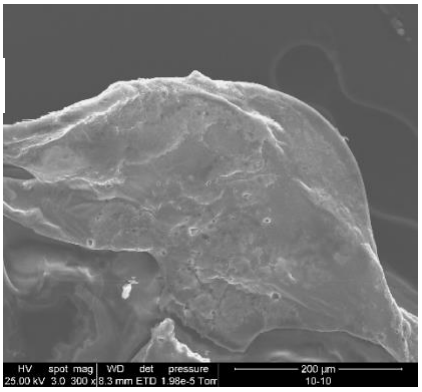

Figure 2.18: (right) 10^{-10} R6G SEM image. Note, the rough R6G and Kitaev AgNP surface

Raman spectrum of 1mM R6G dried on a coverslip was acquired as shown in Figure 2.19. This serves as a reference spectrum for analyte identification and comparison. The SERS (dried) and SLIPSERS spectra of 10^{-7} mol/L R6G with aggregating agent, $MgSO_4$, were acquired with three

accumulations per spectra at an excitation wavelength of 532 nm. The spectra exhibit the expected R6G peaks as shown in Figure 2.20 and 2.21.

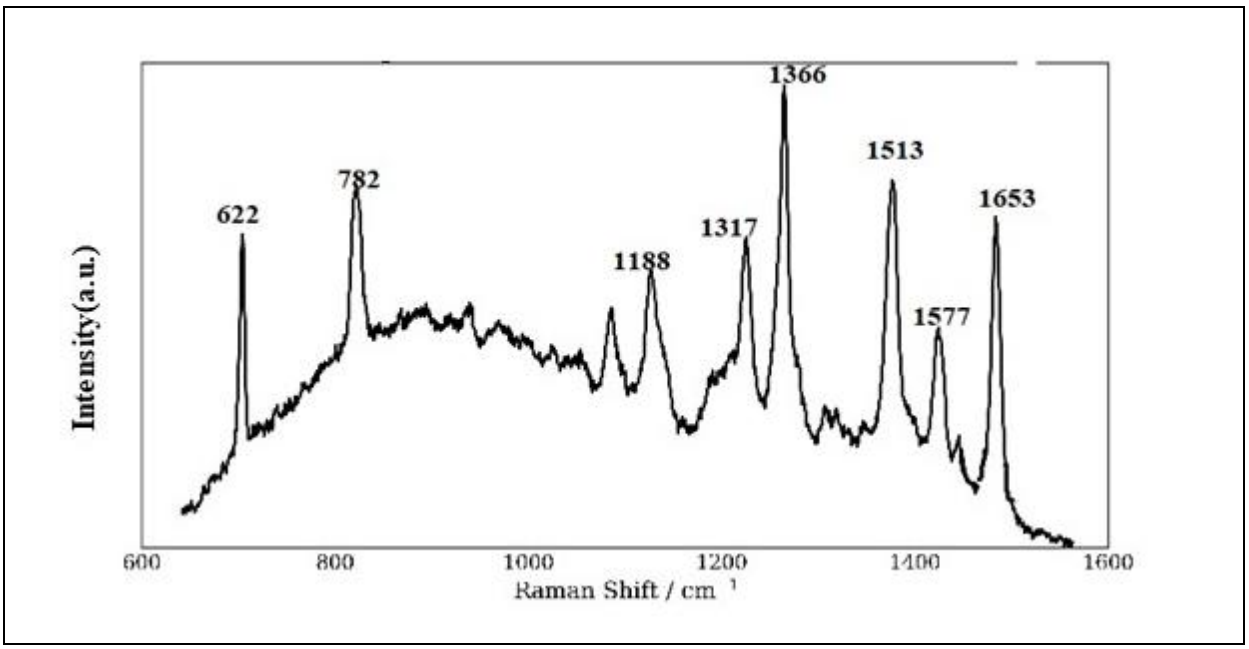

Figure 2.19: Raman spectra of 1mM R6 G acquired at 532 nm laser wavelength with 40 × *objective, laser power of 9 mW and 15 s exposure time with average spectra from four accumulations.*

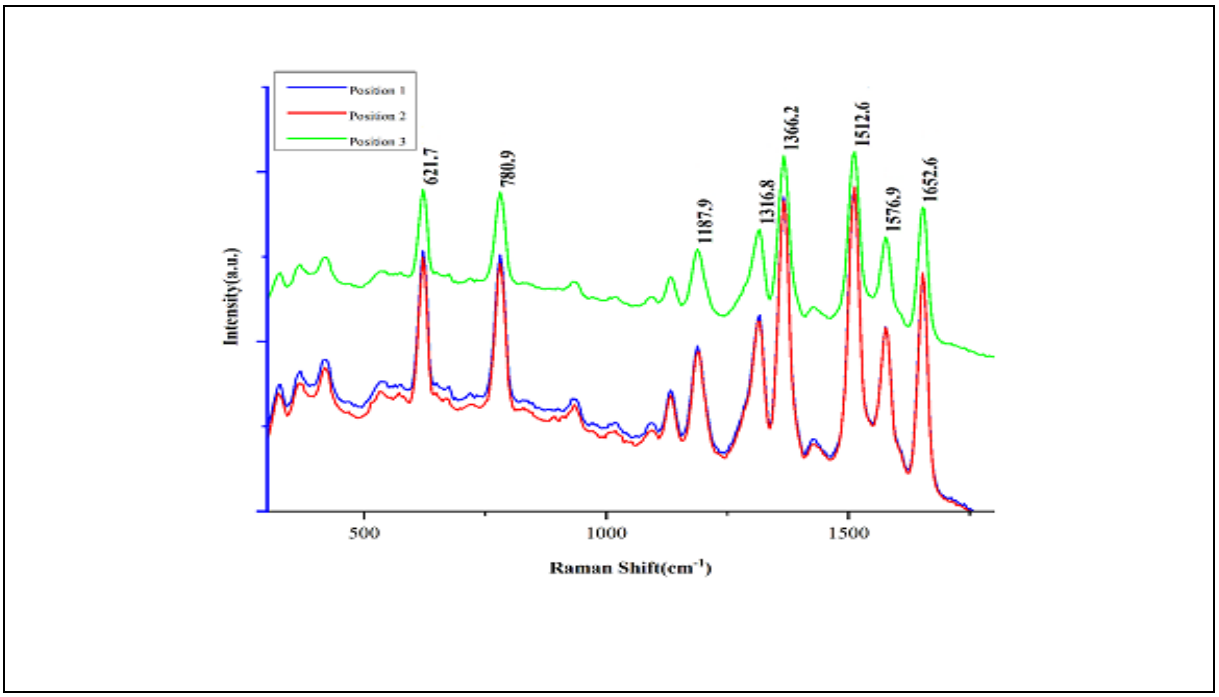

Figure 2. 20: SERS spectra of 10-7 mol/L R6 G with 0.01M $MgSO_4$ acquired at 532 nm laser wavelength with 40 × *objective, laser power of 9 mW and 15 s exposure time with average spectra from four accumulations. Position 1, 2 and 3 are the different random points focused on the substrate.*

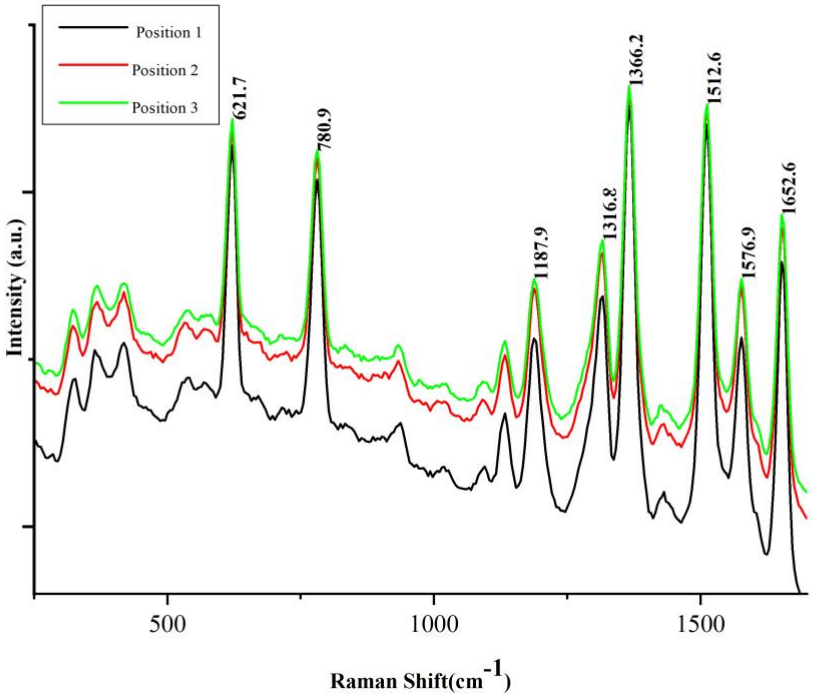

Figure 2. 21: SLIPSERS spectra of 10-7 mol/L R6 G with 0.01M $MgSO_4$ acquired at 532 nm laser wavelength with 40 × *objective, laser power of 9 mW and 15 s exposure time with average spectra from four accumulations. Position1, 2 and 3 are three different random points focused on a substrate.*

The SERS and SLIPSERS spectrum are in good agreement with the literature values. The spectral assignment of 1366, 1513 and 1653 cm-1 bands as aromatic C–C stretching in-ring vibrational bands and band at 622, 776 and 1188 cm-1 as C–C-C ring in-plane, out-of-plane bend and C-C stretching vibrations **[41, 55, and 56].** The detailed assignments are given below in Table 2.1.

Table 2. 1: Assignment of Raman bands obtained from SERS spectra of Rhodamine6G

Raman shift (cm-1)	**Assignment**
622	C–C-C ring in-plane bending
781	C-H out-of-plane bending
1069	C–H in-plane bending
1188	C–H in-plane bending
1317	Aromatic C-C stretching
1366	Aromatic C-C stretching

1513	Aromatic C-C stretching
1577	Aromatic C-C stretching
1653	Aromatic C-C stretching

SERS enhancement factor is comparing the ratio of intensities of SERS and normal Raman spectrum of R6G. We have used a normal Raman spectrum of 1mM aqueous solution of R6G and SERS (and SLIPSERS) spectrum of 10^{-7} mol/L R6G. The most intense peak at 1366 cm^{-1} was the chosen Raman band to determine enhancement factor (EF).

The formula to calculate EF is listed below:

$$EF = I_{SLIPSERS} C_{RAMAN} / I_{RAMAN} C_{SLIPSERS}$$

where $I_{SLIPSERS}$, I_{RAMAN} represents peak intensity with and without Ag nanoparticles and $C_{SLIPSERS}$, C_{RAMAN} are the concentration of R6G with and without Ag nanoparticles.

The enhancement factor for SLIPS and SERS obtained is 7.4×10^7 and 2.9×10^7 respectively. At this concentration (10^{-7} mol/L), both SERS and SLIPSERS are quite a close match. This means if a strong hot spot on the SERS sample was captured then the EF for the SERS sample expected to be very similar to the SLIPSERS sample. The key difference then is with SLIPSERS is to more likely find a hot-spot than SERS, but the hot-spots in both cases give similar enhancement. And this would be an advantage for detecting lower concentrations with ease and improving the sensitivity, which is a challenge.

SERS spectra of 10^{-7} mol/L R6G with 785 nm excitation wavelength was also acquired as a comparison to identify the maximum sensitivity factor. The peak at 1366 cm^{-1} was used to calculate the enhancement factor for R6G. The intensity of R6G at 785 nm observed was quite a low comparative at 532 nm. The enhancement factor calculated for SERS spectrum of 10^{-7} mol/L R6G at 785 nm and 532 nm excitation wavelength was 5.0×10^6 and 2.9×10^7 respectively. At this concentration (10^{-7} mol/L) even it was observed that the location of a few peaks is not the same as per the literature. (Figure 2.22) This might be because different excitation wavelengths have enhanced the different set of modes between the substrate and the adsorbent. As in surface-enhanced Raman spectroscopy, these states can influence relative intensities, and possibly the band frequencies.

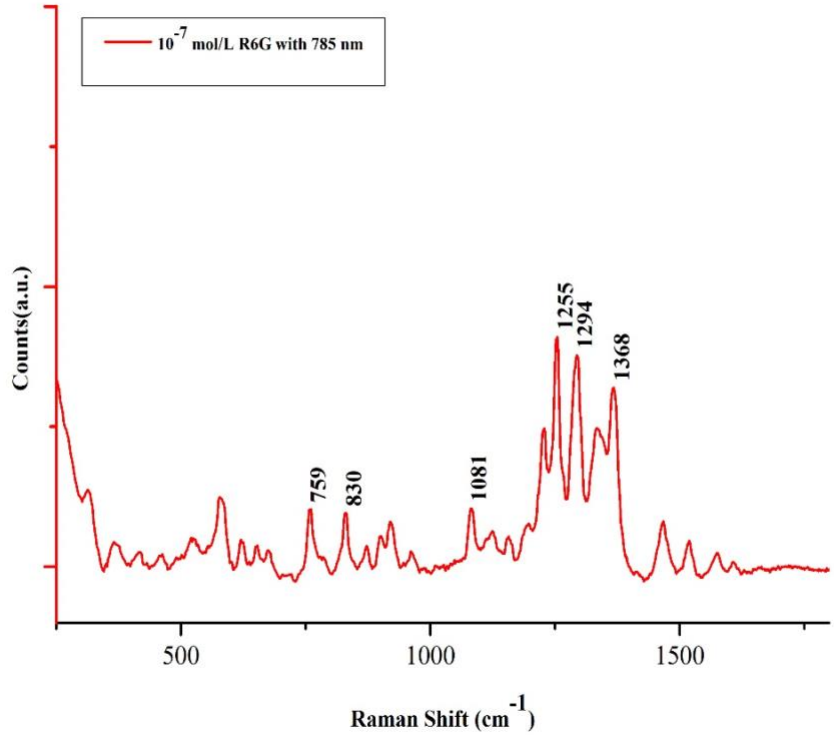

Figure 2. 22: SERS spectra of R6G with Kitaev silver nanoparticles at 785 nm excitation wavelength with 40 × *objective, laser power of 15 mW and 15 s exposure time with average spectra from four accumulations.*

An acceptable parameter for determining LOD is the concentration [66] where:

$$\frac{Peak\ Height}{Signal - to - noise} = 3$$

whereas the limit of quantification (LOQ) is the concentration where

$$\frac{Peak\ Height}{Signal - to - noise} = 10$$

To investigate the LOD of SLIPSERS, we obtained SERS spectra on concentrations ranging from 10^{-10} to 10^{-15} mol/L. (Figure 2.23)

In this concentration range, enhancement has become approximately constant. The reason for this behavior is that below a critical concentration the probability of finding an R6G molecule (or

possibly a small aggregate of R6G molecules) in the focal volume and at a hot-spot becomes quite low. This is the sub-sampling regime, and a certain amount of "luck" is required to find a signal. But if the microscope objective does focus on a hot-spot with R6G, then a signal is obtained, but the signal is roughly the same intensity for each hot-spot (in the same way as the SLIPSERS and SERS EF are roughly the same).

The spectra for 10^{-13} mol/L and below should be treated with caution, as at these concentration levels, extreme measures are required to avoid cross-contamination of glassware, pipettors, and substrates (and this data was obtained without taking these measures). Although, the concentration may be nominally 10^{-15} mol/L, in practice, it could be several orders of magnitude higher due to these cross-contamination issues. The data clearly demonstrate the potential of SLIPSERS for very low detection limits and illustrate how the signal intensity behaves in the sub-sampling regime. The onset of the sub-sampling regime effectively marks the lower limit for detection. Therefore, LOD at this stage was the picomolar level for R6G using SLIPSERS method **[39]**.

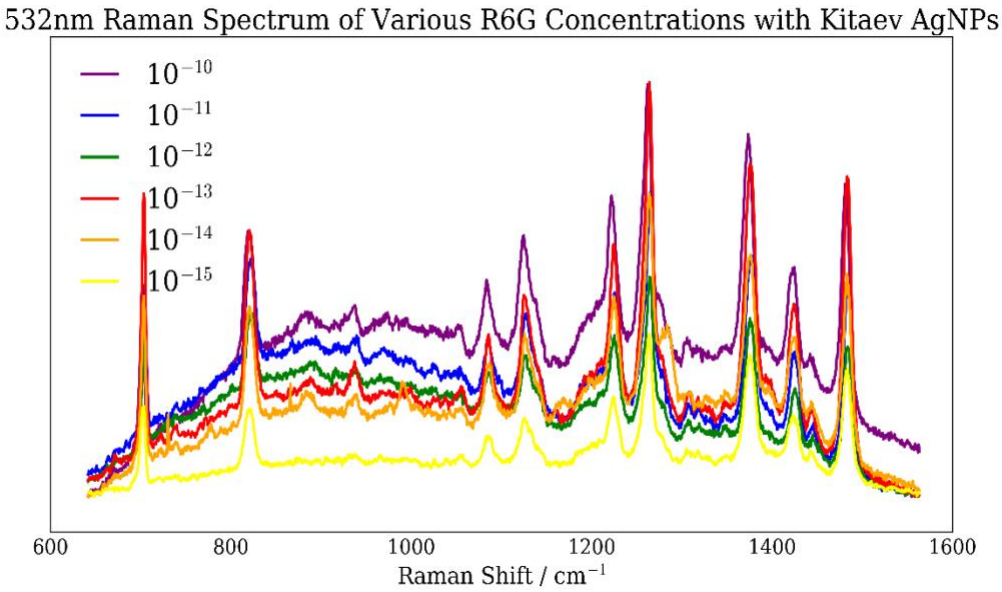

Figure 2. 23: Graph showing how spectra intensity decreases with R6G concentration acquired at 532 nm excitation wavelength with 40 × *objective, laser power of 15 mW and 15 s exposure time with average spectra from four accumulations using SLIPSERS method.*

Such a low concentration region can be analysed using a sub-sampling technique such as Principal Component Analysis (PCA), to identify individual SERS signals. The idea with using PCA to analyse sub-sampling is relevant if there are multiple components in the sample, then multiple spectra will be obtained, and a system with multiple spectra can be analysed with PCA. Such PCA-based SERS technique has the potential to identify the multiple components even at low concentrations from the most significant components by grouping them in different regions. This issue is explained in detail with the investigation of the anesthetic drug, Lidocaine hydrochloride (LHC) in the next chapter.

2.3.3. Conclusion

Here, all three SERS substrate classes are summarized.

Etched silicon was selected as an example of a "top-down" substrate; the idea behind that by carefully controlling the etching conditions the morphology of the etched substrate can be controlled. This gives a level of control which acts as an advantage over randomly aggregated colloids or dendrites. But the method used HF acid which is quite dangerous to use on frequent basis for preparing substrates **[1,9]**. Even the substrate has the detection sensitivity, a very important issue in probing the surface of substrate which also gets oxidised in a very short duration of time. This made to explore other methods of forming SERS substrate which do not suffer from these limitations.

Silver dendrites method serves the purpose of identification of right SERS substrate and delivers enhanced SERS signal for the detection of R6G, used as a standard SERS analyte. The method involves surface galvanic reaction that took place on copper powder. Copper atoms reduce silver ions to silver atoms with the simultaneous release of Cu^{2+} ions that covers the whole copper surface with dendrites in a few minutes. **[61]** Dispersal problem around the edge of dried sample brings variation within spectra and poses challenge in finding the hot-spot. Also, dendritic substrate restricts the detection to a concentration limit beyond which no readable spectra could be achieved.

Colloidal substrates take advantage over that limitation and brings the detection to single molecule regime. Silver colloidal substrates are the most common in the past and recent studies **[17,63]**.

These substrates also have the largest SERS enhancement factor; therefore, it has been used for the entire research presented in this thesis. SERS with dried samples and SLIPSERS method was used to detect R6G down to 10^{-15} mol/L concentration.The SLIPSERS substrate provided the best results in terms of reproducibility and sensitivity because the substrate aims at controlled drying, brings many molecules in the small focal volume and forms a highly concentrated and tight aggregate with near 100% analyte concentration. This aggregate has SERS active sites (hot-spots) almost all over the aggregate and delivers ultra-sensitive detection of analyte of interest.

Use of $MgSO_4$ aggregating agent with silver colloid has greatly enhanced SERS and SLIPSERS signal by creating a large number of hot spots. LOD was picomolar level for R6G using SLIPSERS method knowing that the signal intensity entered in the sub-sampling regime. SLIPSERS overcomes the long-lasting limitations of SERS regarding precise delivery of analytes to SERS hot spots in aqueous solutions.

Using Yang et al.'s, SLIPSERS technique, this opportunity has been rolled out to investigate a variety of analytes in chemical and biological matrixes. Few selected will be discussed in later chapters of this thesis.

References

1. Benoit, C., Bastide, S. & Lévy-Clément, C. SILICON NANOWIRES: CONDITION OF SYNTHESIS AND SIZE SELECTION.
2. Qiu, T., Wu, X., Mei, Y., Chu, P. & Siu, G. 2005. Self-organized synthesis of silver dendritic nanostructures via an electroless metal deposition method. *Applied Physics A,* 81**,** 669-671.
3. Ben-Jacob, E. & Garik, P. 1990. The formation of patterns in non-equilibrium growth. *Nature,* 343**,** 523.
4. Peng, K., Yan, Y., Gao, S. & Zhu, J. 2003, 'Dendrite assisted growth of silicon nanowires in electroless metal deposition', *Advanced Functional Materials*, vol. 13, no. 2, pp. 127-32.
5. Wang, X., Peng, K.-Q., Wu, X.-L. & Lee, S.-T. 2010, 'Single crystalline ordered silicon wire/Pt nanoparticle hybrids for solar energy harvesting', *Electrochemistry Communications*, vol. 12, no. 4, pp. 509-12.

6. Peng, K., Fang, H., Hu, J., Wu, Y., Zhu, J., Yan, Y. & Lee, S. 2006, 'Metal particle induced, highly localized site specific etching of Si and formation of single crystalline Si nanowires in aqueous fluoride solution', *Chemistry–A European Journal*, vol. 12, no. 30, pp. 7942-7.
7. Gu, H.-X., Xue, L., Zhang, Y.-F., Li, D.-W. & Long, Y.-T. 2015. Facile fabrication of a silver dendrite-integrated chip for surface-enhanced Raman scattering. *ACS applied materials & interfaces*, 7, 2931-2936.
8. Gao X, Gu G, Hu Z, Guo Y, Fu X, Song J. 2005. A simple method for preparation of silver dendrites. *Colloids and Surfaces* A 254: 57-61.
9. Peng, K., Hu, J., Yan, Y., Wu, Y., Fang, H., Xu, Y., Lee, S. & Zhu, J. 2006. Fabrication of single crystalline silicon nanowires by scratching a silicon surface with catalytic metal particles. *Advanced Functional Materials*, 16, 387-394.
10. Xiao, J., Xie, Y., Tang, R., Chen, M. & Tian, X. 2001. Novel ultrasonically assisted templated synthesis of palladium and silver dendritic nanostructures. *Advanced Materials*, 13, 1887-1891.
11. Ghiamati E, Manoharan R, Nelson WH, Sperry JF. 1992. UV resonance Raman-spectra of *Bacillus* spores. *Appl Spectrosc* 46(2): 357-64.
12. Shao, M.-W., Zhang, M.-L., Wong, N.-B., MA, D. D.-D., Wang, H., Chen, W. & Lee, S.-T. 2008. Ag-modified silicon nanowires substrate for ultrasensitive surface-enhanced Raman spectroscopy. *Applied Physics Letters,* 93**,** 233118.
13. Qiu, T., Wu, X., Shen, J., HA, P. C. & Chu, P. K. 2006. Surface-enhanced Raman characteristics of Ag cap aggregates on silicon nanowire arrays. *Nanotechnology,* 17**,** 5769.
14. Mulvihill, M. J., Ling, X. Y., Henzie, J. & Yang, P. 2009. Anisotropic etching of silver nanoparticles for plasmonic structures capable of single-particle SERS. *Journal of the American Chemical Society,* 132**,** 268-274.
15. Brune, H., H. Röder, K. Bromann, K. Kern, J. Jacobsen, P. Stoltze, K. Jacobsen, and J. Norskov, 1996, Anisotropic corner diffusion as origin for dendritic growth on hexagonal substrates', *Surface science*, vol. no. LNS-ARTICLE-1996-004, pp. L115-L22.
16. Peng, K., Hu, J., Yan, Y., Wu, Y., Fang, H., Xu, Y., Lee, S. & Zhu, J. 2006. Fabrication of single-crystalline silicon nanowires by scratching a silicon surface with catalytic metal particles. *Advanced Functional Materials,* 16**,** 387-394.
17. Emory RS, Haskins EW, Nie S. 1998. Direct observation of size-dependent optical

enhancement in single metal nanoparticles. *J Am Chem Soc* 120: 8009-10.

18. Han, H., Huang, Z. & Lee, W. 2014. Metal-assisted chemical etching of silicon and nanotechnology applications. *Nano today,* 9**,** 271-304.
19. Yang J, Jiang Z. Facile fabrication of dendritic silver structures and their surface enhanced Raman spectroscopic properties. *J Chem Sci*. 2015;127:173–176.
20. Zhang G, Sun S, Banis MN, et al. Morphology-controlled green synthesis of single crystalline silver dendrites, dendritic flowers, and rods, and their growth mechanism. *Cryst Growth Des*. 2011; 11:2493–2499.
21. Wang X. In situ fabrication of novel Ag dendrites film by a simple replacement reaction on Zn foil substrate. *Synth React Inorg M*. 2016; 46:1579–1583.
22. Nersisyan HH, Lee Y, Joo S, et al. Iron-assisted electroless deposition reaction for synthesizing copper and silver dendritic structures. *CrystEngComm*. 2015; 17:7535–7542.
23. HE, L., LIN, M., LI, H. & KIM, N. J. 2010. Surface-enhanced Raman spectroscopy coupled with dendritic silver nanosubstrate for detection of restricted antibiotics. *Journal of Raman Spectroscopy,* 41**,** 739-744.
24. Wang, Q., Wu, D. & Chen, Z. 2015. Ag dendritic nanostructures for rapid detection of thiram based on surface-enhanced Raman scattering. *Rsc Advances,* 5**,** 70553-70557.
25. Zhang, W., Tan, F., Wang, W., Qiu, X., Qiao, X. & Chen, J. 2012. Facile, template-free synthesis of silver nanodendrites with high catalytic activity for the reduction of p-nitrophenol. *Journal of Hazardous materials,* 217**,** 36-42.
26. Qiu, T., Wu, X., Shen, J., Xia, Y., Shen, P. & Chu, P. K. 2008. Silver fractal networks for surface-enhanced Raman scattering substrates. *Applied Surface Science,* 254**,** 5399-5402.
27. Huang, J., Ma, D., Chen, F., Bai, M., Xu, K. & Zhao, Y. 2015. Ag nanoparticles decorated cactus-like Ag dendrites/Si nanoneedles as highly efficient 3D surface-enhanced raman scattering substrates toward sensitive sensing. *Analytical chemistry,* 87**,** 10527-10534.
28. Zhu, J., Chen, Q., Kutsanedzie, F. Y., Yang, M., Ouyang, Q. & Jiang, H. 2017. Highly sensitive and label-free determination of thiram residue using surface-enhanced Raman spectroscopy (SERS) coupled with paper-based microfluidics. *Analytical Methods,* 9**,** 6186-6193.
29. Wang, J. F., Wu, X. Z., Xiao, R., Dong, P. T. & Wang, C. G. 2014. Performance-enhancing methods for Au film over nanosphere surface-enhanced Raman scattering substrate and

melamine detection application. *PloS one,* 9**,** e97976.

30. Zhu, S.-Q., Zhang, T., Guo, X.-L., Wang, Q.-L., Liu, X. & Zhang, X.-Y. 2012. Gold nanoparticle thin films fabricated by electrophoretic deposition method for highly sensitive SERS application. *Nanoscale research letters,* 7**,** 613.
31. Zhu, H., Du, M., Zou, M., Xu, C. & Fu, Y. 2012. Green synthesis of Au nanoparticles immobilized on halloysite nanotubes for surface-enhanced Raman scattering substrates. *Dalton Transactions,* 41**,** 10465-10471.
32. Bell, S. E. & Sirimuthu, N. M. 2005. Surface-enhanced Raman spectroscopy as a probe of competitive binding by anions to citrate-reduced silver colloids. *The Journal of Physical Chemistry A*, 109, 7405-7410.
33. Bron, M. & Holze, R. 1999. The adsorption of thiocyanate ions at gold electrodes from an alkaline electrolyte solution: a combined in situ infrared and Raman spectroscopic study. *Electrochimica acta,* 45**,** 1121-1126.
34. Barthelmes, J. & Plieth, W. 1995. SERS investigations on the adsorption of pyridine carboxylic acids on silver—influence of pH and supporting electrolyte. *Electrochimica acta,* 40**,** 2487-2490.
35. Beltramo, G., Shubina, T., Mitchell, S. & Koper, M. 2004. Cyanide adsorption on gold electrodes: a combined surface enhanced Raman spectroscopy and density functional theory study. *Journal of Electroanalytical Chemistry,* 563**,** 111-120.
36. Mehigan, S., Smyth, C. A. & Mccabe, E. M. 2015. Bridging the gap between SERS enhancement and reproducibility by salt aggregated silver nanoparticles. *Nanomaterials and Nanotechnology*, 5, 5-5.
37. Zhang, Y., Wang, F., Yin, H. & Hong, M. 2013, 'Nonuniform Distribution of Capping Ligands Promoting Aggregation of Silver Nanoparticles for Use as a Substrate for SERS' *Advances in Nanoparticles*, vol. 2, no. 02, p. 104.
38. Pristinski, D., Tan, S., Erol, M., Du, H. & Sukhishvili, S. 2006, 'In situ SERS study of Rhodamine 6G adsorbed on individually immobilized Ag nanoparticles', *Journal of Raman Spectroscopy: An International Journal for Original Work in all Aspects of Raman Spectroscopy, Including Higher Order Processes, and Brillouin and Rayleigh Scattering*, vol. 37, no. 7, pp. 762-70.
39. Yang, S., Dai, X., Stogin, B., & Wong, T. (2016) Ultrasensitive surface-enhanced Raman

scattering detection common fluids. *Proceedings of the National Academy of Science,* 113(2),268-273.

40. Betz, J. F., Wei, W. Y., Cheng, Y., White, I. M. & Rubloff, G. W. 2014. Simple SERS substrates: powerful, portable, and full of potential. *Physical Chemistry Chemical Physics*, 16, 2224-2239.
41. Lee, P. & Meisel, D. 1982. Adsorption and surface-enhanced Raman of dyes on silver and gold sols. *The Journal of Physical Chemistry*, 86, 3391-3395.
42. Liu, Y., Ji, G., Wang, J., Liang, X., Zuo, Z. & Shi, Y. 2012. Fabrication and photocatalytic properties of silicon nanowires by metal-assisted chemical etching: effect of H_2O_2 concentration. *Nanoscale research letters*, 7, 663.
43. Cai, W.-F., Pu, K.-B., Ma, Q. & Wang, Y.-H. 2017. Insight into the fabrication and perspective of dendritic Ag nanostructures. *Journal of Experimental Nanoscience,* 12**,** 319-337.
44. He, X., He, R., Lan, Q., Duan, F., Xiao, J., Song, M., Zhang, M., Chen, Y. & Li, Y. 2016. A Facile Fabrication of Silver-Coated Copper Nanowires by Galvanic Replacement. *Journal of Nanomaterials,* 2016**,** 10.
45. Xie, S., Zhang, X., Xiao, D., Paau, M.C., Huang, J. & Choi, M.M. 2011, 'Fast growth synthesis of silver dendrite crystals assisted by sulfate ion and its application for surface-enhanced Raman scattering', *The Journal of Physical Chemistry C*, vol. 115, no. 20, pp. 9943-51.
46. Kobayashi, M., Juillerat, F., Galletto, P., Bowen, P. & Borkovec, M. 2005, 'Aggregation and charging of colloidal silica particles: effect of particle size', *Langmuir*, vol. 21, no. 13, pp. 5761-9.
47. Kim, T., Lee, K., Gong, M.-s. & Joo, S.-W. 2005, 'Control of gold nanoparticle aggregates by manipulation of interparticle interaction', *Langmuir*, vol. 21, no. 21, pp. 9524-8.
48. Hunter, R. 1992, 'Foundations of Colloid Science, Clarendon Pres', *London, Great Britain*.
49. Lee, T.G., Kim, K. & Kim, M.S. 1991, 'Raman scattering of α-toluenethiol adsorbed on silver sol', *Journal of Raman spectroscopy*, vol. 22, no. 6, pp. 339-44.
50. Segets, D., Marczak, R., Schäfer, S., Paula, C., Gnichwitz, J.-F., Hirsch, A. & Peukert, W. 2011, 'Experimental and theoretical studies of the colloidal stability of nanoparticles− a general interpretation based on stability maps', *ACS nano*, vol. 5, no. 6, pp. 4658-69.

51. Dong, X., Ji, X., Jing, J., Li, M., Li, J. & Yang, W. 2010, 'Synthesis of triangular silver nanoprisms by stepwise reduction of sodium borohydride and trisodium citrate', *The Journal of Physical Chemistry C*, vol. 114, no. 5, pp. 2070-4.
52. Dong, X., Ji, X., Wu, H., Zhao, L., Li, J. & Yang, W. 2009, 'Shape control of silver nanoparticles by stepwise citrate reduction', *The Journal of Physical Chemistry C*, vol. 113, no. 16, pp. 6573-6.
53. Frank, A.J., Cathcart, N., Maly, K.E. & Kitaev, V. 2010, 'Synthesis of silver nanoprisms with variable size and investigation of their optical properties: a first-year undergraduate experiment exploring plasmonic nanoparticles', *Journal of chemical education*, vol. 87, no. 10, pp. 1098-101.
54. Lee, S.-W., Chang, S.-H., Lai, Y.-S., Lin, C.-C., Tsai, C.-M., Lee, Y.-C., Chen, J.-C. & Huang, C.-L. 2014. Effect of temperature on the growth of silver nanoparticles using plasmon-mediated method under the irradiation of green LEDs. *Materials*, 7, 7781-7798.
55. Zhu, C., Meng, G., Huang, Q., Zhang, Z., Xu, Q., Liu, G., Huang, Z. & Chu, Z. 2011, 'Ag nanosheet-assembled micro-hemispheres as effective SERS substrates', *Chemical Communications*, vol. 47, no. 9, pp. 2709-11.
56. Kruszewski, S. & Cyrankiewicz, M. 2013, 'Rhodamine 6G as a Mediator of Silver Nanoparticles Aggregation', *Acta Physica Polonica, A.*, vol. 123, no. 6.
57. Cao, D.T., Ngan, L.T.Q., Viet, T.V. & Anh, C.T. 2013, 'Effect of $AgNO_3$ concentration on structure of aligned silicon nanowire arrays fabricated via silver–assisted chemical etching', *International Journal of Nanotechnology*, vol. 10, no. 3-4, pp. 343-50.
58. Niauzorau, S., Girel, K., DOLGYI, L. & BONDARENKO, V. 2015, 'Formation of Porous Silicon Nanostructures by Metal-Assisted Chemical Etching', *Physics, Chemistry and application of nanostructures: Proceedings of International Conference Nanomeeting-2015*, World Scientific, pp. 365-8.
59. Han, S. (2015). Optimization of Aggregating agents and SERS Substrates for SERS detection of Cotinine and trans 3'-hydroxycotinine (Doctor of Philosophy (Ph.D.) thesis, University of South Florida, United States). Retrieved from *Scholar Commons Graduate thesis and Dissertations* database.
60. Florindo JB, Sikora MS, Pereira EC, Bruno OM. Characterization of nanostructured material images using fractal descriptors. *Physica A: Statistical Mechanics and its*

Applications. 2013;392(7):1694-701.

61. Wang T, Zhou J, Wang Y. Simple, Low-Cost Fabrication of Highly Uniform and Reproducible SERS Substrates Composed of Ag–Pt Nanoparticles. *Nanomaterials*. 2018;8(5):331.
62. Gutes A, Carraro C, Maboudian R. Silver dendrites from galvanic displacement on commercial aluminum foil as an effective SERS substrate. *Journal of the American Chemical Society*. 2010;132(5):1476-7.
63. Nie S, Emory SR. Probing single molecules and single nanoparticles by surface-enhanced Raman scattering. *Science*. 1997;275(5303):1102-6.
64. Nowicki W, Nowicka G. Verification of the Schulze-Hardy rule: a colloid chemistry experiment. *Journal of Chemical education*. 1994;71(7):624.
65. Lee P, Meisel D. Adsorption and surface-enhanced Raman of dyes on silver and gold sols. *The Journal of Physical Chemistry*. 1982; 86(17):3391-5.
66. Shrivastava, A. & Gupta, V. B. 2011. Methods for the determination of limit of detection and limit of quantitation of the analytical methods. *Chronicles of Young Scientists*, 2, 21.

Chapter 3. SLIPSERS Substrate Characterisation

3.1. Introduction

Most SERS studies focus on surface-enhanced Raman scattering enhancement of hot-spots in interaction with specific analytes. Very few studies have characterised the SERS substrate. Due to hotspots being responsible for the majority of Raman scattering from SERS substrates one approach to characterization of SERS substrates is to scan the location and density of hotspots and to attempt to model the distribution of intensities across a SERS substrate. **[28]** This chapter utilises a line-scan approach, where spectra are recorded at successive points along a line defined over the SERS substrate to look at the location and number of hotspots with analyte that can alter SERS fingerprint which has not been explored before. By accepting that hotspots are highly variable, a statistical approach to characterizing SERS substrates is adopted where the distribution of hot-spots is measured, and the hotspot distributions can then be used to compare other SERS substrates.

There are many challenges in characterization of SERS substrates including spectral variations induced by hot-spots, sample damage due to the "focusing effect" of hotspots and the "blinking" **[29, 30]** behavior of SERS. The blinking refers to frequent SERS fluctuations either due to photobleaching which is a light-induced component **[30]** or thermal effects which is a thermo-activated component **[31]**. It can be a challenge to separate photo-induced effects from purely thermal effects.

Photobleaching depends on laser power density which may bleach the molecules at the hot-spots which results in a change in the Raman cross section. This change in cross-section will produce fluctuations particularly with the molecules at active sites because they have the largest enhancements as compared to other surface non-active or weak sites.

The thermal effect is either heat produced either by the adsorbate or from the highly intense laser which might damage the samples and lead to fluctuations. There is always a significant background to every SERS analyte due to the emission continuum.**[33]** When the background and SERS signals come to the same intensity, then photon count becomes very low. Unlike colloidal SERS,

SLIPSERS uses dried samples – so there is no "solvent bath" to absorb the incident laser energy and therefore cause sample damage through intense local heating. During this study extra caution was taken to identify the carbonaceous species indicating sample damage.

A more common SERS molecule (e.g., R6G) wasn't used here for hot-spot characterisation. The reason is that R6G has strong molecular resonance enhancement as well as plasmon enhancement [refer Chapter 1]. And because R6G itself has strong photon absorption, it may undergo photobleaching, independently of SERS-enhanced photobleaching. Therefore, for characterizing the plasmon enhancement of the SLIPSERS substrate, such an analyte is required that should not have any molecular resonance enhancement. There are many molecules that could have been selected for this purpose like 1,2-di-(4-pyridyl)-ethylene (BPE) **[32]**, but Lidocaine hydrochloride or [(2-(diethylamino)-N-(2, 6-dimethylphenyl) acetamide], also known as lignocaine, was chosen simply because it is of interest as an analyte elsewhere in the thesis.

Therapeutic use of veterinary drugs has increased the risk of residue contamination in animal food products. In humans, lidocaine is also used primarily for local anesthesia at many indications **[1**]. Lidocaine overdose may result in coma, seizures, and death. There was a case of death of a 76-year-old man due to an overdose of lidocaine to treat heart disease **[26**]. There are several other reports of lidocaine exposures resulting in fatality **[27]**. Wrong calculations for drugs or repeated doses for therapeutic purposes are causes of toxicity inducements in humans. To guarantee there is no risk to the consumer and regarding consumer protection, the toxicity of drug residues must be evaluated before the use of a medicinal substance in food-producing animals is legalised.

The lidocaine metabolite 2, 6-xylidine, is categorised as a potential carcinogen in humans. Lidocaine hydrochloride or [(2-(diethylamino)-N-(2, 6-dimethylphenyl) acetamide], also known as lignocaine, a water-soluble local anesthetic agent will be used as an analyte for characterising surface-enhanced Raman scattering generated by SLIPSERS substrate and various factors responsible for surface-enhanced Raman signal in this study.

The single-molecule regime was observed with the R6G in Chapter - 2 with a detection limit down to 10^{-15} mol/L. It was observed that by lowering the concentration the signal intensity eventually becomes approximately constant. This is because below a critical concentration the probability of finding an R6G molecule (or possibly a small aggregate of R6G molecules) in the focal volume ***and at a hot-spot*** becomes quite low. This is the sub-sampling regime, and a certain level of

fortuitousness is required to find a signal. But if the microscope objective does focus on a hot-spot with R6G, a signal is obtained, but the signal is roughly the same intensity for each hot-spot (in the same way as the SLIPSERS and SERS EF are roughly the same).

In this chapter Raman line-scanning of the SLIPSERS substrate is used to characterize the spatial distribution of hot-spots, possibly with the hope of being able to model the sub-sampling with an appropriate distribution. Another motivation for obtaining Raman line-scans is that SLIPSERS data collected on analytes within complex matrices do not give identical spectra which suggests that sub-sampling might be occurring, but the appearance of new features in the Raman spectra might also be due to sample damage as discussed above.

Two hypotheses were assumed before performing line-scan:

(1). The analyte and the "matrix" components are unevenly (i.e. heterogeneously) distributed over the SLIPSERS substrates. If this was true then spectra taken from different spots will be different, meaning, different features will appear in different spectra.

(2). The analyte and matrix are evenly distributed. If this were true, then all spectra should appear similar (meaning the relative intensities of the features in the spectra should be consistent for all the points in the scan).

There was another scenario which was not considered beforehand but does help to explain the results from the mapping data, that is, the sample being damaged, but the damage only occurs at certain points. So, by recording a Raman map, the spectra at different points can be analysed across the substrate to determine if the spectra are different, or not. Finding the best hot-spot was difficult and took longer acquisition times to cover a wide range of areas. Secondly, with complex biological matrices, highly focused laser spots make quantification quite challenging because of signal fluctuations that add to the complexity of analysis. This defines the spatial inhomogeneity problem. If this is the case, then the set of spectra collected from a Raman line scan over the SLIPSERS surface could be classified into subsets. Classification can be achieved using multivariate statistical techniques such as Principal Components Analysis (PCA). **[3]**

To describe briefly the concept and history of line-scan Raman mapping, in 1975, Delhaye and Dhamelincourt **[2]** firstly introduced the concept of the "Raman microprobe" and described two approaches to Raman imaging. These imaging methodologies were classified as either direct

(raster) imaging technique or serial imaging also known as line-scan mapping. For direct imaging, the detection system detects a single wavenumber using a monochromator, and the spectrum is acquired by scanning the monochromator. The Raman image would have been acquired by setting the monochromator to a fixed position and raster scanning the sample. This is entirely different from a modern Raman microscope where a spectrograph and multichannel CCD (Charge Coupled Device) detector acquires the entire spectrum at each microscope position. However, the "spatial" information is still obtained in the same manner – by raster scanning the sample relative to the objective lens of the Raman microscope. The only advantage of line-scan on a multichannel detection system is acquisition time. Spatial resolution remains the same.

Most SERS measurements are obtained by capturing single spectra at a few points of interest in a sample. This acquisition process can be cumbersome and may yield random results. A line-scan is performed to scan the sample point-by-point over a line where each pixel of the resulting image corresponds to a complete Raman spectrum. This generates multiple spectrum files with short acquisition time less than 100 milliseconds as shown in Figure 3.1.

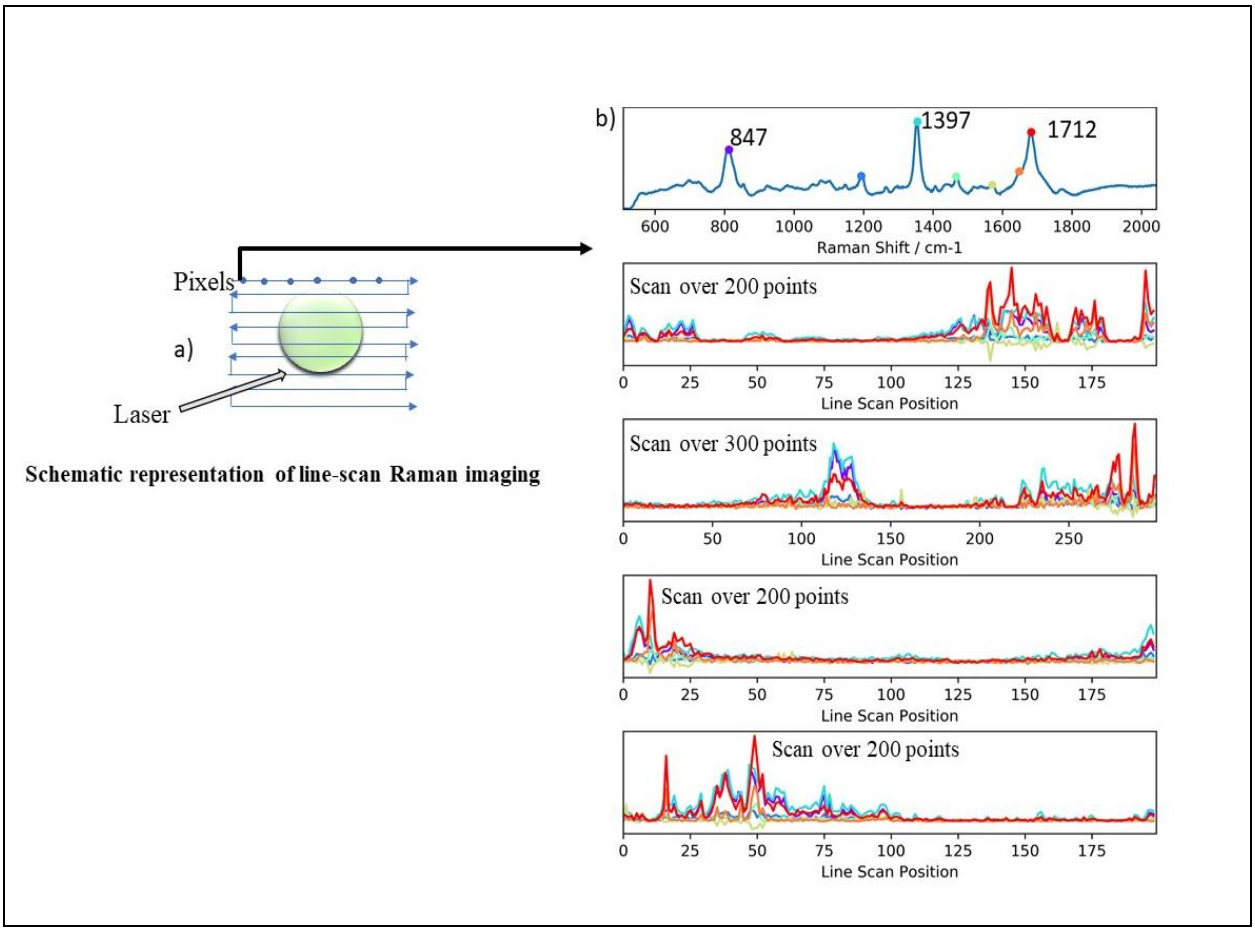

Figure 3. 1: a) Schematic representation of line-scan Raman mapping generating b) average SLIPSERS spectra of 10-3 mol/L Lidocaine hydrochloride concentration (top) with three line-scans (bottom) acquired at 532 nm excitation wavelength with the acquisition time of 0.5 s using 50X objective.

The aim of this work was to characterise different SERS substrates by analysing hotspot distributions using line scan Raman imaging and finally PCA to identify "classes" within a sample set across the line-scans. Because SLIPSERS substrates are relatively new and because they purposefully set out to produce a very high density of hotspots, it is of interest to characterise the hotspot distributions in SLIPS aggregates. Furthermore, as the hotspot distribution could provide some sort of reproducible measure of a SLIPS Raman performance, it is hoped that the hotspot distributions could be used as a basis for rationally improving not only SLIPS substrates but other types of SERS substrates.

3.2. Experimental

SERS and SLIPSERS samples were prepared as described in experimental Chapter -2. The only change is the different analyte which is lidocaine hydrochloride in this case. For this study, lidocaine hydrochloride was obtained from the Institute of Veterinary, Animal and Biomedical Sciences, Massey University, New Zealand. All solutions were prepared in Milli-Q water having a resistivity of 18MΩ. All the chemicals were of high analytical grade.

To investigate the sample in depth, the Raman spectra were collected as a line-scan along a line of the sample (200 - 300 points on a scan), with an integration time of 0.5 seconds per spectrum. SERS spectra were acquired under ambient conditions with a WiTec alpha300R+ confocal Raman microscope equipped with a 532 nm excitation laser. A 50X objective was used to focus the excitation laser light spot on the samples operating in 180° backscattering geometry. Raman edge filters were used to block Rayleigh scattering from the sample. A 600 lines/mm grating spectrograph equipped with a 1340 × 400-pixel CCD camera dispersed and detected the Raman scattered light. This data was collected at University of Otago (with the assistance of Dr. Sara Fraser). For the high reproducibility of the experiments, the laser power was determined using a power meter integrated in the optical path. 0.1milliwatt was set for collection and analysis of samples. The entire Raman data set has been collected within an hour, with several line-scans being acquired for each sample. Removal of the baseline and cosmic spikes thus enhances the Raman images and provides a constant background in the images. Mark Waterland scripted the Python algorithm for generating PCA spectra using Python 3 software.

3.3. Results and Discussion

3.3.1. Optical imaging using line-scan

With our custom-built setup at Massey University, a 1 – 2-micron spot was used with 532 nm excitation laser with 2 mW power. The large spot size gives a low irradiance (i.e., mW cm^{-2}), which limits sample damage. But such a setup is not capable of giving enough spatial resolution to properly characterize the spatial distribution of hotspots in the sample.

The WiTEC system at the University of Otago has a diffraction-limit spot size (approx. 300 nm). However, this represents a significant increase in irradiance as the illuminated area is now almost 50 times smaller than the spot size of the custom-built system.

Sample damage is always a consideration in surface-enhanced Raman spectroscopy due to highly focused incident light and plasmon enhancement. It is visible in the optical image (Figure 3.3) with a faint imprint of a line which shows damage and the red line represents the line-scan. There are certain hot-spots that are very efficient at increasing the electric field strength at the hot spot which is equivalent to focusing the field at the hot spot and at these hot spots the sample breaks down, possibly due to dielectric breakdown, or due to localised heating of the sample or both. Under these conditions, the organic sample is converted into some sort of graphitic material. The background spectra (Figure 3.2) were obtained by applying the asymmetric least squares algorithm that attempts to "follow" the local baseline of the Raman spectrum by penalizing any fitted points that lie above the recorded data. Dark areas correspond to noise with no hot-spots found. These scans were acquired with a very low laser power (0.1 mW). The figure below shows that the shape of the average baseline matches the graphite spectrum in Figure 3.4 quite nicely.

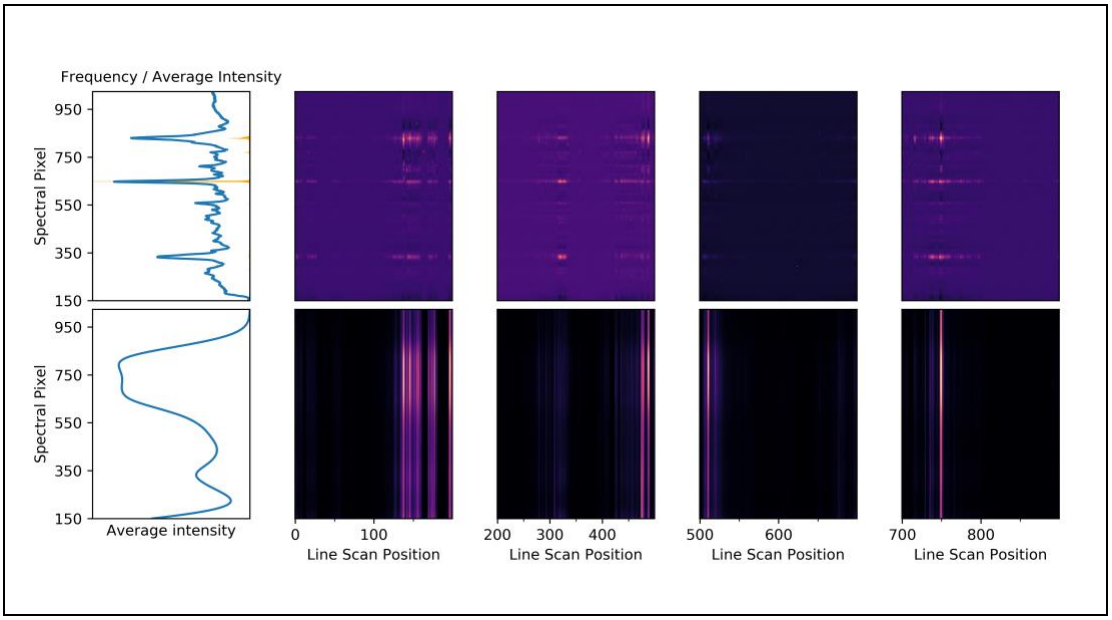

Figure 3.2. SLIPSERS spectra of LHC 10^{-3} mol/L concentration showing highly intense peaks in line scan and baseline spectra underneath for each scan.

The graphitic spectra were found in the samples where the imprint of the line confirms the sample damage indicating carbonization of the sample. Hence, after several trials of power adjustment, 0.1 milliWatt was set for collection and analysis of samples considering sample damage threshold, photodegradation, or even sample drying. **[4]** It is not possible to use the same laser power on different experimental setups. WiTEC has a limited diffraction spot, so this gives the smallest possible spot size, and hence, for a given laser power, the highest possible irradiance (power per cm^2). But high irradiance leads to sample damage. Therefore, 0.1 mW was set as optimum laser power that gives no sample damage.

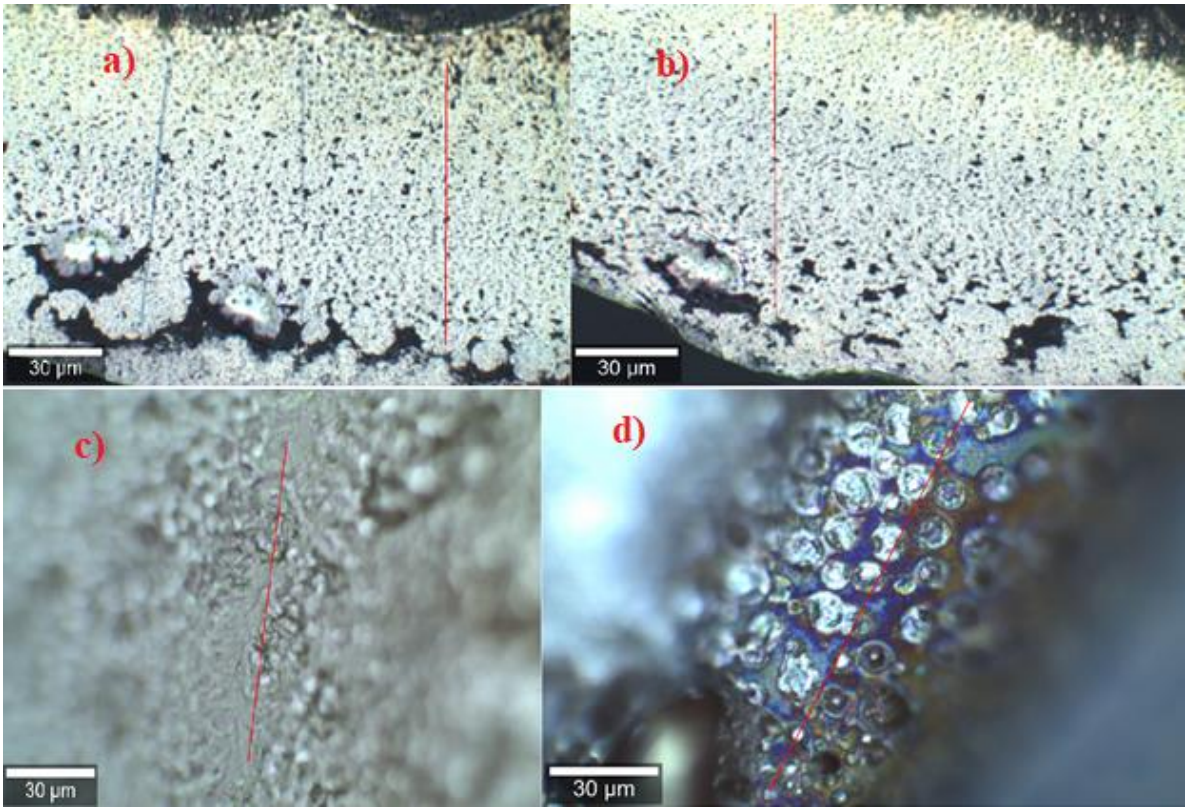

Figure 3. 3: Optical images of a) SERS LHC/Ag nanoparticle aggregate which clearly shows the sample damage with faint line after line scan b) SERS of LHC/Ag nanoparticle aggregate with minimal laser power 0.1 mW c) SERS of dog plasma d) SLIPSERS LHC sample.

The laser "burns" the sample and produces a carbonised material that has some graphite content (as evidenced by the G-band). The graphite has a lot of defects, as evidenced by the D-band. The D-mode at about 1350 cm^{-1} is caused by damaged graphite lattices. The G-mode is at about 1583

cm-1 and arises from the stretching of the C-C bond in graphitic materials and is common to all sp2 carbon systems.**[5]**

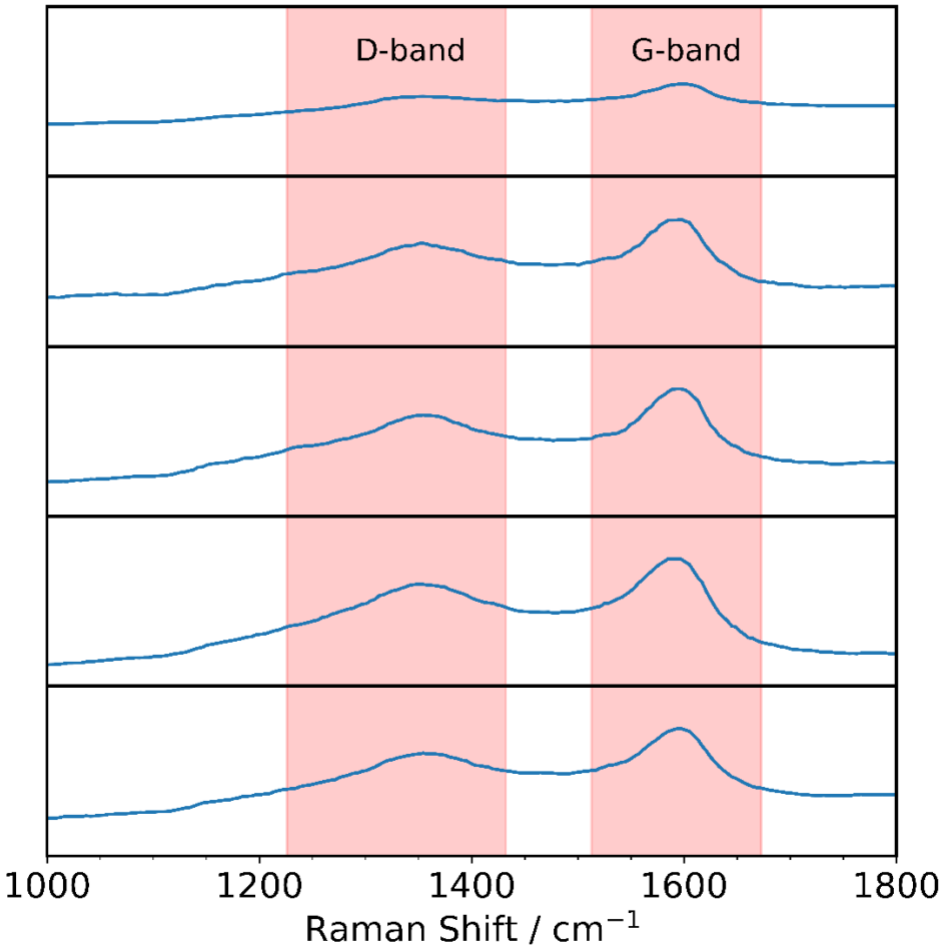

Figure 3. 4: Raman spectra graphite samples showing different extent of damage to the graphite lattice via the intensity of the D-band

The intense electric field at the sample is partly due to the strongly focused beam and partly due to the plasmon enhancement in the SLIPSERS measurements which is enough to induce a carbonisation process in samples, even at milliWatt levels of laser power. As will be shown below, the carbonisation only appears at the hotspots and this observation supports the idea that strong plasmon enhancement not only gives strong Raman scattering but runs the risk of sample damage.

The possibility of sample damage at the hotspots has implications for analytical applications of SERS, where sample damage is very rarely considered.

3.3.2. Spectral characterisation using line-scan

Several line scans were taken for selected sample concentrations. Line-scans ranged in length from 200 to 300 points. **[34]** Average spectra of SERS (Figure 3.5) and SLIPSERS substrates (Figure 3.6) for 10^{-3} mol/L and 10^{-8} mol/L lidocaine hydrochloride concentrations were generated. There are few dips around 1592, and 1796 cm^{-1} (Figure 3.5) are artifacts from the asymmetric least squares baselining algorithm which attempts to fit a smooth baseline to noisy spectra but sometimes fails in regions with strongly varying intensity (where no obvious "baseline" exists).

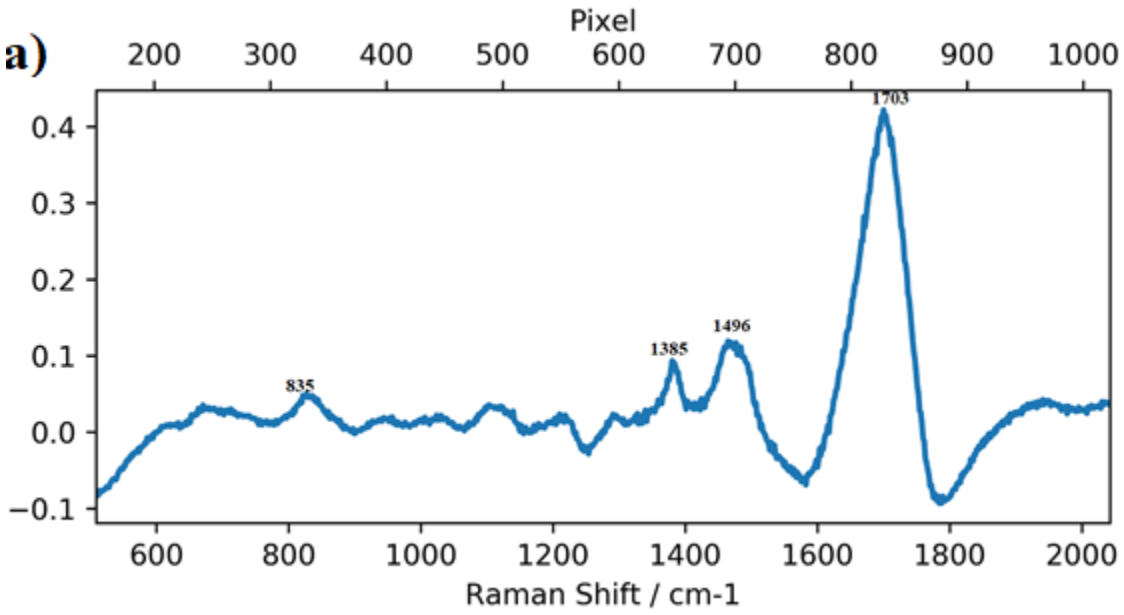

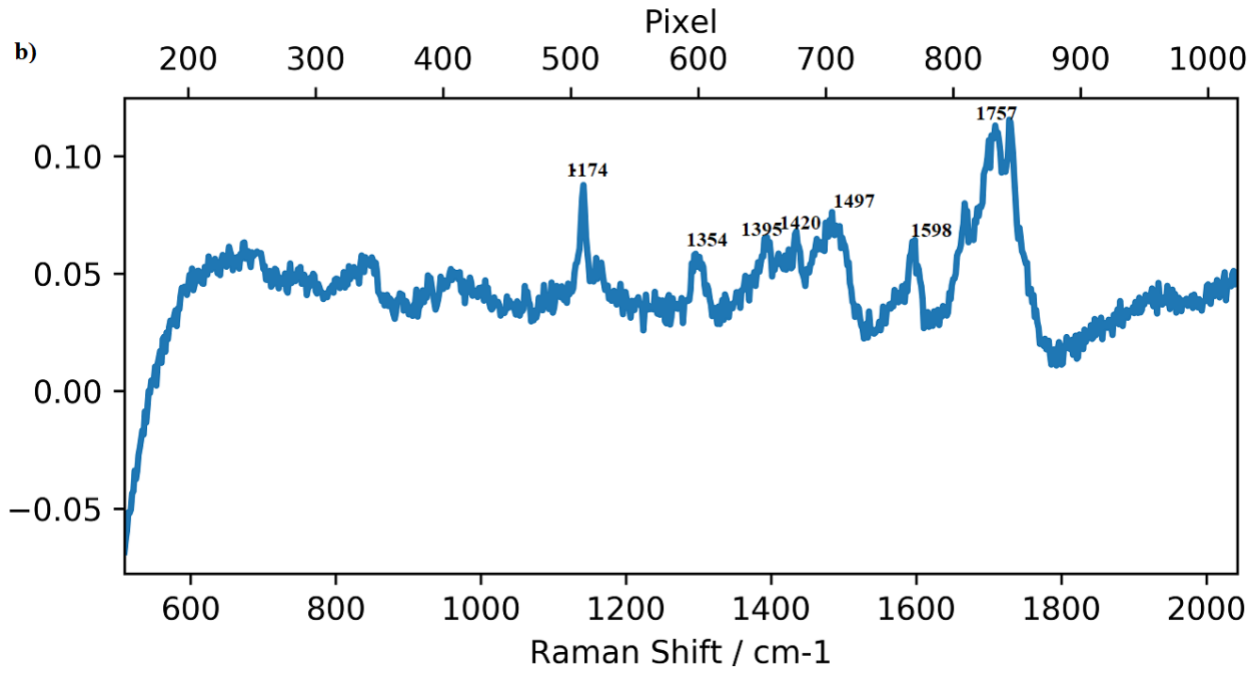

Figure 3. 5: Average SERS spectra of line-scan imaging of Lidocaine hydrochloride (a)10-3 mol/L and (b) 10-8 mol/L(bottom) concentration acquired at 532 nm excitation wavelength with the acquisition time of 0.5 s using 50X objective.

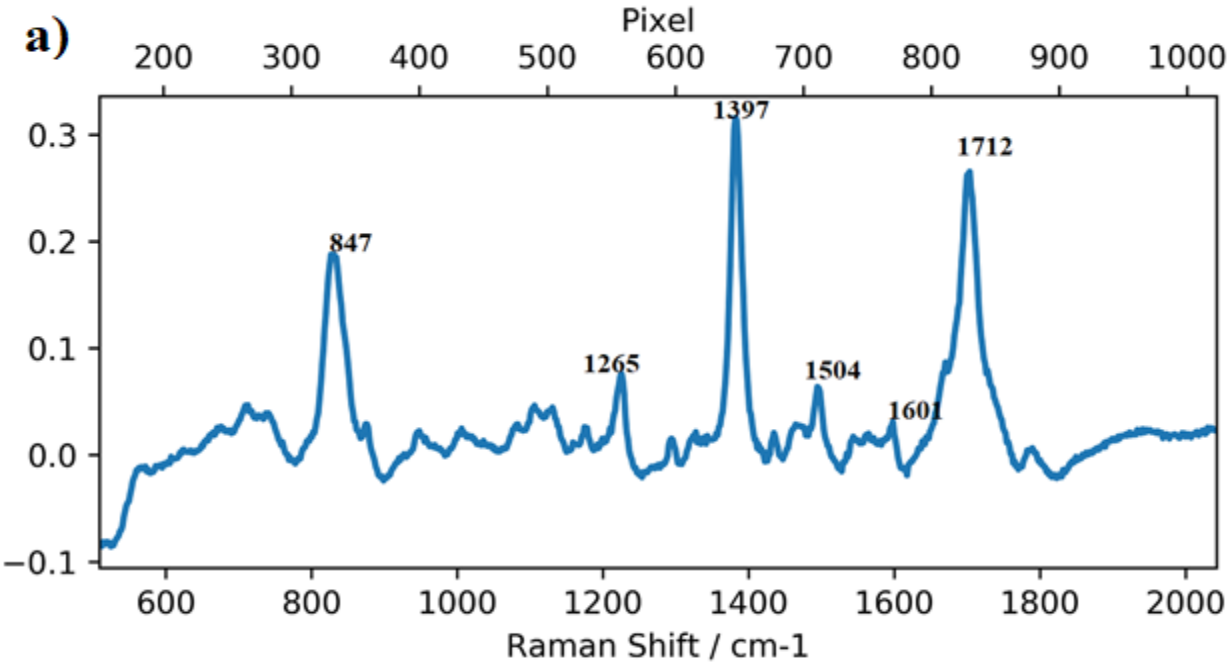

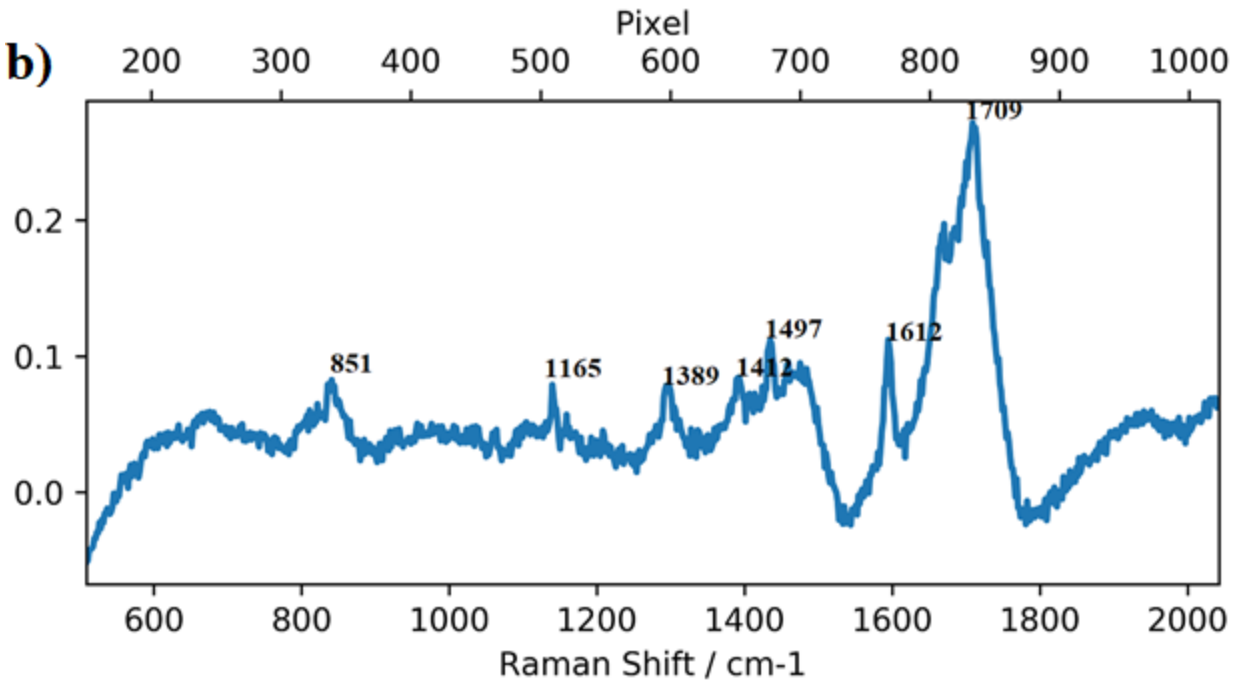

Figure 3. 6: Average SLIPSERS spectra of line-scan imaging of Lidocaine hydrochloride (a) $10^{-3}$and (b)10^{-8} mol/L(bottom) concentrations acquired at 532 nm excitation wavelength with the acquisition time of 0.5 s using 50X objective.

There is a strong band at 1174 cm^{-1} in the 10^{-8} mol/L SERS spectra in Figure 3.5. that doesn't appear in the 10^{-3} mol/L spectrum. For the SLIPSERS spectra, the strongest Raman peaks observed were 847, 1397 and 1712 cm^{-1} for 10^{-3} mol/L sample which were quite different from the peaks obtained from 10^{-8} mol/L concentration (Figure 3.6.)

Somewhat surprisingly, the pattern of enhancements between the SLIPSERS and SERS spectra do not closely agree with each other and even within concentrations which illustrates the inhomogeneity of hot-spots over the substrates. There could be a change in the molecular orientation inside the hot-spots due to different fabrication procedure for SERS and SLIPSERS substrates. SERS has a variety of hot-spots which are spread non-uniformly over the edge of dried drop ("coffee-ring effect") which in contact with LHC can attribute to different spectral features compared to SLIPSERS where controlled drying brings a uniform and confined region of silver nanoparticles to an aggregate with many hot-spots containing analyte giving relatively different enhancement of Raman signal.

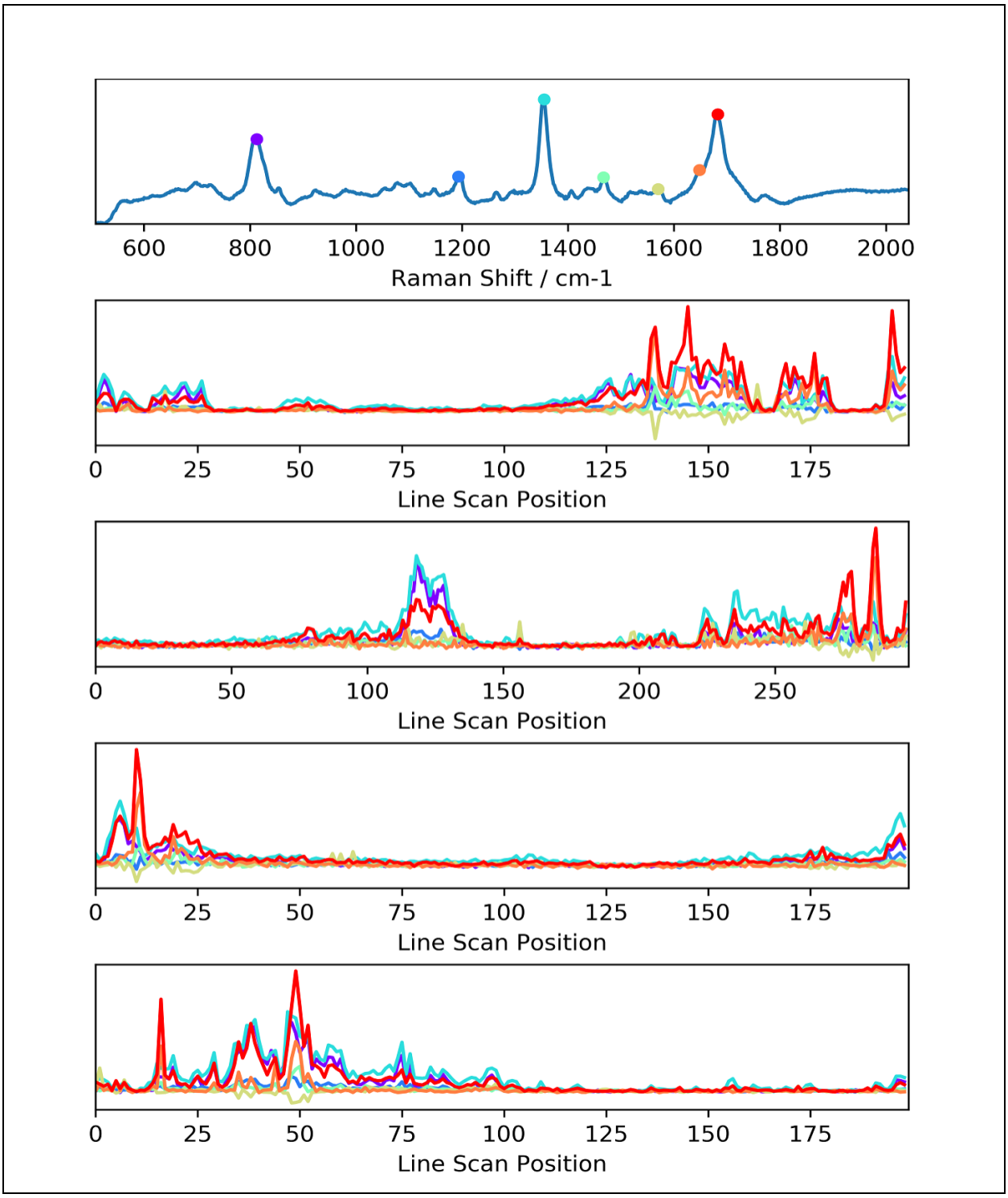

Figure 3. 7: Average SLIPSERS spectra of 10^{-3} mol/L Lidocaine hydrochloride concentration (top) with three line-scans (bottom) acquired at 532 nm excitation wavelength with the acquisition time of 0.5 s using 50X objective.

Another reason for variations within each substrate at different concentrations could be that only a few points gets enhancement over the surface of substrate for one concentration whereas for another concentration different pixels get enhanced. This bring non-uniform distribution of hot-spots within the concentration and even within substrates.

Figure 3.7. represents the scanning the samples along a line using 532 nm laser at various points to create a visual image from the simultaneous measurement of spectra. SLIPSERS substrate was used for characterization due to highly confined region to focus for hot-spots. Line-scans for selected peaks in the ***average*** spectrum are shown, coloured according to the selected peak. 10^{-3} mol/L SLIPSERS sample was run for four scans with first scan for 200 points in a line, second for 300 points, third for 200 points and fourth for another 200 points. It was found that the most intense peak at 1397 cm^{-1} (cyan) in the average spectrum is not consistently the highest peaks during the scans whereas peak at 1712 cm^{-1} (red) is strongest at more locations. But surprisingly this red peak is not observed at one fixed position during the line-scan it keeps on changing to find the best hot-spot for enhancement. Therefore, it demonstrates that when the sample is placed under Raman the entire surface of the substrate gets enhanced and that can be observed as spectral variations at different positions across line-scans. (Figure 3.8(b)) If the hot-spot distribution was uniform, then the most intense peaks will be found at the same location and it amplifies with scans (Figure 3.8(a))

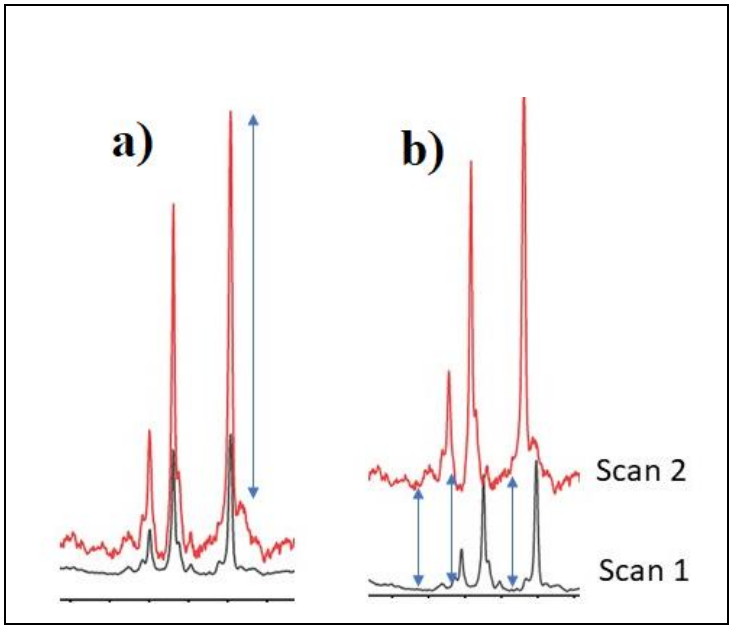

Figure 3. 8: a) Uniform hot-spot distribution with most intense position same for most pixels b) non-uniform hot-spot distribution with shift in position for enhancing most pixels.

Looking down at low concentration 10^{-8} mol/L LHC SLIPSERS samples (Figure 3.9.), the intense spectral peaks were quite noisy. It was found that at low concentrations generally used in single molecule detection, the probability for a molecule to be located exactly in a hotspot is extremely low, which leads to the large portion of unoccupied hotspots, i.e., a minimum number of detectable SERS signals.

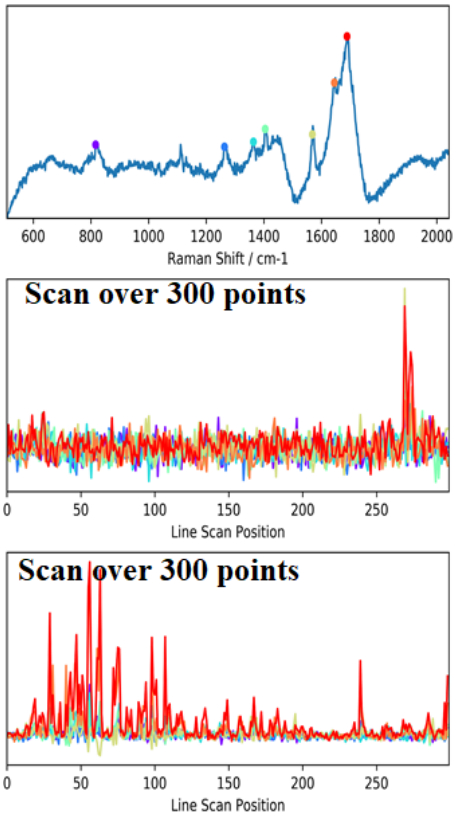

Figure 3. 9: SLIPSERS spectra of LHC 10^{-8} mol/L concentrations with average spectra (top) and high intensity spectral points of each scan (bottom two)

3.3.3. Spectral Histograms

The "spectral histograms" are generated by finding the pixel that corresponds to the maximum intensity for each spectrum. This process is repeated for each position in the line-scan.

Then, a histogram is created for these "maximum pixels". The histogram then shows how many spectra have their maximum value at each pixel. Looking at the output (Figure 3.10(a)) for

lidocaine hydrochloride 10^{-3} mol/L concentration, two pixels dominate the histogram (ignoring a couple of pixels either side, that could be assigned to minor intensity variations that shift the peak maximum to a neighbouring pixel).

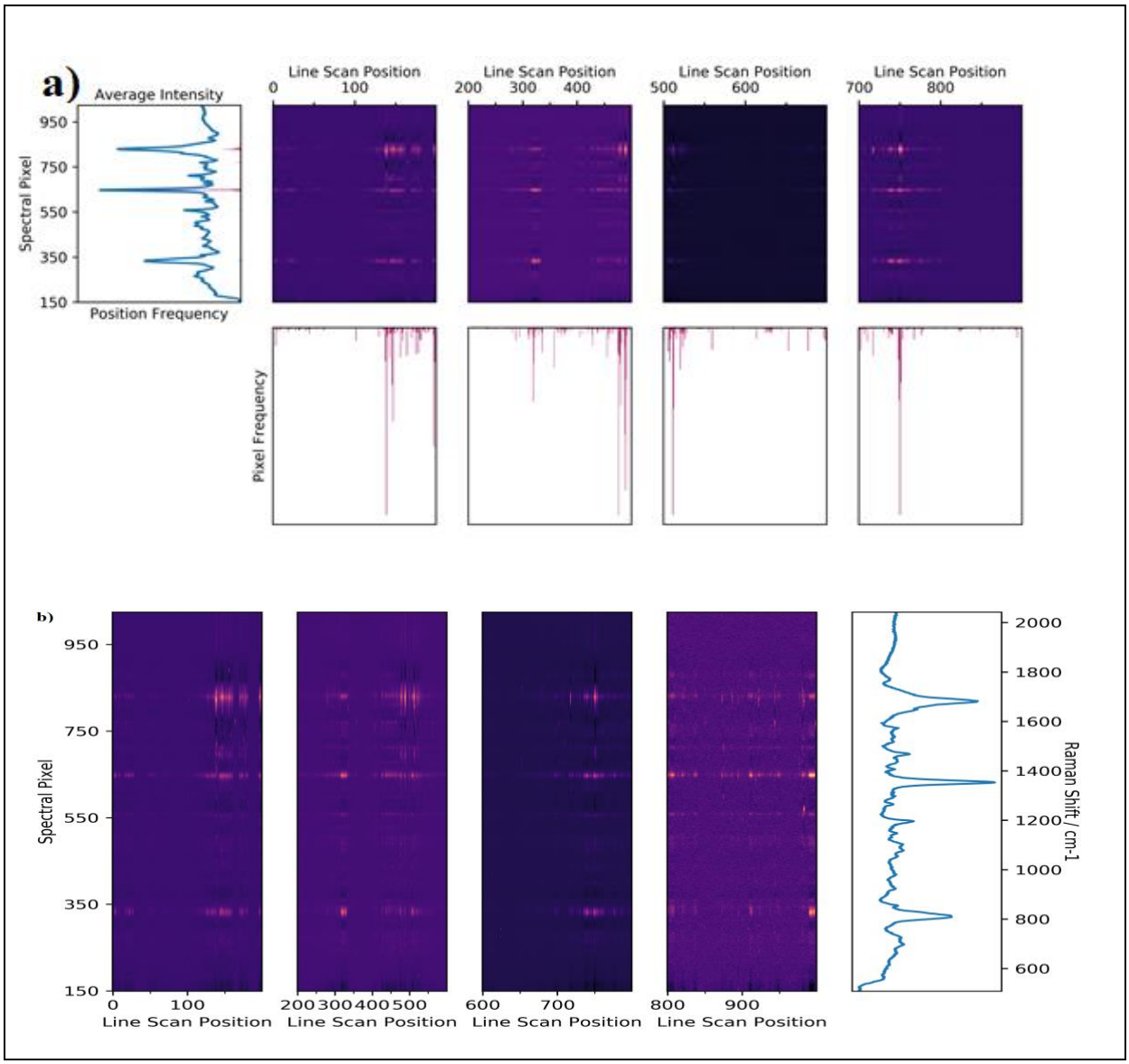

Figure 3. 10: a) SLIPSERS spectra of LHC 10^{-3} mol/L concentration showing spectral histogram as a line scan and scan histogram underneath for each scan. b) zoomed version of with highly intense spectral peaks of LHC 10^{-3} mol/L reflecting as red shining line in the line scan image.

If it was assumed that all molecules receive the same enhancement (meaning all band intensity ratios are the same for every molecule) across the entire substrate, then only one pixel should be the maximum pixel for ***all spectra*** and the histogram should have a single "peak". But clearly, this

was not the case, because there seems to be an even split between the peaks at 1397 and 1712 cm-1 for maximum Raman shift honours. This mean there must be some variation in the enhancement between molecules, so might expect some variation in enhancement between sites. In this case, a single peak with the maximum value was found. So different hotspots must enhance different modes to different extents.

The spectral histogram is over ***all scans*** in the data set. Looking at individual line-scans, it looks like the peak at 1712 (red) is the most intense peak for the first, third and fourth line-scan. But for the second scan, it looks like peak 1397 (blue colour) is the most intense peak 1397 is also the most intense peak in the average spectrum. Individual histograms for each line-scan have been generated.

3.3.4. Scan Histograms

The "scan histograms" are generated by finding the position (in the scan) that has the maximum intensity. This process is done for all the pixels.

Then, a histogram of the "scan max" was generated. The histogram shows how many ***pixels*** have their maximum value at each position.

The scan histogram shows the ability of each location to enhance the signal strength. Consider an idealized situation, such as one "super hot-spot" that enhances the scattering while the remaining positions have very weak signal strength. This means the intensity of every pixel in the "super hot-spot" spectrum is greater than the maximum value of the remaining spectra. **[8]**

It was observed that one or two positions account for nearly all the most intense pixels. This suggests that the enhancement is highly localised to one or two hot-spots, and it also indicates that scattering increases from nearly ***all*** the pixels in a spectrum (this is reasonable because, to a first approximation, resonance with the plasmonic transition increases the Raman cross-section of vibrational modes uniformly). **[7]** As mentioned in the introduction, strong SERS enhancement is often accompanied by a broad background of enhanced emission continuum and this enhanced background also contributes the enhancement of many pixels in a spectrum over neighbouring spectra. **[33]** What is surprising is that this enhanced background which is usually completely ignored in analysis of SERS spectra) can have greater intensity than Raman scattering from

neighbouring spots. If SERS generates an emission continuum then this will be observed as an increase in intensity of most of the pixels in the spectrum, and this explains the appearance of the SERS histograms.

3.3.5. Hot-spot to hot- spot variations

It is necessary to understand how the enhancement distributions may change from one hot-spot to another. This study is important to understand a series of measurements where one single hot-spot may be measured at any given time, but not necessarily the same one each time. The below intensity distribution charts (Figures 3.11.) represents another way of how signals vary on a substrate with variable hot-spots.

Maximum pixel distribution chart shows the number of scans having maximum pixel intensity whereas maximum scan distribution shows which pixel has maximum intensity, for example, '**199**' pixel in one scan has maximum intensity than other and it arranges the intensity in decreasing trend.

There is some statistics associated with the distribution of SERS intensities, which suggests that the Pareto principle or 80/20 rule (first applied to wealth distribution in economic systems), applies to the distribution intensity. Relating the Pareto principle to SERS says that 80% of the signal will come from 20% of the SERS sites. As per literature, Pareto distribution of SERS **[11]**, for a high concentration means there are large number of molecules on the surface, then the observed SERS signal have little fluctuations. It means many hot-spots are located on the surface. The fluctuations are then reasonably small but still present. This principle was tested on SLIPSERS 10^{-3} mol/L LHC data and the same trend was observed with SLIPSERS substrate for lidocaine detection.

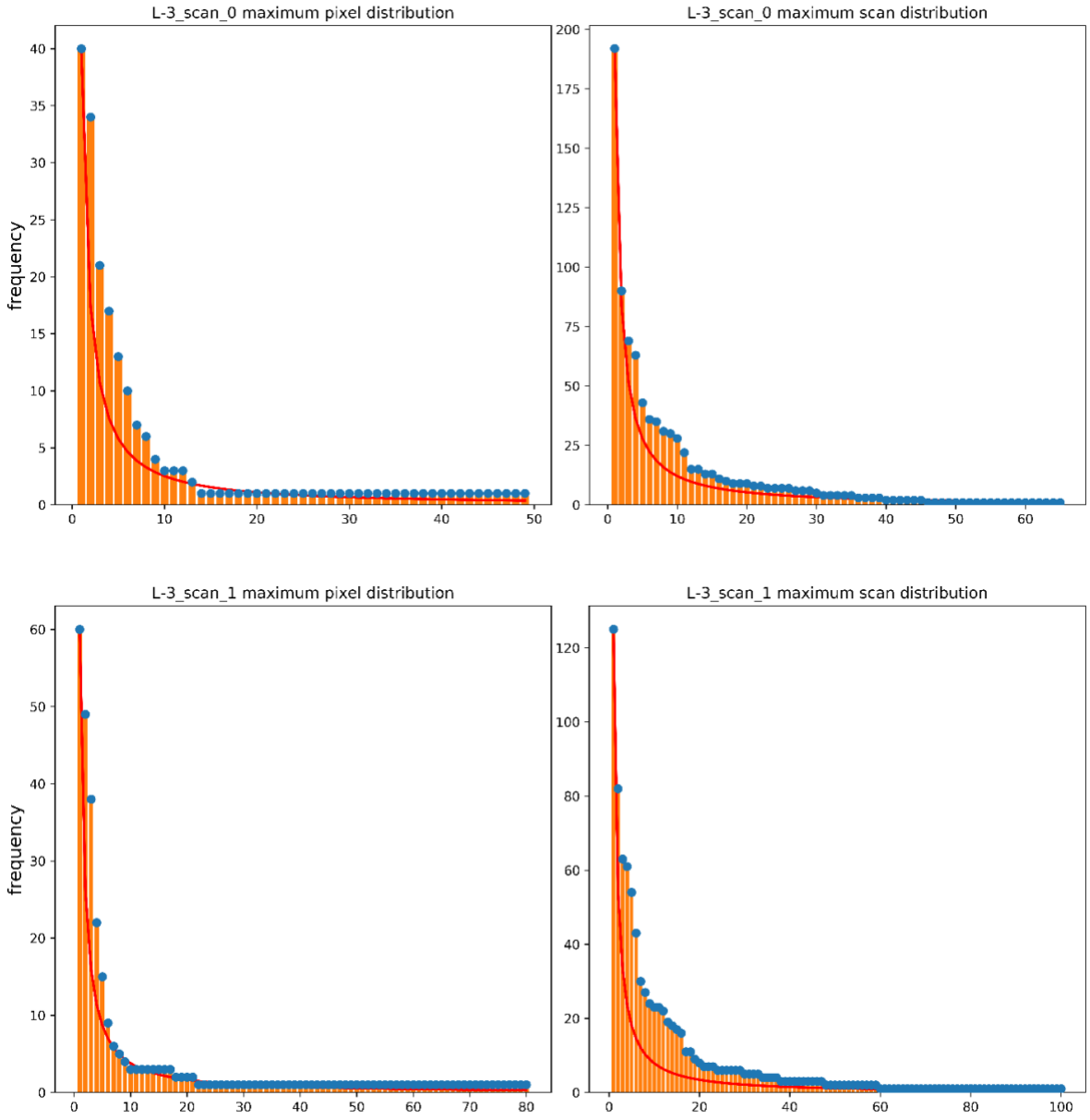
L-3_scan_0 maximum pixel distribution
L-3_scan_0 maximum scan distribution
L-3_scan_1 maximum pixel distribution
L-3_scan_1 maximum scan distribution
frequency
frequency

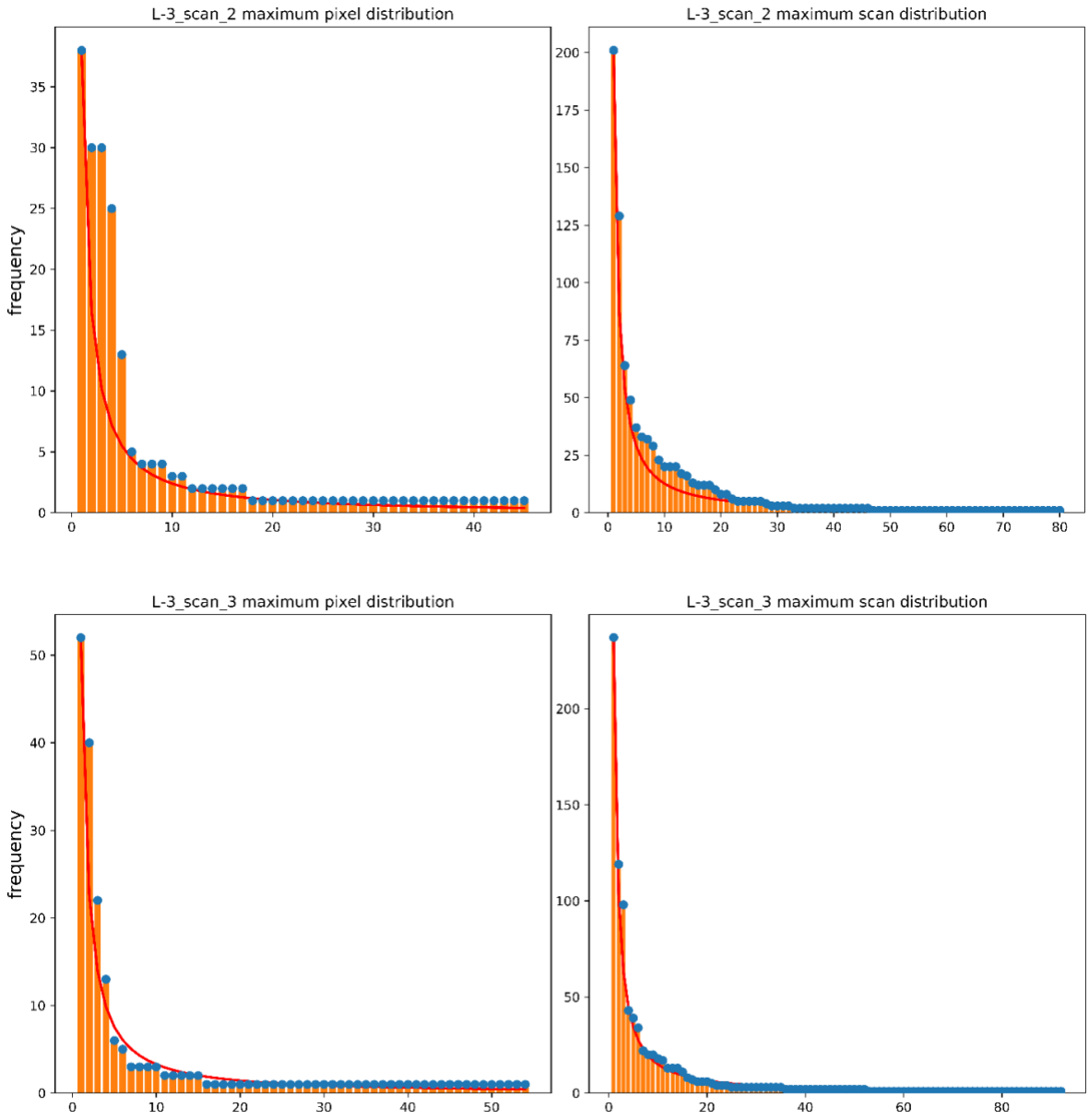

Figure 3. 11: Maximum pixels and scan distribution of intensities for SLIPSERS spectra of highly concentrated lidocaine hydrochloride 10-3 mol/L for four scans.

Figures 3.11. is the best example of Pareto distribution of enhancements that leads to a distribution of SERS intensities with a high-intensity tail to skew line covering the fit scale**. [14, 15]** The intensity is just fluctuations added to SERS signal represented as a line of dots in a series. Only a little proportion of the colloids were active, that means only the ones where the molecule was by chance at the hot-spot region. **[12,13]** As we move to lower concentrations, it becomes tough to

find single hot-spot due to single molecule regime, which means there is indeed less than one molecule in the scattering aggregate. In such case, the SERS signal will only be detected if it is located close to hot-spots or within the crevices of a hot-spot region which is expected to have sufficiently high enhancement. Moreover, the intensity of these series of line-scan events will fluctuate depending molecule location to the hot-spot. Hence both SERS (Nie *et al*.) **[22]** and SLIPSERS behaviour relate with each other in terms of the limit of concentrations, but it is extremely challenging to find several detectable spots, or which one is better in terms of identification of hot spots due to no prior statistical information on SLIPSERS.

Colloidal SERS systems are known to fit Pareto distributions. The objective of the study is interested in knowing if there is something different about SLIPSERS due to the controlled drying and high density of hotspots. The results of the Pareto fits show that the SLIPSERS and SERS give very similar distributions which suggests that there is nothing inherently special about SLIPSERS substrates apart from the higher concentration of analyte due to the drying process.

3.3.6. Multivariate analysis

As mentioned in the introduction two scenarios were proposed regarding the composition and distribution of the analyte over the substrate:

First, that an analyte might occupy one hot-spot, and the matrix components could occupy different hot-spots. So hot-spot selection, which unfortunately is a random process, becomes quite critical. If this was the case, then the full set of spectra collected over the Raman line-scan should show different “types” of spectra.

An alternative hypothesis is that the matrix and analyte are uniformly distributed over the SLIPSERS substrate. In this case, the “same” spectrum should be obtained regardless of hot-spot location.

The aim of this section is to classify the variations between the spectra to determine which scenario is present in our samples. This objective was accomplished by applying multivariate analysis, to 10^{-3} mol/L SLIPSERS data.

Multivariate analysis can be used to quickly characterise the "types" or "classes" of spectra present in a large data set, such as a Raman map. Principal Components Analysis (PCA) is an unsupervised method that means it makes no a priori assumptions about the number of components or factors that are required to distinguish the samples. Because of significant intensity variations between SERS peaks, each image was intensity scaled to visualize the corresponding distribution of the molecules better. Multivariate analysis is advantageous as it can make use of all spectral information obtained from an image recorded. It can be very challenging to detect few spectral changes during an experiment where hundreds of spectra are acquired within a short time. Thus, multivariate statistical analysis has become significant in the study of Raman spectra.

Principal Component Analysis is widely used to classify samples into "natural groups" by analysing the covariance of the data set. For the line-scan data, there were 1340 intensity "variables" (labeled by their pixel value, x, or Raman Shift value, ω) and typically 300 points in a line-scan. Each point in a line-scan is equivalent to a sample or observation. It is useful to represent the data set in two ways, first, as a matrix of observations:

	x_1	⋯	x_j	⋯	x_m
$Scan\ 1$	I_{11}		I_{1j}		I_{1m}
⋮					
$Scan\ i$	I_{i1}		I_{ij}		I_{im}
⋮					
$Scan\ n$	I_{n1}		I_{nj}		I_{nm}

Note that, each "spectrum" appears as a row in this presentation, this form is known as the standard form (in statistics) and then as a list of column vectors, labeled by each pixel value:

$$\boldsymbol{X} = [\boldsymbol{X_1}, \ldots, \boldsymbol{X_j}, \ldots, \boldsymbol{X_m}]$$

Using this vector notation the covariance matrix, $\boldsymbol{K_{XX}}$, is then

$E\begin{bmatrix}(X_1 - E[X_1]) \times \\ (X_1 - E[X_1])\end{bmatrix}$	⋯	$E\begin{bmatrix}(X_1 - E[X_1]) \times \\ (X_j - E[X_j])\end{bmatrix}$	⋯	$E\begin{bmatrix}(X_1 - E[X_1]) \times \\ (X_m - E[X_m])\end{bmatrix}$
⋮				
$E\begin{bmatrix}(X_i - E[X_i]) \times \\ (X_1 - E[X_1])\end{bmatrix}$		$E\begin{bmatrix}(X_i - E[X_i]) \times \\ (X_j - E[X_j])\end{bmatrix}$		$E\begin{bmatrix}(X_i - E[X_i]) \times \\ (X_m - E[X_m])\end{bmatrix}$
⋮				
$E\begin{bmatrix}(X_n - E[X_n]) \times \\ (X_1 - E[X_1])\end{bmatrix}$		$E\begin{bmatrix}(X_n - E[X_n]) \times \\ (X_j - E[X_j])\end{bmatrix}$		$E\begin{bmatrix}(X_n - E[X_n]) \times \\ (X_m - E[X_m])\end{bmatrix}$

Where E denotes the expected value operation (i.e. average). Thus, K_{12}

$$E[(X_1 - E[X_1]) \times (X_2 - E[X_2])]$$

is obtained by subtracting the average values for X_1 and X_2, from each value in X_1 and X_2, multiplying together and then finding the average value of the products.

A graphical representation can be given for a data set with two variables ($X = [\boldsymbol{X_1}, \boldsymbol{X_2}]$

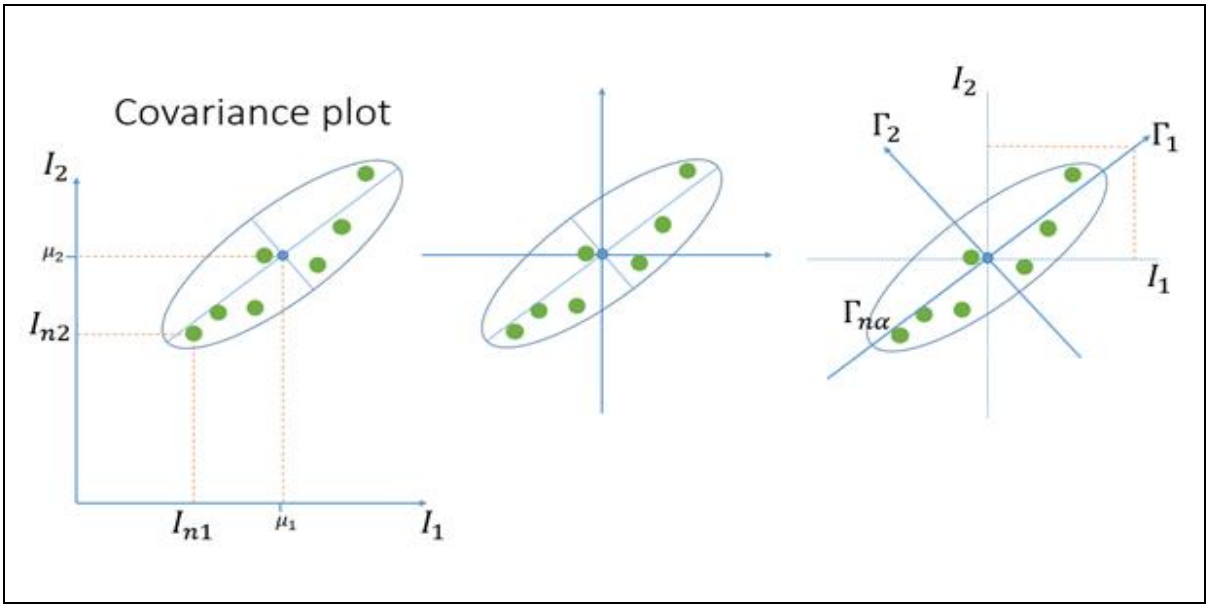

Figure 3.12. Covariance plot with two variables from the data set.

where Γ_1 and Γ_2 denote the principal component vectors – PC1 and PC2. Figure 3.12. also illustrates the important point that the principal components are a specific combination of the original variables. μ_1 and μ_2 are the means of each variable.

In this case both intensity variables have approximately the same variance and they are highly correlated with one another. A vector can be passed through the long axis (Γ_1) of the cloud of points and a second vector (Γ_2) placed at right angles to the first, with both vectors passing through the centroid of the data (Fig 3.12)

Once the principal components are known the coordinates of the data points relative to these two perpendicular vectors can be plotted against Γ_1 and Γ_2 on a scores plot.

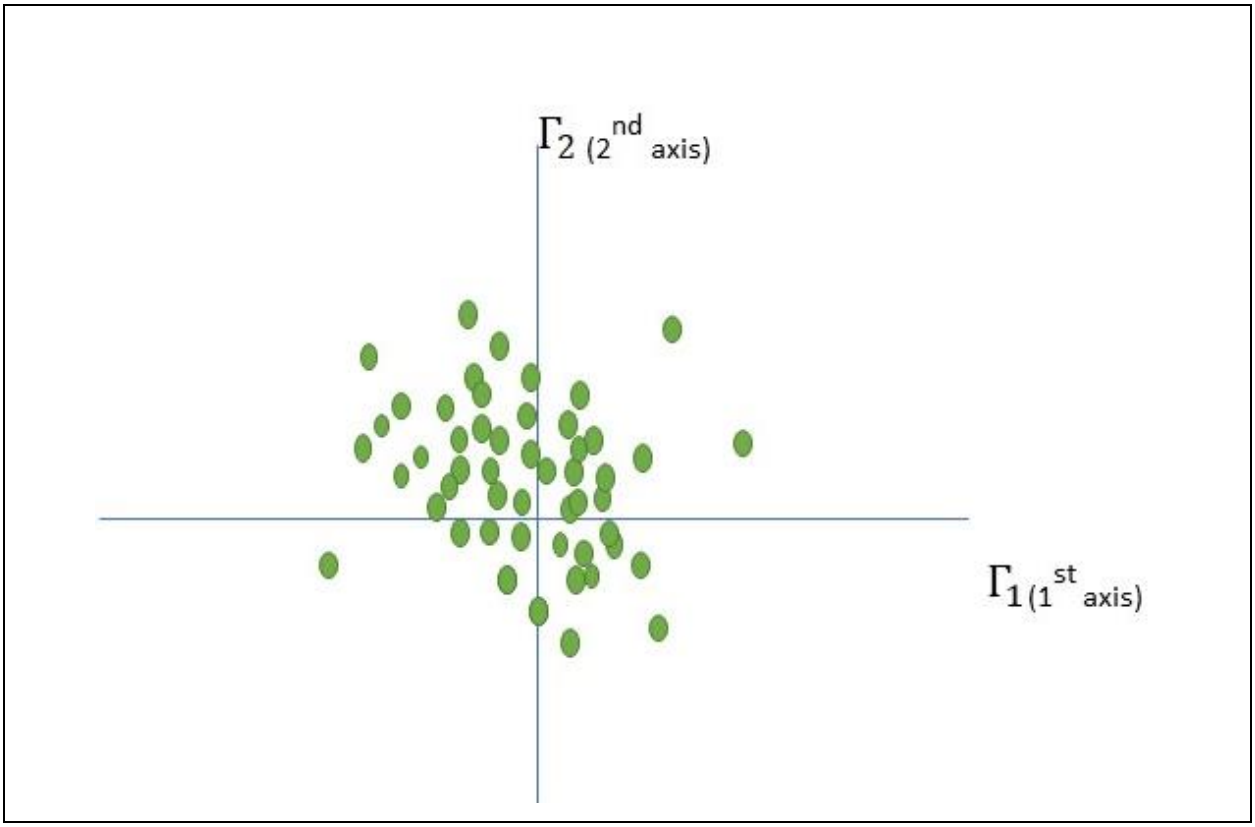

Figure 3.13. A new reference frame with PC1 and PC2.

In this new frame of principal components in Figure 3.13., variance is greater along 1st axis than it is on 2nd axis but the spatial relationships of the points are unchanged; the process has just rotated the data. There are few points which are uncorrelated. Mathematically, the orientations of the axes with respect to the original variables are called the ***eigenvectors***, and the variances along these axes are called the ***eigenvalues***.

The principal components are found from the eigenvalues and eigenvectors of the covariance matrix. The eigenvector determines the "***direction***" of the principal component and the square-root of the eigenvalue gives the "***length***" of the principal component.

By performing such a rotation, the new axes give some relevant explanations. When dealing with data set of many variables, this process shows relationships among variables very clearly. The variance of some axes may be large, whereas the variance on others may be so small that they can be ignored. This is called as ***reducing the dimensionality*** of a data set. For example, initially if there are fifty original variables, we might end with only two or three meaningful axes. This approach of rotating data such that each successive axis displays a decreasing amount of variance is known as ***Principal Components Analysis***, or PCA. PCA produces linear combinations of the original variables to generate the axes, also known as principal components, or PCs.

The data, as mentioned above, is in standard matrix form, with n scans of samples and m columns of pixels giving different intensity at every pixel. The data are first centered on the means of each variable. This generates the cloud of data centered on the origin of principal components. The first principal component ($\boldsymbol{\Gamma_1}$) is given by a linear combination of the variables X1, X2, ..., Xm.

$$\Gamma_1 = a_{11}I_1 + a_{12}I_2 + \cdots + a_{1n}I_n$$

The first principal component is calculated such that it accounts for the greatest possible variance in the data set. The second principal component is calculated that it is uncorrelated with (i.e., perpendicular to) the first principal component and accounts for the next highest variance.

$$\Gamma_2 = a_{21}I_1 + a_{22}I_2 + \cdots + a_{2n}I_n$$

This continues until a total of n principal components have been calculated, equal to the original number of variables.

Eigenvalues are commonly plotted on a ***screeplot*** to show the decreasing rate at which variance is explained by additional principal components.

The positions of each observation in this new coordinate system of principal components are called ***scores***.

Because reduction of dimensionality is a goal of principal components analysis, few principal components can be selected looking at the screeplot with maximum variance, ignoring the last PCs whose explained variation are all roughly equal.

The results obtained from PCA analysis of SLIPSERS data of 10^{-3} mol/L LHC is presented in Figure 3.14. The four columns are four scans and first row correspond to screeplot, the second row corresponds to the scores plot for the entire data set, third row corresponds to zoomed version of clustered variables and fourth row belongs to loadings plot.

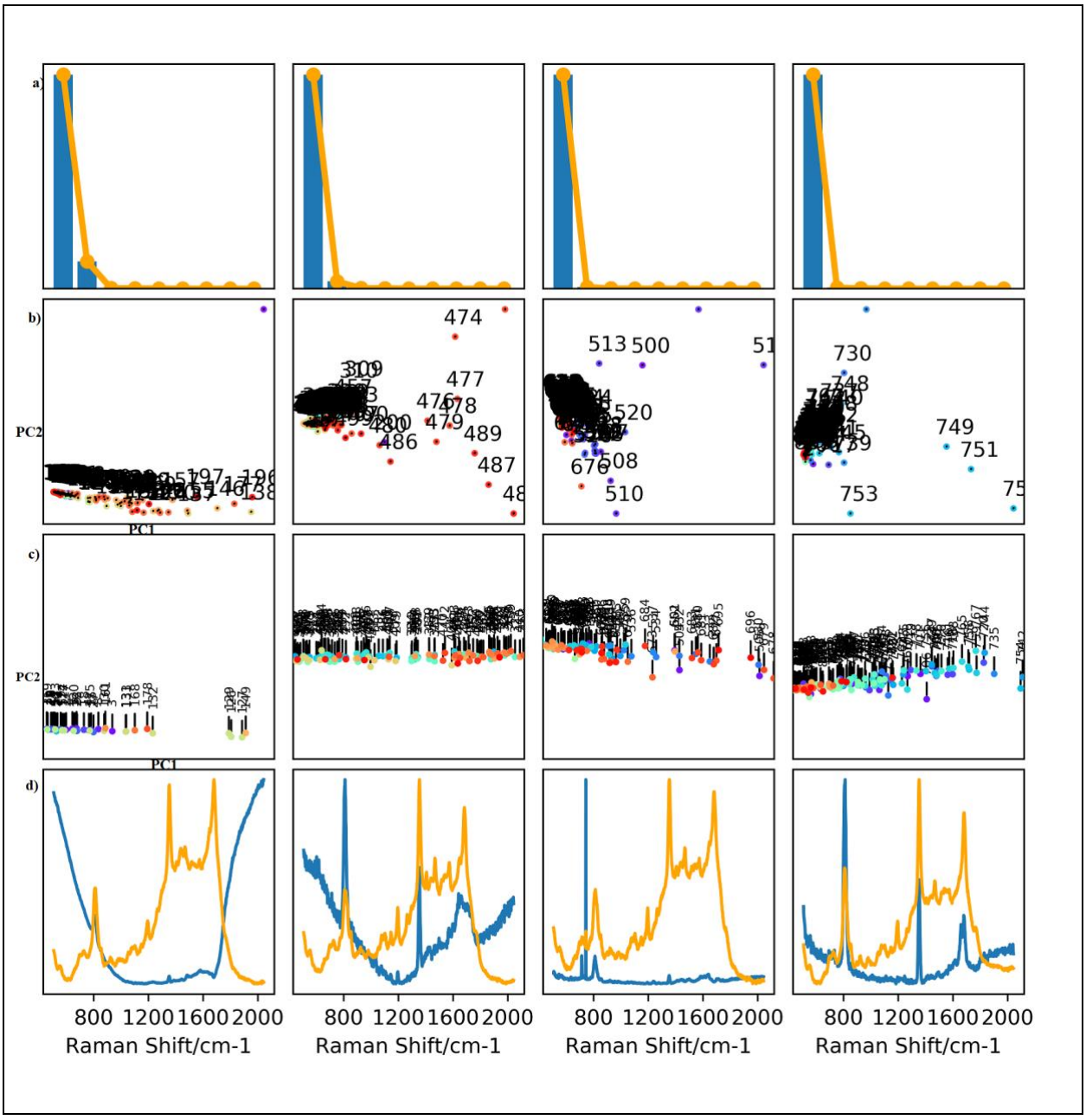

Figure 3. 14: PCA output of SLIPSERS lidocaine hydrochloride sample of 10-3 concentrations. a) screeplot of first two components - PC1 and PC2. (b) Scatter plot of the score values of each single Raman spectrum for the second component c) Zoomed version of cluster d) Loadings plot of PC1 and PC2 (blue); the average (non-baselined) spectrum for the scan is shown in orange.

The scree plot (Figure 3.14.a.) shows the contribution of each principal component to the total variance for the line-scan. The scree plot indicates how many principal components should be used

to construct the scores plots in order to identify any clusters in the data set. The scree plots show that one component dominates the variance which can be assigned to the SERS enhancement.
The scores plots (Figure 3.14.b.) show the projections of each spectrum in the line-scan plotted onto the principal components. The first two principal components were selected in each case. Figure 3.14.c. scores plots zoomed in to highlight the small number of spectra that are slightly separated from the rest. The most interesting feature observed is that nearly all the spectra are tightly clustered, which means the spectra are all similar and do not separate into groups. This might be due to the components in the matrix and being uniformly distributed across the aggregate which can be due to intensity fluctuations. But there are a small number of spectra that are starting to separate from the main cluster, and this does suggest that there are a very small number of points in the line-scan that do have different spectra. **[18-20]**

PC1, first principal component, accounts for the largest variance and PC2, second principal component, accounts for the second-largest variance within the data set. Only the first few PCs contain an essential information about the data; the rest is generally noise. Figure 3.14.d. shows the loadings for the first principal component (PC1) on x -axis and second principal component (PC2) on y-axis. The loadings indicate which peaks contribute most to the variance described by the principal component. In the loadings plots the average spectrum for each scan is also shown (in orange). It is very re-assuring to see the main bands appearing in the loading's plots. Interestingly the band at 800 cm^{-1} makes a larger contribution to the variance than the stronger bands at higher frequency. This suggests that some bands are more variable than others which agrees with literature that some bands show more enhancement than others.**[35]** This can be due to nonuniformity of fabricating nanostructures on SERS substrates which lead to inhomogeneity in SERS enhancement due to exposure of any random hot-spots from nanoaggregate.

3.4. Conclusion

The objective of this study is to characterize the plasmon enhancement of the SLIPSERS substrate using an analyte lidocaine hydrochloride which doesn't have any molecular resonance like rhodamine 6G. A line-scan approach was adopted to scan different lines over the substrate and at all successive points along a line several spectra were recorded. This technique has allowed to characterisation of the spatial distribution of hotspots and to identify the cause of spectral variations.

There are several challenges for these spectral variations like photobleaching, thermal effect which can damage the sample and convert sample into graphitic material as observed in baseline spectra or high laser power. It was assumed that if the hot-spot distribution was uniform, then the most intense peaks will be found at the same location and it amplifies with scans which is not observed in the study. The average spectra showed the intense Raman peaks at different locations that is the result of non-uniform distribution of hot-spots within the concentrations and even within substrates. Spectral and scan histograms highlight the non-uniform distribution of hot-spots over different line scan positions and further classified by statistical charts and Pareto distribution. The results of the Pareto fits show that the both SLIPSERS and SERS give very similar distributions apart from SLIPSERS substrates with higher concentrations of analyte due to the drying process.

To revalidate the hypothesis on whether the analyte and matrix components are heterogeneously distributed, PCA was employed as a method for identifying two classes - "analyte" spectra and "matrix" spectra. But PCA resulted in showing one cluster in the scores plots which suggested that all spectra are very similar with few different variables. PCA also helped in making the differentiation by showing the variable spectra, which must have been due to something else from the matrix, not the possible analyte. This demonstrates that PCA is not the best algorithm to show the variations but good to show a few prominent bands common to all line scans.

Therefore, the line-scan technique coupled with surface-enhanced Raman spectroscopy demonstrates the potential for characterizing SERS substrates before using these for a wide range of applications such as life sciences, pharmaceuticals, environmental monitoring, product quality analysis, drug detection and many more. This proof of concept work helps in understanding the

'Background' of SERS which needs special attention before interpreting the Raman fingerprint data with no errors.

References

1. Aleman, M., Davis, E., Knych, H., Guedes, A., Smith, F. & Madigan, J. 2016. Drug Residues after intravenous anesthesia and intrathecal lidocaine hydrochloride euthanasia in horses. Journal of veterinary internal medicine, 30, 1322-1326.
2. Delhaye, M. & Dhamelincourt, P. 1975. Raman microprobe and microscope with laser excitation. *Journal of Raman Spectroscopy*, 3, 33-43.
3. Moskovotis, M. 1982. Surface selection rules. *The Journal of Chemical Physics*, 77, 4408-4416.
4. Schlucker, S., Schaeberle, M. D., Huffman, S. W. & Levin, I. W. 2003. Raman microspectroscopy: a comparison of point, line, and wide-field imaging methodologies. *Analytical Chemistry,* 75**,** 4312-4318.
5. Ramadurai K, Cromer CL, Dillon AC, Mahajan RL, Lehman JH. Raman and electron microscopy analysis of carbon nanotubes exposed to high power laser irradiance. *Journal of Applied Physics*. 2009;105(9):093106.
6. Qi, J. & Shih, W.-C. 2014. Performance of line-scan Raman microscopy for high-throughput chemical imaging of cell population. *Applied Optics,* 53**,** 2881-2885.
7. De Grauw, C., Otto, C. & Greve, J. 1997. Line-scan Raman microspectrometry for biological applications. *Applied spectroscopy,* 51**,** 1607-1612.
8. Sudheendran, N., Qi, J., Young, E. D., Lazar, A. J., Lev, D. C., Pollock, R. E., Larin, K. V. & Shih, W.-C. 2014. Line-scan Raman microscopy complements optical coherence tomography for tumor boundary detection. *Laser Physics Letters,* 11**,** 105602.
9. Le Ru, E., Meyer, S., Artur, C., Etchegoin, P., Grand, J., Lang, P. & Maurel, F. 2011. Experimental demonstration of surface selection rules for SERS on flat metallic surfaces. *Chemical Communications,* 47**,** 3903-3905.

10. Palla, M., Bosco, F. G., Yang, J., Rindzevicius, T., Alstrom, T. S., Schimdt, M. S., Lin, Q., Ju, J. & Boisen, A. 2015. Mathematical model for biomolecular quantification using large-area surface-enhanced Raman spectroscopy mapping. *RSC advances,* 5**,** 85845-85853.
11. Maher, R. C. 2012. SERS hot spots. *Raman spectroscopy for nanomaterials characterization.* Springer.
12. Yang, J., Palla, M., Bosco, F. G., Rindzevicius, T., A Alstrom, T. S., Schimdt, M. S., Boisen, A., Ju, J. & Lin, Q. 2013. Surface-enhanced Raman spectroscopy based quantitative bioassay on aptamer-functionalized nanopillars using large-area Raman mapping. *Acs Nano,* 7**,** 5350-5359.
13. Etchegoin, P. G., Meyer, M. & Le Ru, E. 2007. Statistics of single molecule SERS signals: is there a Poisson distribution of intensities? *Physical Chemistry Chemical Physics,* 9**,** 3006-3010.
14. McCreery, R. L. 2005. *Raman spectroscopy for chemical analysis*, John Wiley & Sons. New York, 2000; Chapter 11.
15. Williams, K. P. J.; Pitt, G. D.; Smith, B. J. E.; Whitley, A.; Batchelder, D. N.; Hayward, I. P. J. Raman Spectrosc. 1994, 25, 131-138.
16. Etchegoin, P. G. & Le Ru, E. 2008. A perspective on single molecule SERS: current status and future challenges. *Physical Chemistry Chemical Physics,* 10**,** 6079-6089.
17. Bakonyi, M., Gacsi, A., Kovacs, A., Szucs, M.-B., Berko, S. & Csanyi, E. 2018. Following-up skin penetration of lidocaine from different vehicles by Raman spectroscopic mapping. *Journal of pharmaceutical and biomedical analysis*, 154, 1-6.
18. Le Ru, E. C. & E Etchegoin, P. G. 2013. Quantifying SERS enhancements. *MRS bulletin,* 38**,** 631-640.
19. Le Ru, E. & E Etchegoin, P. 2009. Phenomenological local field enhancement factor distributions around electromagnetic hot spots. AIP.
20. Kneipp, K., Wang, Y., Kneipp, H., Perelman, L. T., Itzkan, I., Dasari, R. R. & Feld, M. S. 1997. Single molecule detection using surface-enhanced Raman scattering (SERS). *Physical review letters,* 78**,** 1667.
21. Le Ru, E., E Etchegoin, P. & Meyer, M. 2006. Enhancement factor distribution around a single surface-enhanced Raman scattering hot spot and its relation to single molecule detection. *The Journal of chemical physics,* 125**,** 204701.

22. Qian, X., Peng, X.-H., Ansari, D. O., Yin-Goen, Q., Chen, G. Z., Shin, D. M., Yang, L., Young, A. N., Wang, M. D. & Nie, S. 2008. In vivo tumor targeting and spectroscopic detection with surface-enhanced Raman nanoparticle tags. *Nature biotechnology,* 26**,** 83.
23. Zhang, D.; Hanna, J. D.; Jiang, Y.; Ben-Amotz, D. Appl. Spectrosc. 2001, 55, 61-65.
24. Bohndiek, S. E., Wagadarikar, A., Zavaleta, C. L., Van De Sompel, D., Garai, E., Jokerst, J. V., Yazdanfar, S. & Gambhir, S. S. 2013. A small animal Raman instrument for rapid, wide-area, spectroscopic imaging. *Proceedings of the National Academy of Sciences,* 110**,** 12408-12413.
25. Bernard, S., Beyssac, O. & Benzerara, K. 2008. Raman mapping using advanced line-scanning systems: geological applications. *Applied spectroscopy*, 62, 1180-1188.
26. Kudo, K., Nishida, N., Kiyoshima, A. & Ikeda, N. 2004, '3. A Fatal Case of Poisoning by Lidocaine Overdosage–Analysis of Lidocaine in Formalin-Fixed Tissues', *Medicine, science and the law*, vol. 44, no. 3, pp. 266-71.
27. Tierney, K.J., Murano, T. & Natal, B. 2016, 'Lidocaine-induced cardiac arrest in the emergency department: effectiveness of lipid therapy', *The Journal of emergency medicine*, vol. 50, no. 1, pp. 47-50.
28. Chen, T., Wang, H., Chen, G., Wang, Y., Feng, Y., Teo, W. S., . . . Chen, H. J. A. N. (2010). Hotspot-induced transformation of surface-enhanced Raman scattering fingerprints. *4*(6), 3087-3094.
29. Qian, X.-M., & Nie, S. M. J. C. S. R. (2008). Single-molecule and single-nanoparticle SERS: from fundamental mechanisms to biomedical applications. *37*(5), 912-920.
30. Emory, S. R., Jensen, R. A., Wenda, T., Han, M., & Nie, S. J. F. d. (2006). Re-examining the origins of spectral blinking in single-molecule and single-nanoparticle SERS. *132*, 249-259.
31. Nie, S., & Emory, S. R. J. s. (1997). Probing single molecules and single nanoparticles by surface-enhanced Raman scattering. *275*(5303), 1102-1106.
32. Blackie EJ, Le Ru EC, Etchegoin PG. Single-molecule surface-enhanced Raman spectroscopy of nonresonant molecules. *Journal of the American Chemical Society*. 2009;131(40):14466-72.

33. Mahajan S, Cole RM, Speed JD, Pelfrey SH, Russell AE, Bartlett PN, et al. Understanding the surface-enhanced Raman spectroscopy "background". *The Journal of Physical Chemistry C*. 2009;114(16):7242-50.
34. Wendel A, Underwood J. Extrinsic parameter calibration for line scanning cameras on ground vehicles with navigation systems using a calibration pattern. *Sensors*. 2017;17(11):2491.
35. Lee HK, Lee YH, Koh CSL, Phan-Quang GC, Han X, Lay CL, et al. Designing surface-enhanced Raman scattering (SERS) platforms beyond hotspot engineering: emerging opportunities in analyte manipulations and hybrid materials. *Chemical Society Reviews*. 2019; 48(3):731-56.

Chapter 4. Ultrasensitive surface-enhanced Raman scattering detection of brodifacoum and sodium monofluoroacetate in aqueous solution.

Abstract

A simple and highly sensitive method, coupling omniphobic surfaces with borohydride reduced silver nanoparticles as a substrate, was developed to detect rodenticides at very low concentrations. Their performance was evaluated for the limit of detection and quantification.

In this work, a universal platform for detection and quantification of brodifacoum and sodium monofluoroacetate (commonly called 1080) was used. This platform is called slippery liquid-infused porous surface-enhanced Raman scattering (SLIPSERS). This method demonstrated good reproducibility with high sensitivity.

Analyte anions were detected down to a concentration of 10^{-14} M for brodifacoum and 10^{-9} M 1080. There is a linear relationship (R^2 close to 1) in this concentration range. This approach is designed as a simple method to detect brodifacoum, sodium monofluoroacetate (1080) and similar other harmful contaminants to monitor environmental impact. A comparative study was performed on two different substrates - one using an omniphobic surface substrate (SLIPSERS) and the second drop casting the silver nanoparticle analyte mixture on the substrate (SERS). SLIPSERS overcomes some of the limitations of SERS and can meet the emerging needs of environmental monitoring and food safety analysis.

Keywords: Surface enhanced Raman scattering, brodifacoum, sodium monofluoroacetate, slippery liquid-infused porous surfaces, and hot-spots.

4.1. Introduction

Brodifacoum is now one of the world's most widely used pesticides. It is a highly effective lyophilic anticoagulant with a relatively long biological half-life. Due to its persistence, it is possible for brodifacoum to accumulate in animal tissues to a level where clotting abnormalities or haemorrhage could occur. Sodium monofluoroacetate (also known as 1080) is a highly toxic pesticide that is used in the United States for predator control and control of introduced mammal pest species (e.g., possums) in New Zealand **[1]**. The residuals of these rodenticides in the environment are sufficient to cause fatality among non-target animals, either through scavenging the carcass of pests killed by brodifacoum and 1080 or consuming food products obtained from livestock that have been exposed to these rodenticides.

The problem of animal pests in New Zealand is relatively very high. Pests harm the native flora and fauna and create a threat to the national economy as vectors for diseases such as bovine tuberculosis. Hence, rodenticides are used to control the population of possums and rats in the environment. The most commonly used rodenticides are brodifacoum, sodium monofluoroacetate (popularly known as ten-eighty, 1080), warfarin and a few other coumarin-based coagulants. These toxins are used by farmers, landowners and community groups to control the population of these rodents from damaging their crops and farms to a large extent **[2]**.

Monofluoroacetate was originally produced from the South African gifblaar plant which causes death in cattle. Today, monofluoroacetate has been used as a critical tool by the Department of Conservation, New Zealand to protect the environment from pest species. Baits of monofluoroacetate and brodifacoum are toxic to mammals, aquatic micro-organisms and present a secondary poisoning hazard to non-target animals. Brodifacoum impairs blood coagulation leading to death whereas 1080 'blocks' the citrate cycle by aconitase enzyme inhibition, leading to accumulation of citrate in tissues which causes heart failure **[3,4]**. The commercial availability of these compounds has resulted in an increase of risk of accidental or intentional use for both animals and humans. 1080 is now a restricted product, and not commercially available because of the potential terrorist incident that occurred in November 2014, when Fonterra, a multinational dairy company received a package of infant formula milk laced with 1080. **[2]**

There are several methods to analyse rodenticides, but a challenge is to obtain high sensitivity with a trace level of detection, high reproducibility, and specificity. Most common methodologies used are gas chromatography-mass spectrometry (GC-MS) **[5-7]**, liquid chromatography-mass spectrometry (LC-MS) **[8, 9]** and high-performance liquid chromatography (HPLC) **[10-12]**. These methods require time-consuming sample extraction and preparation, and calibration by internal standards. The different chemical and physical properties of brodifacoum and 1080 require separate methodologies for each compound, which adds to the cost of the analysis. In this work, we have used a recently developed Raman spectroscopy technique that displays a remarkable versatility and sensitivity, for detection of brodifacoum and 1080 under identical operating conditions.

SERS utilises nanostructured silver or gold as a substrate due to the ability of the optical response of the metal nanostructures to enhance the Raman scattering efficiency by many orders of magnitude **[13]**. A necessary condition for SERS is close contact between the analyte and the substrate. In the aqueous phase, surface chemistry controls the analyte/substrate interaction, and this often limits SERS applications to a limited set of analytes that adsorb strongly to metal substrates.

Recently, as described in Chapter 1, the SLIPSERS method that overcomes these limitations was introduced **[15]**. SLIPSERS eliminates the restrictions of aqueous phase surface chemistry by merely removing the aqueous phase i.e., drying a small droplet of the aqueous analyte containing a small number of metal nanoparticles. Drying of the droplet is carefully controlled using an omniphobic surface with very low surface energy that avoids contact line pinning (which produces the so-called coffee ring effect **[14]**) and results in the volume of the droplet reducing to the volume occupied only by the nanoparticles. Because the analyte is trapped in the droplet volume, it must eventually encounter the nanoparticles and hence strong SERS is guaranteed. Effectively, the surface tension and Laplace pressure of the droplet overcomes any unfavourable surface chemistry interactions between the analyte and the silver nanoparticles, while avoiding the collapse of the droplet early in the drying process. In addition to the strong SERS effect, the droplet volume reduces by several orders of magnitude, so the effective analyte concentration increases by a similar amount. Furthermore, under ideal conditions, the volume of the dried droplet can approach the focal volume of the focused Raman laser, which means every analyte molecule can contribute to the signal.

A significant advantage of the SLIPSERS method is its simplicity. The nanostructured metals are metal nanoparticles synthesised in a single step from common lab reagents in ambient conditions. Similarly, the omniphobic surface is fabricated from readily available laboratory supplies. Surface preparation and droplet drying are highly reproducible which provides reliable results. Another advantage is the high density of hotspots – if every dried droplet has a high density of hotspots, there is an excellent chance that the SERS enhancement will be high for every dried droplet. Without controlled drying, we are relying on random aggregation at low concentration, which might not always give a hotspot and the aggregates will be spread over a larger area too, so chances of detection decrease.

Raman spectra are then acquired from the dried drops using a standard Raman microscope using common operating parameters. A SLIPSERS substrate was employed for the detection of two rodenticides with very different chemical structures and behavior, namely, brodifacoum and 1080 with the objective of attaining highly sensitive and specific detection. **[15]**

4.2. Experimental

4.2.1. Materials and Methods

Sodium monofluoroacetate was purchased from MPbiomedicals Limited (Solon, OH, USA). Brodifacoum was purchased from Sigma-Aldrich (New Zealand). A stock solution of 0.01 M of sodium monofluoroacetate was prepared by dissolving in Milli-Q water (resistivity > 18 MΩ). Similarly, a stock solution of 0.01 M of brodifacoum was prepared by dissolving in acetone: water (1:1) mix. Silver nanoparticle **[16]**, SERS and SLIPSERS sample preparation remain the same as described in Chapter -2.

4.2.2. Instrumentation

This study was done during the initial year using an older spectrograph and CCD detector (which was replaced by the FERGIE system described in Chapter 2 after catastrophic failure of an amplifier board in the CCD detector). The laser, microscope and collection optics were the same as for the system described in Chapter 2,with collected light dispersed by an Acton Spectrapro® 2500i, 0.500m focal length triple-grating imaging monochromator/spectrograph, and detected with a liquid-nitrogen-cooled Roper Scientific Spec-10 CCD detector operating at -110 °C. A 1200 g/mm holographic grating and a slit width of 150 μm were used.

The spectrometer was calibrated using standard Raman bands of polymethylmethacrylate (PMMA), which was initially calibrated against Argon and Neon atomic emission lines. Winspec software was used for the collection and analysis of Raman spectra. Spectra were obtained using 532 nm excitation wavelength (with 12-14 mW laser power) focused onto the sample using a 40×, 0.65 NA objective. Scattered light was collected in a back-scattered geometry (using a converted Olympus IX70 inverted fluorescence microscope).

Rayleigh scattering was rejected using a custom Raman edge-filter from Iridian Spectral Technologies. Spectra were acquired with a 15 s exposure time and 4 accumulations. UV-Vis spectra were acquired with a Shimadzu1800 and zeta-potential and nanoparticle size was measured using Malvern Zetasizer Nano ZS. All spectra were processed using OMNIC, Origin 8.5.1 and Python 3.6 software.

4.3. Results and Discussion

4.3.1. Characterisation of silver nanoparticles

Silver colloidal particles were prepared using borohydride reduction method according to Frank et al. **[16].** Figure 4.1 presents the surface plasmon resonance peak of the silver nanoparticles using UV-Vis spectroscopy. The absorption maximum occurred at 410 nm. The inset shows an SEM image of silver nanoparticles aggregated with magnesium sulphate salt. These nanoparticles had a mean diameter of 45.78 nm and a zeta potential of -55 mV as measured by a Malvern Zetasizer in close agreement with literature data. **[17]**

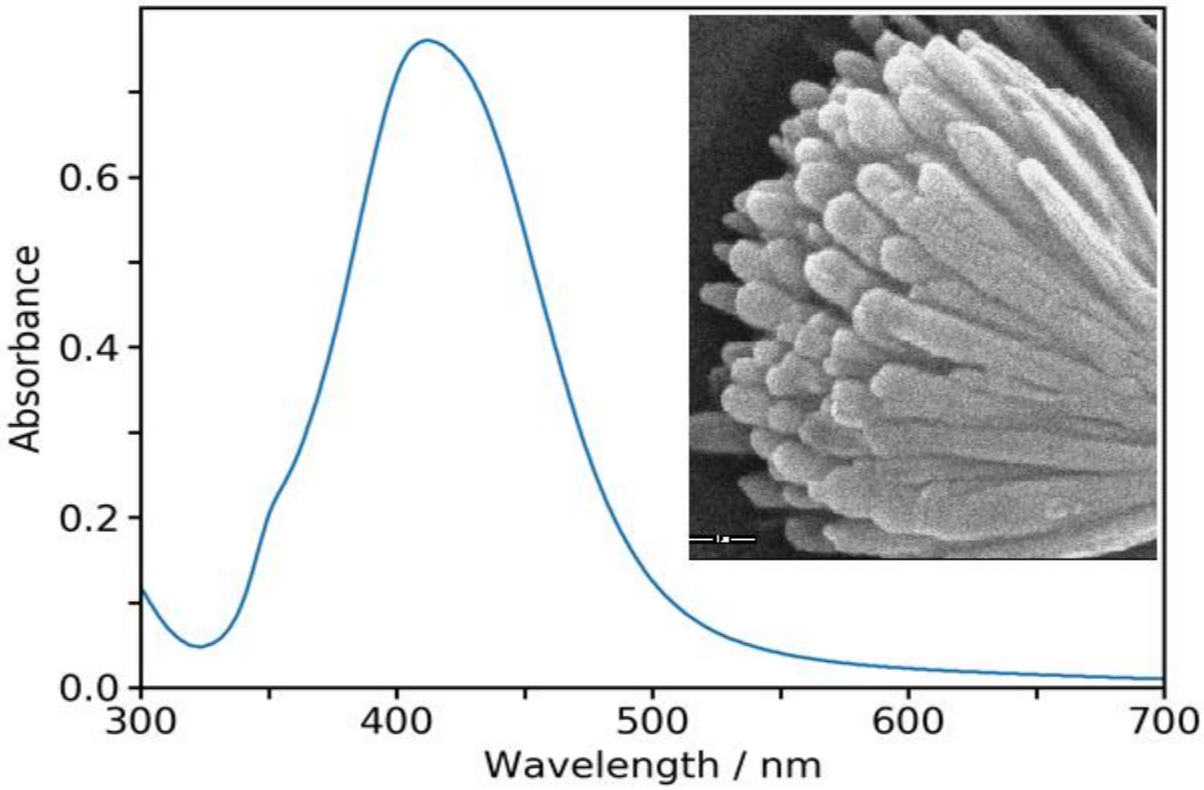

Figure 4. 1: UV-Vis spectrum of colloidal silver nanoparticles, inset shows SEM image of aggregated silver nanoparticles in the solution. Scale bar is 10µm.

4.3.2. Raman Spectra of brodifacoum and sodium monofluoroacetate (1080)

a) Sodium monofluoroacetate (1080)

1080 is a small compound with no aromatic rings or polarisable groups and so behaves as a poor Raman scatterer due to its inherently low Raman scattering cross-section. An aqueous solution of 1080 (0.01 M) was used for acquiring a non-resonant, solution phase, Raman spectrum as a reference but did not show any peaks even at this relatively high concentration

[18]. Therefore, a Raman spectrum of solid 1080 was tried to collect at 532 nm laser with 40 × objective and with a long acquisition time of 30 minutes, but there was no success in obtaining any Raman signal, but instead a broad unstructured background, presumably due to fluorescence from an impurity in the solid was obtained instead. Generally, very small Raman scattering cross section of non-resonant molecule like 1080 hampers **[46]** the spectroscopic investigation at high concentration and can be easily overwhelmed by fluorescence signals (Figure 4.2). Such molecules require an ensemble of nanoparticles for detection that can quench fluorescence and makes the detection possible. This is what observed in SERS and SLIPSERS detection for 1080.

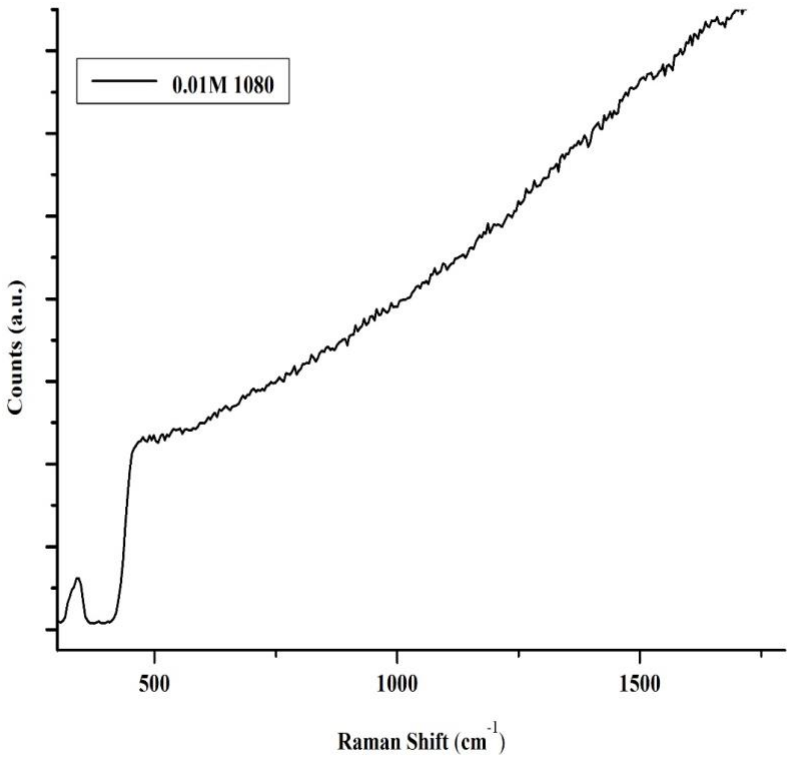

Figure 4. 2: Raman spectrum of 0.01M 1080 acquired at 532 nm laser wavelength with 40 × *objective, laser power of 12 mW and 30 minutes exposure time with average spectra from four accumulations. The edge filter cuts off the signal and at approx. 250 cm-1 is an artefact from the filter.*

As a 1080 Raman spectrum could not be obtained in any form experimentally, density functional theory (DFT) was used to produce a calculated spectrum for reference purposes. DFT methods are used to calculate the vibrational mode energies and associated normal modes. Verification with experimental frequencies is usually carried out but comparison with intensities is more challenging due to the various factors that affect measured intensities in a Raman spectrum. However, the calculated intensities, reported as differential Raman scattering cross section provide a useful guide to the expected intensity patterns in the experimental spectra. **[31]**.

Density functional methods were used with the B3LYP functional and a 6-31+G(d) basis set. Dr. Mark Waterland calculated differential Raman cross section values for 1080 and provided the results. A polarizable continuum model (using water as the solvent) was used to model the environment. To prove the reliability of Gaussian calculations, the non-resonant Raman cross section of methanol was compared where the experimental value for methanol at 1030 cm^{-1} reported by Le Ru et al. **[31]** is 21×10^{-32} cm^2 sr^{-1} and the calculated value is 4.0×10^{-32} cm^2 sr^{-1} which shows that the calculations are reliable to within an order of magnitude.

The spectrum of trifluoroacetate was also calculated using the B3LYP functional set, as the SERS spectrum of this compound has been reported in the literature. The analyte of interest, 1080, has the molecular structure as shown in Figure 4.3. Raman active modes with symmetry class, frequency and differential Raman cross section are described in Table 4.1.

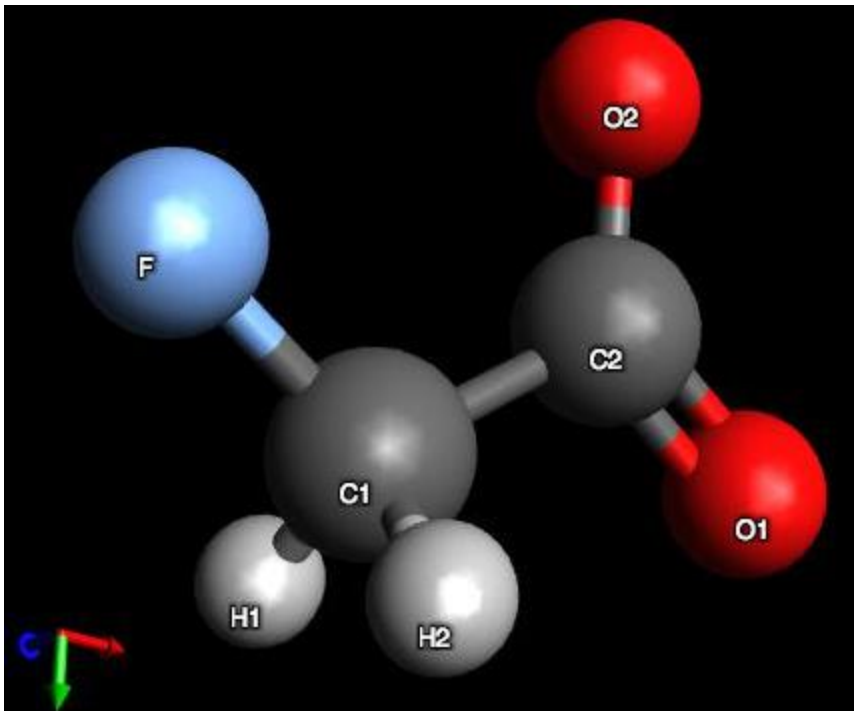

Figure 4. 3: Schematic drawing of structure of sodium monofluoroacetate

Table 4.1. Raman active modes of 1080, methanol **[51]** and trifluoroacetate **[52]** with their calculated differential Raman cross sections

Mode	Symmetry Class	Freq / cm^{-1}	diff. Raman XS / 10^{-32} cm^2 sr^{-1}	Description
		1080		
1	**A´**	94.2	37.1	FCCO torsion
2	**A´**	249.35	0.78	FCC / CCO in-phase bend
3	**A´**	476.43	10.23	CO_2 rock
4	**A"**	581.35	2.40	COO torsion
5	**A´**	667.01	4.01	FCC / CCO out-of-phase bend
6	**A´**	899.31	12.27	FCC bend / C-C stretch
7	**A´**	993.85	6.51	C-F Stretch
8	**A´**	1025.89	0.008	COO out-of-plane bend
9	**A´**	1255.6	5.55	Antisymmetric CH_2 wag
10		1354.70	8.74	Symmetric CH_2 wag

11	**A´**	1419.28	5.73	C-C stretch/COO symmetric stretch
12	**A´**	1479.72	4.62	CH_2 bend
13	**A´**	1626.14	3.23	O-C=O antisymmetric stretch
14	**A"**	3082.525	18.538	C-H symmetric stretch
15	**A´**	3139.327	9.468	C-H antisymmetric stretch
Methanol				
1	**A´**	323.69	3.35	Torsion
2	A´	1028.85	3.96	C-O stretch
3	A´	1075.94	4.01	CH_3 rock (symmetric)
4	A˝	1177.86	2.76	CH_3 rock (antisymmetric)
5	A´	1371.64	1.41	O-H bend
6	A˝	1488.53	2.46	CH_3 deformation
7	A´	1505.54	6.52	C-H antisymmetric bend
8	A´	1519.26	6.61	C-H symmetric bend
9	**A´**	3029.28	19.94	C-H symmetric stretch
10	A"	3085.25	11.376	C-H antisymmetric stretch
11	**A´**	3144.46	9.37	C-H antisymmetric symmetric stretch
12	A´	3753.71	5.40	O-H stretch
trifluoroacetate				
1	**A´**	-20.53	1304.76	Torsion
2	A"	249.26	7.99	Torsion
3	A"	252.51	0.18	FCC/ CCO in-phase bend
4	A"	378.91	10.0	CF_3 bend / CC stretch
5	A'	416.05	5.2	FCC/ CCO out-of-phase bend
6	A"	503.59	1.84	CF_3 deformation
7	A'	573.45	5.02	FCC/ CCO out-of-phase bend
8	A'	698.6	1.57	CF_3 deformation (in phase)
9	A'	782.56	0.614	CO_2 deformation (out-of-plane)

10	A'	797.51	9.84	CC Stretch /COO Bend
11	A'	1066.7	1.470	C-F stretch (out-of-phase)
12	A'	1116.09	1.471	C-F stretch (out-of-phase)
13	A"	1182.53	1.155	C-F Stretch (in-phase)
14	A'	1399.68	16.82	CC Stretch /COO Bend
15	A"	1700.12	2.45	COO antisymmetric stretch

1080 has a mirror plane and the irreducible representations are classified by their behaviour under reflection in this plane (A' and A"). The properties belonging to irreducible representation A' are symmetric to both the identity operation E as well as reflection through the mirror plane. Those properties belonging to irreducible representation A" are symmetric with respect to the identity operation E but antisymmetric with respect to reflection through the mirror plane. **[50]**

The calculation predicts one of the strongest modes for 1080 is at 1354 cm^{-1}, and 3082 cm^{-1} and 3139 cm^{-1}, which in reasonable agreement with electrochemical SERS data reported by Rodes. **[32]** The vibrational mode of C-H in-plane bending at 1365 cm^{-1} has good correlation with our experimental 1080 data of 1372 cm^{-1} band (Figure 4.7). Another strongest mode for 1080 observed at 1504 cm^{-1} and 1644 cm^{-1} from SERS spectra are also an agreement with above-calculated frequency values, but 1504 cm^{-1} is not found in Rodes data. It was assumed that there could not be an exact match with Rodes data to our experimental data as they have observed modes using electrochemical SERS whereas colloidal SERS was used for this thesis, and the interaction with the substrate as well as the enhancement itself could explain the differences in intensity. As per Rodes et al., solid trifluoroacetate has the strongest Raman bands at 1440 cm^{-1} and 832 cm^{-1} which closely matches with the larger Raman cross sections from Table 4.1. Also, the Raman spectrum of an aqueous solution of monofluoroacetate anions has strong bands at 1408 cm^{-1} and 3073 cm^{-1} which are closely related to one of the strongest Raman band. Therefore, trifluoroacetate calculations do give reasonable agreement with the literature and therefore provide some confidence that the calculated 1080 spectrum is a good model for the true 1080 spectrum.

b) Brodifacoum:

The molecular structure of brodifacoum is shown in Figure 4.4. It has several aromatic rings and extensive conjugation. Raman spectra of highly concentrated solution (0.001M) of brodifacoum is shown in figure 4.5. The characteristic bands of Raman spectra of brodifacoum ranging from 1200 cm^{-1} to 1720 cm^{-1} were quite prominent.

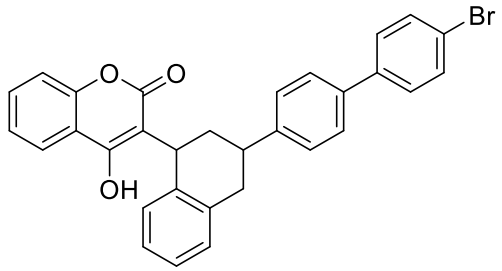

Brodicafoum

Figure 4.4: Structure of brodifacoum

.

The strong Raman bands of brodifacoum according to the literature are the C=O stretching that contributes to the bands at 1717 cm^{-1}, C=C bond at 1657 cm^{-1}, C-C stretching band at 1554 cm^{-1} and single bonded C-O stretching were observed around 1300 cm^{-1}. The assignments obtained for the brodifacoum are in very good agreement with the literature **[19]**.

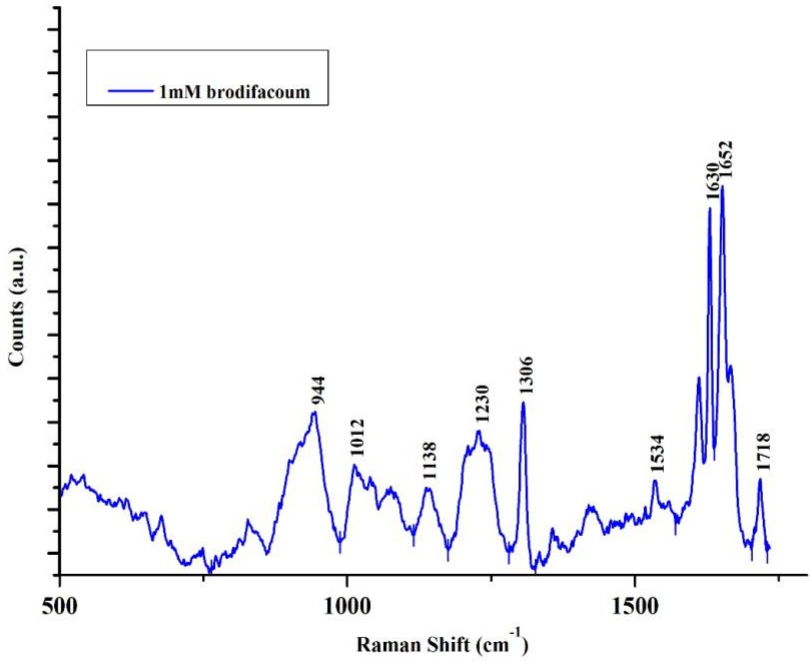

Figure 4.5: Raman spectrum of 0.001M brodifacoum acquired at 532 nm laser wavelength with 40 × *objective, laser power of 12 mW and 15 s exposure time with average spectra from four accumulations.*

4.3.3. Characterisation of SERS substrates

Standard borohydride reduced nanoparticles were prepared by reduction of silver nitrate using sodium borohydride and trisodium citrate to stabilise the silver nanoparticles.

SERS spectra of these silver nanoparticles gave a few weak Raman peaks (Figure 4.6(e)) but they do not appear either in brodifacoum (Figure 4.6) or in 1080 (Figure 4.7) bands which suggests that these can be simply assigned as 'silver nanoparticle bands. Even SERS frequencies for citrate at the surface of borohydride reduced silver nanoparticles mentioned by Munro et al. **[48]** work did

not show any such Raman peaks which confirms the spectrum is coming from silver nanoparticles. the Kitaev nanoparticles have no background (or at least no citrate bands), which is useful because any Raman bands must then be due to the analyte. No citrate bands observed suggests either that the analyte has displaced citrate at the nanoparticle surface, or the analyte has a much larger scattering cross-section **[22, 23]**. Munro et al. only observed citrate bands under certain conditions. The borohydride reduced nanoparticles provided a useful reference against the citrate reduced nanoparticles.

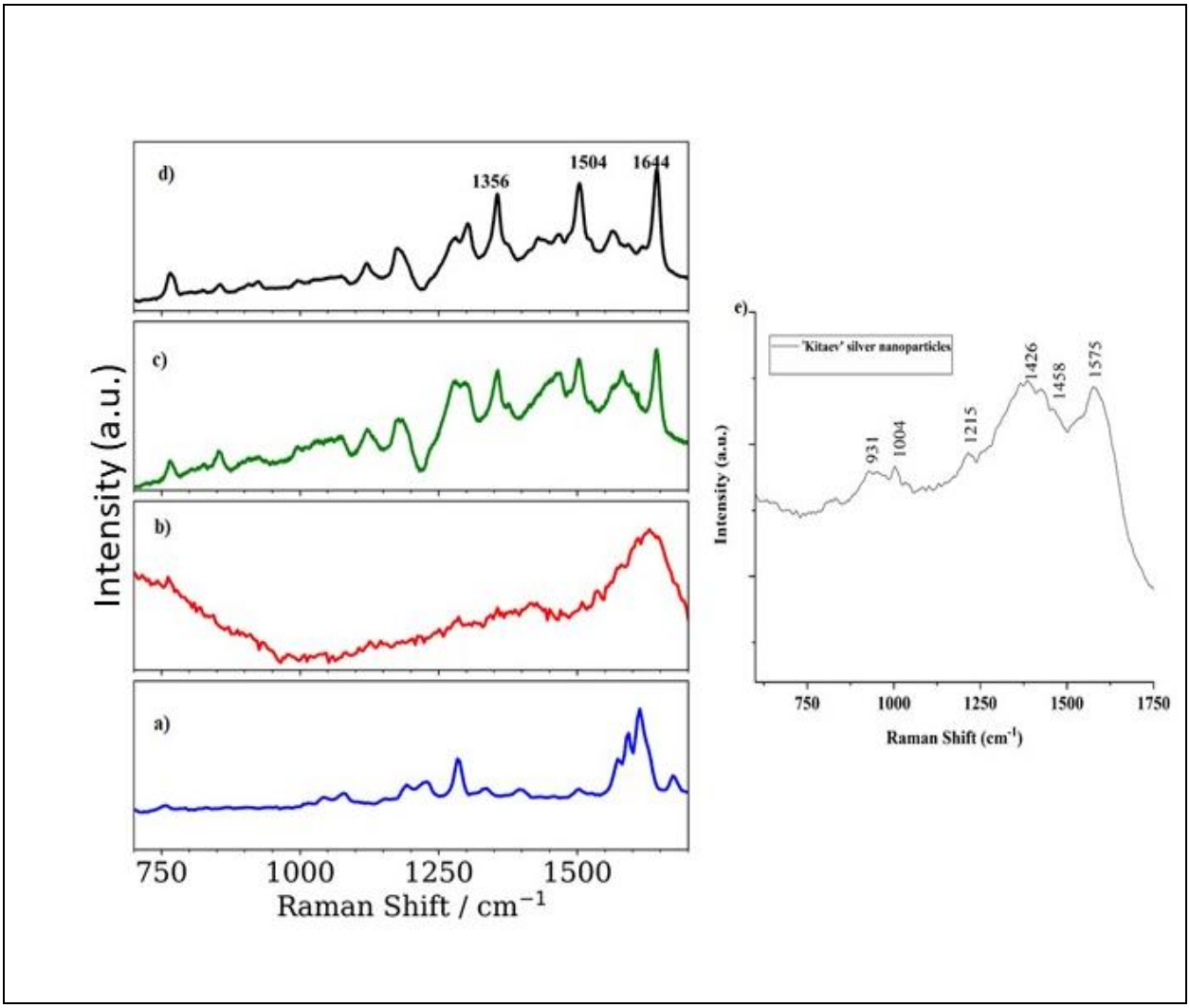

Figure 4.6: a) Normal Raman spectra of solid brodifacoum, b) SERS spectrum of 10-6 mol/L brodifacoum without $MgSO_4$, c) SERS spectrum of 10-6 mol/L brodifacoum with 0.1 mol/L $MgSO_4$ and d) SLIPSERS spectrum of 10-6 mol/L brodifacoum acquired at 532 nm laser wavelength with 40 × *objective, laser power of 12 mW and 15 s exposure time with average spectra from four accumulations; e) Kitaev silver nanoparticles without any analyte(brodifacoum or 1080).*

The SERS spectra of brodifacoum and 1080 were recorded in an aqueous solution of 10^{-6} mol L^{-1} analyte concentration. SERS produced strong and enhanced signals after aggregation due to 'hot spots' that are in the junctions between colloids. As per Bell et al. **[20]**, sulfate as an aggregating agent doesn't bind to the surface and so will not compete with the analyte for surface binding. There is very weakly bound citrate (as shown by the absence of strong citrate bands in Fig 4.6(e)) but this is displaced by the analyte.

There is a possibility to get some citrate background at very low concentrations with some other analytes due to poor binding of analyte on the citrate giving few peaks of citrate spectrum. But brodifacoum and 1080, both were benefitted by aggregation using $MgSO_4$ and displaced citrate layer of the silver nanoparticle giving enhancement of brodifacoum and 1080 bands. SERS (dried) and SLIPSERS samples were prepared as described in Chapter 2 for Raman measurements using 0.1 M of magnesium sulphate, aggregating agent.

4.3.4. Design and Characterisation of SLIPSERS

The potential of the SLIPSERS platform and its method of fabrication have been previously described, in this section we use SLIPSERS to determine the sensitivity of detection of brodifacoum **[21]**.

The relative performance of SERS and SLIPSERS under similar conditions were compared. A comparative study was carried out by analysing SERS and SLIPSERS spectra of different concentrations of brodifacoum and 1080 extending to the lowest detection concentration.

Effect of aggregating agent.

SERS spectra of brodifacoum and 1080 with or without $MgSO_4$ were obtained to confirm that the strong SERS signals observed were entirely due to the analyte of interest and there is no background interference from colloid itself or aggregating salt **[20]**.

The Raman spectrum of solid brodifacoum was acquired as shown in Figure 4.6(a) to identify the prominent brodifacoum peaks for comparison with SERS and SLIPSERS spectra. In the absence of $MgSO_4$, no identifiable peaks were observed but with 0.1 M $MgSO_4$ definite peaks were observed, though at relatively low intensity. SERS is observed from brodifacoum after aggregation. Even the fluorescence observed in normal Raman of 1080 (Figure 4.2) was quenched and good SERS signal was observed.

In contrast, the SLIPSERS spectrum shown in Figure 4.6(d) has significantly improved signal-to-noise and the peaks observed were highly enhanced.

Vibrational assignments for brodifacoum and 1080

For a better understanding of SERS and SLIPSERS spectra of brodifacoum and 1080, assignment of vibrational modes is made by reference to the literature. **[43]** Carbonyl stretching vibrational modes observed the highest intensity at 1644 cm^{-1} was considered as the characteristic band for brodifacoum. $\nu(C\text{-}C)_{Ph}$ and $\delta(C\text{-}C)_{ip}$ also give rise to strong intensity band in SLIPSERS spectrum. Medium Raman bands were observed at 1165 cm^{-1} and 1125 cm^{-1} due to ν (C-O) and $\delta\ (CCH)_{ip(C)}$. Brodifacoum ring deformation mode, Ring $_{ip(Ph)}$ was detected as a weak Raman band at 885 cm^{-1}.

Table 4. 2**.** Observed Raman peaks and assignments for brodifacoum

Raman shift	**Intensity**	**Assignment**
1644	strong	ν(C=O) symmetric stretching
1506	strong	$\nu\ (C\text{-}C)_{Ph} + \delta(C\text{-}C)_{ip}$
1356	strong	$\delta(COH)_{ip} + \nu\ (C\text{-}O)$
1165	medium	$\nu\ (C\text{-}O) + \delta\ (CCH)_{ip(C)}$
1125	medium	$\delta\ (CCH)_{ip(C)}$
885	weak	Ring $_{ip(Ph)}$
772	strong	$\delta\ (COH)_{op}$

Ph, Phenyl; ip, in-plane; op, out-of-plane; (c), coumarin;

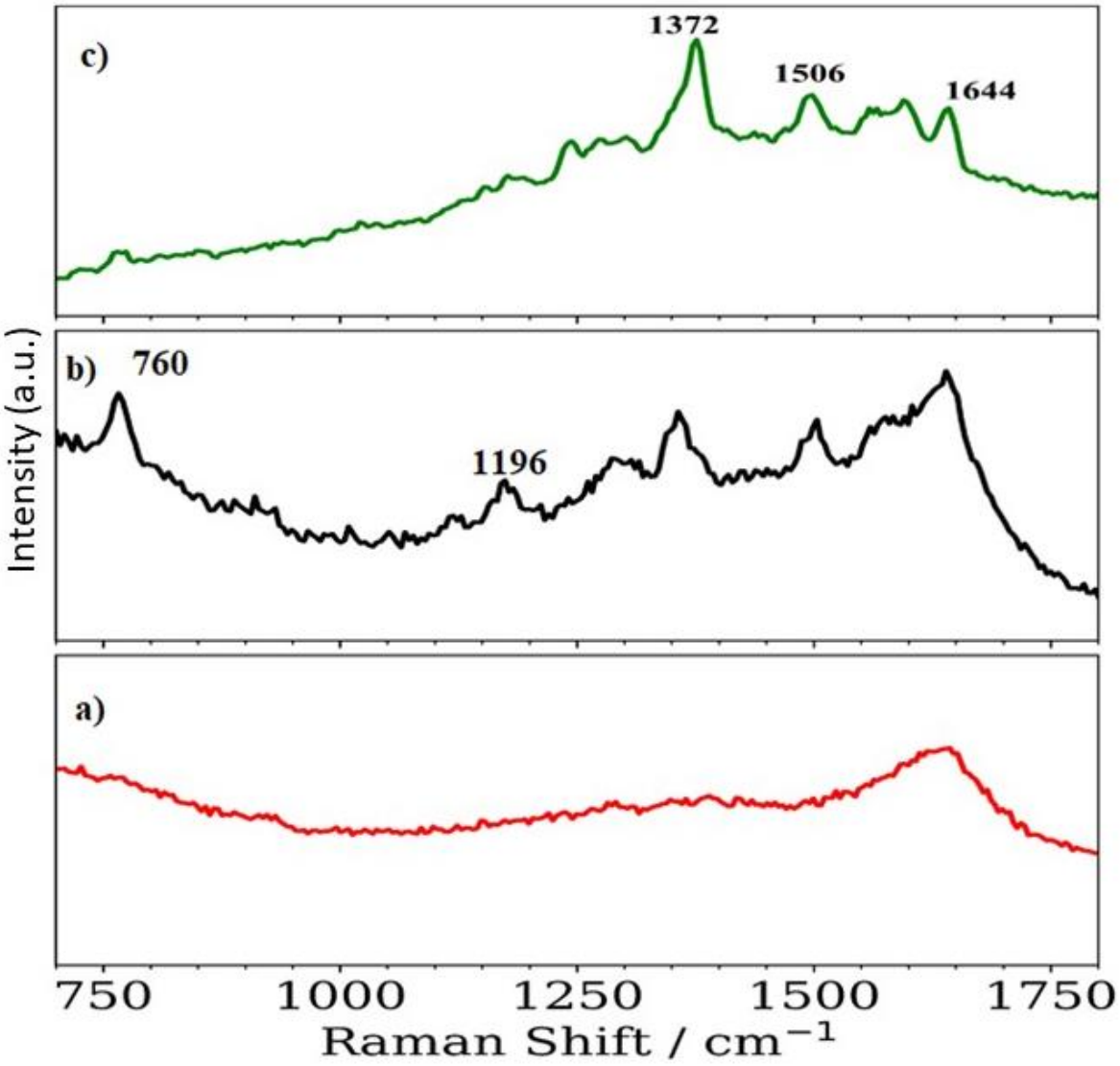

Figure 4. 7: a) 1080 SERS without $MgSO_4$; b) 1080 SERS with $MgSO_4$; c) 1080 SLIPSERS (10^{-6} mol/L) with $MgSO_4$ acquired at 532 nm laser wavelength with 40 × *objective, laser power of 12 mW and 15 s exposure time with average spectra from four accumulations.*

As stated in the earlier section of this chapter, normal Raman of 1080 is very weak whereas SERS and SLIPS of 1080 are quite achievable. To have a good idea of strong Raman bands in agreement with Gaussian calculated values from Table 4.1, the vibrational frequency assignments were obtained and listed in Table 4.3. From the calculated spectrum, the band at 1372 cm^{-1} is due to in-plane bending of C-H bond and 1644 cm^{-1}; the most intense peak corresponds to O-C-O stretching band of the carboxylate group. This peak is expected due to the presence of carboxylate group in both whose stretching frequency lies in the range from 1645 cm^{-1} to 1690 cm^{-1}. Besides these vibrational modes for monofluoroacetate, there is also some C-F stretching signal at 1196 cm^{-1}.

Table 4. 3**.** Observed Raman peaks and assignments for sodium monofluoroacetate

Raman shift(cm^{-1})	**Gaussian Calculated frequencies (cm^{-1})**	**Intensity**	**Assignment**
1644	1626.1	strong	ν(C=O) symmetric stretching
1372	1354.7	strong	ν (C-O)
1255	1255.6	medium	ν (C-O) + $\delta (CCH)_{ip}$
1196	-	medium	δ (C-F)
760	-	strong	$\delta (CC)_{op}$

ip, in-plane; op, out-of-plane

A few observations were noted while analyzing the spectra of 1080. There are bands at 760 cm^{-1} and 1196 cm^{-1} in above 1080 spectra that are strongly enhanced in the SERS spectrum but not observed in the SLIPSERS. It was assumed that the relative intensities change as the coverage of the analyte moves from sub-monolayer to several layers. **[40]** Even though the concentration of 1080 is the same for SERS and SLIPSERS, the different methodologies for sample preparation result in different orientations of the analytes on the nanoparticle surface or possibly a preference for one binding mode over another. This could explain the relative increase in intensity of the 1372 cm^{-1} band in the SLIPSERS spectrum. It was clearly observed in Figure 4.6 and 4.7 that there was a dramatic transformation in the SERS spectrum after aggregation. All SERS analytes behave differently and not all showed a change in the fingerprint upon hot-spot formation. **[41]**

Another observation looking at the spectra of both brodifacoum and 1080 was the characteristic peak at 1644 cm^{-1} which is one of the strongest Raman bands. This peak is expected due to the presence of carboxylate group in both whose stretching frequency lies in the range from 1645 cm^{-1} to 1690 cm^{-1}. As per Rodes work, where SERS spectra were acquired from molecules adsorbed on the surface of a silver electrode in an electrochemical cell, this peak is missing in the 1080 spectrum and spectrum is quite different from our experimental data. This allowed us to put forward a few possible assumptions:

1. The surface charge of an electrochemical surface and silver colloidal could be quite different. The electrochemical surface potential could potentially change from negative to positive, depending on the electrode potential. The strongest electrochemical SERS obtained at an applied potential of +1.2 V, so the electrode has a positive polarity. The positive electrode binds the negative monofluoroacetate anion and strong SERS is observed. Adsorption will be very different on a positive surface. Synthesis of positively charged silver colloids was attempted by modifying borohydride-reduced silver colloid with thiocholine chloride to create a positive surface that should attract the negative anions **[17]** and give strong SERS but unfortunately, it was unsuccessful with no obtainable results. Self-induced aggregation was observed which makes nanoparticles unstable and gives spectral variations in SERS spectra. It was hoped that the unfavourable electrostatic interactions (i.e., negatively charged silver colloids and negatively charged anions) could be overcome by the controlled drying method of SLIPSERS. The Laplace pressure and surface tension of the solvent will overcome these interactions. **[18]** Therefore, it was assumed that positive surface charge could give different adsorption resulting in a different spectrum compared to the colloidal silver nanoparticles SERS spectrum.

2. The binding mode is also another point. Gaussian calculations are for a "free ion" in solution. A lot of work has been done on the binding of carboxylic acids to metal (and metal oxide) surfaces (especially TiO_2 surfaces), there is a very famous review by Deacon **[42]** that assigns the binding mode of carboxylates based on infrared frequencies and intensities. Any conclusions about the effect of binding on carboxylate frequency that is obtained from IR studies will apply to Raman – our calculations are for "free" or unbound carboxylate, but our experiments probably measure bound carboxylate - so change in frequency is expected. The binding mode, unidentate or bidentate, will determine the observed frequency.

SLIPSERS undoubtedly performed best in detecting analytes of higher intensity with 10^{-6} mol/L concentration. The high density of hot spots and analyte concentration by controlled drying demonstrated high sensitivity. (Figure 4.11) **[15]** Density of hotspots can be demonstrated using Raman line-scan which was discussed in the earlier section of this thesis.

Thus, this comparative study demonstrated the detection capability and high collection efficiency of SLIPSERS.

4.3.5. SLIPSERS analysis of brodifacoum for ultrasensitive detection

SERS measurements were performed on analyte-nanoparticle aggregate formed on SLIPS substrate (method described in Chapter 2).

Brodifacoum is a large molecule with several aromatic rings and extensive conjugation and thus has larger Raman cross-section. SEM micrograph of the dried aggregates of 10^{-3} and 10^{-8} M concentration of brodifacoum was recorded. Both images show the difference in surface structure where the lower concentration appears shiny whereas 10^{-8} M image looks rough and dry. These aggregates give an indication of level of concentration adsorbed at the surface which can be reason of loss of signal at high concentration.

When higher concentrations of brodifacoum are present in the colloidal solution, it appears that the analyte molecules completely cover the nanoparticle surfaces and then subsequently form multiple layers so that the SEM image (Figure 4.8.) shows only a molecular layer over the underlying nanoparticles. **[44]**

The aggregate structures are visible in the left image, but in the right image, the aggregates are obscured by the dried analyte. It was observed that for higher concentrations, a crystallized brodifacoum structure formed on top of the AgNP aggregates. There appeared to be a maximum concentration of analyte that gave an observable signal. The molecules are either scattering or absorbing the incident laser so very little radiation reaches the plasmonic silver nanoparticles and and therefore very little SERS enhancement occurs at high analyte concentration. Hence, for this study, the upper limit of concentration for brodifacoum was 10^{-5} M.

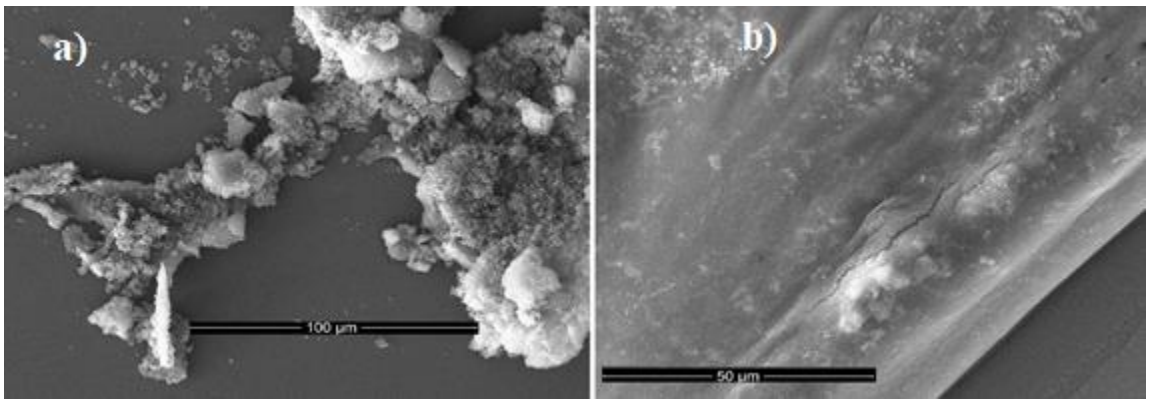

Figure 4. 8: SEM image of a) 10^{-3} mol/L and b) 10^{-8} mol/L brodifacoum on SERS substrate.

To support the observation that the analyte can completely cover the aggregate at higher concentrations as shown in Figure 4.9, volume of analyte particles and volume of nanoparticles in total solution was calculated:

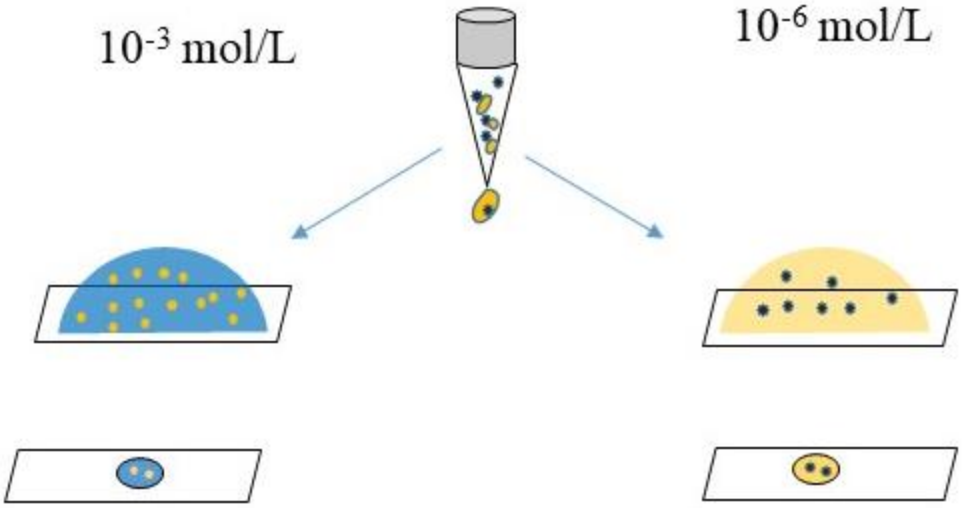

Figure 4. 9: SLIPS substrate preparation using high (*10^{-3} mol L^{-1}*) and low concentration (*10^{-6} mol L^{-1}*) of 10µL analyte (blue) with 50 µL of nanoparticles to demonstrate volume of analyte covering the aggregate.

Assuming the colloid as a sphere with radius $R = 23\ nm$ (diameter of silver colloid as obtained from Malvern Zetasizer was 45 nm) and concentration of nanoparticles calculated by finding the number of nanoparticles in colloidal solution is 1.2×10^{12} nanoparticles L^{-1}(NP L^{-1}). For higher analyte concentration, say 10^{-3} mol L^{-1}, the volume of total nanoparticles ($V_{total\ np}$) and volume of total analyte $V_{total\ analyte}$ in a dried aggregate is calculated as shown below.

$$N_{analyte} = 10^{-3}\ mol\ L^{-1} \times 10^{-6} L\ (volume\ used\ for\ SLIPS) \times N_A$$

$$= 6 \times 10^{14}$$

$$N_{nanoparticle} = 1.2 \times 10^{12} \text{nanoparticles}\ L^{-1}\ \times 50 \times 10^{-6}\ L\ (volume\ used\ for\ SLIPS)$$

$$= 6 \times 10^{7}\ NP$$

$$V_{total\ np} = V_{np}\ \times N_{nanoparticle} = \ 2.8 \times 10^{12}\ \text{nm}^3$$

$$V_{total\ analyte} = V_{analyte\ molecule}\ \times N_{analyte} = 1.2 \times 10^{16}\ \text{nm}^3$$

This demonstrates that the analyte volume is much larger than the nanoparticle volume by a factor of 10^4 for high concentrations whereas with a decrease in concentration we can find a close match of an analyte and nanoparticle volumes or an analyte volume less than the nanoparticle volumes. For comparison, we also calculated the volume of total analyte ($V_{total\ np} = 2.8 \times 10^{12}\ \text{nm}^3$ and

volume of total nanoparticles $V_{total\ analyte} = 1.2 \times 10^{12}$ nm^3 in a dried aggregate for 10^{-6} mol L^{-1} concentration where both volumes are almost a close match. This value supports the selection of 10^{-5} mol L^{-1} as the upper limit for detection in SLIPSERS measurements.

To understand whether SLIPS is capable to reproduce results with low concentration from randomly selected points on the substrate, SERS spectra were recorded at ten random spots. The waterfall diagram in Figure 4.10 clearly demonstrates that silver nanoparticles deliver an excellent reproducibility at high concentration of brodifacoum (10^{-6} M) by selecting 10 random spots on SLIPSERS substrate. Relative standard deviation (RSD) is the special form of standard deviation which helps in identifying how precise the data is. Smaller the percentage value, the more accurate the data is.

$$RSD = 100 \times Standard\ deviation \div Absolute\ mean$$

The reproducibility of brodifacoum obtained is extremely good and the relative standard deviation is 5.98% within the acceptable standard limit of less than 20% (Figure 4.11), which proves it as a reliable SERS detection technique **[24]**.

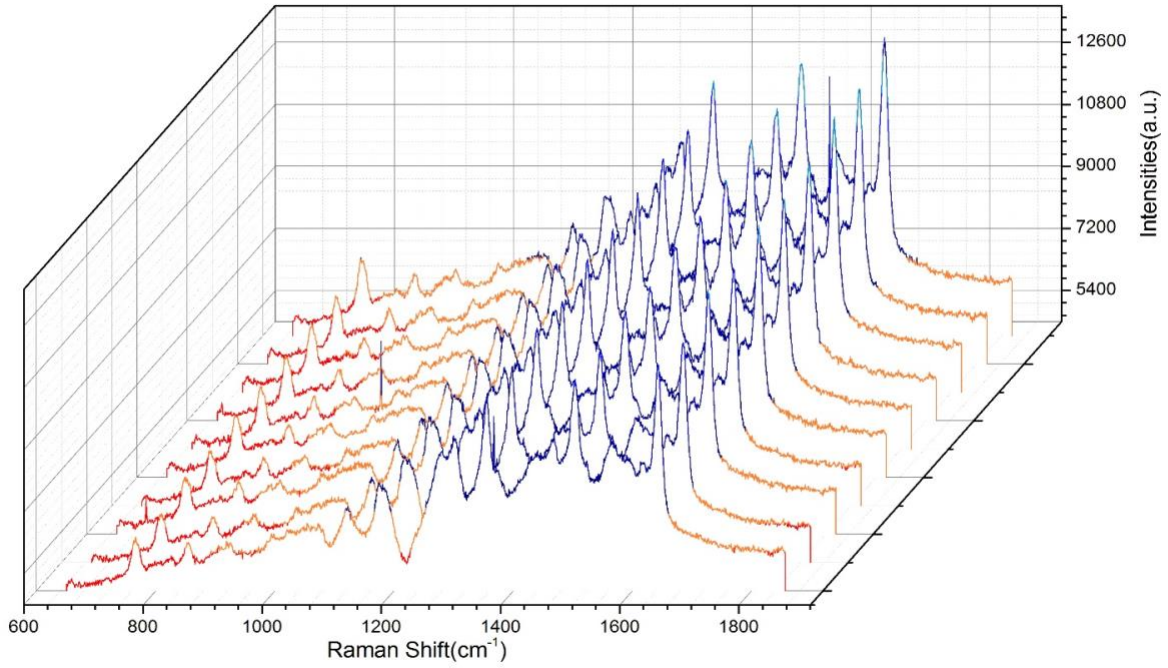

Figure 4. 10: Waterfall plot of SLIPSERS spectra of brodifacoum at 10^{-6} M obtained from 10 different spot measurements at 532 nm excitation wavelength, 12 mW laser power and 10 seconds exposure time for 3 accumulations.

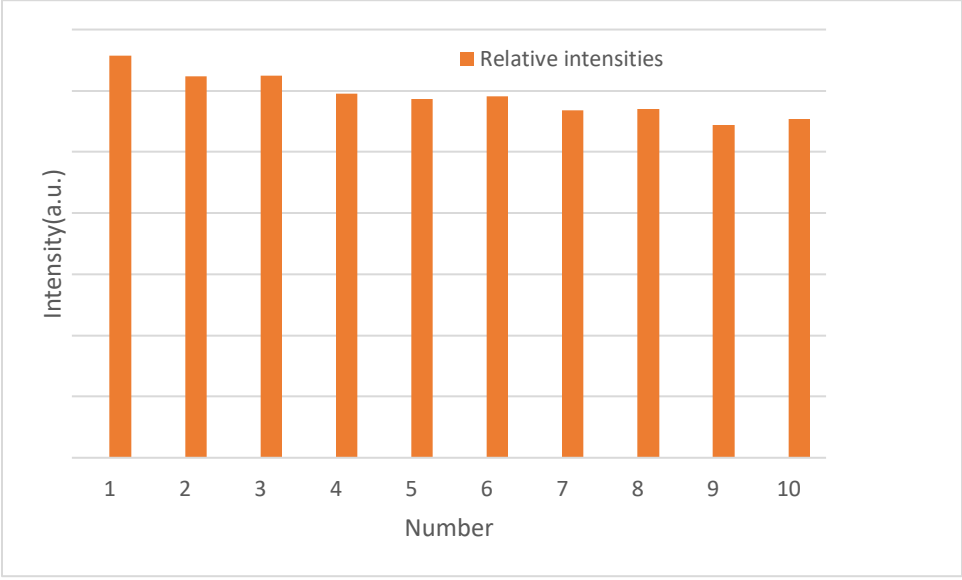

Figure 4. 11: Relative standard deviation of strong Raman band at 1644 cm^{-1} of 10^{-6} M brodifacoum from 10 random spots.

Quantitative detection is relevant to determine the concentration of a particular analyte or several other interfering compounds present in the sample. Here, it was performed to evaluate the limit of detection of brodifacoum ranging from 10^{-6} M to 10^{-14} M. It was observed with decrease in concentration levels it becomes more difficult to locate a strong Raman signal and this is presumably due to the low density of analyte molecules – at very low concentration the probability of a molecule being located in the scattering volume decreases to a point where no molecules are located in the scattering volume.

But this is unlike the SERS case where the low density is due to the large area the nanoparticles are spread over, with SLIPSERS the low density is due to a low number of analyte molecules. **[25]** As the concentration of analyte decreases, the number of single analyte molecule decreases as compared to AgNP's. Le Ru et al. demonstrated that there are many randomly oriented single analytes molecule at the surface, but the intensity is quite varied. Therefore, few selected highly enhanced signal from hotspots were captured with the largest intensities. **[31]** This is the subsampling problem, that is, the analyte concentration becomes so low that there is less than one molecule (on average) in the focal volume of the laser. So, there is a reasonable chance that no signal will be observed if a random point on the AgNP aggregate is selected. Note that the hotspot density does not change so the hot spots can still be found easily.

But the probability of a molecule being at a hotspot that is illuminated by the laser starts to decrease once the analyte concentration reaches a critical concentration.

Once the analyte has adsorbed onto the nanoparticle surfaces, it is the density (number of molecules per unit area) that is the critical parameter. Subsampling is observed once the density of analyte molecules falls below a critical value. In the subsampling regime, there is no longer a linear relationship between the concentration of an analyte in solution and the SLIPSERS intensity.

This is similar to the problem faced with the coffee ring effect for the SERS measurements. For the SERS measurements, the analyte density drops below a critical value and subsampling is observed, but this time, the density decreases due to a significant increase in the effective area that the analyte occupies on the substrate surface (rather than a decrease in the number of molecules). Of course, the critical density is very different for two cases, with SLIPSERS, Figure 4.15 shows the critical density is approx. 1×10^{-11} mol L^{-1} for SLIPSERS.

Figure 4.12 and 4.13 below shows the SLIPSERS spectra of brodifacoum with concentration down to 10^{-14} M. Hence, lowest level of brodifacoum detection (LOD) in a sample which can be detected but not quantitated as exact and reliable value found experimentally was 10^{-14} M whereas the detection limit of brodifacoum among all concentrations can be reliably detected and quantified (LOQ) was 10^{-12} M. The major peaks clearly observed in brodifacoum spectra were 1356, 1504 and 1644 cm^{-1}.

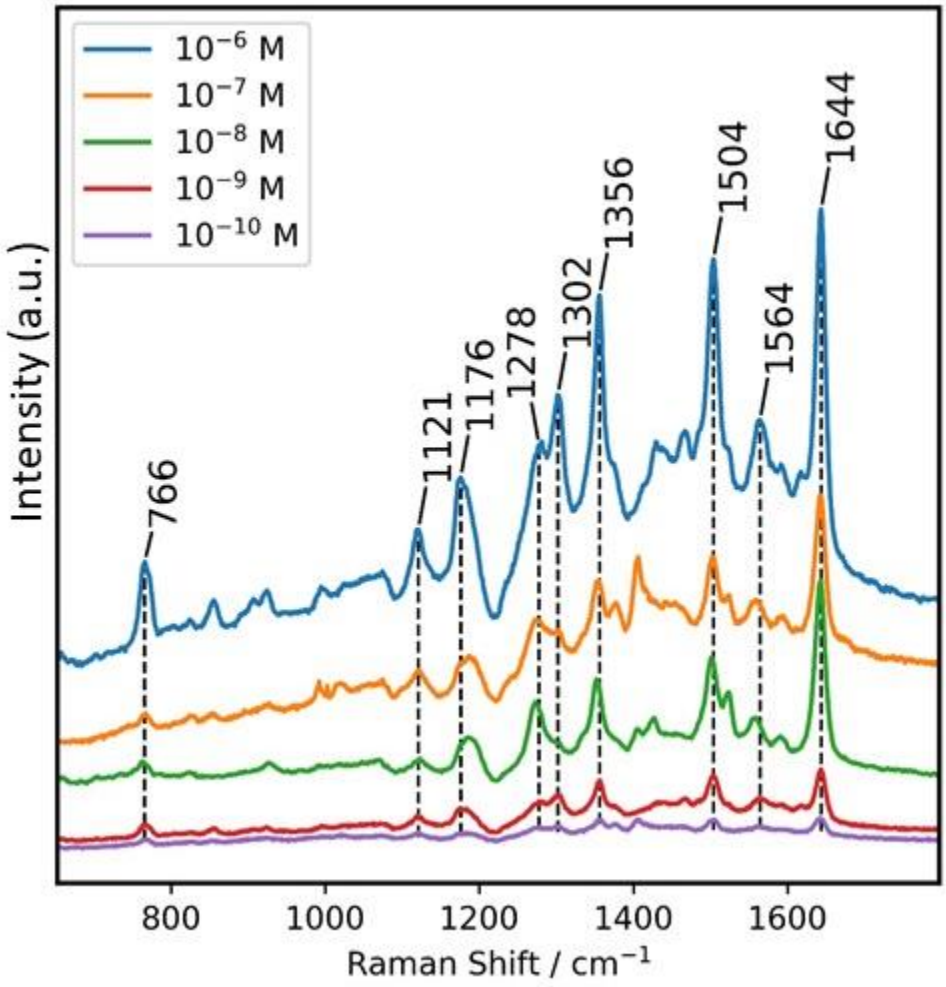

Figure 4. 12: SLIPSERS detection of brodifacoum molecules in aqueous solutions at different concentration (10^{-6} to 10^{-10} M) (top to bottom) acquired at 532 nm laser wavelength with 40 × *objective, laser power of 12 mW and 15 s exposure time with average spectra from four accumulations*

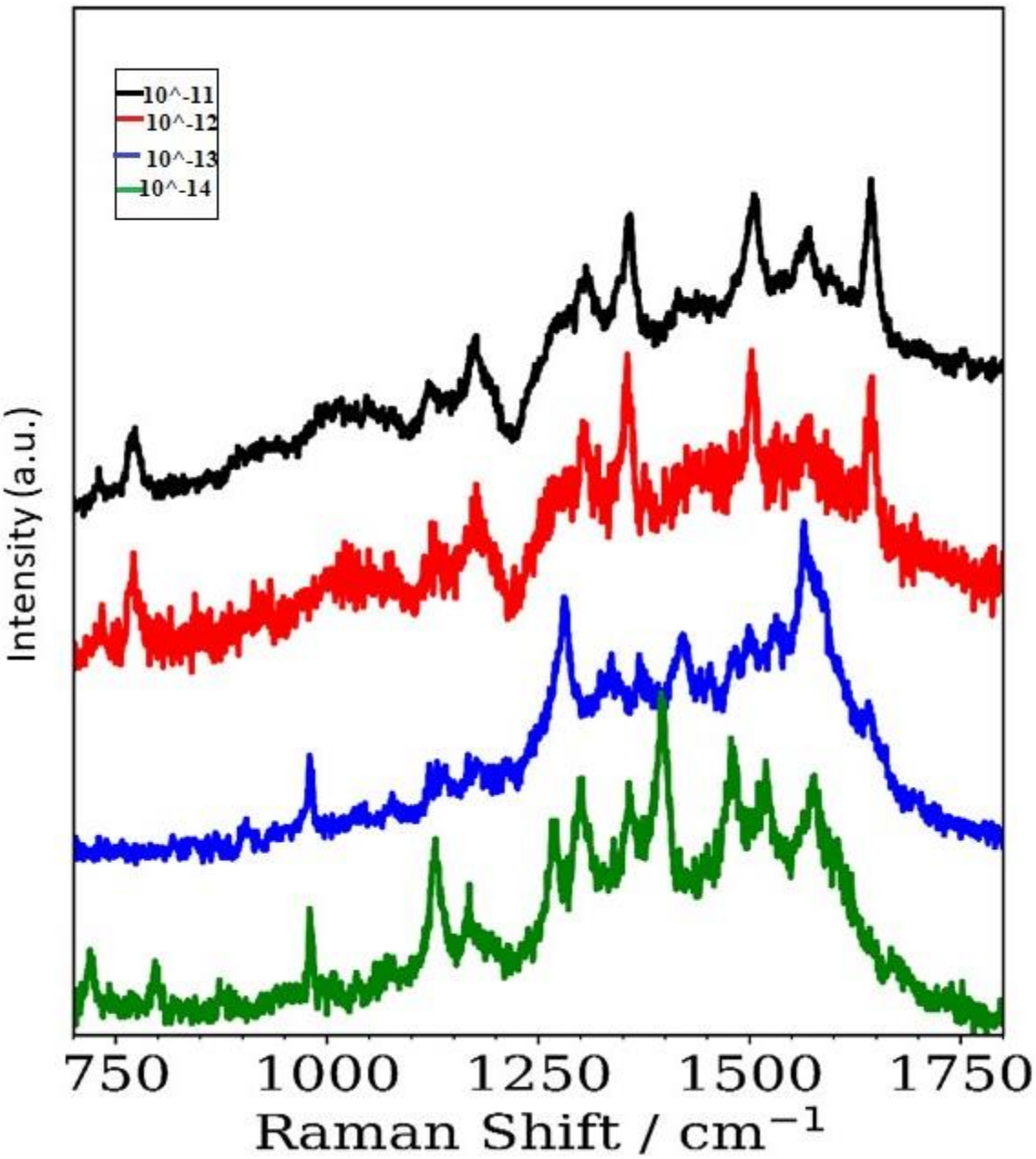

Figure 4. 13: SLIPSERS detection of brodifacoum molecules in aqueous solutions at different concentration (10-11M, top to 10-14M, bottom) acquired at 532 nm laser wavelength with 40 × *objective, laser power of 12 mW and 15 s exposure time with average spectra from four accumulations.*

It was found from the Figure 4.13, 10^{-11} M and 10^{-12} M concentration spectra agree closely with each other with Raman bands almost at the same values, but 10^{-13} M and 10^{-14} M has a very different set of enhancing bands representing shift in peaks. This is because brodifacoum molecules at such low concentrations has reached to single molecule regime and there will be no averaging over sites and no orientational averaging because the nanoparticles are fixed. So, the variations in the intensities are due to molecules in different orientations relative to the surface and incident laser polarization at the position of highest enhancement, so called hot-spots. Only the smallest fraction of molecules is observed at the single molecule level.

4.3.6. Quantitative analysis of Brodifacoum with SLIPSERS (Performance of the method)

a) Linearity

The linearity is its ability to elicit results that are directly proportional to the concentration of an analyte in a sample within a given range.

Performance of the method for brodifacoum was evaluated by taking four calibration standard points against the intensity of brodifacoum SLIPSERS peak for a broader range of concentrations from 10^{-6} to 10^{-12} M at 1644 cm^{-1} peak for quantification. (Figure 4.12). The calibration band at 1644 cm^{-1} was chosen due to its strong intensity of C=O stretching vibrations. Detailed assignments of SERS bands for brodifacoum and 1080 were already described before in this chapter.

Logarithmic transformation of data is quite useful in handling the wide concentration range and is frequently used for SERS calibration curves [**15, 44-45].** The log concentration vs intensity spreads out the data so that the shape and quality of the fit are clearly visible when the concentrations cover a wide range. When the data is exhibited in log concentration, the data yields a linear model that shows concentration between $10^{-6} - 10^{-10}$ mol/L. All spectra were averaged using three random points on each sample substrate to get reliable data.

The calibration curve for brodifacoum in aqueous solution is shown in Figure. 4.14, where the error bars indicate the standard error of Raman intensity for each concentration. The curve gave a linear trend and the R_2 value is closer to 1. Residuals gave the difference between the observed y value and the y value calculated using the equation of the fitted line.

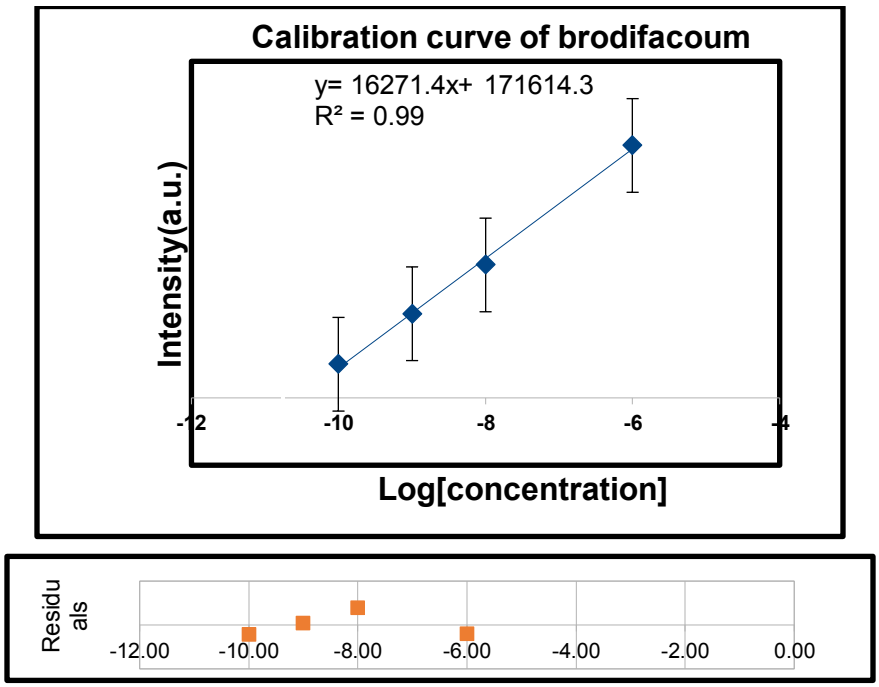

Figure 4.14: Calibration curve for SLIPSERS detection of different concentration of brodifacoum to intensity at 1644 cm-1 with error bars represent the standard error.

Table 4. 4**.** Statistical data for brodifacoum by Raman method

Parameter	**Concentration of brodifacoum(mol/L)**
Linear range	$10^{-6} - 10^{-10}$
Slope	1.6×10^{4}
Intercept	1.7×10^{5}
Standard deviation (Error) of slope	5.8×10^{2}
Standard deviation (Error) of intercept	4.9×10^{3}
% Error of Slope	3.61%
% Error of Intercept	2.87%
Standard deviation of residuals	7.3%

b) Limit of Detection & Limit of Quantification

The range of SLIPSERS intensities gave a linear response against log concentration. At high concentration, SLIPSERS intensity is lost due to the analyte forming a "blocking layer" that prevents the incident laser generating plasmon enhancement and at low concentration, the low density of analyte on the AgNP aggregates leads to subsampling. In this section, the linear range is characterized to determine the limit of detection and limit of quantification.

With the decrease in concentration between 10^{-6} and 10^{-10} mol L^{-1} there was a subsequent decrease in intensity level which is considered as the 'quantification region' whereas concentrations lower than 10^{-10} mol L^{-1} gives almost similar intensity as only very few analyte molecules exist within laser spot region. This means it is possible to see the subsampling effects (i.e., the signal from random hotspots), but the signal might be coming from several molecules at the hot spot and might be labeled as the '*single-molecule region'*. (Figure 4.15) This region requires rigorous search of the sample for signal, as they are very limited, only being found at random sites within the SLIPSERS aggregate.

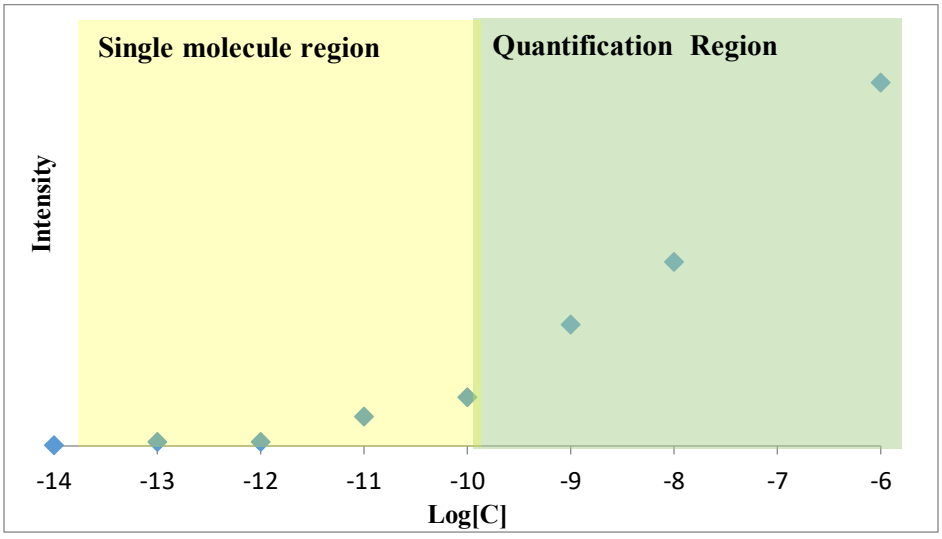

Figure 4. 15: SLIPSERS intensity at 1644 cm^{-1} as a function of different concentrations of brodifacoum.

The lowest amount of an analyte in a sample, which can be detected but not necessarily, quantified due to low signal to noise, referred as limit of detection (LOD) is estimated as 10^{-12} M by comparing the lowest concentration with the blank for a highly intense peak at 1644 cm^{-1} and the lowest amount of brodifacoum in aqueous solution which can be determined quantitatively with a suitable precision and accuracy (LOQ) was 10^{-10} M. **[35]**. An acceptable parameter for determining LOD is the concentration where:

$$\frac{Peak\ Height}{Signal - to - noise} = 3$$

whereas the limit of quantification (LOQ) is the concentration where

$$\frac{Peak\ Height}{Signal - to - noise} = 10$$

c) Precision & Accuracy

Triplicate analysis was done using two concentrations: 10^{-6} mol/L and 10^{-10} mol/L at three different positions at peak 1644 cm^{-1}. To evaluate precision and accuracy, the coefficient of variance (CV) and relative standard deviation (RSD) from the predicted values were measured from the regression equation **[25]**.

Coefficient of variation, also known as relative standard deviation is used to measure precision and repeatability of the results. RSD (%) was calculated after dividing the standard deviation by the average intensity of three replicated for a specific concentration.

Accuracy is the exactness or closeness of the test results obtained by the method to the true value. The accuracy % was determined by comparing the mean calculated concentration of the samples with the true value obtained from the calibration curve. Accuracy can also termed as recovery, that is, the ability to detect the amount of analyte present in a sample. So, the recovery rate was calculated by comparing the known analytical concentration of brodifacoum or 1080 in the solution with the predicted concentration obtained from the regression equation and this can determine the accuracy of the chosen method **[49]**.

$$Accuracy\ \% = (Predicted\ concentration \div Known(added)\ concentration) \times 100$$

The table below demonstrates the values obtained that provide a satisfactory level of quantification with relative deviation of both higher and lower concentration of less than 3%.

Table 4. 5. Different concentrations (10^{-6} and 10^{-10} mol/L) of brodifacoum at 1644 cm^{-1} used to calculate the precision (RSD) and accuracy.

Log[Concentration]	Intensity	Average ± SD	CV)	RSD(%)	Accuracy(%)
-6	77401	777168 ± 207.94	0.002	0.26	98
-6	77105				
-6	77000				
-10	9000	9000 ± 100	0.011	1.1	99
-10	9101				
-10	8900				

Therefore, the accuracy and precision values are excellent and were well within the acceptable limits of RSD<20% **[34]**.

d) Sensitivity Enhancements

Analytical enhancement factor (as defined by Le Ru) is used to evaluate SERS performance at any two specific levels of concentration. [**12]** AEF was calculated using the equation:

$$AEF = I_{SLIPSERS} C_{RAMAN} / I_{RAMAN} C_{SLIPSERS}$$

where $I_{SLIPSERS}$, I_{RAMAN} represents peak intensity with and without Ag nanoparticles and $C_{SLIPSERS}$, C_{RAMAN} are the concentration of brodifacoum with and without Ag nanoparticles. **[28-30]**. SERS and SLIPSERS EF was measured using the brodifacoum 1644 cm^{-1} peak intensity.

SERS and SLIPSERS enhancement factor of 10^{-6} mol/L brodifacoum obtained was 1.207×10^6 and 2.5×10^7 respectively. Enhancement factor with SLIPSERS is higher than SERS due to the presence of an increased number of hotspots in dried aggregate creating strong enhancement. This proves the potential of SLIPSERS for further investigation of different complex systems.

4.3.7. SLIPSERS analysis of 1080

The same methodology was applied for the detection of 1080. As shown in Figure 4.5, 1080 is a very weak Raman scatterer. Even solid 1080 shows no discernible Raman bands, presumably due to a fluorescence impurity generating a broad (but relatively weak background). SLIPSERS spectra for 1080 are shown below in Figure 4.16. 1080 on colloidal silver nanoparticles (with an aggregating agent) (using the same procedure as for brodifacoum) significantly enhanced the signal and made detection possible. Similar to the preparation of brodifacoum samples, 10^{-6} down to 10^{-10}M concentration of 1080 were prepared and recorded the SERS spectra. For a 1080 concentration of 10^{-10}M prominent peaks are not observed, only spectral noise. The major peaks observed in 1080 spectra were 1373, 1502 and 1643 cm^{-1}. The calibration curve for brodifacoum in aqueous solution is shown in Figure. 4.17.

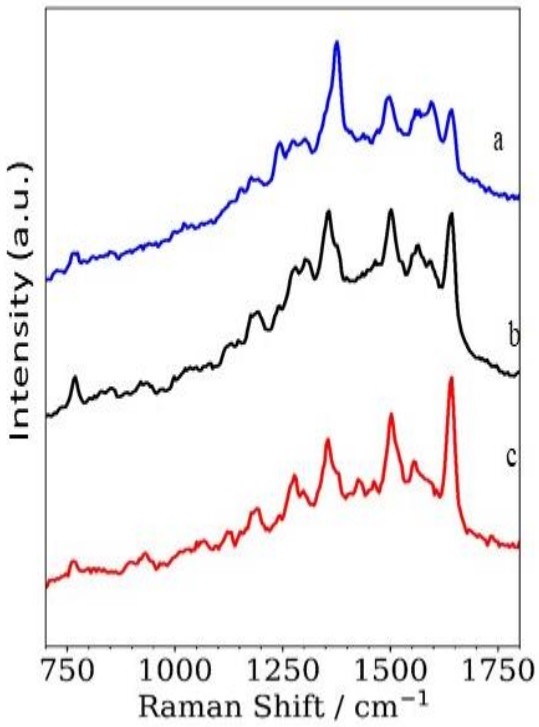

Figure 4.16: SLIPSERS detection of 1080 (a)10-6M, (b) 10--7M (c)10--8M in aqueous solution acquired at 532 nm laser wavelength with 40 × *objective, laser power of 12 mW and 15 s exposure time with average spectra from four accumulations.*

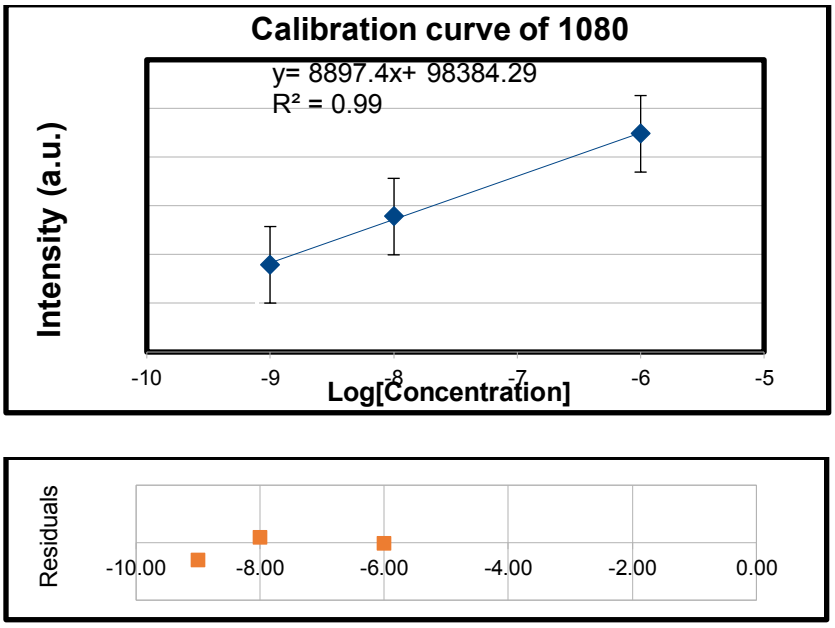

Figure 4.17: Calibration curve for SLIPSERS detection of different concentration of 1080 to intensity at 1373 cm-1 with error bars represent the standard error.

With 1080, detection levels are quantitated for three concentrations: 10^{-6}, 10^{-7} and 10^{-8} M as below 10^{-9}M it went to single molecule region. Hence, the lowest amount of 1080 in a sample, which can be detected but not quantified, is estimated as 10^{-9} M (LOD) and the lowest amount of 1080 in a sample which can be determined quantitatively with a suitable precision and accuracy (LOQ) was 10^{-8} M **[25]**.

Table 4. 6**.** Statistical data for 1080 by Raman method

Parameter	**Concentration of 1080(mol/L)**
Linear range	$10^{-6} - 10^{-8}$
Slope	8.89×10^{3}
Intercept	9.83×10^{4}
Standard deviation (Error) of slope	3.44×10^{2}
Standard deviation (Error) of intercept	2.67×10^{3}
% Error of Slope	3.87%
% Error of Intercept	2.72%
Standard deviation of residuals	2.2%

Hence, with this experimental demonstration SLIPSERS has proven its ability to detect 1080 with the detection limit of 10^{-8} M that is quite hard to determine with normal Raman or SERS.

Brodifacoum and 1080 both are rodenticides; one a conjugated structure with aromatic rings while the other is a simple anion with no aromaticity. Brodifacoum showed high SERS activity with good enhancement factor that is a new addition in literature in the list of SERS probing molecules. 1080 is poor Raman scatterer due to its small cross section whereas SLIPSERS for 1080 is quite achievable. Therefore, it is evident that SLIPSERS can detect two analytes that have a similar biological and environmental function but very different physical and chemical properties. So, these results show that SLIPSERS has the potential for environmental and bioanalytical applications. **[15]**

Several studies have been done for the detection of anti-coagulant rodenticide residues in dog's liver, human blood and water using GC-MS, LC-MS or HPLC but no SERS detection has been attempted to date. Ray et al have detected brodifacoum in dog liver using GC-MS with LOD as 1.1 mg/Kg **[36]** and Yan et al. have provided LOD in whole blood as 10 ng/mL using LC-MS **[37].** In this chapter, a simple system of rodenticide detection in aqueous solution was investigated and compared the LOD values for such a system with different analytical methods from the literature presented in Table 4.7.

Table 4. 7**.** Comparison of current method with other analytical techniques:

S. No.	Type of matrix	Detection method	Detection limit	Reference
1	Brodifacoum in stream water	HPLC	0.02 ng/mL	38
2.	Brodifacoum in waste water	HPLC	0.2 ng/mL	38
3.	1080 in water	GC-MS	0.1 ng/mL	39
4.	Brodifacoum in aqueous	SLIPSERS	0.0005 ng/mL	Current work
5	1080 in aqueous	SLIPSERS	0.1 ng/mL	Current work

Looking at the above values, SLIPSERS has demonstrated its promising potential of detecting brodifacoum to a concentration 100-fold lower than those reported in literature whereas 1080 also has achieved similar lowest detection through SLIPSERS.

4.4. Conclusion

This chapter has demonstrated the capability of SERS using an omniphobic substrate, SLIPS, that overcomes the drawback faced by SERS regarding the density of hot-spots. Both compounds are rodenticides but have very different physical and chemical properties. SLIPSERS provides a versatile platform for the rapid detection of trace amounts of brodifacoum and 1080 that brings the lowest detection concentration to a picomolar level. SLIPSERS is much faster, simpler and provides a lower detectable concentration than SERS and other analytical techniques like HPLC, GC-MS and LC-MS as discussed in the last section.

References

1. Cooney, T.P., Varelis, P. & Bendall, J.G. 2016, 'High-Throughput Quantification of Monofluoroacetate (1080) in Milk as a Response to an Extortion Threat', *Journal of food protection*, vol. 79, no. 2, pp. 273-81.
2. Eason, C.T., Murphy, E.C., Wright, G.R. & Spurr, E.B. 2002, 'Assessment of risks of brodifacoum to non-target birds and mammals in New Zealand', *Ecotoxicology*, vol. 11, no. 1, pp. 35-48.
3. Littin, K.E. 2004, 'The behaviour, pathophysiology and pathology of brushtail possums (Trichosurus vulpecula) poisoned with 1080 or brodifacoum, and the implications for possum welfare: a dissertation presented in partial fulfilment of the requirements for the degree of Ph. D in Physiology at Massey University, Palmerston North, New Zealand', Massey University.
4. Pelfrène, A.F. 2010, 'Rodenticides', *Hayes' Handbook of Pesticide Toxicology (Third Edition)*, Elsevier, pp. 2153-217
5. Duffield, P., Duffield, A., Kennedy, M., Birkett, D. & Wade, D. 1979, 'Warfarin and warfarin-alcohol levels in anticoagulated patients', *Australian and New Zealand journal of medicine*, vol. 9, no. 5, pp. 534-7.

6. Ray, A., Murphy, M., DuVall, M. & Reagor, J. 1989, 'Determination of brodifacoum and bromadiolone residues in rodent and canine liver', *American journal of veterinary research*, vol. 50, no. 4, pp. 546-50.
7. Jin, M.c., OuYang, X.k., Xu, X.m., Ren, Y.p. & Chen, X.h. 2007, 'Rapid Determination of Coumatetralyl in Human Serum by High-Performance Liquid Chromatography Coupled with Electrospray Ionization Tandem Mass Spectrometry', *Analytical letters*, vol. 40, no. 4, pp. 737-46.
8. Jin, M.c. & Chen, X.h. 2006, 'Rapid determination of three anticoagulant rodenticides in whole blood by liquid chromatography coupled with electrospray ionization mass spectrometry', *Rapid communications in mass spectrometry*, vol. 20, no. 18, pp. 2741-6.
9. Vindenes, V., Karinen, R., Hasvold, I., Bernard, J.P., Mørland, J.G. & Christophersen, A.S. 2008, 'Bromadiolone poisoning: LC–MS method and pharmacokinetic data', *Journal of forensic sciences*, vol. 53, no. 4, pp. 993-6.
10. Kieboom, A.J. & Rammell, C.G. 1981, 'Determination of brodifacoum in animal tissues by HPLC', *Bulletin of environmental contamination and toxicology*, vol. 26, no. 1, pp. 674-8.
11. Hunter, K., Sharp, E. & Newton, A. 1988, 'Determination of diastereoisomers of bromadiolone, an anticougulant rodenticide, in animal tissues by high-performance liquid chromatography', *Journal of Chromatography A*, vol. 435, pp. 83-95.
12. Kelly, M., Chambers, J. & MacNicoll, A. 1993, 'Simple and rapid method for the determination of the diastereomers of difenacoum in blood and liver using high-performance liquid chromatography with fluorescence detection', *Journal of Chromatography B: Biomedical Sciences and Applications*, vol. 620, no. 1, pp. 105-12.
13. Srivatsan, T. 2014, 'Practical Raman Spectroscopy: An Introduction: Peter Vandenabeele, Wiley, John & Sons, Incorporated, 2013, 192 Pp., ISBN: 9780470683187', Taylor & Francis.
14. Yunker, P.J., Still, T., Lohr, M.A. & Yodh, A. 2011, 'Suppression of the coffee-ring effect by shape-dependent capillary interactions', *Nature*, vol. 476, no. 7360, p. 308.
15. Yang, S., Dai, X., Stogin, B., & Wong, T. (2016) Ultrasensitive surface-enhanced Raman scattering detection common fluids. *Proceedings of the National Academy of Science, 113* (2), 268-273

16. Frank, A.J., Cathcart, N., Maly, K.E. & Kitaev, V. 2010, 'Synthesis of silver nanoprisms with variable size and investigation of their optical properties: a first-year undergraduate experiment exploring plasmonic nanoparticles', *Journal of chemical education*, vol. 87, no. 10, pp. 1098-101.
17. Stewart, A., Murray, S. & Bell, S. 2015, 'Simple preparation of positively charged silver nanoparticles for detection of anions by surface-enhanced Raman spectroscopy', *Analyst*, vol. 140, no. 9, pp. 2988-94.
18. Le Ru, E. & Etchegoin, P. 2008, *Principles of Surface-Enhanced Raman Spectroscopy: and related plasmonic effects*, Elsevier.
19. Arjunan, V., Santhanam, R., Sakiladevi, S., Marchewka, M. & Mohan, S. 2013, 'Synthesis and characterization of an anticoagulant 4-hydroxy-1-thiocoumarin by FTIR, FT-Raman, NMR, DFT, NBO and HOMO–LUMO analysis', *Journal of Molecular Structure*, vol. 1037, pp. 305-16.
20. Bell, S.E. & Sirimuthu, N.M. 2005, 'Surface-enhanced Raman spectroscopy as a probe of competitive binding by anions to citrate-reduced silver colloids', The Journal of Physical Chemistry A, vol. 109, no. 33, pp. 7405-10.
21. Wyss Institute. (2017). *SLIPS (Slippery Liquid-Infused Porous Surfaces)*. Retrieved from https://wyss.harvard.edu/technology/slips-slippery-liquid-infused-porous-surfaces/
22. Mehigan, S., Smyth, C. A. & Mccabe, E. M. 2015. Bridging the gap between SERS enhancement and reproducibility by salt aggregated silver nanoparticles. *Nanomaterials and Nanotechnology*, 5, 5-5.
23. Zhang, Y., Wang, F., Yin, H. & Hong, M. 2013, 'Nonuniform Distribution of Capping Ligands Promoting Aggregation of Silver Nanoparticles for Use as a Substrate for SERS'.
24. Lu, Y., Lu, D., You, R., Liu, J., Huang, L., Su, J. & Feng, S. 2018, 'Diazotization-Coupling Reaction-Based Determination of Tyrosine in Urine Using Ag Nanocubes by Surface-Enhanced Raman Spectroscopy', *Nanomaterials*, vol. 8, no. 6, p. 400.
25. Jin, Y., Ma, P., Liang, F., Gao, D. & Wang, X. 2013, 'Determination of malachite green in environmental water using cloud point extraction coupled with surface-enhanced Raman scattering', *Analytical Methods*, vol. 5, no. 20, pp. 5609-14.
26. Wang, B., Zhang, L. & Zhou, X. 2014, 'Synthesis of silver nanocubes as a SERS substrate for the determination of pesticide paraoxon and thiram', *Spectrochimica Acta Part A:*

Molecular and Biomolecular Spectroscopy, vol. 121, pp. 63-9.

27. Hasna, K., Lakshmi, K., Jayaraj, M.K.E., Kumar, K.R. & Matham, M.V. 2016, 'Development of high-sensitive, reproducible colloidal surface-enhanced Raman spectroscopy active substrate using silver nanocubes for potential biosensing applications', *Journal of Nanophotonics*, vol. 10, no. 2, p. 026020.
28. Jiang, T., Li, J., Zhang, L., Wang, B. & Zhou, J. 2014, 'Microwave assisted in situ synthesis of Ag–NaCMC films and their reproducible surface-enhanced Raman scattering signals', *Journal of Alloys and Compounds*, vol. 602, pp. 94-100.
29. Ben-Jaber, S., Peveler, W.J., Quesada-Cabrera, R., Sol, C.W., Papakonstantinou, I. & Parkin, I.P. 2017, 'Sensitive and specific detection of explosives in solution and vapour by surface-enhanced Raman spectroscopy on silver nanocubes', *Nanoscale*, vol. 9, no. 42, pp. 16459-66.
30. Huang, J.-A., Zhao, Y.-Q., Zhang, X.-J., He, L.-F., Wong, T.-L., Chui, Y.-S., Zhang, W.-J. & Lee, S.-T. 2013, 'Ordered Ag/Si nanowires array: wide-range surface-enhanced Raman spectroscopy for reproducible biomolecule detection', *Nano letters*, vol. 13, no. 11, pp. 5039-45.
31. Le Ru, E., Blackie, E., Meyer, M. & Etchegoin, P. G. 2007. Surface enhanced Raman scattering enhancement factors: a comprehensive study. *The Journal of Physical Chemistry C*, 111, 13794-13803.
32. Delgado, J. M., Blanco, R., Orts, J. M., Pérez, J. M. & Rodes, A. 2008. DFT and In-Situ Spectroelectrochemical Study of the Adsorption of Fluoroacetate Anions at Gold Electrodes. *The Journal of Physical Chemistry C*, 113, 989-1000.
33. Gao, X., Zheng, P., Kasani, S., Wu, S., Yang, F., Lewis, S., Nayeem, S., Engler-Chiurazzi, E. B., Wigginton, J. G. & Simpkins, J. W. 2017. Based Surface-Enhanced Raman Scattering Lateral Flow Strip for Detection of Neuron-Specific Enolase in Blood Plasma. *Analytical chemistry*, 89, 10104-10110.
34. Mabbott, S., Xu, Y. & Goodacre, R. 2017. Objective assessment of SERS thin films: comparison of silver on copper via galvanic displacement with commercially available fabricated substrates. *Analytical Methods*, 9, 4783-4789.
35. Shrivastava, A. & Gupta, V. B. 2011. Methods for the determination of limit of detection and limit of quantitation of the analytical methods. *Chronicles of Young Scientists*, 2, 21.

36. Ray, A., Murphy, M., Duvall, M. & Reagor, J. 1989. Determination of brodifacoum and bromadiolone residues in rodent and canine liver. *American journal of veterinary research,* 50, 546-550.
37. Yan, H., Zhu, L., Zhuo, X., Shen, M. & Xiang, P. 2016. Anticoagulant rodenticide intoxication in east China: a three-year analysis. *Forensic Sciences Research*, 1, 22-27.
38. Hunter K 1983. Determination of coumarin anticoagulant rodenticide residues in animal tissue by high-performance liquid chromatography: I. Fluorescence detection using post-column techniques. *Journal of Chromatography* **270:** 267–276.
39. Ozawa H, Tsukioka T 1987. Gas chromatographic determination of sodium monofluoroacetate in water by derivatization with dicyclohexylcarbodiimide. *Analytical Chemistry* 59: 2914–2917.
40. Solovyeva, E.V. 2019, 'Surface-enhanced Raman scattering of 4, 4' diaminostilbene: Dependence of spectral features and resonant enhancement on surface coverage', *Journal of Raman Spectroscopy.*
41. Chen, T., Wang, H., Chen, G., Wang, Y., Feng, Y., Teo, W. S., Wu, T. & Chen, H. 2010. Hotspot-induced transformation of surface-enhanced Raman scattering fingerprints. *Acs Nano*, 4, 3087-3094.
42. Deacon, G., Huber, F. & Phillips, R. 1985. Diagnosis of the nature of carboxylate coordination from the direction of shifts of carbon - oxygen stretching frequencies. *Inorganica chimica acta*, 104, 41-45.
43. Arjunan, V., Santhanam, R., Sakiladevi, S., Marchewka, M., & Mohan, S. J. J. o. M. S. (2013). Synthesis and characterization of an anticoagulant 4-hydroxy-1-thiocoumarin by FTIR, FT-Raman, NMR, DFT, NBO and HOMO–LUMO analysis. *1037*, 305-316.
44. Sarfo, D. K., Sivanesan, A., Izake, E. L., & Ayoko, G. A. J. R. A. (2017). Rapid detection of mercury contamination in water by surface enhanced Raman spectroscopy. *7*(35), 21567-21575.
45. Jiang, F., Chen, S., Cao, Z., & Wang, G. J. P. (2016). A photo, temperature, and pH responsive spiropyran-functionalized polymer: *Synthesis, self-assembly and controlled release. 83*, 85-91.
46. Pescaglini A, Secco E, Martin A, Cammi D, Ronning C, Cantarero A, et al. Non-resonant Raman spectroscopy of individual ZnO nanowires via Au nanorod surface plasmons.

Journal of Materials Chemistry C. 2016;4(8):1651-7.

47. Yu, Y., Wang, Y., Lin, K., Hu, N., Zhou, X. & Liu, S. 2013. Complete Raman spectral assignment of methanol in the C–H stretching region. *The Journal of Physical Chemistry A,* 117**,** 4377-4384.
48. Munro C, Smith W, Garner M, Clarkson J, White P. Characterization of the surface of a citrate-reduced colloid optimized for use as a substrate for surface-enhanced resonance Raman scattering. *Langmuir.* 1995; 11(10):3712-20.
49. Vicario, A., Sergo, V., Toffoli, G. & Bonifacio, A. 2015. Surface-enhanced Raman spectroscopy of the anti-cancer drug irinotecan in presence of human serum albumin. *Colloids and Surfaces B: Biointerfaces,* 127, 41-46.
50. Ruedenberg K. Chemical Applications of Group Theory. By FA Cotton. *Inorganic Chemistry*. 1964; 3(5):784.
51. Wang X, Perry DS. An internal coordinate model of coupling between the torsion and C–H vibrations in methanol. *The Journal of chemical physics*. 1998; 109(24):10795-805.
52. Christe KO, Naumann D. Vibrational spectra of trifluoroacetates. *Spectrochimica Acta Part A: Molecular Spectroscopy.* 1973; 29(12):2017-24.

Chapter 5: Highly sensitive surface-enhanced Raman scattering detection of brodifacoum and 1080 rodenticide in milk.

(Detection of rodenticides in liquid milk section of this chapter is already presented and published in SPIE conference proceedings, USA)

Abstract

Surface-enhanced Raman scattering (SERS) is a powerful technique for food inspection because of its readiness, sensitivity, and minimum sample preparation requirements. **[1]** Milk is a vulnerable target for contamination. In this work, we demonstrate a reliable SERS method for detecting toxins in milk focusing on brodifacoum, an anticoagulant rodenticide, and sodium fluoroacetate, also commonly known as 1080. Surface-enhanced Raman spectroscopy is an advanced Raman technique for ultrasensitive detection of chemical and biological species. Liquid milk presents further challenges due to the complex colloidal nature of milk itself; producing much weaker SERS. Milk is opaque and limits the optical detection technique. The very strong Rayleigh scattering from milk is an immediately obvious problem. Also, surface-active species present in milk along with large surface areas on the milk colloids will compete for analyte binding. These active other components like proteins; lipids have the potential to mask the analyte and may produce false spectral results.

Therefore, an omniphobic surface platform was employed, which has the potential to deliver near 100% analyte concentration by constant contact angle drying (and consequently no contact line pinning). Such omniphobic SERS substrates, so-called Slippery liquid-infused porous surfaces (SLIPS) were recently reported **[2]**. SLIPSERS method coupled with the dilution of rodenticide spiked milk samples then extraction with a mixed solvent of methanol: water (3:1) was performed for rodenticide detection. **[3]** All the spectra were taken on an in-house Raman spectrometer based on a Princeton Instruments FERGIE spectrometer using 532 nm excitation wavelength (with 7-8 mW

laser power) focused onto the sample using a 40 × 0.65 NA objective. A series of diluted concentrations of each rodenticide ranging from 8-fold dilution to 1600-fold dilution were used to construct a calibration curve. There is an excellent linear relationship (R_2=0.9897) in this concentration range.

A critical challenge in detecting bioanalytes in complex systems like milk is to achieve high specificity, high throughput, and trace-level detection **[4]**. The approach adopted in this work can be extended to detect various molecules in complex chemical and biological matrices.

Keywords: Surface enhanced Raman scattering, brodifacoum, sodium monofluoroacetate, and slippery liquid-infused porous surfaces

5.1. Introduction

Milk is an essential part of a human's diet. It is not only a rich source of calcium but is very important for bone development and health. It is also a basis of other dairy products. Pesticides covers wide range of compounds including rodenticides, insecticides, and fungicides to control pests and protecting the agricultural output from them. These compounds are lethal to the targeted pests but causes harm to non-target species like animals feeding on these pests or the crop sprayed with these chemicals. There are several deaths reported worldwide due to pesticide poisoning. There were some residues found in bovine milk at high concentration **[4, 29, and 30]**. Due to short shelf life, fresh milk reaches consumers in a short period leaving little time for analytical procedures to detect the presence of adulterants or harmful additives. Hence, rapid methodologies are required for the early detection of contamination.

There are several techniques employed for detection of contaminants like HPLC, LC-MS **[5-7]** but these are time-consuming and expensive. Surface-enhanced Raman spectroscopy is an advanced Raman technique for ultrasensitive detection of chemical and biological species. Surface-enhanced Raman spectroscopy (SERS) has the potential for trace level detection with high molecular specificity and sensitivity. It requires a reproducible substrate with a strong resonant interaction with an incident laser light source to generate highly efficient Raman scattering. Nanostructured noble

metal substrates provide the necessary resonant interaction between the laser and scattering molecule. Silver nanoparticles (AgNPs) have a stronger absorption coefficient that gives stronger enhancement relative to gold nanoparticles (AuNPs) of the same size, which increases SERS sensitivity **[8]**.

Single molecule detection is possible with SERS under ideal conditions. Although hot-spots give strong SERS, they tend to be randomly distributed throughout the substrate. So sub-sampling becomes a problem when using tightly focused excitation via a microscope objective. The analyte must be adsorbed onto the silver nanoparticle surface, and then a drop of the nanoparticle suspension is dried onto a supporting surface (e.g., a glass slide).

Due to the so-called coffee ring effect, the analyte dries **[5]** creating a large diameter ring structure of nanoparticle aggregates with hot-spots dispersed around the perimeter of the "coffee-ring" edge which makes it challenging to locate highly sensitive SERS regions when using a highly focused laser source (via a microscope objective). At the same time, SERS for liquid milk is low due to diffuse scattering by various colloidal structures in milk.

The results from the previous chapters has demonstrated the ability of SLIPSERS substrate to detect rodenticides to very low levels in aqueous solutions. One of the aims of this chapter is to determine if the SLIPSERS substrates can be extended to detection of rodenticides in complex mixtures like milk. But the problem is that there are so many other constituents in milk besides analyte that when the sample dries, a large aggregate of matrix material is formed which blocks SERS active sites on the substrate and generates no or weak SERS signal.

In this chapter the following sequence of experiments were performed with the objective of applying the SLIPSERS substrates to complex biological samples.

1. Solid mixtures of 1080 and brodifacoum in milk powder were prepared to identify the rodenticide peaks in the presence of the milk components. Raman analysis was performed to investigate the complex mixture as "real world samples" and characterise the composition. Samples were prepared using a geometric dilution approach to provide a broad concentration range of rodenticide in the milk powder matrix.

2. Investigation of detection of analytes in milk without dilution using SERS and SLIPSERS technique. These measurements highlighted the problems associated with the high concentration of matrix components which interfered with the aggregation process during drying and prevented approach of the analyte to the SLIPSERS colloid surface.
3. Investigation of multi-fold dilution of the milk matrix to allow the analyte to compete for surface binding for SLIPSERS detection of analytes.

5.2. Experimental Data

5.2.1. Sample preparation for milk powder

Raman analysis was performed on commercial milk powder spiked with brodifacoum. Commercial Pams Whole milk powder was purchased and mixed with different concentrations of brodifacoum using geometric dilution method. This method is used to make more homogeneous mixtures of two solid powders – milk and brodifacoum.

Briefly, 10 milligrams (mg) of brodifacoum was mixed with another 10 milligram of milk powder to obtain a total mass of 20 mg giving 50-50 % contribution of both in a mixture. Later, from this sample 1, 16 mg was taken and mixed further with 24 mg of milk powder thereby decreasing the concentration of brodifacoum in milk powder and gives 20%. This process continues sequentially for two more levels till a minimum number was obtained. This study was performed as a proof of concept to understand the Raman spectra of solid mixtures of study before for investigating liquid milk.

Sample 1: $Mass\ percent\left(\%\frac{w}{w}\right) = mass_{brodi} \div mass_{total}$

$$= 10 \div 20 = 0.5 = 50\%$$

Sample 2: Mass percent $\% = (16\ mg \times 0.5) \div 40\ mg$

$$= 0.2 = 20\%$$

Sample 3: Mass percent $\% = (24.2\ mg \times 0.2) \div 80\ mg$

$$= 0.0605 = 6.1\%$$

Sample 4: Mass percent $\% = (56.1\ mg \times 0.0605) \div 100\ mg$

$$= 0.34 = 3.4\%$$

Table 5.1 illustrates the composition of each sample prepared. Samples contained five concentrations of brodifacoum measured in percent w/w.

Table 5. 1: Process of sample mixture preparation.

Sample	Mass of brodifacoum added (mg)	Mass of milk added(mg)	Total mass(mg)	Concentration of brodifacoum(w/w)	Mass percent(%w/w)
1	10	10	20	0.5	50.0
2	16	24	40	0.2	20.0
3	24.2	55.8	80	0.0605	6.1
4	56.1	43.9	100	0.0339405	3.4

Samples were ground using a mortar and pestle to get a fine powder and then packed into a 21-well microwell plate for Raman investigation. Raman spectra were obtained using 532 nm laser with laser power of 8 mW with exposure time of 10 seconds for four accumulations. Triplicate analysis was performed for each concentration and univariate analysis was later performed to quantify the method.

5.2.2. Sample pretreatment and SLIPS preparation for liquid milk

A 0.001 mol/L brodifacoum and 1080 stock solution was prepared with Milli-Q water. The milk sample was spiked with this stock solution to get the desired concentration of 10^{-4} mol/L brodifacoum and 1080 spiked milk sample. The standard spiked solutions were then diluted with Milli-Q water to 8-fold, 80-fold, 200-fold, 800-fold and 1600-fold dilutions. A control was also prepared without any rodenticide.

Spiked milk samples were deproteinised using methanol-water, v/v (3:1 ratio). After vortexing for one minute, the samples were sonicated for 10 minutes at 10 %. Then, the treated samples were spun for 20 minutes with portable mini centrifuge (Fisher Scientific) at 8000 revolutions per minute. Finally, the supernatant was collected for further SERS analysis. The schematic pretreatment procedure of milk followed by

SERS detection is shown in Figure 5.1. SERS (dried) and SLIPSERS samples were prepared as described in Chapter 2.

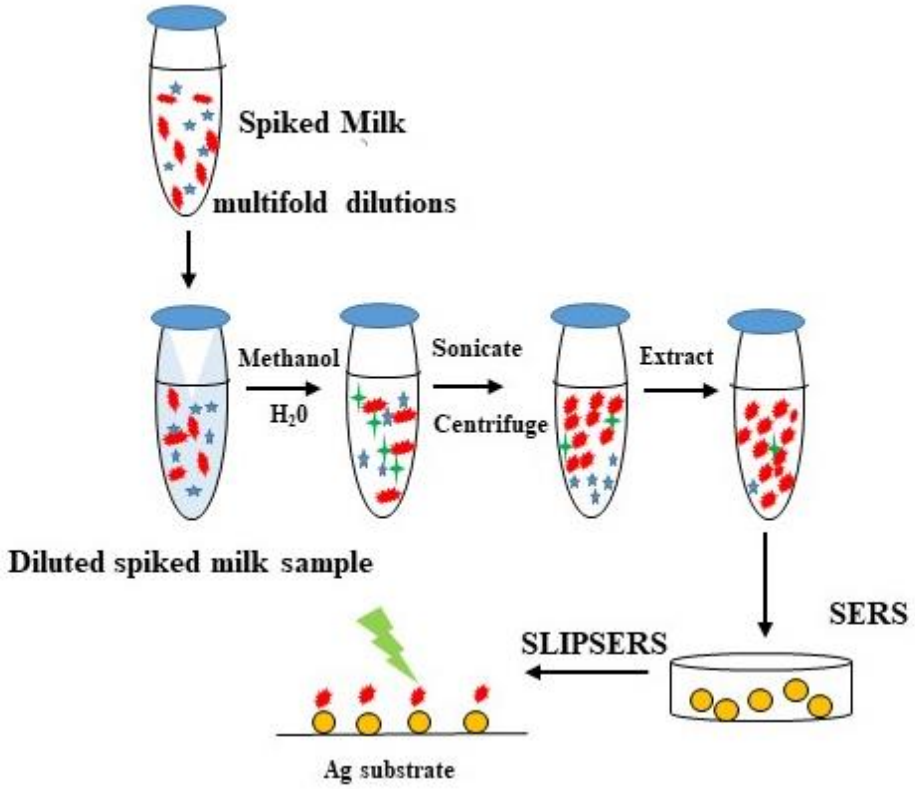

Figure 5. 1: Schematic representation showing the pretreatment of spiked milk samples followed by SLIPS substrate preparation

SERS and SLIPSERS samples preparation are already described in Chapter - 2. All samples were tested for at least 5 random spots per sample.

5.3. Results and Discussion

5.3.1. Characterisation of silver nanoparticles

Silver colloidal particles were prepared using borohydride reduction method according Frank *et al* **[10]**. Figure 5.2 represents the surface plasmon resonance peaks of silver nanoparticles using UV-Vis spectroscopy. The UV-Vis spectroscopy was used to show the maximum absorbance of silver nanoparticles in the wavelength region of 300 - 700

nm. The large plasmon peak is for unaggregated silver nanoparticles in solution. The absorption maximum occurred at 410 nm. Inset shows the SEM image of borohydride reduced silver nanoparticles with rodenticide spiked milk samples. These nanoparticles had a mean diameter of 45.78 nm and a zeta potential of -55 V as measured by Malvern Zetasizer. The results obtained were in close agreement to the literature data **[11]**.

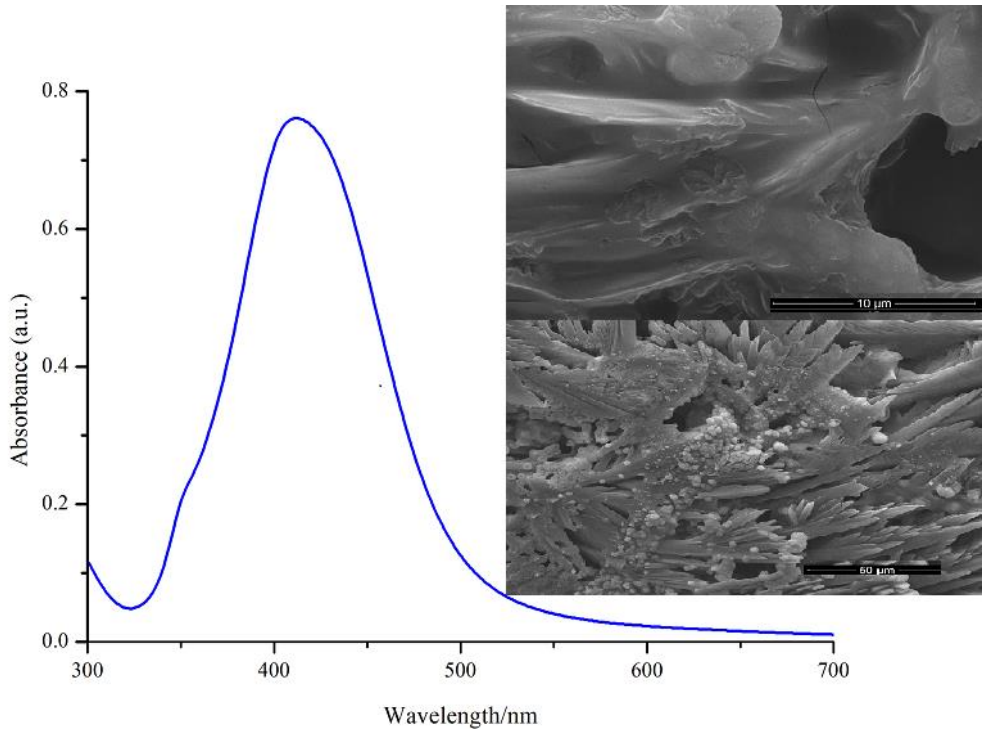

Figure 5. 2: UV-Vis absorption spectrum of colloidal Ag NPs, inset shows SEM images of Ag NPs with brodifacoum spiked milk sample (top; scale: 10µm) and Ag NPs with 1080-spiked milk sample (bottom; scale: 50 µm).

5.3.2. Experiment 1: Detection of brodifacoum in milk powder

This experiment was performed to understand the Raman spectral features of solid milk powder spiked with rodenticide, brodifacoum, at different concentrations **[12]**. A Raman spectrum of milk powder was taken as a control. (Figure 5.3) The method of Gordon *et al.* **[13]** was developed for the detection of calcium phosphate, but here it was adapted for brodifacoum detection.

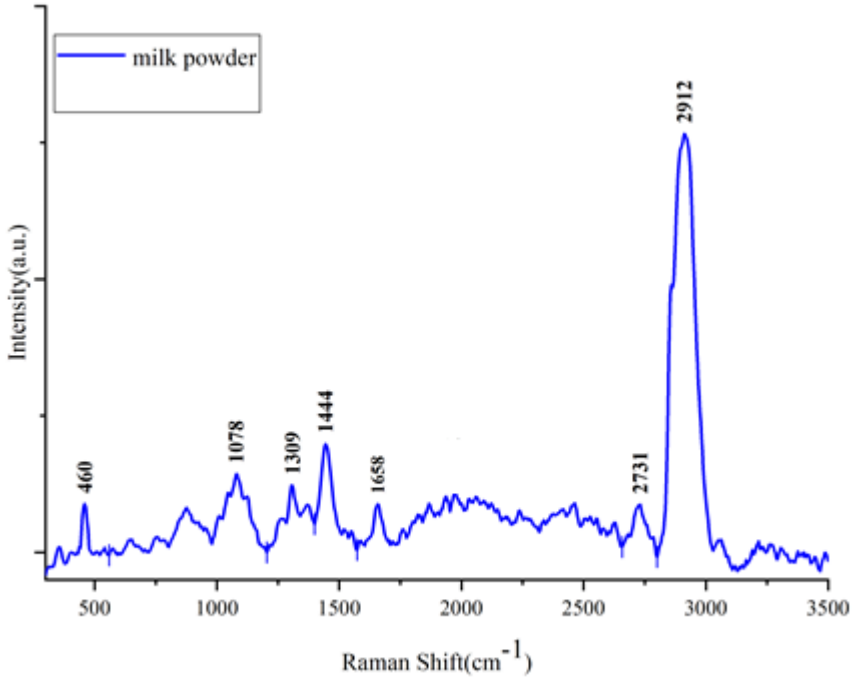

Figure 5. 3: Raman spectra of milk powder acquired at 532 nm excitation wavelength with 40 × *objective, 10 seconds exposure time and four accumulations.*

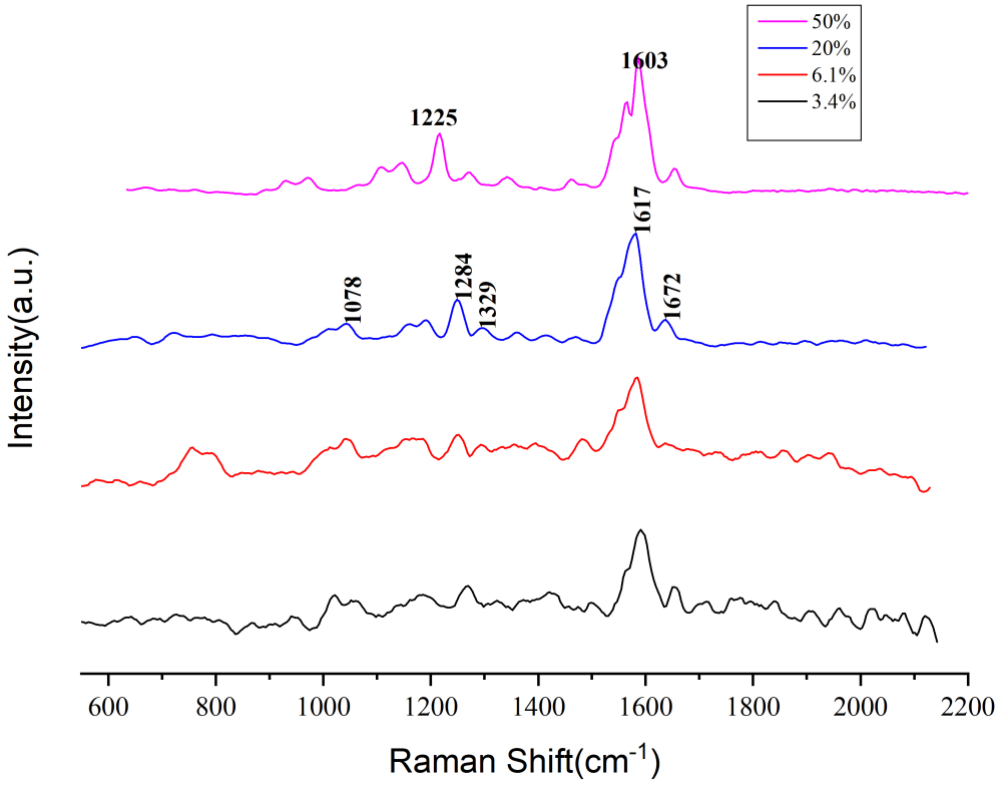

Figure 5. 4: Raman spectra of brodifacoum spiked milk powder at different concentrations (50% to 10% spiked level) acquired at 532 nm excitation wavelength with 40 × *objective, 10 seconds exposure time and four accumulations.*

Spectra of milk powder spiked with brodifacoum show a significant change in Raman spectra of milk powder. The prominent peaks in milk powder are 460, 1078, 1309, 1444, 1656, 2731 and 2912 cm^{-1} that are attributable to proteins, fats, and lactose. The 460 cm^{-1} band is due to milk fats ν(C-H) torsion mode and peaks in the range of 1635-1896 cm^{-1} attributed to the ν(C=O) mode whereas 1078 cm^{-1} attributed to the ν(C-C) indicate an amino acid specific mode and 2731 and 2912 are attributed to C-H stretch belonging to fats or lipids in milk. **[21]** Table 5.2 shows the detailed vibrational assignments of brodifacoum-spiked milk powder.

Table 5. 2: Observed Raman peaks and peak assignments for Milk powder and brodifacoum spiked milk powder

Raman Shift (cm^{-1})	Intensity	Assignments	
460	strong	Lactose	**Milk**
1078	strong	C-C stretching	
1309	medium	C-H_2 twisting	
1444	strong	C-H_2 scissoring	
1603 -1620	strong	C-C stretching	**Brodifacoum**
1635	weak	C=O torsion	
1266	strong	C-O stretch + CCH in-plane bending	
1656	strong	C=C stretch	**Milk**
2731, 2912	strong	C-H stretch	

Figure 5.4 shows the Raman spectra of brodifacoum-spiked milk powder with strongest peak lying in the range of 1603 -1617 cm^{-1} due to ν(C-C) stretching vibrations. There is a shift of 12-15 cm^{-1} in the C-C stretch from 50% w/w concentration of brodifacoum to other concentrations. The reason could be due to the interaction of other constituents in milk to the conjugated brodifacoum rings.

It was observed that there is a shift in the peaks towards the lower wavenumber from brodifacoum in aqueous solution spectra obtained in Chapter – 4 where strongest peak found was at 1644 cm^{-1} and here the band shifts to 1603 cm^{-1} **[22]**. The shift is observed because this is a "normal" Raman spectra without any plasmon enhancement. The

SLIPSERS spectra in Chapter 4 show the plasmon enhanced modes which might be quite different from the modes with inherent Raman intensity. So it might not be band shifts, but changes in band intensity that explains the different appearance of the spectra **[23]**.

There is a good linear relation within the concentration range from 50% w/w to 3.4% w/w, and this can be represented by the linear equation y = 326.3x + 4995.3 with a correlation coefficient of 0.99.

As the concentration of brodifacoum decreased, there was a decrease in the intensity of the Raman peaks too. Figure 5.4 is a clear example of this obvious result.

Performance of the method for brodifacoum was evaluated by taking four calibration standard points against the intensity of brodifacoum in milk peak at 1603 cm^{-1} for quantification. The obtained equation for the calibration curve (Figure 5.5) with measurements is listed below (Table 5.3). The curve gave a linear trend, and the R^2 value is closer to 1. **[14, 15]** Residuals gave the difference between the observed y value and the y value calculated using the equation of a fitted line.

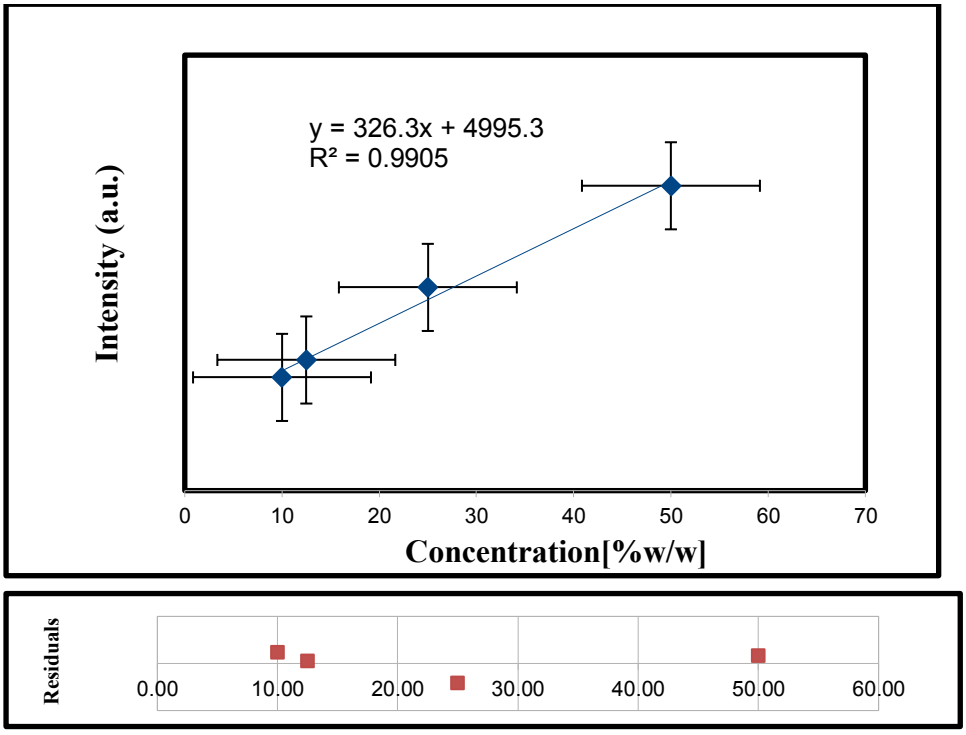

Figure 5. 5: Plot of intensity versus concentration of brodifacoum in milk powder at 1591 cm^{-1} with error bars represents the standard error.

The calibration curve was plotted on intensity against a linear concentration axis whereas in chapter 4, log scale was used. The difference here is that there is no plasmon enhancement, so perhaps plasmon enhancement is somehow responsible for the log scale seen in chapter 4.

Table 5. 3: Statistical data for brodifacoum by Raman method

Parameter	Concentration of brodifacoum (%w/w)
Linear range	3.4-50
Slope	326.34
Intercept	4995.3
Standard deviation (Error) of slope	22.6
Standard deviation (Error) of intercept	658.1
% Error of Slope	6.94%
% Error of Intercept	13.17%
Standard deviation of residuals	5.0%

LOD and LOQ obtained for brodifacoum is 3.4% w/w. The results support the visual inspection for LOD and LOQ.

5.3.2. Experiment 2: SERS detection of brodifacoum in liquid milk and after sample drying.

Initially liquid milk was spiked with high concentration, i.e., 0.1 M of brodifacoum for SERS analysis. Spiked liquid samples were directly added to the cuvette for SERS measurements. Sharp brodifacoum peaks were observed in milk at 0.1 M concentration, but it is quite difficult to detect lower concentrations of brodifacoum. Liquid milk presents further challenges due the complex colloidal nature of milk itself; the obvious optical opacity is due to strong Rayleigh scattering from large colloids in the milk that swamp the much weaker Raman scattering SERS; and the various proteins, fats and

other surface-active components in milk cause aggregation of the silver nanostructures. Several steps would be required to remove all the protein, and fat from the milk matrix to successfully detect analytes in a milk sample. Therefore, it was found that detection of brodifacoum by SERS in liquid milk is limited to high analyte concentration.

Different concentrations of brodifacoum spiked milk samples were prepared and added to the colloid as per the SERS sample preparation protocol. The mixture obtained was dried onto a coverslip at room temperature. Few spectra were collected but no useful SERS signal was obtained, therefore SLIPSERS method was tried.

5.3.4. Experiment 3: SLIPSERS detection of brodifacoum and 1080 in liquid milk after dilution

Extraction of brodifacoum and 1080 from complex milk matrix is quite challenging. Several attempts were made to detect brodifacoum in the presence of the milk components but was unsuccessful, so the next step was to find the simple extraction method to remove components that might be interfering with the SLIPSERS. Ideally the extraction method should be simple and quick, washing with a suitable solvent.

Initially, extraction of fat and other components from milk was done with acetonitrile, but this was unsuccessful. Acetonitrile as the solvent is present in high concentration and has a weak but sufficient affinity for silver (due to the coordinating properties of acetonitrile) **[14]** that presumably displaces the analyte from the surface, thus suppressing resonant enhancement of the rodenticide and so only acetonitrile was prominent on SERS detection. A non-coordinating solvent, methanol, was tried as extraction solvent. **[33, 34]** When milk samples mixed with methanol, SERS detection of liquid sample mixture only shows methanol whereas when dried on SERS substrate, brodifacoum peaks were present but those were not reproducible.

It was observed that on drying the SLIPSERS substrate at 62˚ C the rodenticide spiked milk sample dried to a small yellow pellet, Figure 5.6, which gave no useful SERS signal.

The yellow pellet formed after drying the sample is the non-volatile components of the milk matrix, that completely envelope the silver nanoparticles upon drying, shielding the nanoparticles from the laser source. This demonstrates that matrix molecules are deposit on the substrate blocking the hot-spots of analyte aggregated silver nanoparticles. Therefore, to avoid this problem, based on the observations from Chapter 4 where only concentrations below a critical value gave useful SERS enhancement, diluting the milk samples was considered, before adding silver nanoparticles. As discussed in Chapter 4 even low concentrations (10^{-5} M) of analytes or any other molecules will result in complete coverage of the nanoparticle surface and prevent adhesion of the analyte.

Although diluting the spiked milk will also dilute the analyte concentration, the results from Chapter 4 suggest there is a strong affinity between the analyte and the substrate and that, hopefully, the analyte would successfully compete with the matrix components for binding on the nanoparticle surface.

Milk samples were diluted to avoid the formation of "yellow" aggregates that consists of non-volatile solids from the milk which eventually suppress the hot spots on SERS substrate. Hence, diluting the milk samples to different levels of concentrations, then extracting using methanol: water (3:1) solvent was performed. The entire process took not more than 30 minutes.

Figure 5. 6: non-uniform solid pellet formed after evaporation of undiluted rodenticide spiked milk sample.

2.5 mL of 10^{-3} mol/L brodifacoum and 1080 was used to spike milk to create a spiked milk sample containing 10^{-4} mol/L brodifacoum and 1080. The obtained spiked milk

samples were diluted 8 fold, 80 fold, 200 fold, 800 fold and 1600 fold. Colloidal silver nanoparticles after mixing with milk without dilution gives weak SERS signal. After dilution, samples were deproteinised and defatted with methanol. 50 µL of the supernatant were used to prepare SLIPSERS samples (method as described in Chapter -2) for brodifacoum and 1080 detection **[2]**. Pure milk without an analyte and dilution also went through deproteinization step as a control. SLIPSERS sample of the control was prepared and the spectrum obtained is shown in Figure 5.7.

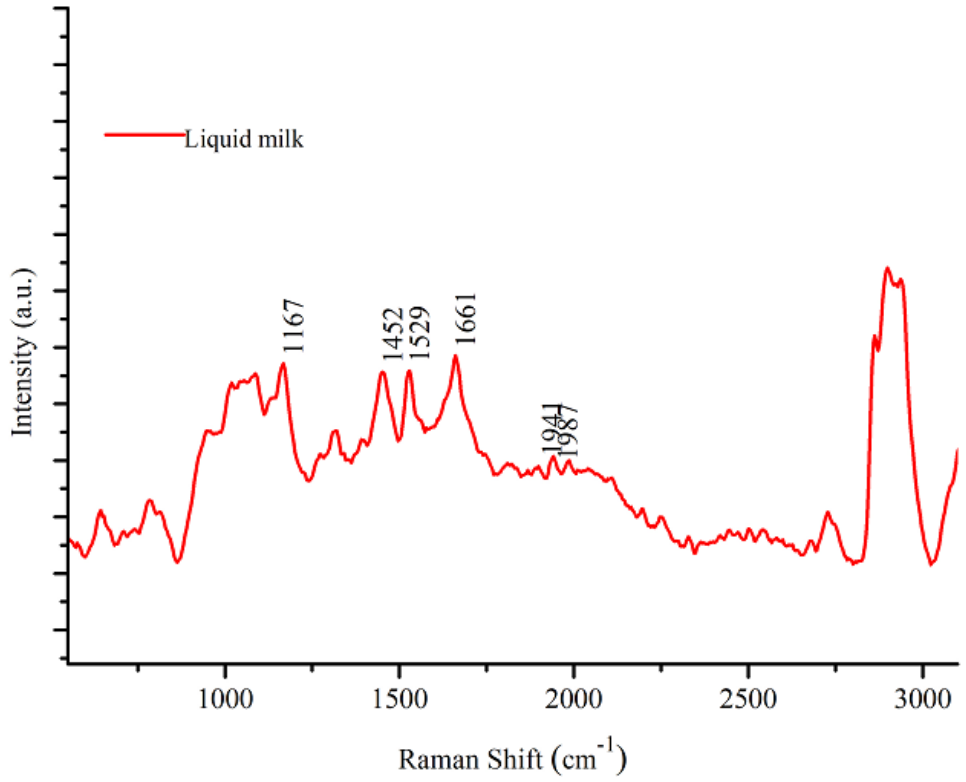

Figure 5. 7: SLIPSERS of liquid milk (control) without brodifacoum acquired at 532 nm excitation wavelength with 40 × *objective, 10 seconds exposure time and three accumulations.*

The prominent peaks observed from SLIPSERS of liquid milk after pre-treatment were mostly milk fats composed of several fatty acids. The peaks at 1167 is due to (C-C) stretch, 1452 (δ(C-H) $_{scissoring}$), 1529 (C=C) stretch due to carotenoids; a natural antioxidant, 1661(ν(C=C)) cis-double bond stretching and 2650 cm^{-1} and 2650 cm^{-1} are symmetric and asymmetric stretching (ν (C-H)) vibrations **[25]**.

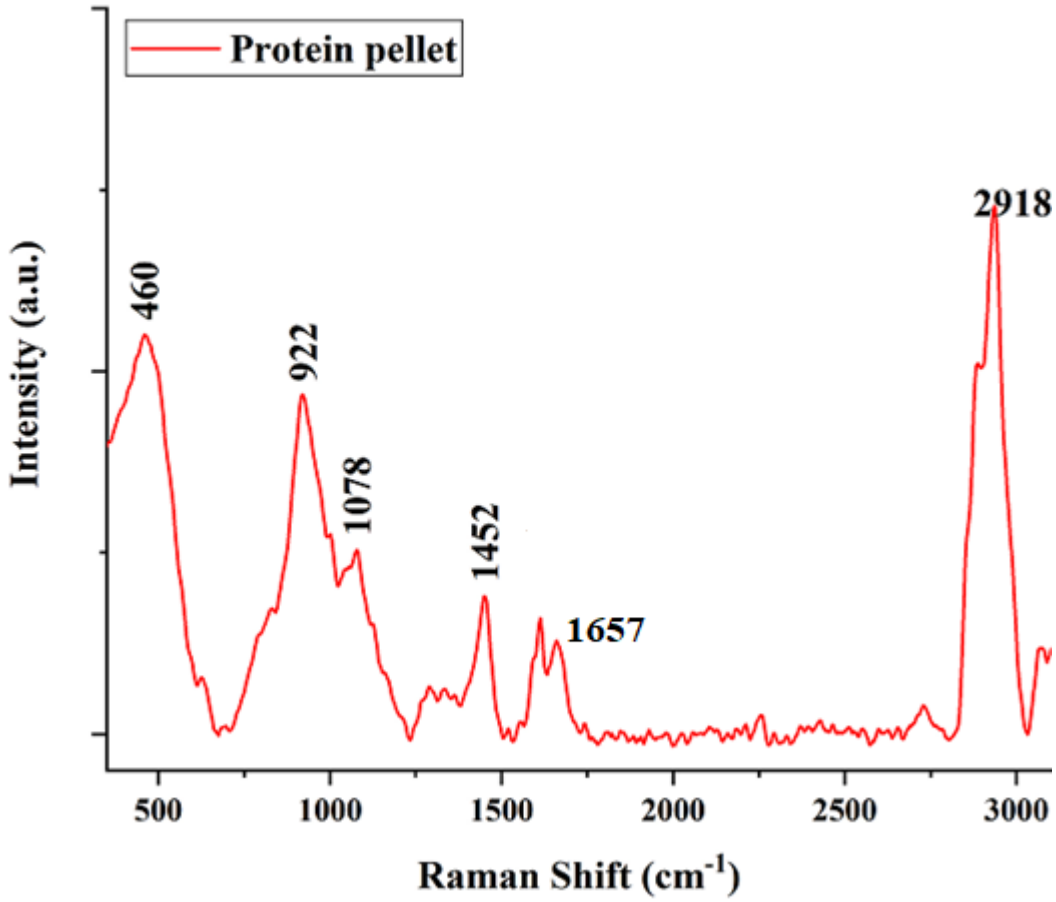

Figure 5. 8: Raman spectra of 10-4 mol/L brodifacoum spiked milk pellet after deproteinisation.

To investigate whether there is any significant amount of analyte partition with protein pellet, 10-4 mol/L brodifacoum spiked milk pellet (after deproteinization) was used for Raman analysis. It was observed that pellet has mostly proteins with unidentifiable traces of brodifacoum. (Figure 5.8) The peaks obtained relate to Raman spectra of solid milk powder (shown in Figure 5.3). On the other hand, supernatant, the clear liquid obtained has significant peaks of brodifacoum which was used further for SLIPSERS measurements.

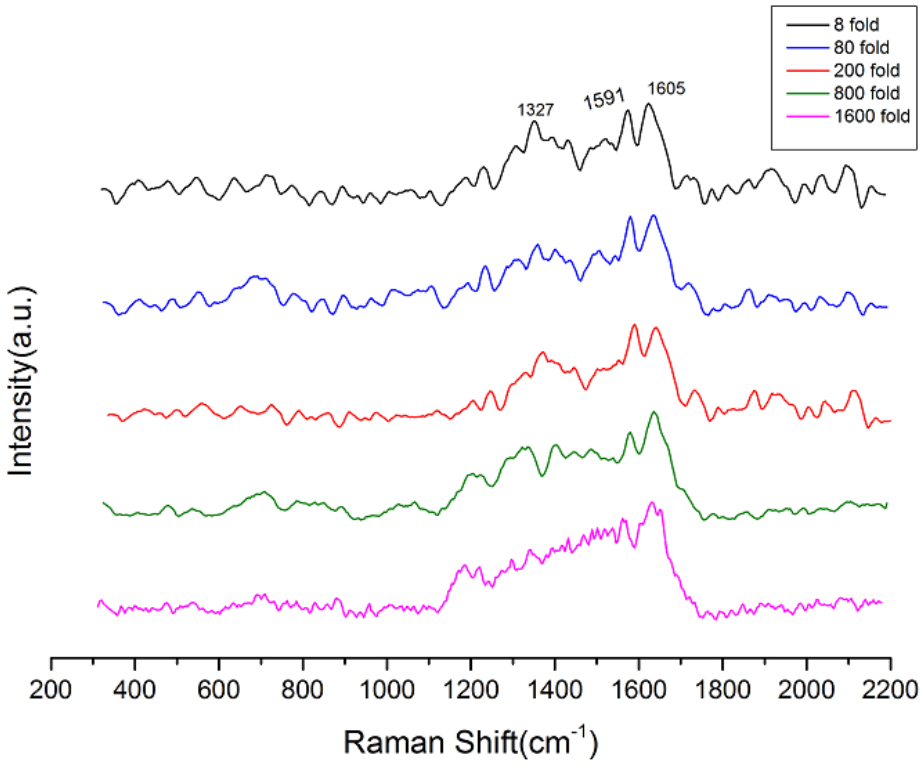

Figure 5. 9: SLIPSERS spectra of brodifacoum spiked milk sample from different dilution levels acquired at 532 nm excitation wavelength with 40 × *objective, 10 seconds exposure time and three accumulations.*

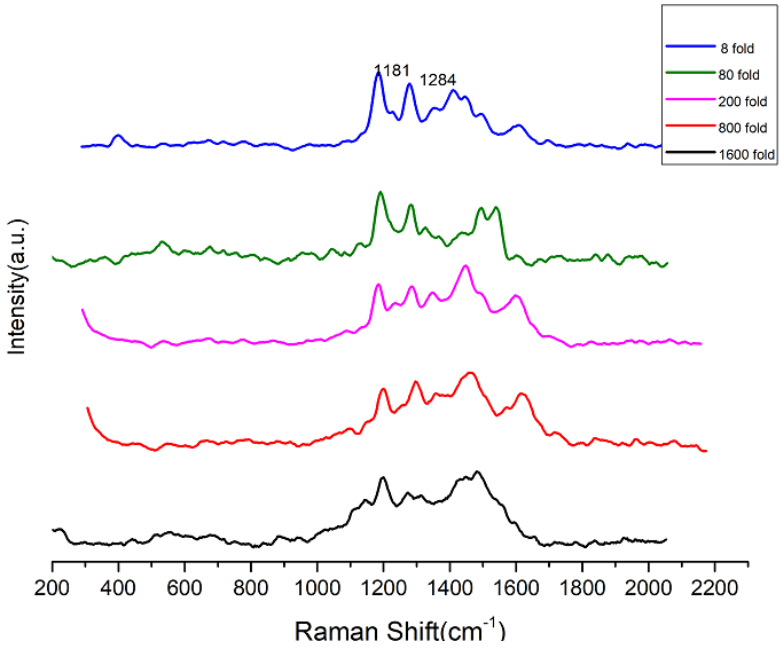

Figure 5. 10: SLIPSERS spectra of 1080 spiked milk sample from different dilution levels acquired at 532 nm excitation wavelength with 40 × *objective, 10 seconds exposure time and three accumulations.*

Figure 5.9 and 5.10 shows the SLIPSERS spectra of brodifacoum and 1080 in diluted milk samples. The major peaks clearly observed in the brodifacoum spectra were 1327, 1591 and 1605 cm-1. The intensity of the rodenticide SERS peaks decreases with increase in dilution level. Brodifacoum peaks become more prominent in the diluted samples (although the signal-to-noise level drops at 1600 x dilution).

Hence, the lowest level of detection (LOD) and quantification (LOQ) of brodifacoum in milk was 6.25×10^{-8} mol L^{-1}. The significant peaks observed in 1080 spectra were 1183, 1284 and 1458 cm-1. In addition, the lowest level of detection found experimentally was also 6.25×10^{-8} mol L^{-1} but 1.25×10^{-7} mol L^{-1} gives an achievable level of quantification.

Again, a different spectrum for brodifacoum spiked in liquid milk was observed compared to the milk powder. The brodifacoum marker Raman band in Figure 5.4 was 1603 cm-1 whereas SLIPSERS spectra of brodifacoum spiked milk demonstrate bands at 1591 and 1605 cm-1. The reason for this could be the different enhancement system **[26]** as both are different states of milk; solid milk powder and liquid milk. Even different Raman spectra of milk powder was found where all lipids and proteins are clearly observed whereas liquid milk SLIPSERS without any rodenticide shows mostly fatty acids bands. Therefore, a shift in Raman bands could be due to different chemical enhancement **[27]**. However, peaks observed in liquid milk SLIPSERS spectra are in agreement with the literature value. Hence, 1591 cm-1 and 1605 cm-1, both were considered as brodifacoum bands. Similarly, 1181 cm-1 and 1284 cm-1 were the prominent peaks found with SLIPSERS spectra of 1080. With the decrease in concentration, a few more peaks were observed in range of 1450 -1600 cm-1 but were not consistent going down the concentration. The reason could be either the rearrangement of negatively charged citrate layer at the surface with decreasing concentrations of cationic analyte, sodium monofluoroacetate or another reason could be the potential for the many and varied milk components to be interfering with the adhesion process at different concentrations. This hinders the effect of adsorption at the colloidal surface and few citrate peaks might interfere the analyte spectra **[31]**.

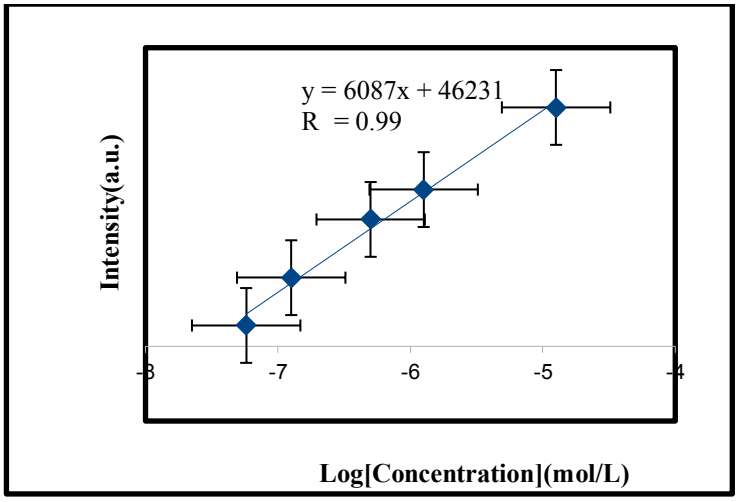

Figure 5. 11: Calibration curve of intensity versus concentration of brodifacoum in milk at 1591 cm-1 with error bars represent the standard error.

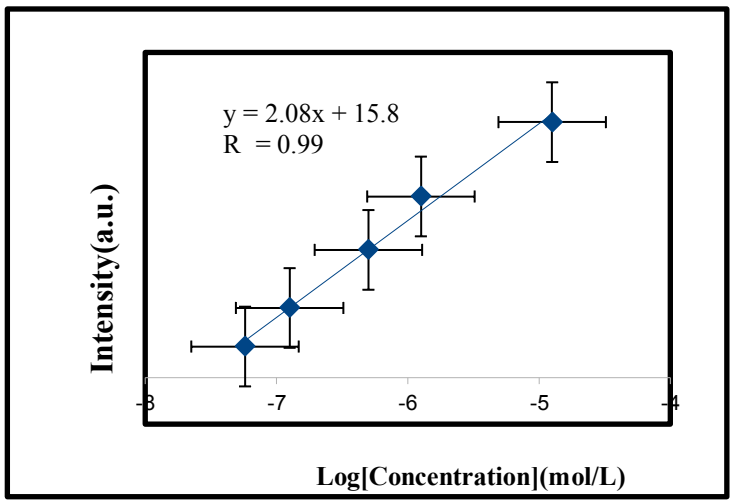

Figure 5. 12: Calibration curve of intensity versus concentration of 1080 in milk at 1181 cm-1 with error bars represent the standard error.

With decreasing analyte concentration, there was decrease in intensity of Raman peaks. Logarithmic transformation of data is quite useful in handling the very low concentration values of wide range and used quite often by researchers for SERS calibration curves. **[28, 32]** The linearity of an analytical method is its ability to elicit test results that are directly related to the concentration of an analyte in the sample within a defined range. **[18, 19]** The linearity for SLIPSERS of brodifacoum was evaluated by taking five calibration standard points against the intensity of brodifacoum. The peak intensity as a function of brodifacoum and 1080 molar concentration is depicted in Figure 5.11 and 5.12 respectively in the range 10^{-4} M–10^{-8} M. A good correlation (R^2 = 0.99) between the intensity of the peak and brodifacoum

and 1080 molar concentration is observed. SLIPSERS peak at 1591 cm^{-1} and 1080 at 1181 cm^{-1} was used for quantification. The parameters from a regression analysis are listed below (Table 5.4).

Table 5. 4: Statistical data for brodifacoum and 1080 in milk samples by Raman method

Parameter	Concentration of brodifacoum (mol/L)	Concentration of brodifacoum (mol/L)
Linear range	$10^{-4} - 10^{-8}$	$10^{-4} - 10^{-8}$
Slope	6.1×10^{4}	2.1
Intercept	4.6×10^{4}	15.8
Standard deviation (Error) of slope (%)	5.71%	5.8%
Standard deviation (Error) of intercept (%)	4.7%	4.8%
Standard deviation of residuals (%)	10.3%	8.8%

Furthermore, to prove the feasibility of SLIPSERS method, the results obtained from the linear equation of each calibration curve are summarized above in Table 5.4. The recovery of residuals for brodifacoum and 1080 in milk ranges from 85-95% with the relative standard deviation between 8-11% **[20]**. The results proved that SLIPSERS method has the potential for ultra-sensitive and fast detection of rodenticide residues in milk.

5.4. Conclusion

Herein, a simple and highly sensitive detection of residues of rodenticides brodifacoum and 1080 in milk, using slippery infused porous surface-enhanced Raman scattering (SLIPSERS) method was presented. This method was combined with a simple pre-

treatment process, which is essential for analyte detection in milk to avoid interferences from complicated constituents in the matrix **[9]**. It was observed that without dilution, the complex matrix suppresses the SERS effect due to weak adsorption of analyte and colloidal surface **[24,31]**. The results obtained indicate that dilution has significantly improved the enhancement by effectively reducing the effect of the matrix. The limit of detection of brodifacoum and 1080 in milk is 6.25×10^{-8}mol/L and for 1080, 1.25×10^{-7} mol/L, gives the possible level of quantification. Compared with traditional methods, SLIPSERS can serve as a universal platform for multiple analytes with rapid detection of even trace amounts of organic analytes such as rodenticides but the disadvantage observed in this study was the possible interference by milk components which hinder SERS detection.

There are several other methods for the analysis of rodenticides in milk but this is the first application of SERS for the detection of 1080 and brodifacoum in milk. This work can be presented as SERS signature for several rodenticides. Successful detection of these analytes in milk allows going further into more complex matrices like biological samples for drug residue detection or similar areas of bioanalytical applications.

References

1. Srivatsan, T. 2014. Practical Raman Spectroscopy: An Introduction: Peter Vandenabeele, Wiley, John & Sons, Incorporated, 2013, 192 Pp., ISBN: 9780470683187. Taylor & Francis.
2. Yang, S., Dai, X., Stogin, B., & Wong, T. (2016) Ultrasensitive surface-enhanced Raman scattering detection common fluids. *Proceedings of the National Academy of Science, 113* (2), 268-273.
3. Cooney, T. P., Varelis, P. & Bendall, J. G. 2016. High-Throughput Quantification of Monofluoroacetate (1080) in Milk as a Response to an Extortion Threat. *Journal of food protection*, 79, 273-281.
4. Eason, C. T., Murphy, E. C., Wright, G. R. & Spurr, E. B. 2002. Assessment of risks of brodifacoum to non-target birds and mammals in New Zealand. *Ecotoxicology*, 11, 35-48.
5. Witkowska, E., Korsak, D., Kowalska, A., Księżopolska-Gocalska, M.,

Niedziółka-Jönsson, J., Roźniecka, E., Michałowicz, W., Albrycht, P., Podrażka, M. & Hołyst, R. 2017, 'Surface-enhanced Raman spectroscopy introduced into the International Standard Organization (ISO) regulations as an alternative method for detection and identification of pathogens in the food industry', *Analytical and bioanalytical chemistry*, vol. 409, no. 6, pp. 1555-67.

6. Álvarez-Ordóñez, A., Prieto, M., Bernardo, A., Hill, C. & López, M. 2012, 'The acid tolerance response of Salmonella spp.: an adaptive strategy to survive in stressful environments prevailing in foods and the host', *Food Research International*, vol. 45, no. 2, pp. 482-92.
7. Jaworska, A., Fornasaro, S., Sergo, V. & Bonifacio, A. 2016, 'Potential of surface enhanced raman spectroscopy (SERS) in therapeutic drug monitoring (TDM). A critical review', *Biosensors*, vol. 6, no. 3, p. 47.
8. Yunker, P. J., Still, T., Lohr, M. A. & Yodh, A. 2011. Suppression of the coffee-ring effect by shape-dependent capillary interactions. *Nature*, 476, 308-311.
9. Lee, P. & Meisel, D. 1982, 'Adsorption and surface-enhanced Raman of dyes on silver and gold sols', *The Journal of Physical Chemistry*, vol. 86, no. 17, pp. 3391-5.
10. Frank, A. J., Cathcart, N., Maly, K. E. & Kitaev, V. 2010. Synthesis of silver nanoprisms with variable size and investigation of their optical properties: a first-year undergraduate experiment exploring plasmonic nanoparticles. *Journal of Chemical Education*, 87, 1098-1101.
11. Bell, S.E. & Sirimuthu, N.M. 2005, 'Surface-enhanced Raman spectroscopy as a probe of competitive binding by anions to citrate-reduced silver colloids', The *Journal of Physical Chemistry A*, vol. 109, no. 33, pp. 7405-10.
12. Smith, G., Gordon, K. & Holroyd, S. 2013. Raman spectroscopic quantification of calcium carbonate in spiked milk powder samples. *Vibrational Spectroscopy,* 67**,** 87-91.
13. Almeida, M. R., Oliveira, K. D. S., Stephani, R. & De Oliveira, L. F. C. 2011. Fourier-transform Raman analysis of milk powder: a potential method for rapid quality screening. *Journal of Raman Spectroscopy,* 42**,** 1548-1552.
14. Chen, Y., Li, X., Yang, M., Yang, L., Han, X., Jiang, X. & Zhao, B. 2017. High sensitive detection of penicillin G residues in milk by surface-enhanced Raman scattering. *Talanta*, 167, 236-241.

15. Giovannozzi, A. M., Rolle, F., Sega, M., Abete, M. C., Marchis, D. & Rossi, A. M. 2014. Rapid and sensitive detection of melamine in milk with gold nanoparticles by Surface Enhanced Raman Scattering. *Food Chemistry*, 159, 250-256.
16. Le Ru, E. C., Grand, J., Sow, I., Somerville, W. R., Etchegoin, P. G., Treguer-Delapierre, M., Charron, G., Felidj, N., Levi, G. & Aubard, J. 2011. A scheme for detecting every single target molecule with surface-enhanced Raman spectroscopy. *Nano letters*, 11, 5013-5019.
17. Le Ru, E.C., Meyer, M. & Etchegoin, P.G. 2006, 'Proof of single-molecule sensitivity in surface enhanced Raman scattering (SERS) by means of a two-analyte technique', *The Journal of physical chemistry B*, vol. 110, no. 4, pp. 1944-8.
18. Hasna, K., Lakshmi, K., Jayaraj, M.K.E., Kumar, K.R. & Matham, M.V. 2016, 'Development of high-sensitive, reproducible colloidal surface-enhanced Raman spectroscopy active substrate using silver nanocubes for potential biosensing applications', *Journal of Nanophotonics*, vol. 10, no. 2, p. 026020.
19. Jiang, T., Li, J., Zhang, L., Wang, B. & Zhou, J. 2014, 'Microwave assisted in situ synthesis of Ag–NaCMC films and their reproducible surface-enhanced Raman scattering signals', *Journal of Alloys and Compounds*, vol. 602, pp. 94-100.
20. Lu, Y., Lu, D., You, R., Liu, J., Huang, L., Su, J. & Feng, S. 2018, 'Diazotization-Coupling Reaction-Based Determination of Tyrosine in Urine Using Ag Nanocubes by Surface-Enhanced Raman Spectroscopy', *Nanomaterials*, vol. 8, no. 6, p. 400.
21. Mcgoverin, C., Clark, A., Holroyd, S. & Gordon, K. 2010. Raman spectroscopic quantification of milk powder constituents. *Analytica Chimica Acta,* 673**,** 26-32.
22. Georgieva, I., Kostova, I., Trendafilova, N., Rastogi, V., Bauer, G. & Kiefer, W. 2006. Raman, FT-IR and DFT studies of ortho, meta and para pyridinomethylene substituted di (4 hydroxy coumarin) and their Ce (III), La (III) and Nd (III) complexes. *Journal of Raman Spectroscopy: An International Journal for Original Work in all Aspects of Raman Spectroscopy, Including Higher Order Processes, and also Brillouin and Rayleigh Scattering,* 37**,** 742-754.

23. Chen, T., Wang, H., Chen, G., Wang, Y., Feng, Y., Teo, W. S., Wu, T. & Chen, H. 2010. Hotspot-induced transformation of surface-enhanced Raman scattering fingerprints. *Acs Nano,* 4**,** 3087-3094.
24. Rajapandiyan, P., Tang, W.-L. & Yang, J. 2015. Rapid detection of melamine in milk liquid and powder by surface-enhanced Raman scattering substrate array. *Food Control,* 56**,** 155-160.
25. El-Abassy, R., Eravuchira, P., Donfack, P., Von Der Kammer, B. & Materny, A. 2011. Fast determination of milk fat content using Raman spectroscopy. *Vibrational Spectroscopy,* 56**,** 3-8.
26. Haynes, C. L., Mcfarland, A. D. & Duyne, R. P. V. 2005. Surface-enhanced Raman spectroscopy. *ACS Publications*.
27. He, L., Liu, Y., Lin, M., Awika, J., Ledoux, D. R., Li, H. & Mustapha, A. 2008. A new approach to measure melamine, cyanuric acid, and melamine cyanurate using surface enhanced Raman spectroscopy coupled with gold nanosubstrates. *Sensing and Instrumentation for Food Quality and Safety,* 2**,** 66-71.
28. Gao, X., Zheng, P., Kasani, S., Wu, S., Yang, F., Lewis, S., Nayeem, S., Engler-Chiurazzi, E. B., Wigginton, J. G. & Simpkins, J. W. 2017. Based Surface-Enhanced Raman Scattering Lateral Flow Strip for Detection of Neuron-Specific Enolase in Blood Plasma. *Analytical chemistry*, 89, 10104-10110.
29. Aktar W, Sengupta D, Chowdhury A. Impact of pesticides use in agriculture: their benefits and hazards. *Interdisciplinary toxicology*. 2009;2(1):1-12.
30. Eason C, Miller A, Ogilvie S, Fairweather A. An updated review of the toxicology and ecotoxicology of sodium fluoroacetate (1080) in relation to its use as a pest control tool in New Zealand. *New Zealand Journal of Ecology*. 2011;35(1):1-20.
31. Munro C, Smith W, Garner M, Clarkson J, White P. Characterization of the surface of a citrate-reduced colloid optimized for use as a substrate for surface-enhanced resonance Raman scattering. *Langmuir*. 1995;11(10):3712-20.
32. Botta R, Rajanikanth A, Bansal C. Silver nanocluster films for glucose sensing by Surface Enhanced Raman Scattering (SERS). *Sensing and bio-sensing research*. 2016; 9:13-6.
33. Tran, B. N., Okoniewski, R., Storm, R., Jansing, R. & Aldous, K. M. 2009. Use of methanol for the efficient extraction and analysis of melamine and cyanuric acid residues in dairy products and pet foods. *Journal of agricultural and food*

chemistry, 58**,** 101-107.

34. Hu, Y., Feng, S., Gao, F., Li-Chan, E. C., Grant, E. & Lu, X. 2015. Detection of melamine in milk using molecularly imprinted polymers–surface enhanced Raman spectroscopy. *Food chemistry,* 176**,** 123-129.

Chapter 6. Highly sensitive surface-enhanced Raman scattering detection of lidocaine hydrochloride in deer velvet antler using silver colloid SERS substrate.

Abstract

This study focused on investigating the detection of lidocaine hydrochloride in antler velvet by surface-enhanced Raman spectroscopy (SERS). The anesthetic drug, lidocaine, is widely used in veterinary procedures and is a matter of concern due to the potential risk for the consumer resulting from the use of lidocaine in food-producing species. A simple and sensitive SERS method along with ultrasensitive and advanced SERS technique called SLIPSERS was employed for residue detection in antler tissue. Selecting the best extraction method for sample clean-up to enhance analyte interaction with silver nanoparticles is very important for successful detection. This can effectively remove all the interferences generated from the compounds in the matrix and provide a highly enhanced SERS signal. Under the optimal conditions, the limit of detection of LHC residues in antler velvet is 0.235 ng/mL, which is lower than obtained from other methods. There is a good linear relationship (R_2 = 0.985) in the concentration range of $10^{-4} - 10^{-9}$ mol/L. By this method, the recovery of LHC residues in antlers ranges from 94% to 100 % with the relative standard deviation less than 10%.

6.1. Introduction

Velvet antlers grow from the pedicle structure of the frontal bone of male cervids. Growing antlers are soft, blood-filled tissue covered by skin with a velvet-like texture. They grow very fast, about 2 cm in a day. These velvet antlers are harvested in most countries where commercial production of deer is a part of the agricultural economy. As per the New Zealand Medical Journal, New Zealand produces 430 million tonnes of deer velvet antler (DVA) and export at a price of $160 per kg. This would generate a value of approximate $46 million. New Zealand exports DVA to China

(~$14 million), and Korea (~$12 million). There is a significant commercial market of velvet antler in China, Russia and Korea where it is used as a Chinese medicine either in form of capsules or liquid form. It has several medicinal applications like it is claimed to improve the immune system, improves athletic performance, increases strength, reduces stress, decreases fatigue, improves sleep and has anti-cancer properties. **[21]**

Lidocaine hydrochloride (LHC) (2-(diethylamino) - N- (2, 6-dimethylphenyl) acetamide hydrochloride), is a water-soluble local anesthetic, used when harvesting velvet antlers. There is concern that harvesting of antlers will introduce drug residues into the antler. Recent research by the European Medicines Agency (EMA) revealed that there are major products containing lidocaine obtained from food producing species due to lack of authorized anesthetics in those species. **[1]** LHC is used as a sterile solution of anesthesia to sheep, goat, horses, cattle and deer prior to surgery. There is no maximum residue limit set for lidocaine

This issue gives the motivation to develop a rapid and sensitive method for detecting LHC. As antlers are processed shortly after harvesting into dietary supplements, immediate action is required to identify whether lidocaine drug residues create any toxicity to humans and animals. Some chromatographic and mass spectrometric methods (GC/MS, LC/MS) have been performed for the determination of LHC in biological fluids and velvet antler. **[1][3] [14][15]** The utilization of these instruments is also not convenient for on-site rapid detection of lidocaine, as the method involves extensive sample preparation and clean-up procedure before running the sample for detection. The limit of detection **[2]** determined for LHC in antlers using LC/MS was 20 ng/g. There has been no such study conducted using surface-enhanced Raman spectroscopy to detect residues of LHC in any biological samples. Literature reveals the use of Raman spectroscopy for detection of lidocaine hydrochloride in saliva to detect overdose of drugs **[26]**, but no study was found for SERS or SLIPSERS. **[22]** Therefore, this work can be presented as SERS and SLIPSERS signature for detection of drugs in several other biological matrices.

The objective of the current study was to compare and detect the drug residues in velvet antler using silver nanoparticles and employing the SLIPSERS method. Hence, this experiment has again utilized less toxic and biocompatible silver nanoparticles for rapid, highly simple and sensitive, cost-effective detection of lidocaine hydrochloride in velvet antler.

For the first time, we have worked on drug screening in antler skeletal remains targeting the residues that can pose toxicity to animals and humans. The SLIPS substrate was prepared as described in chapter 2. An easy clean-up sample extraction technique using perchloric acid followed by methanol was used to obtain a supernatant from the extracted antler velvet, removing any interferent residues like proteins, fats, minerals from the antler velvet. SLIPS and SERS substrates were prepared using the supernatant and spectra obtained were recorded for analysis. To the best of my knowledge this is the first report on detection of LHC in antler velvet using surface-enhanced Raman spectroscopy.

6.2. Experimental

6.2.1. Material and Reagents

For SLIPS preparation all materials and chemicals used were described in Chapter 2. For this study, lidocaine hydrochloride and deer velvet antlers were obtained from the School of Veterinary Sciences, Massey University, New Zealand. 100% pure methanol, chloroform and 60% perchloric acid were used for the extraction method. All solutions were prepared in Milli-Q water having a resistivity of 18 MΩ. All the chemicals were of high analytical grade.

The top hard skin of antlers was removed, and inner soft tissue was minced manually first with a surgical blade to get fine pieces and then further homogenized with a MICCRA D-9 homogenizer (Germany) for two minutes.

6.2.2. LHC extraction methods

Different extraction techniques were adopted to find out the best method compatible with SERS and SLIPSERS. The experimental design adopted is shown in Figure 6.1.

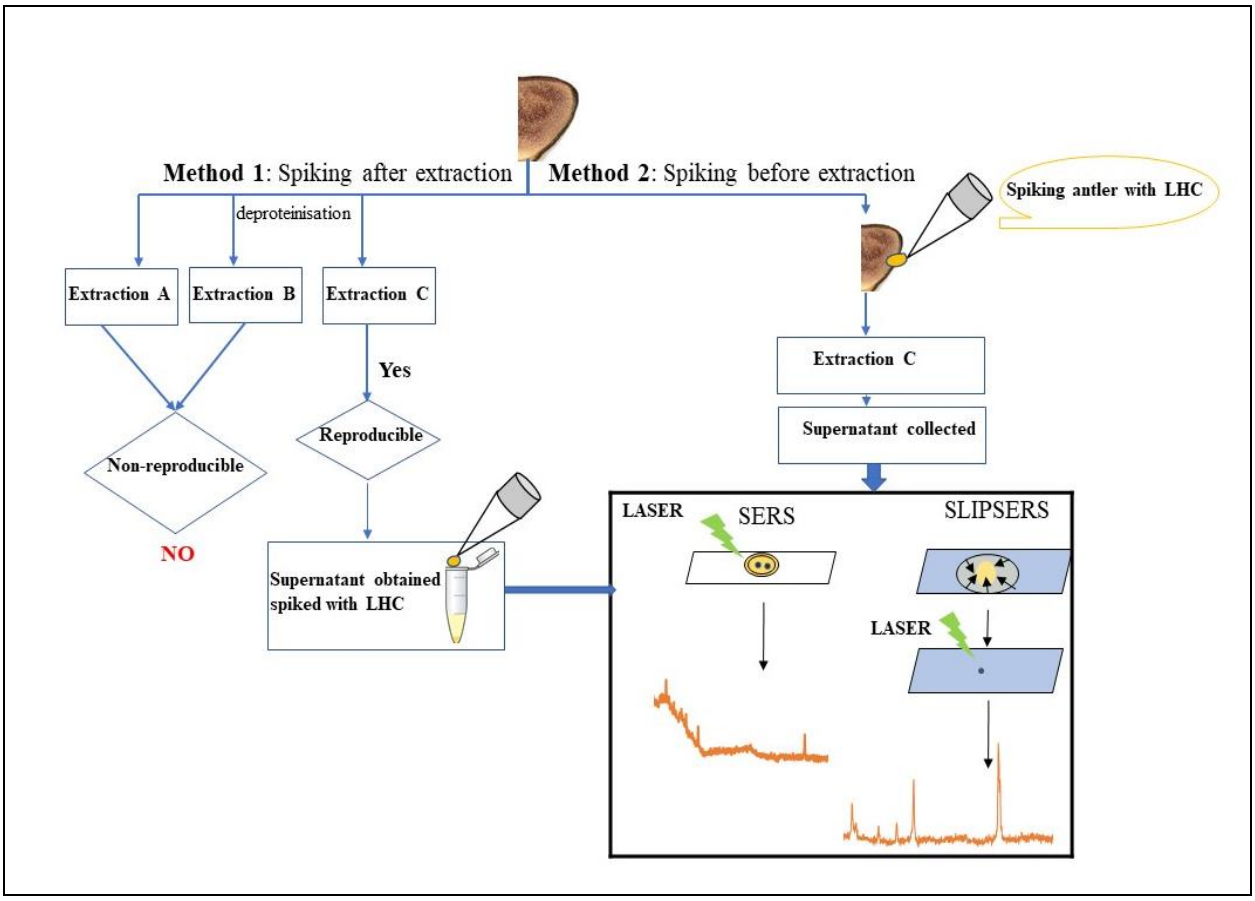

Figure 6. 1: Experimental model with two methods used for SERS and SLIPSERS analysis of LHC in antler velvet.

Antler extract A was prepared according to Eerola et al. **[3]** using 0.4 mol/L cold perchloric acid (PCA) to remove lipids from the sample. PCA is a strong oxidant when heated so using cold PCA digests the antler velvet without damaging the analyte. 1 g antler velvet was weighed and homogenized with 5 mL of 0.4 mol/L perchloric acid for around 2 minutes. The homogenate was left for 30 minutes to digest then it was centrifuged for 10 minutes at 2300 × g and the supernatant obtained was passed through a 0.45 µm syringe filter.

Antler extract B was prepared with some modifications to the Reid et al. **[4]** method. 0.5 g of velvet antler was weighed and homogenized with 2.5 mL of 0.4 mol/L cold perchloric acid for around 2 minutes. The homogenate was left for 30 minutes to digest. 500 µL of borate buffer was added to the homogenate and vortexed for 5 minutes. The mixture was allowed to sit for another 10 minutes and then 500 µL of chloroform: methanol mixture in a ratio 4:1 was added. The mixture

was vortexed again and then centrifuged for 10 minutes at 4200 ×g. The upper layer was extracted and passed through a 0.45 µm syringe filter.

Antler extract C was prepared using the two-step process - cold perchloric acid followed by methanol. 0.5 g of velvet antler was weighed and homogenized with 2.5 mL of 0.4 mol/L perchloric acid for around 2 minutes. The homogenate was left undisturbed for 30 minutes to digest and briefly vortexed for 1 minute. It was then centrifuged for 10 minutes at 2300 × g and the supernatant obtained was passed through a 0.45 µm syringe filter.

At the second stage, the filtrate obtained was further cleaned using methanol to remove any protein present. 1 mL of supernatant was mixed with 2.5 mL of pure methanol, sonicated at 10% amplitude for 5 minutes and then centrifuged for 10 minutes at 2300 × g and the supernatant obtained was again passed through a 0.45 µm syringe filter.

6.2.3. Sample preparation for SERS and SLIPSERS measurements

Two procedures were employed for SERS and SLIPSERS analysis –

- ***spiking LHC after extraction*** to isolate the effect of matrix on the binding process and
- ***spiking LHC before extraction*** to simulate a real sample with LHC present in deer antler.

The procedure for spiking after extraction is described below. The purpose of spiking after extraction was to determine if the LHC was being lost during extraction or if components in the supernatant were interfering with the binding of LHC on the silver nanoparticle surface. Both of these effects would result in reduced LHC signal in the SLIPSERS measurements. However, by measuring only samples that were spiked before extraction it would be difficult to isolate the two effects. Therefore, spiking after extraction was suggested as a method to investigate negative interactions with the LHC and the supernatant.

For spiking the velvet antler before the start of the extraction procedure, a specific volume of known concentration of LHC was added to 0.5 g of minced antler, allowed to sit for an hour to digest inside the tissue, and then extracted as per the procedure mentioned above to get the final

filtered supernatant. Finally, Kitaev nanoparticles and the supernatant was used for SERS and SLIPSERS measurements.

Kitaev silver colloid **[22]** was prepared as described in Chapter 2. To avoid any sample degradation of biological samples, deer velvet antler (DVA) was kept at 4 °C and brought to room temperature before use. The colloid was vortexed for 20 seconds to remove any sedimentation. 0.01 mol/L $MgSO_4$ was used as an aggregating agent.

A stock solution of lidocaine hydrochloride 0.01 mol/L was prepared in Milli - Q water. Then, lidocaine hydrochloride aqueous solutions in a concentration range of 1×10^{-4} - 1×10^{-9} mol/L were prepared.

Two separate mixtures were prepared with supernatant obtained from spiking *after extraction*.

Mixture A - LHC Spiked Extract: For spiking the supernatant with LHC, 6 µL of different concentrations of LHC were added to 20 µL of velvet tissue extract, vortexed for 30 seconds and allowed to sit for 10 minutes for complete digestion.

Mixture B – Aggregated colloid: 0.5 µL of 0.01mol/L $MgSO_4$ was added to 20 µL of silver colloid and again vortexed for 30 seconds.

Then, 4 µL of mixture A was added to mixture B and vortexed again for 30 seconds. 2 µL of this final sample prepared was pipetted onto the quartz coverslip and allowed to dry at room temperature. Once dried, the sample slide was used for recording SERS measurements.

For SLIPSERS, the same procedure was followed as described in Chapter 2 **[5]**. In previous work for preparing the SLIPSERS substrate, 50 µL of an analyte and 10 µL of colloidal solution was used to get a SLIPSERS aggregate but here, the volume of colloid used was increased. It was assumed that the extract has several components, due to its biological nature, that block the nanoparticle surfaces and result in formation of a gel like aggregate which gives no SERS. Therefore, the 4 µL of velvet extract - LHC solution mixture, 20 µL of silver colloid and 0.5 µL of 0.01mol/L $MgSO_4$ was added onto the SLIPS substrate. The final aggregate was used for SLIPSERS analysis.

6.2.4. Instrumentation

All SERS and SLIPSERS spectra were taken on an in-house Raman spectrometer based on a Princeton Instruments FERGIE spectrometer using 532 nm excitation wavelength (with 2 mW laser power) focused onto the sample using a 40 × 0.65 NA objective.

Quartz coverslips were used for SERS analysis as it produces very low Raman background as compared to common glass slides. UV-Vis spectra were acquired with a Shimadzu1800. Using Origin 8.5 Software (Origin Lab Corporation, Northampton, MA, USA) baseline correction and 5-point Savitzky-Golay averaging smoothing algorithm was performed on all spectra to reduce the baseline variability between 500 cm^{-1} to 2000 cm^{-1}

6.3. Results and Discussion

6.3.1. Characterisation of silver nanoparticles with velvet antler extract

SERS and SLIPSERS substrates spiked with LHC were characterised by SEM and the obtained images are reported in Figure 6.2 below.

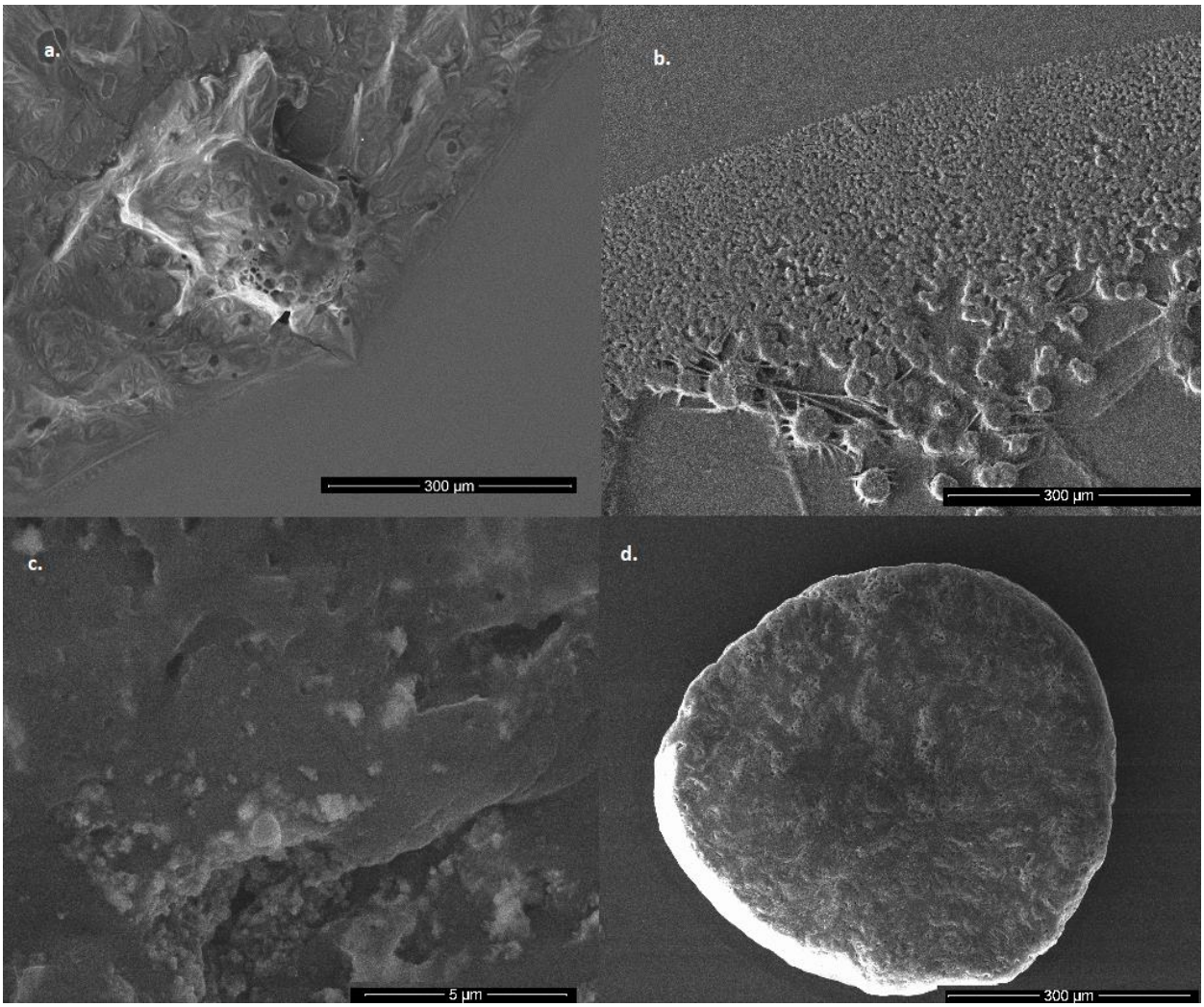

Figure 6. 2: SERS and SLIPSERS substrates for LHC analysis a) blank (just the antler extract without drug and nanoparticles b) 10^{-7}mol/L LHC spiked antler extract on SERS substrate and c, d) 10^{-7}mol/L LHC spiked antler extract on SLIPS substrate at low and high magnification scale of 5 µm and 300 µm under scanning electron microscope.

SEM images show the interaction of aggregated nanoparticle with a drug on SERS and SLIPSERS substrate. SEM image of blank refers to antler extract without lidocaine and nanoparticles as seen in Figure 6.2(a) looked like an amorphous matrix as expected from the biological extract on the coverslip. After extraction and spiking with LHC, SERS substrate in Figure 6.2(b) shows fractal growth giving a reasonable number of hot spots in the large meshy surface **[18, 19]**. This is the famous coffee ring effect. The pinned contact line running down from the top right corner was observed and noticed how the scale of the fractal changes as we move away from the contact line.

The synergic effect of nanoparticles with aggregating agent leads to the dense layer formation of nanoparticles with the drug on the surface that increases hot spots for analysis. This dense structure (Figure 6.2(b)) looks with some fibres stretching from the pores and highly concentrated form of micrometer size. The analyte matrix looks completely adsorbed on silver nanoparticle surface forming a flat layer

(Figure 6.2(c)) SLIPS substrate has an advantage of getting 100% analyte concentrated to one tiny aggregate, which looks like the image in Figure 6.2(d). which is the perfect example of a SLIPSERS aggregate. The different scales of aggregates mean different fractal formation again. Although, these are not individual silver nanoparticles but clear aggregates of nanoparticles.

It was also observed while spiking the colloidal solution with LHC that the yellow Kitaev silver colloid changes to a red-brown colour which is due to interaction with the extract components. **[8]** A dense aggregate was formed, and presumably, due to the drying process, the analyte adhered to the silver colloid surface. This colour change was used as an easy and selective method of determination of aggregation and binding of the drug with analyte extract.

6.3.2. UV-Vis spectrophotometry

UV-Vis spectrometry was used to investigate the effect of LHC on silver nanoparticles. UV-Vis spectrum as shown in Figure 6.3, display that the addition of LHC causes a substantial red-shift of the plasmon absorbance peak.

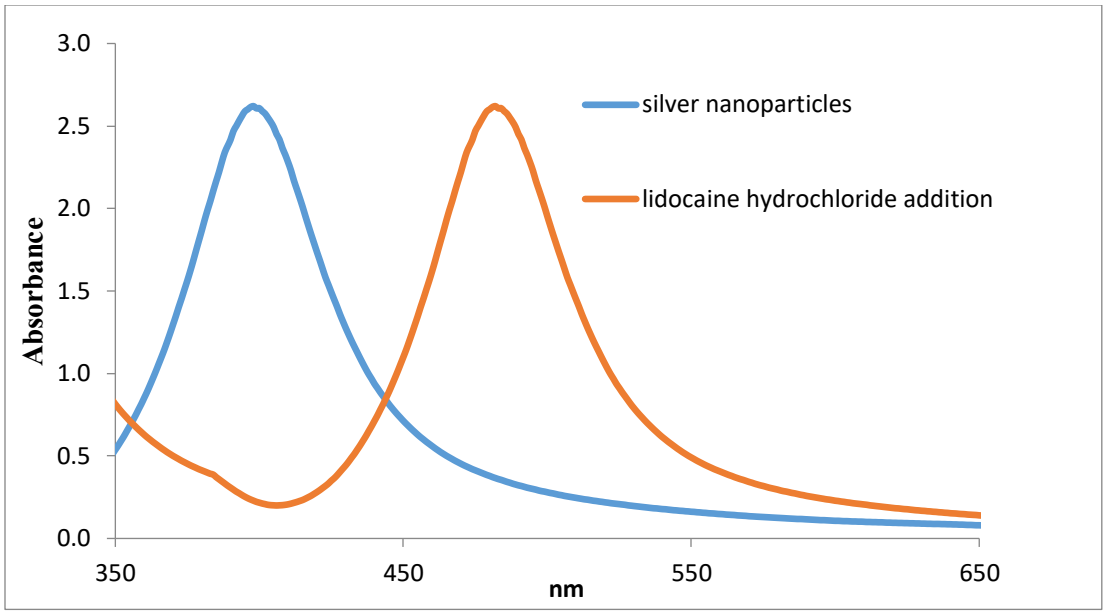

Figure 6. 3: UV-vis spectra of silver nanoparticles before and after addition of 0.1M-lidocaine hydrochloride.

As mentioned in Chapter -1, SERS relies on resonance with the electronic transitions of the system. The UV-Vis spectrum shows that LHC addition shifts the plasmon resonance due to modifying aggregation. This could be due to a decrease in the inter-particle distance between nanoparticles resulted in a change in colour from yellow to red and shifting to a higher wavelength **[8, 11],** or a change in the refractive index of the medium due to the extract components, or most likely, a combination of both effects. This might suggest that the optimum wavelength for SERS might have also shifted from 532 nm to a longer wavelength. This red shift is also observed visually as yellow nanoparticle colour changed to red after the addition of lidocaine.

6.3.3. Mechanism of LHC binding with silver nanoparticles

Lidocaine hydrochloride's amide group has a lone pair of electrons that can easily interact through H - bonding with carboxy group (-COO) group of citrate ion as shown in Figure 6.4. This results in aggregation of citrate-stabilized silver colloids on the addition of LHC creating a redshift. **[8]**

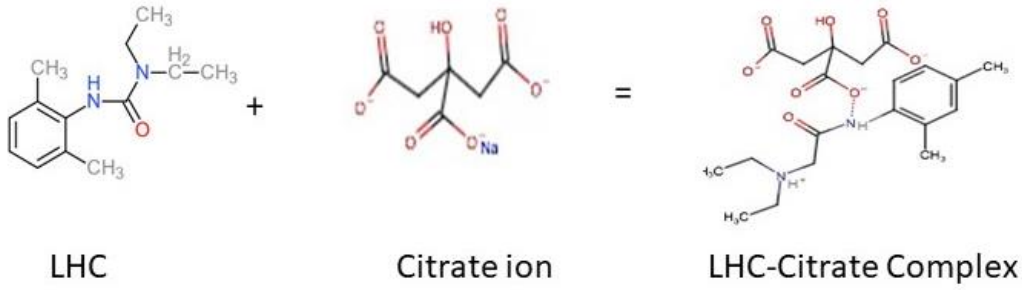

Figure 6. 4: Mechanism of interaction of lidocaine hydrochloride with silver nanoparticles

6.3.4. Selection of laser excitation wavelength using normal Raman measurements.

The excitation wavelength should be selected to optimize the SERS intensity. In practice, this is difficult because lasers have fixed, discrete wavelengths, but, at least, the intensity of the SERS signal should be investigated at a wavelength that is different to our 'standard' wavelength of 532 nm (that we assume is the best choice). 785 nm was selected as an alternative wavelength to investigate any resonance effects.

Figure 6.5 and 6.6 presents the Raman spectrum of solid LHC at 532 nm and 785 nm excitation wavelength and Figure 6.7 presents the Raman spectrum 10^{-6} mol/L LHC at 532 nm excitation wavelength.

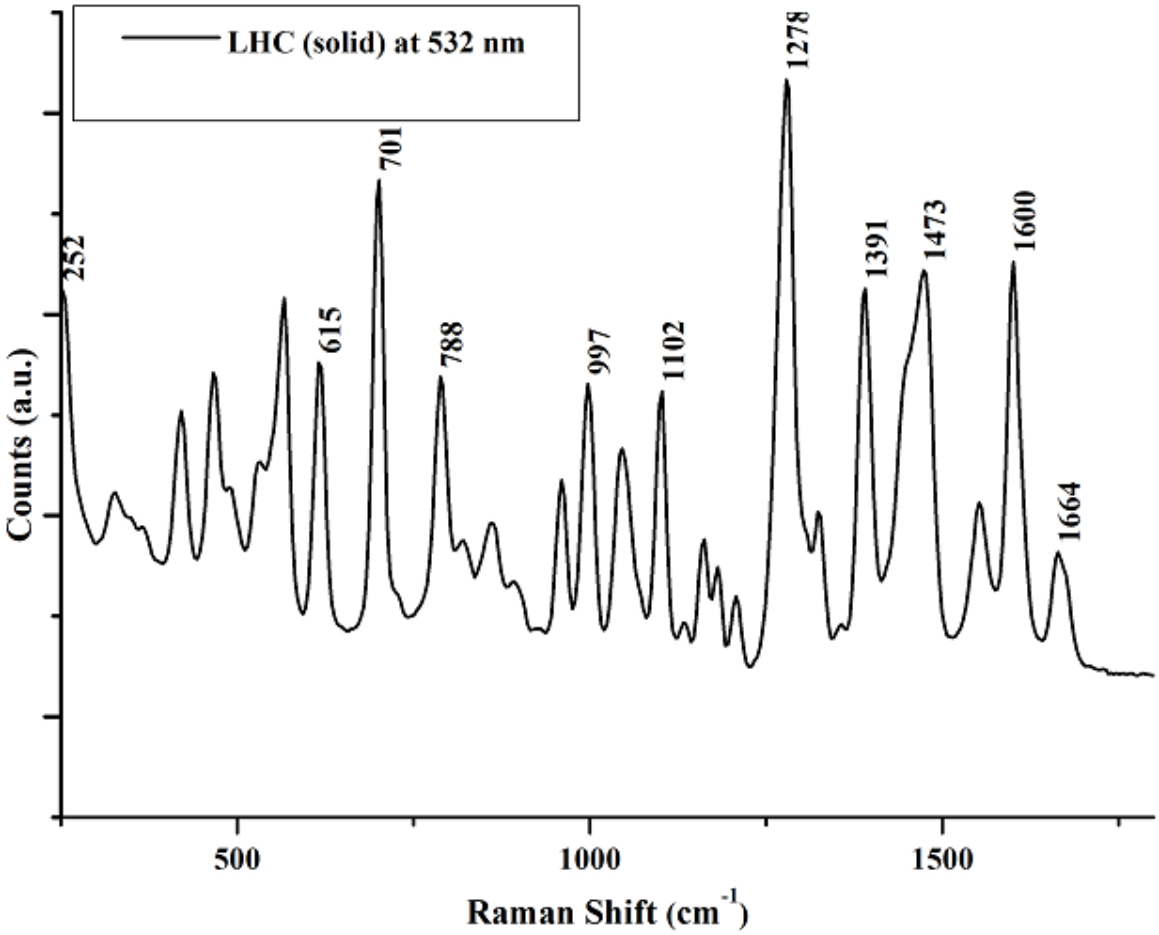

Figure 6. 5: Raman spectrum of solid lidocaine hydrochloride acquired at 532 nm excitation wavelength with 40 × objective, laser power 8mW for 10 seconds exposure time and three accumulations.

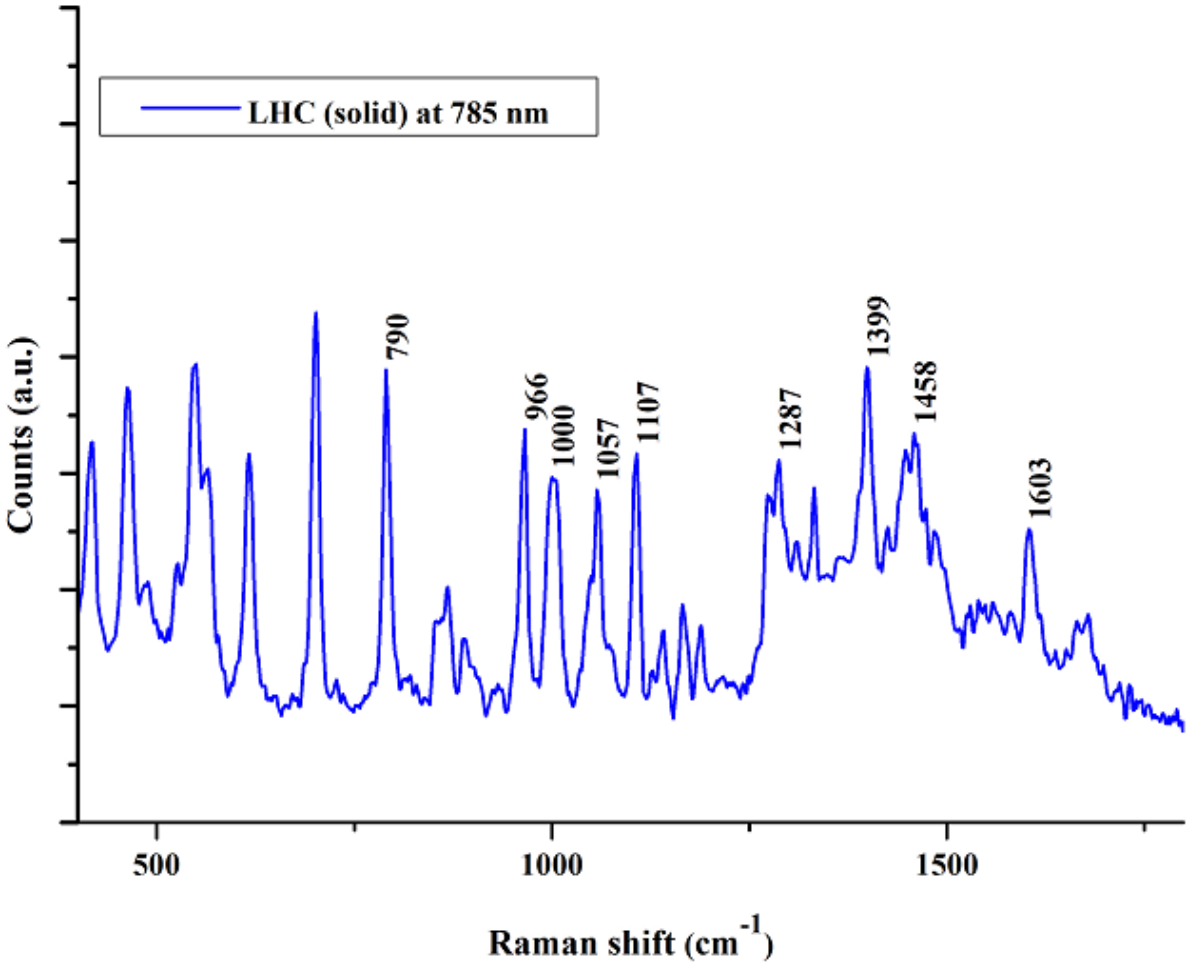

Figure 6. 6: Raman spectrum of solid lidocaine hydrochloride acquired at 785 nm excitation wavelength with 40 × objective, laser power 8mW for 10 seconds exposure time and three accumulations.

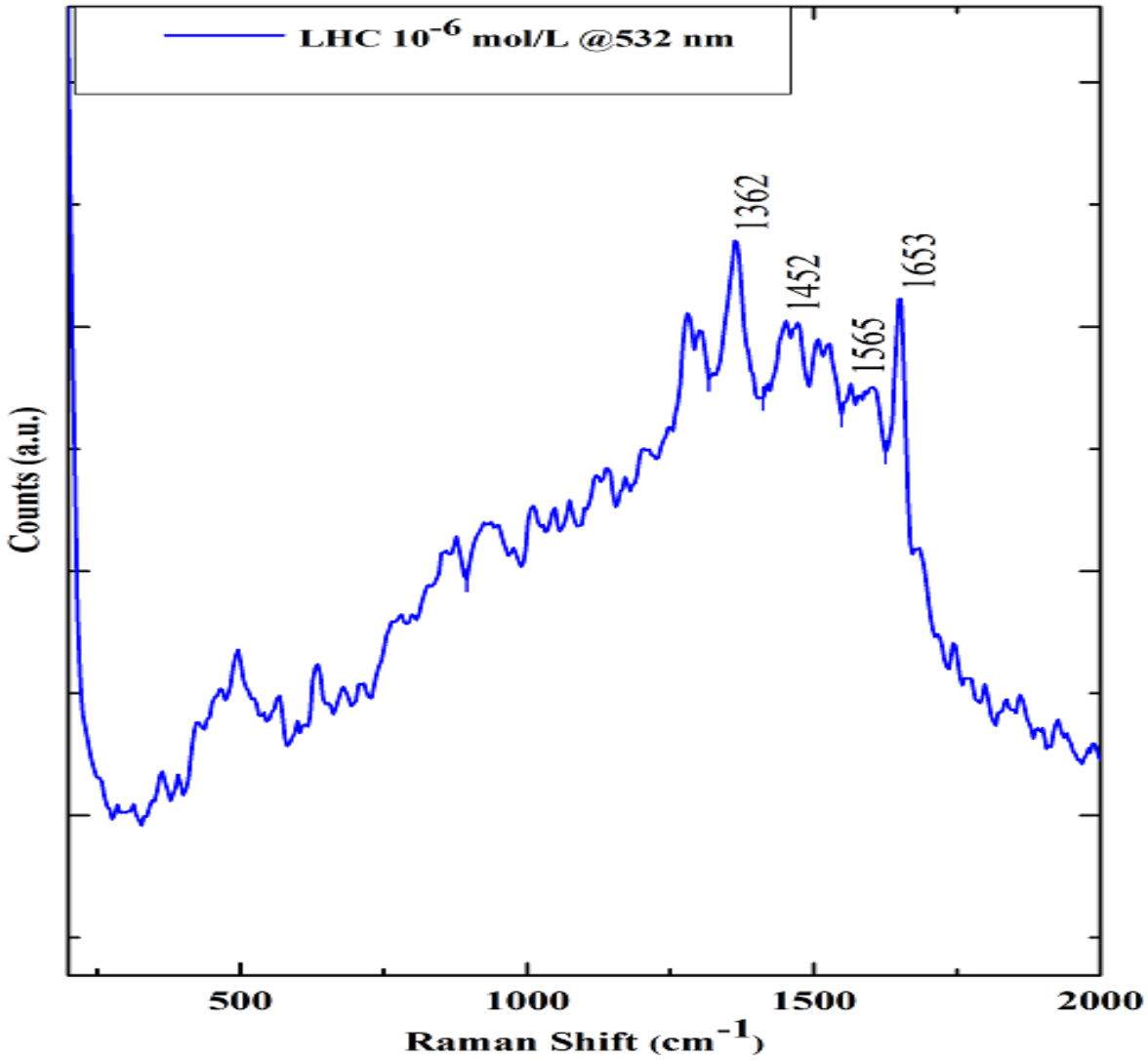

Figure 6. 7: Raman spectrum of 10-6 mol/L lidocaine hydrochloride solution acquired at 532 nm excitation wavelength with 40 × objective, laser power 8 mW for 10 seconds exposure time and three accumulations.

The first part of the study was to investigate the spectral signatures of lidocaine hydrochloride salt and aqueous solution at the different excitation wavelength. This enables us to identify the prominent Raman bands of LHC with SERS and SLIPSERS substrate. The characteristic Raman bands with vibrational assignments are presented in Table 6.1 based on Ref. **[23]**.

Table 6. 1: Observed Raman peaks and peak assignments for lidocaine hydrochloride

Raman Shift(cm^{-1})	Intensity	Assignments
252	very strong	ortho-CC wag
460	strong	ortho-CC bend; CH_2 rock
610	very strong	NCO wag
701	very strong	HNC wag
788	strong	HNC wag, ring torsional deformation
997	strong	CH_2 rock, CH wag
1047	medium	methyl rock
1102	strong	methyl rock, CH2 twist
1278	strong	meta-CH bend, ortho-CC symmetric stretching, amide NH stretching, CC stretching
1391	very strong	CH_2 wag
1473	very strong	Methyl anti-symmetric deformation
1600	medium	HNC scissor deformation, NC amide stretching, methyl antisymmetric deformation
1664	very strong	C=O stretching, HNC scissor deformation

A minor shift in peaks was observed while acquiring Raman spectrum of solid lidocaine hydrochloride using 532 and 785 nm excitation wavelength (the spectrometer resolution is approximately 3 – 4 cm^{-1} for each system) but still are in good agreement with the literature. The 532 nm laser and detection system have better throughput. The dependence on excitation wavelength for normal Raman scattering is due mostly to the absolute Raman intensity being

proportional to λ^{-4}, so $\frac{I_{532}}{I_{785}} \propto \frac{785^4}{532^4} = 4.74$. This explains the improved signal-to-noise level in the 532 nm spectrum compared to 785 nm. Only a few prominent peaks were observed for the 10^{-6} mol/L aqueous solution of LHC, although, in the absence of any resonance enhancement this is a reasonably good signal-to-noise level for a solution with μM concentration. Therefore, it was assumed with high confidence that enhancement is coming from the absorption spectrum. As stated in Chapter 1 that Raman enhancement is proportional to the absorption cross-section.

So, from Figure 6.3, it was found that the absorbance at 785 nm is negligible, so no enhancement was expected at 785 nm, therefore, 532 nm excitation wavelength is selected for quantitative analysis of spiked lidocaine in antler extract.

A SERS spectrum of silver colloid is shown in Figure 6.8. which shows some broad bands that are probably citrate bands or look similar to the background observed in the line scan data due to some carbonization of the citrate on the dried colloid. This produces some graphitic carbon, but these bands are displaced by LHC. This serves as a good background for analyte identification and quantification. SERS spectra of LHC aqueous solution with silver colloid without any antler extract has prominent lidocaine peaks at 613, 772, 1271, 1354 and 1647 cm^{-1} attributed to CNC ring, and amide modes, respectively.

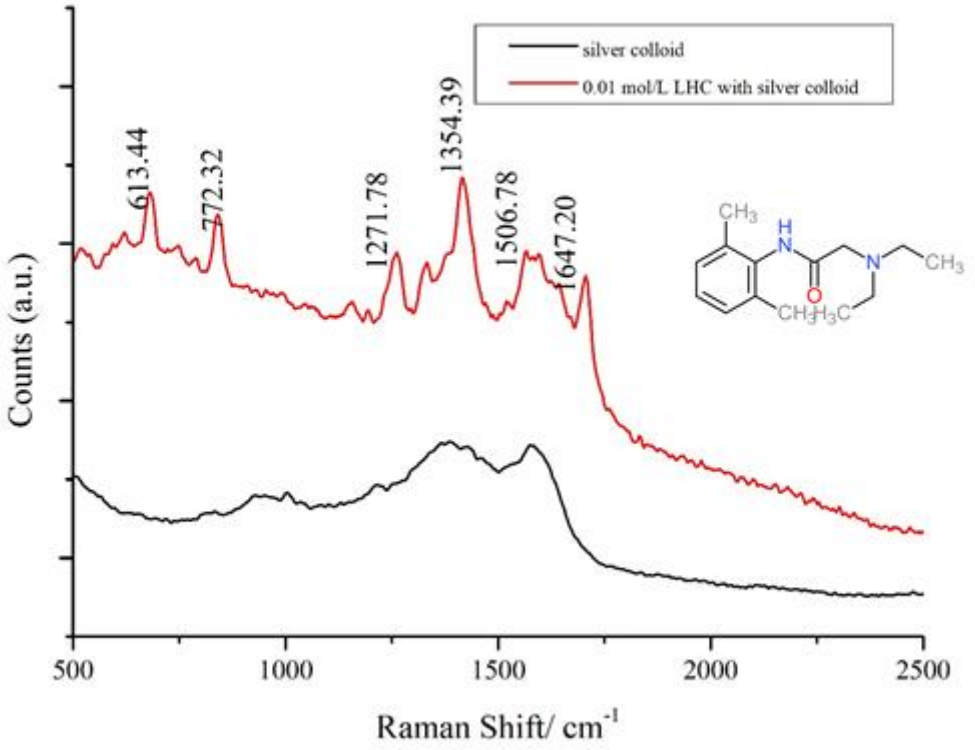

Figure 6. 8: SERS spectrum of dried Kitaev silver colloid and SERS spectra of 0.01M LHC with silver colloid acquired at 532 nm excitation wavelength with 40 × objective, 10 seconds exposure time and three accumulations.

6.3.5. Optimisation of sample extraction technique

To select the best extraction technique, the SERS spectra for samples obtained with each of the extraction methods as described in section 6.2.2 were investigated.

Figure 6.9 presents the Raman spectra of the blank (extract without LHC), and the SERS spectra of different concentrations of LHC spiked in extract A, extract B and extract C.

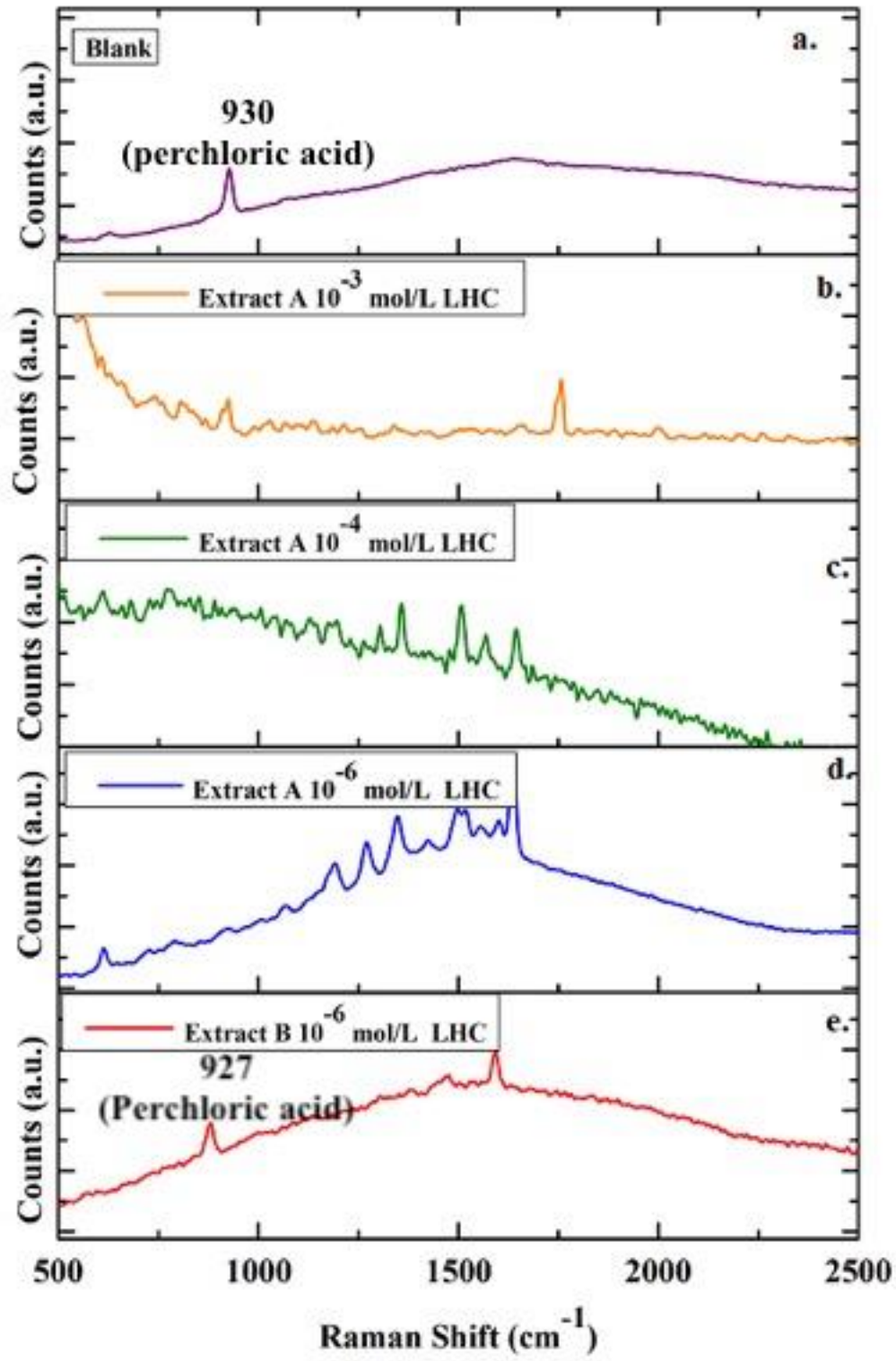

Figure 6. 9: a) Raman spectra of extracted deer antler without lidocaine(blank), spectral variations observed in SERS spectra of antler extract A spiked with different concentrations b)10^{-3} mol/L, c) 10^{-4} mol/L and d) 10^{-6} mol/L and e) extract B with 10^{-6} mol/L LHC concentration acquired at 532 nm excitation wavelength with laser power of 2 mW.

Extraction Method A: Perchloric acid (PCA) precipitation is one of the most widely used deproteinisation technique to remove most of the protein from the sample prior to analysis. **[8, 27]** Extraction using only perchloric acid produced variations between replicates and between samples with different LHC concentration. This leads to low reproducibility. It was observed in Figure 6.9, for extract A, the highest concentration (10^{-3} mol/L) gives the weakest SERS signal; the lower the concentration (10^{-6} mol/L), the more enhanced are the SERS bands. As explained in Chapter 4, this is because the analyte can completely cover the aggregate at higher concentrations blocking the surface-active sites and reducing SERS intensity. At lower concentration of analyte either there are more binding sites than molecules, or the analyte does not form a layer that scatters the radiation away from the colloid surface. Even the liquid SERS samples did not show any analyte peaks just perchloric acid was prominent throughout. **[8]** The sample did not dry into a tight aggregate on instead it formed a jelly-like aggregate that appeared to melt under laser excitation.

Extraction Method B: The chloroform-methanol solvent extraction is another common extraction technique for removing protein and hydrophilic metabolites **[9]** but didn't work for LHC detection as bands from blank were prominent without giving any analyte signal. This is due to interferences from other components in the antler extract that compete for binding sites with LHC on the colloid surfaces and reduce SERS. It is not always that other components in the matrix could reduce SERS, sometimes the most intense SERS bands come from these components and gives false classification of analyte.

Extraction Method C: A combination of perchloric acid and methanol was used for Method C. Polar organic solvents such as methanol are typically mixed with water to extract hydrophilic metabolites and lipids. **[28]** Methanol is a simple solvent for extraction, which provides a consistent background by cleaning lipids from the matrix. PCA precipitation for deproteinisation followed by methanol extraction for purification was successful for LHC detection and removing the interfering compounds from the matrix. This combination resulted in high reproducibility and sensitivity for detection of lidocaine hydrochloride. Thus, analyzing the sample before and after extraction provides a measure of how the SERS signal and reproducibility is improved by the extraction procedure. The spectral evidence of using this extraction technique is shown in Figures 6.11, 6.12 and 6.13.

6.3.6. Factors that affect SERS analysis of the sample

Some of the factors that influence SERS and SLIPSERS signal were considered in this study.

First, the volume of extract and nanoparticles for SLIPSERS plays an important role in the enhancement of signal. With SERS, the drying process bears no difficulty as it forms the usual coffee-ring like structure whereas for, SLIPS substrate, the problem of a gel-like aggregate created difficulty in detection. The need for modification in volumes was visible while pipetting the extract drop onto the SLIPS substrate. The drop was completely wetting the substrate suggesting that the matrix has components that were lowering the surface tension and preventing the formation of a tight aggregate on the surface (Figure 6.10). After some trial and error, a tight aggregate was formed by increasing the colloid volume and decreasing the analyte volume. This effectively lowered the concentration of the components that were causing wetting of the substrate. 20 µL of colloid and 4 µL of velvet antler extract was used for making the desired SLIPS substrate with aggregate drying in highly concentrated form to a tiny solid dot.

Figure 6. 10: Bead formation for SLIPS aggregate

Second, interference from the other components in the biological sample can also affect the enhancement of the signal. The presence of these contaminants on the nanoparticle surface has three consequences:

(1) the other components may hinder the adsorption of the molecules of interest at the surface which hinder the formation of tiny aggregate for SLIPS and weakens the detection signal;

(2) the SERS signals generated by other components from biological matrix will also interfere with the signals of target molecules and even overwhelm the detected signal;

(3) the decomposition of the other components induced by the thermal effect because of plasmon excitation during the SERS measurement can result in the signal of amorphous carbon, which produces peaks that will overwhelm the SERS signals from analytes even if the analytes themselves do not decompose.

These interfering signals from impurities make it difficult to identify the target molecules, and methods are required to remove these components. Extraction method C was found to effectively remove the majority of the components of the biological matrix

Third, controlling the interaction of SERS with biological environment of an analyte**.** The biological system is very complex. When such fabricated nanostructures are exposed to biological environments such as antler tissues, in this case, the performance of the nanomaterial changed due to unknown physical, chemical phenomena that can be due to aggregation, absorption at random sites of biological matrix. In this case, the interaction between nanomaterial and biological systems must be nicely controlled before bioanalytical SERS can become a practical and reliable analysis technique**. [7]**

Lastly, fluctuations in SERS intensity due to molecules moving into/out of hotspot regions. When the molecule is in the hot spot region, it can produce a very strong SERS signal. However, a molecule may move out of the hot spot, the Raman signal of the molecule cannot be efficiently enhanced and the detected signal will be contributed by Raman signals of the various interferences like solvent or impurity, fluorescence etc. **[6]** Because we acquire the SERS spectra as a series of 10 s exposures (and then average over the exposures) the average spectra will contain contributions from exposures where little or no signal is present. By analyzing each exposure ***before*** averaging, spectra containing signal from the analyte can be retained and those spectra containing only background can be discarded (the average intensity must then be normalized using the fraction of retained exposures). In this way, we can significantly improve the SERS detection by removing the noisy spectra. Furthermore, by matching the exposure time to the average "residence time" for

an analyte molecule in a hotspot this filtering process can be optimized (the residence time is roughly determined mostly by trial and error, by observing the frequency at which the signal intensity flops between high and low levels). The exposure time needs to be evaluated for each sample.

6.3.7. SERS and SLIPSERS analysis of LHC residues in antler velvet.

The SERS spectra of LHC spiked antler extract A and B were not considered reliable due to poor reproducibility. Both extracts have some interfering components in the extract, which resulted in additional bands. **Extraction method C** did remove interfering compounds and was therefore used as the final extraction method for SERS and SLIPSERS measurements.

6.3.7.1. Method 1: Spiked after extraction

In Method 1, the supernatant first was obtained using the extraction C procedure (as explained in sample preparation section 6.2.2.) and then subsequently spiked with LHC. Spiking is done after extraction to isolate the effect of the matrix on the binding process.

As stated in the Chapter - 3, for biological samples minimal power is required for excitation. Hence, all measurements for this work was captured at 2mW power with 5 seconds accumulations as higher accumulation time creates fluorescence with no observable Raman bands. Three points on the sample were randomly measured in the sample. Different spots were focused on recording the SERS spectra. **[12]** The signal-to-noise is roughly the same for each spectrum which suggests the SLIPS substrate is providing excellent enhancement across this concentration range. The signal intensity decreases as concentration decreases, and the decrease is approximately linear with log (concentration). Finally, at very low concentration (10^{-9} mol L^{-1}) the signal strength drops to the point where the noise is observable.

Results obtained from SERS and SLIPSERS are presented in Figure 6.11 and Figure 6.12.

SERS spectra of “spiking-after-extraction” samples show strong bands at 779, 940, 1364, 1507 and 1651 cm^{-1}. It is observed that there is a strong peak at 940 cm^{-1}, which is coming from perchloric acid but not observed in the SLIPS data. The spiking-after-extraction method produced a gel-like aggregate with SLIPS, which prevented the desired formation of the dense SLIPS aggregate. After trial and error, the right volume of analyte and colloid was determined which is different as compared to a standard SLIPS volume measurement **[5]**. It was found that the colloid volume should be more than analyte volume. The Raman signal from spiking-after-extraction samples degraded over a period of a few days and so fresh samples were prepared each day. This includes both fresh extracts and fresh SLIPS aggregates.

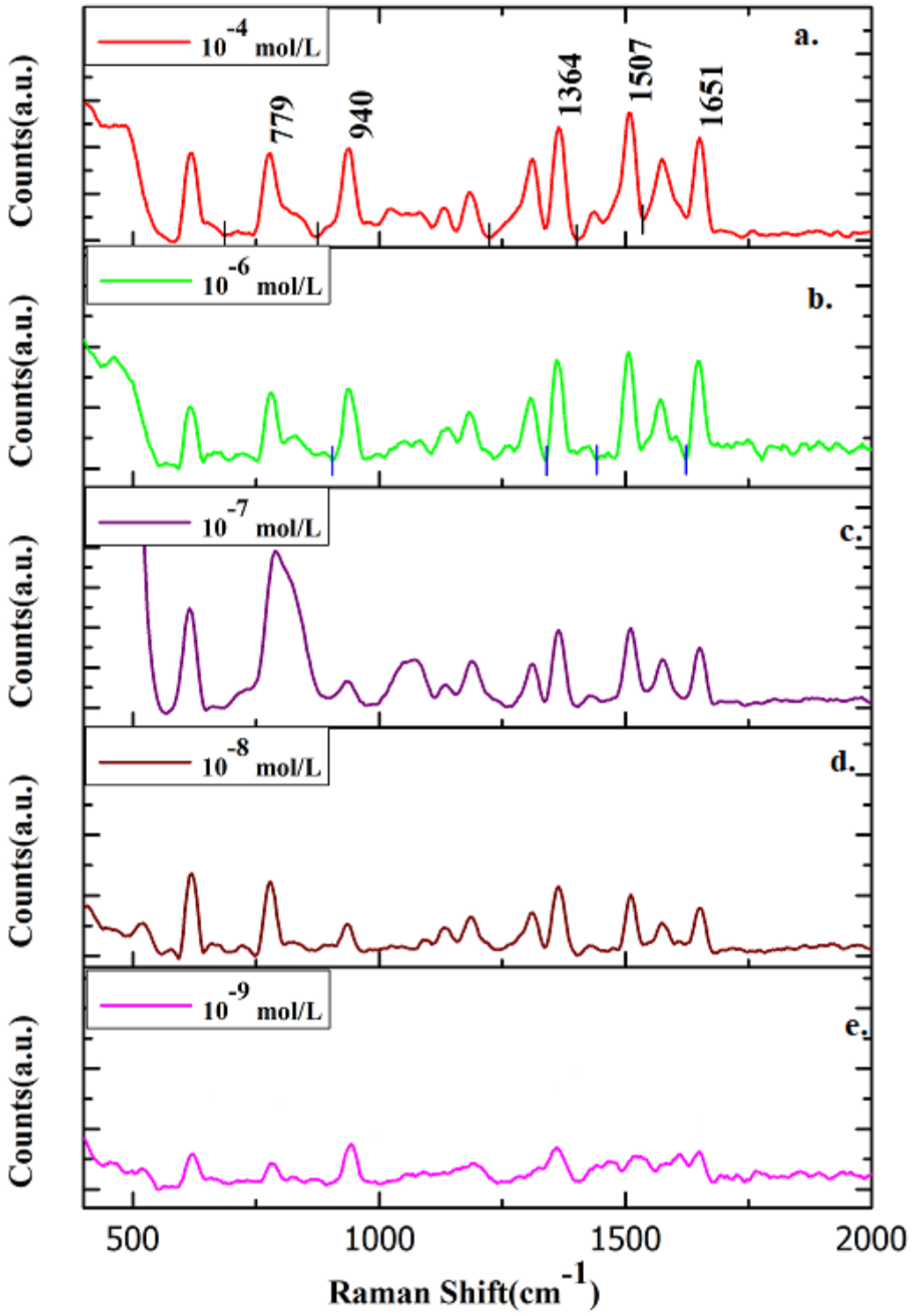

Figure 6. 11: SERS spectra of extracted antler velvet spiked with a)10^{-4}, b)10^{-6}, c)10^{-7}, d) 10^{-8} and e) 10^{-9} mol/L LHC after extraction (method C) acquired at 532 nm excitation wavelength with 40 × objective, 10 seconds exposure time and three accumulations with laser power of 2mW.

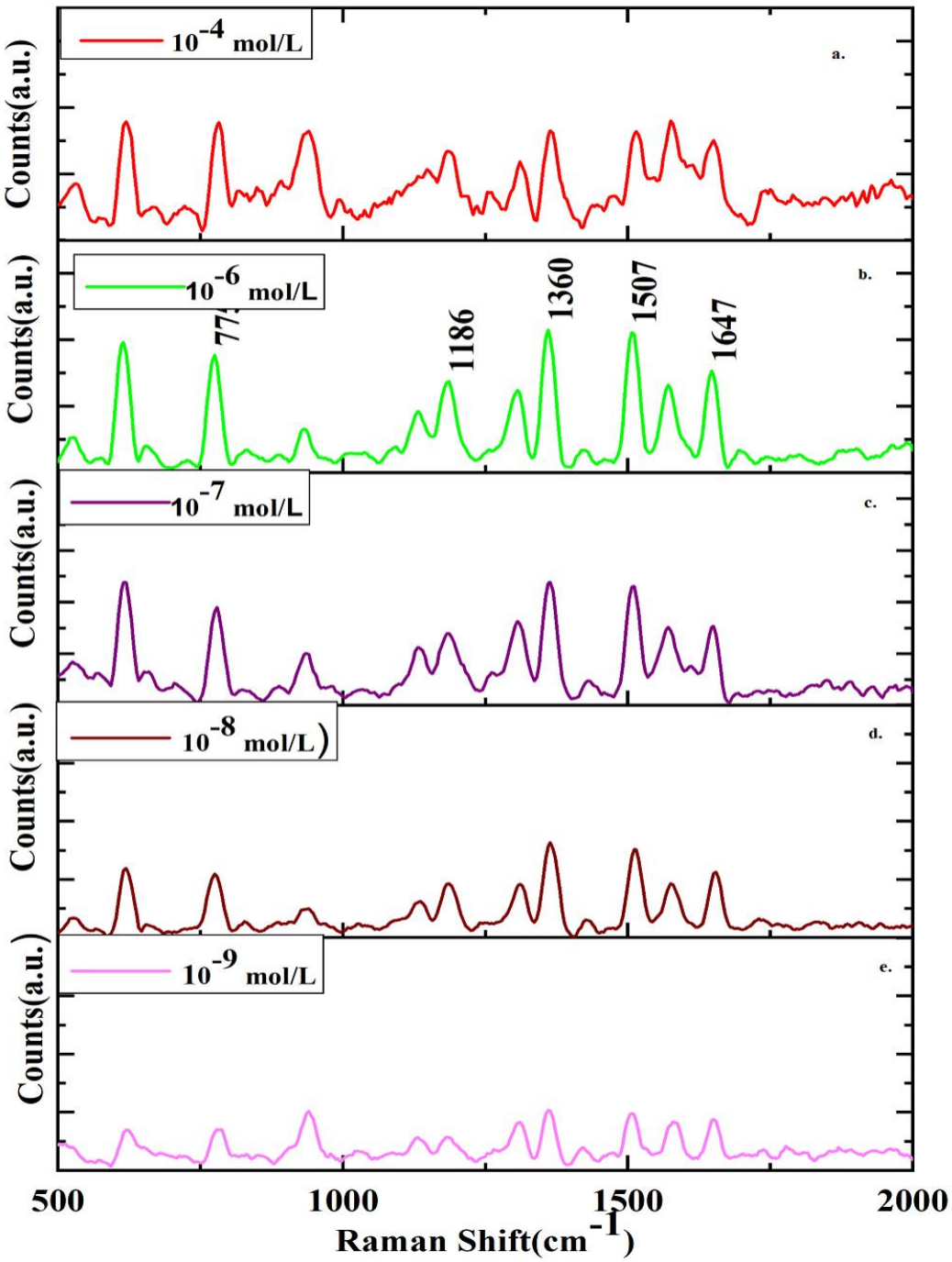

Figure 6. 12: SLIPSERS spectra of extracted antler velvet spiked with a)10^{-4}, b)10^{-6}, c)10^{-7}, d)10^{-8} and e)10^{-9} mol/L LHC after extraction (method C) acquired at 532 nm excitation wavelength with 40 × objective, 10 seconds exposure time and three accumulations with laser power of 2mW.

6.3.7.2. Method 2: Spiked before extraction

The antler tissue was spiked with LHC to the desired concentration range (in mg/kg) before extraction and supernatant collected at the end of extraction was used for SERS analysis.

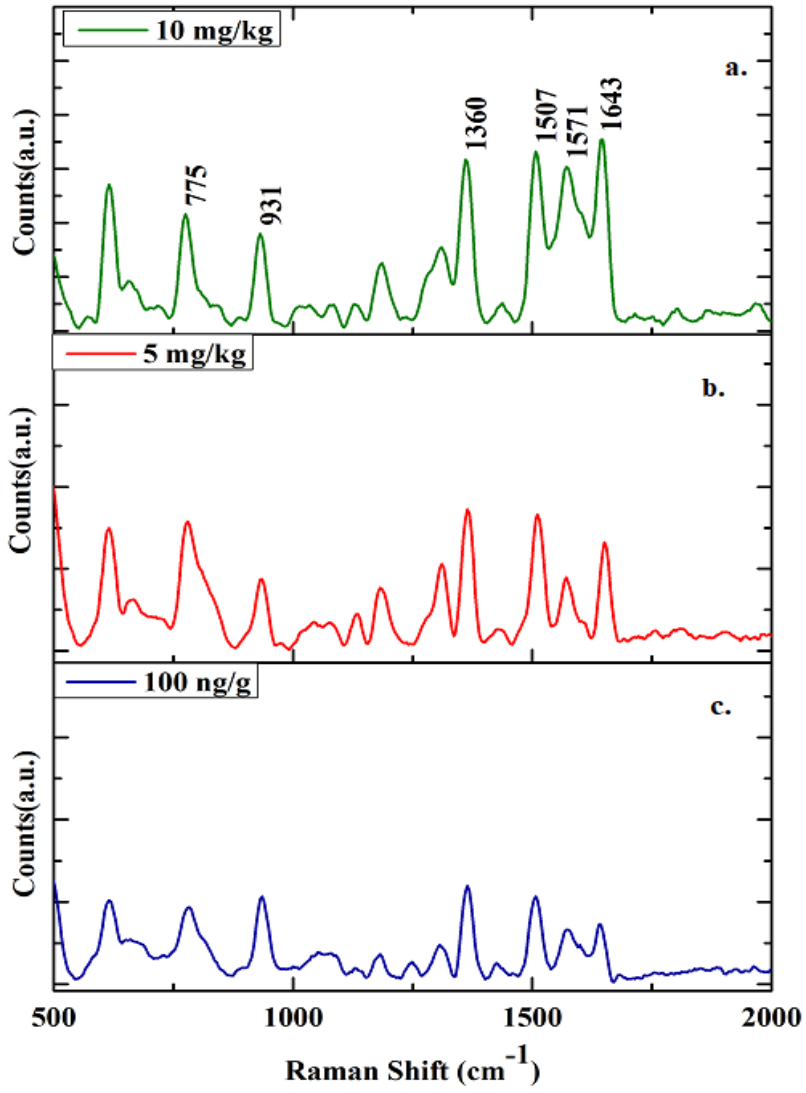

Figure 6. 13: SERS spectra of antler velvet spiked with LHC before extraction (method C) to get desired concentration of a) 10 mg/kg, b) 5 mg/kg and c) 100 ng/g acquired at 532 nm excitation

wavelength with 40 × objective, 10 seconds exposure time and three accumulations with laser power of 2mW.

The significant bands observed throughout the concentration range shown in Figure 6.13. were 775, 931, 1360, 1507, 1571 and 1643 cm^{-1} that are in close agreement with SERS spectral data obtained in Figure 6.11. Therefore, SERS spectra of spiked-after-extraction and spiked-before-extraction confirmed the presence of LHC in antler velvet. Three random points on each sample were focused for measuring SERS signal. Even at 100 ng/g concentration level, SERS signal is highly enhanced, there is a possibility to go further down the concentration range to get the lowest detection possible. Therefore, the proposed SERS method has proved its potential to investigate real samples. Results obtained from SERS were presented in Figure 6.13.

On the other hand, the SLIPS substrate was unsuccessful in giving any signal for these real samples (i.e., LHC spiked antler before extraction samples). The lack of signal from the SLIPSERS might be due to other components in the matrix interfering with the LHC binding. Presumably the drying process in SLIPS, leads to a sufficiently high concentration of components that can compete for binding with the analyte on the nanoparticle surface. Therefore, LHC residues were not detected with SLIPS for spiked-before-extraction samples.

6.3.8. Validation methods

The quantitative relation between the concentration of LHC and intensity of Raman band at 1364 cm^{-1} was calculated for SERS and SLIPSERS for the spiking-after-extraction method. The calibration curves (Figure 6.14, 6.15 and 6.16) are linear with a R^2 value close to one. The limit of detection of LHC in velvet antlers using SERS and SLIPSERS for spiking-after-extraction is estimated as 0.235 ng/mL whereas the limit of detection obtained by SERS for spiking-before-extraction is 100 ng/mL with the potential to go further down the concentration. Hence, the actual limit of detection was not established, but **at least** 100 ng/mL of LHC was detected in this study.

Table 6. 2: LOD derived from current SERS and SLIPSERS method

Method	Linear range	Regression equation	Correlation coefficient (R_2)	LOD
Method 1 - SERS	$10^{-4} - 10^{-9}$ mol/L	y = 4320x + 38850	0.97	0.235 ng/ml
Method 1- SLIPSERS	$10^{-4} - 10^{-9}$ mol/L	y = 911x + 8101.34	0.98	0.235 ng/ml
Method 2 - SERS	10 – 0.1 mg/Kg	y = 238x + 549	0.99	100 ng/ml

Hoogenboom *et al* **[2]** reported that the LOD of LHC residue in cow's milk after 48.5 hours was 229 µg kg_{-1}. The method proposed was compared with other techniques for LHC detection in biological matrices. It was observed that SERS is more sensitive and reproducible method than other methods.

Table 6. 3: Comparison of current method with other analytical techniques:

S. No.	Type of matrix	Detection method	Detection limit	Reference
1	Serum	HPLC	1ng/mL	13
2.	Blood and vitreous humor	UV-Vis	0.05 ng/mL	14
3.	Plasma	GC-MS	2.5 ng/mL	15
4.	Velvet antler	SERS (spiked after extraction)	0.235 ng/mL	Current work
		SERS (spiked before extraction)	100ng/mL	

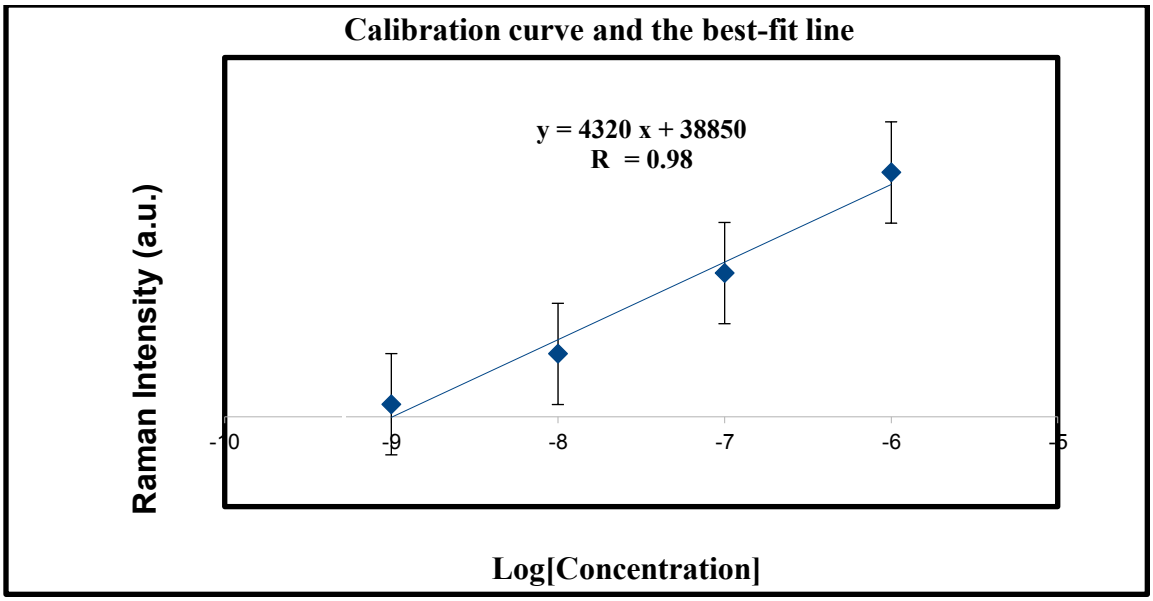

Figure 6. 14: The plot of intensity of SERS peak at 1364 cm^{-1} versus LHC concentration spiked after extraction method with error bars represents the standard error.

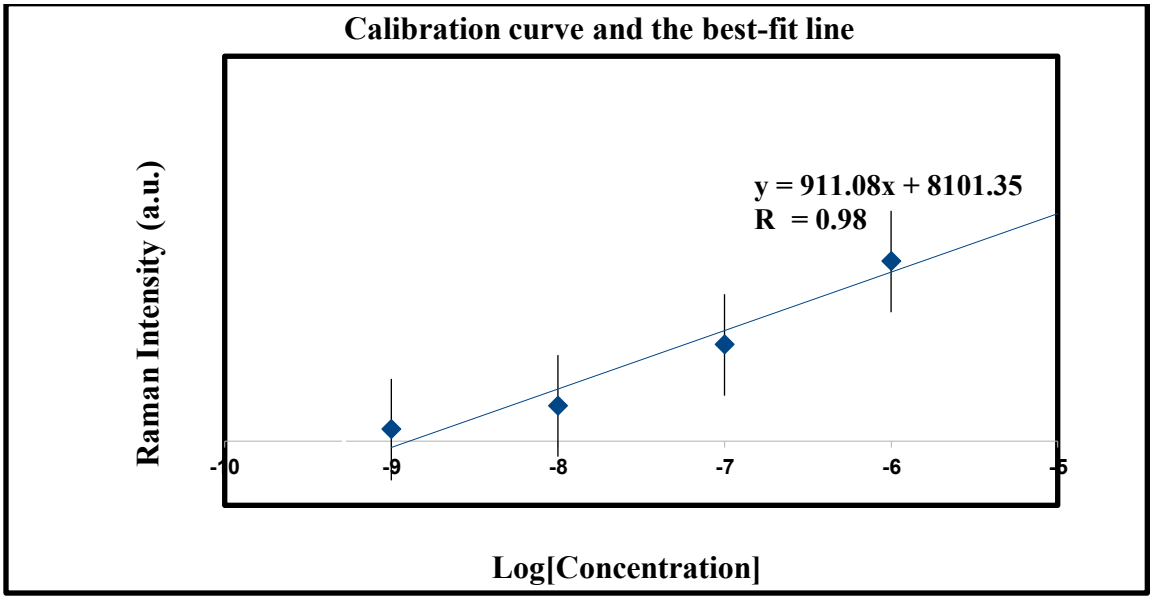

Figure 6. 15: The plot of intensity of SLIPSERS peak at 1360 cm^{-1} versus LHC concentration spiked after extraction method with error bars represents the standard error.

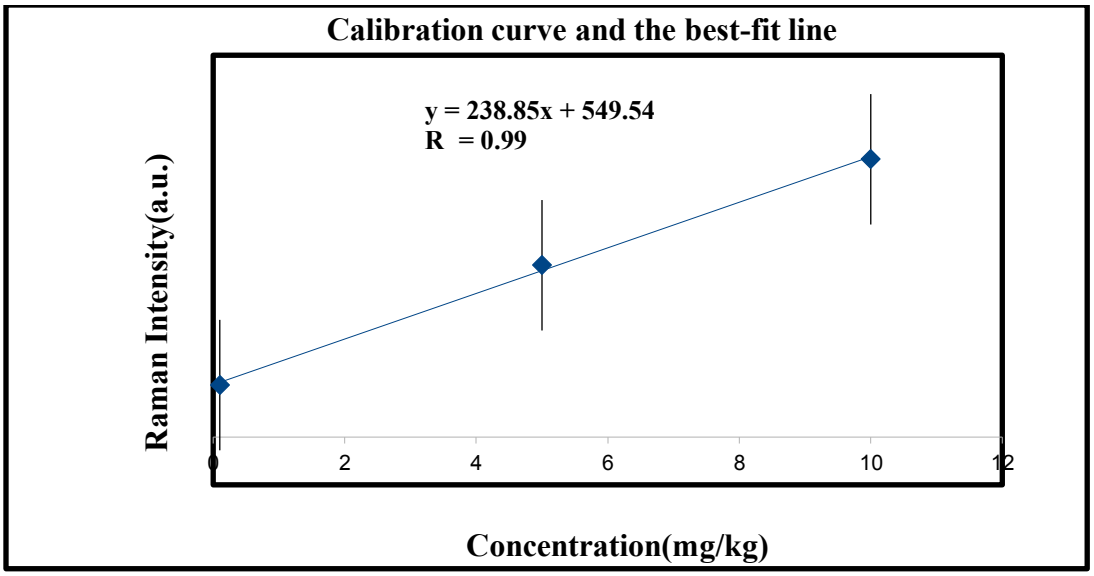

Figure 6. 16: The plot of intensity of SERS peak at 1360 cm^{-1} versus LHC concentration spiked before extraction method with error bars represents the standard error.

6.3.9. Feasibility of method for LHC detection

To determine the feasibility of the current method, recovery (%) was calculated from the concentrations used for SERS and SLIPSERS analysis. Recovery refers to the ability to detect the amount of analyte present in a sample. So, the recovery rate was calculated by comparing the spiked concentration in the matrix with the predicted concentration obtained from the regression equation and this can only be used for spiked samples to determine the accuracy of the chosen method. Based on the linear equation obtained from the calibration curve, **[15, and 16]** the recovery was determined with LHC concentrations in velvet antler for both methods – spiked after and before extraction.

$$Recovery\ \% = (Predicted\ concentration \div Spiked\ concentration) \times 100$$

Triplicate analysis was performed using two concentrations: 10^{-6} mol/L and 10^{-9} mol/L at three different positions of the detection region. To evaluate precision and accuracy, relative standard deviation and relative deviation from the predicted values were measured from the regression

equation. Table 6.4 and 6.5 below demonstrates the values obtained to provide a satisfactory level of acceptance with a relative deviation of both higher and lower concentration less than 3%.

Table 6. 4. Recovery of LHC residues in velvet antlers for method A (supernatant spiked after extraction).

SLIPSERS - Log(LHC concentration (mol/L)		Recovery %
Spiked after extraction concentration	**Measured**	
-4	-3.9	98.8
-6	-5.8	96.9
-7	-7.2	103.5
-8	-8.2	103.6
-9	-8.7	96.6
SERS - Log (LHC concentration (mol/L)		**Recovery %**
Spiked after extraction concentration	**Measured**	
-6	-5.8	97.4
-7	-7.1	102.1
-8	-8.1	102.2
-9	-8.8	98.1

Table 6. 5. Recovery of LHC residues in velvet antlers for method B (antlers spiked with LHC before extraction).

Concentration of LHC in antlers (mg/Kg)		Recovery (%)
Spiked before	**Measured**	
10	9.861796	98.61
5	5.279752	100.3
0.1	0.099154	99.15

Table 6. 6. Different concentrations (10^{-6} and 10^{-9} mol/L) of LHC residues used to calculate the precision (RSD) and accuracy (recovery) for SERS detection

Log [LHC]	Intensity	Average ± SD	CoV	RSD (%)	Recovery (%)
-6	13648	13815.6 ± 118.9	0.0086	0.86	104.5
-6	13888				
-6	13911				
-9	642	562.6 ± 32.5	0.05	5.7	91.9
-9	400				
-9	548				

a. CoV = Coefficient of Variance b. RSD = Relative Standard Deviation

Therefore, the accuracy and precision values are excellent and were well within the recommended value of RSD < 20%. The validation assessments reveal that the proposed method of SERS for LHC detection in antlers was precise, highly sensitive and reproducible **[17, 20]**.

6.4. Conclusion

Enhancement of SERS signals is a highly challenging technique which is influenced by laser power fluctuation, collection efficiency, substrate properties, aggregating agent and interfering components of a sample matrix, it was necessary to understand and determine the best combination of extraction method and optimization parameters for SERS measurements.

Three methods for extracting LHC from deer antler tissue were investigated, out of these Extraction Method C (perchloric acid and methanol) was successful for SERS detection of LHC from the velvet matrix.

Only SERS was capable of LHC detection in real antler samples. The problems associated with complex biological matrices that were found with SLIPSERS in milk samples were again observed with the antler tissue samples. Further improvements are required to obtained SLIPSERS signal considering parameters like interactions with the omniphobic surface, the type of hydrophobic liquid (or possibly changing viscosity of the polyfluoropolyether oil), concentration of analytes

and other methods for extracting the drug from the biological matrices without the generation of interfering signals.

Limit of detection (LOD) for SERS and SLIPSERS for 'LHC spiked after extraction' samples (method A) was 0.235 ng/mL and LOD for SERS for 'LHC spiked before extraction samples' determined was at least 100 ng/mL. These results show that SERS method can be used for the detection of LHC in complex biological matrices.

To the best of my knowledge, this is the first work in the field of SERS for detection of LHC in biological samples.

References

1. Bagonluri, M. T., Woodbury, M. R., Reid, R. S. & Boison, J. O. 2005. Analysis of lidocaine and its major metabolite, monoethylglycinexylidide, in elk velvet antler by liquid chromatography with UV detection and confirmation by electrospray ionization tandem mass spectrometry. *Journal of agricultural and food chemistry*, 53, 2386-2391.
2. Hoogenboom, R. L., Zuidema, T., EssersS, M., Van Vuuren, A. M., Van Wikselar, P. G., Van Eukeren, J. C., Mengelers, M. J., ZEILMAKER, M. J. & BULDER, A. S. 2015. Concentrations of dimethylaniline and other metabolites in milk and tissues of dairy cows treated with lidocaine. *Food Additives & Contaminants: Part A*, 32, 1256-1264.
3. Eerola, S., Hinkannen, R., Lindfors, E. & Hirvi, T. 1993. Liquid chromatographic determination of biogenic amines in dry sausages. *Journal-AOAC International*, 76, 575-575.
4. Dou, Y., Yang, X., Liu, Z. & Zhu, S. 2013. Homocysteine-functionalized silver nanoparticles for selective sensing of Cu2+ ions and Lidocaine hydrochloride. *Colloids and Surfaces A: Physicochemical and Engineering Aspects*, 423, 20-26.
5. Yang, S., Dai, X., Stogin, B., & Wong, T. (2016) Ultrasensitive surface-enhanced Raman scattering detection common fluids. *Proceedings of the National Academy of Science*, 113 (2), 268-273.

6. Hudson, S. D. & Chumanov, G. 2009. Bioanalytical applications of SERS (surface-enhanced Raman spectroscopy). *Analytical and bioanalytical chemistry*, 394, 679-686.
7. Chander, N. G. 2018. Nano–bio interactions. *The Journal of Indian Prosthodontic Society*, 18, 187.
8. Ansari, N., Lodha, A., Pandya, A., Sutariya, P. G. & Menon, S. K. 2015. Lab-on-phone citrate-capped silver nanosensor for lidocaine hydrochloride detection from a biological matrix. *Analytical Methods*, 7, 9084-9091.
9. Janci, T., Mikac, L., Ivanda, M., Marusic Radovcic, N., Medic, H. & Vidacek, S. 2017. Optimization of parameters for histamine detection in fish muscle extracts by surface-enhanced Raman spectroscopy using silver colloid SERS substrates. *Journal of Raman Spectroscopy*, 48, 64-72.
10. Bompart, M., De Wilde, Y. & Haupt, K. 2010, 'Chemical Nanosensors Based on Composite Molecularly Imprinted Polymer Particles and Surface-Enhanced Raman Scattering', *Advanced materials*, vol. 22, no. 21, pp. 2343-8.
11. Lu, Y., Lu, D., You, R., Liu, J., Huang, L., Su, J. & Feng, S. 2018, 'Diazotization-Coupling Reaction-Based Determination of Tyrosine in Urine Using Ag Nanocubes by Surface-Enhanced Raman Spectroscopy', *Nanomaterials*, vol. 8, no. 6, p. 400.
12. Marcaida, I., Magurguei, M., Morillas, H., Garcia-Florentino, C., Pintus, V., Aguayo, T., Campos-Vallette, M. & Madariaga, J. M. 2017. Optimization of sample treatment for the identification of anthraquinone dyes by surface-enhanced Raman spectroscopy. *Analytical and bioanalytical chemistry*, 409, 2221-2228.
13. Aleman, M., Davis, E., Knych, H., Guedes, A., Smith, F. & Madigan, J. 2016. Drug Residues after intravenous anesthesia and intrathecal lidocaine hydrochloride euthanasia in horses. *Journal of veterinary internal medicine*, 30, 1322-1326.
14. Al Nebaihi, H. M., Primrose, M., Green, J. S. & Brocks, D. R. 2017. A High-Performance Liquid Chromatography Assay Method for the Determination of Lidocaine in Human Serum. *Pharmaceutics*, 9, 52.
15. Ohshima, T. & Takayasu, T. 1999. Simultaneous determination of local anesthetics including ester-type anesthetics in human plasma and urine by gas chromatography–mass spectrometry with solid-phase extraction. *Journal of Chromatography B: Biomedical Sciences and Applications*, 726, 185-194.

16. Vicario, A., Sergo, V., Toffoli, G. & Bonifacio, A. 2015. Surface-enhanced Raman spectroscopy of the anti-cancer drug irinotecan in presence of human serum albumin. *Colloids and Surfaces B: Biointerfaces,* 127, 41-46.
17. Bai, P., Wang, J., Yin, H., Tian, Y., Yao, W. & Gao, J. 2017. Discrimination of human and nonhuman blood by Raman spectroscopy and partial least squares discriminant analysis. *Analytical Letters*, 50, 379-388.
18. Stosch, R., Henrion, A., Schiel, D. & Güttler, B. 2005, 'Surface-enhanced Raman scattering based approach for quantitative determination of creatinine in human serum', *Analytical chemistry*, vol. 77, no. 22, pp. 7386-92.
19. Basu, S., Ghosh, S.K., Kundu, S., Panigrahi, S., Praharaj, S., Pande, S., Jana, S. & Pal, T. 2007, 'Biomolecule induced nanoparticle aggregation: effect of particle size on interparticle coupling', *Journal of colloid and interface science*, vol. 313, no. 2, pp. 724-34.
20. Guideline on bioanalytical method validation. Available online: https://www.ema.europa.eu/documents/mrl-report/lidocaine-summary-report-committee-veterinary-medicinal-products_en.pdf (accessed on 15 November 2017)
21. Gilbey, A. & Perezgonzalez, J. D. 2012. Health benefits of deer and elk velvet antler supplements: a systematic review of randomised controlled studies. *NZ Med J,* 125**,** 80-86.
22. Frank, A.J., Cathcart, N., Maly, K.E. & Kitaev, V. 2010, 'Synthesis of silver nanoprisms with variable size and investigation of their optical properties: a first-year undergraduate experiment exploring plasmonic nanoparticles', *Journal of chemical education*, vol. 87, no. 10, pp. 1098-101.
23. Bakonyi, M., Gacsi, A., Kovacs, A., Szucs, M.-B., Berko, S. & Csanyi, E. 2018. Following-up skin penetration of lidocaine from different vehicles by Raman spectroscopic mapping. *Journal of pharmaceutical and biomedical analysis*, 154, 1-6.
24. Xu, Y., Du, Y., Li, Q., Wang, X., Pan, Y., Zhang, H., Wu, T. & Hu, H. 2014, 'Ultrasensitive detection of enrofloxacin in chicken muscles by surface-enhanced raman spectroscopy using amino-modified glycidyl methacrylate-ethylene dimethacrylate (GMA-EDMA) powdered porous material', *Food Analytical Methods*, vol. 7, no. 6, pp. 1219-28.

25. Farias, M. & Carneiro, R. 2014, 'Simultaneous quantification of three polymorphic forms of carbamazepine in the presence of excipients using Raman spectroscopy', *Molecules*, vol. 19, no. 9, pp. 14128-38.
26. Farquharson, S., Shende, C., Sengupta, A., Huang, H. & Inscore, F. 2011, 'Rapid detection and identification of overdose drugs in saliva by surface-enhanced Raman scattering using fused gold colloids', *Pharmaceutics*, vol. 3, no. 3, pp. 425-39.
27. Aristoy, M.C. & Toldra, F. 1991, 'Deproteinization techniques for HPLC amino acid analysis in fresh pork muscle and dry-cured ham', *Journal of Agricultural and Food Chemistry*, vol. 39, no. 10, pp. 1792-5.
28. Lin, C.Y., Wu, H., Tjeerdema, R.S. & Viant, M.R. 2007, 'Evaluation of metabolite extraction strategies from tissue samples using NMR metabolomics', *Metabolomics*, vol. 3, no. 1, pp. 55-67.

Chapter 7. Conclusions and Future Work

7.1. Conclusion

The ultimate objective of this dissertation is to develop a highly rapid, sensitive and reliable technique of SERS coupled with free of pinning omniphobic substrate, SLIPS, for ultra-sensitive detection of environmental and biological contaminants in various solvents. The goal has been achieved through the detailed study presented in Chapters 2 - 6. Achieving high sensitivity remains a challenge for SERS that was taken care of by SLIPSERS technique by reducing the sample volume by controlled drying allowing detection down, possibly to single molecule detection level. With SLIPSERS, controlled drying on the SLIPS surface concentrates the silver nanoparticles into a small aggregate with a consistently high hotspot density and a strong signal can be observed from a much higher proportion of the sample.

The SLIPSERS technique was employed in comparison with SERS throughout this research, and it demonstrates as an excellent method for almost all of our analytes of interest like brodifacoum and 1080. With biological matrices, a few challenges were faced in terms of poor adhesion of the analyte which is the result of interference or competition for binding sites from biological matrix and the problem of wetting (i.e., contact line pinning) the SLIPS substrate rather than forming a droplet. No single extraction technique fits all due to the complex nature of biological matrices. Hence, dealing with the sample first was the foremost job to accomplish than simply relying on SERS or SLIPSERS for efficient detection.

Three substrate development methods– metal-assisted chemical etching method, silver dendrites nanoparticles and silver colloidal nanoparticles also termed as ‘Kitaev nanoparticles (KNP)’ were demonstrated. KNP provided the best enhancement in delivering strong SERS signal as compared to other methods. Two different substrates - one using an omniphobic surface substrate (SLIPSERS) and the second drop casting the silver nanoparticle analyte mixture on the substrate (SERS) were used in the study to demonstrate the pros and cons of both substrates. SLIPSERS overcomes some of the limitations of SERS due to its controlled drying feature that gives excellent

reproducibility. A significant advantage of SLIPSERS method is its simplicity. The omniphobic surface is fabricated from readily available laboratory supplies. Surface preparation and droplet drying are highly reproducible which provides reliable results. Another advantage is the high density of hotspots – if every dried droplet has a high density of hotspots, there is an excellent chance that the SERS enhancement will be high for every dried droplet. Without controlled drying, there is a need for relying on random aggregation at low concentration, which might not always give a hotspot and the aggregates will be spread over a larger area too, so chances of detection decrease. Use of $MgSO_4$ as an aggregating agent ensures it does not bind and compete with the analyte on the surface. It displaces citrate layer from the surface of the silver nanoparticle giving enhancement of brodifacoum and 1080 bands. R6G being a highly resonant SERS molecule was used as a test analyte for SLIPSERS substrate and LOD for R6G went down to picomolar level. Therefore, findings from Chapter -2 has motivated the use of SLIPSERS technique for a variety of analytes in chemical and biological matrixes.

After the selection of SLIPSERS substrate for analyte detection, Chapter - 3 deals with substrate characterisation using lidocaine hydrochloride, a molecule which does not have any molecular resonance enhancement like R6G, so SLIPSERS substrate was characterised for just plasmon enhancement. The single-molecule regime was observed with the R6G in Chapter - 2 with a detection limit down to 10-15 mol/L. It was observed that by lowering the concentration the signal intensity eventually becomes approximately constant. This is because below a critical concentration the probability of finding an R6G molecule in the focal volume and at a hot-spot becomes quite low. This is the sub-sampling regime, and a certain coincidence is required to find a signal. To solve this subsampling problem, Raman line-scanning was used for characterising the spatial distribution of hotspots possibly with the hope of being able to model the sub-sampling with an appropriate distribution and to evaluate the subtle spectral variation using Pareto distribution charts and Principal Components Analysis (PCA).Very low power (0.1mW) was required to avoid sample damage with SLIPSERS substrate. The line scan analysis also reveals that the hot spots with the highest enhancements or sensitivity are also responsible for the most sample damage, which has implications for accurate detection of molecules using plasmonic enhancement.

Chapter - 4 fully exploit the potential of SERS and SLIPSERS for ultrasensitive detection of brodifacoum to picomolar level and sodium monofluoroacetate (called as 1080) to nanomolar level in aqueous solution. Silver colloidal nanoparticles were characterised using UV-vis spectroscopy giving absorption peak at 410 nm. Brodifacoum was a good SERS and SLIPSERS analyte like R6G with strong molecular and plasmon enhancement. But 1080, a small compound has low Raman scattering cross section which makes it a weak Raman scatterer. A comparative study was performed using SERS, SLIPSERS (with or without an aggregating agent) for both rodenticides to demonstrate the detection capability and high collection efficiency. SLIPSERS has shown its promising potential of detecting brodifacoum to a concentration 100-fold lower than those reported in literature whereas 1080 has reached the same literature value of detection of 0.1ng/mL. These results laid the foundation to detect multiple analytes in complex chemical and biological matrices.

Chapter - 5 extended the SLIPSERS branches to investigate the same rodenticides – brodifacoum and 1080 in complex mixtures like milk. Initially, solid milk powder spiked with brodifacoum was investigated to understand the behavior of rodenticide on interaction with milk powder using a geometric dilution approach. Normal Raman analysis was performed on such samples. The results obtained were quite promising with the limit of detection of 3.4% w/w. Later SERS and SLIPSERS analysis was performed on aqueous milk solution spiked with rodenticides. Sample preparation involved dilution of milk followed by deproteinsation step using methanol. SERS of liquid milk without extraction creates a challenge for lower detection due to the complex colloidal nature of milk itself that swamp the much weaker Raman scattering SERS; and the various proteins, fats and other surface active components in milk cause aggregation of the silver nanostructures. SLIPSERS with diluted milk samples spiked with brodifacoum and 1080 was $6.25 \times 10^{-8}\,\mathrm{mol\,L^{-1}}$ and $1.25 \times 10^{-7}\,\mathrm{mol\,L^{-1}}$. The recovery of residuals for brodifacoum and 1080 in milk ranges from 85-95% with a relative standard deviation between 8-11%. The results again proved that SLIPSERS method is an excellent technique for ultra-sensitive detection of rodenticide residues in milk and can be further explored for biological samples such as deer antler velvet.

Chapter - 6 brings the quantitative analysis of the bioanalytical application of SLIPSERS. Finding the best extraction technique for sample clean up using perchloric acid and methanol, then optimizing several parameters like volume of extract, laser excitation wavelength, and laser power were the necessary steps taken to obtain SERS. Under the optimal conditions, limit of detection of 'LHC spiked antler velvet after extraction' for SERS and SLIPSERS was 0.235 ng/ml that is lower than obtained from other methods. Only SERS was capable of LHC detection in real antler samples. LOD for SERS for 'LHC spiked before extraction samples' was 100 ng/mL. This experiment has again utilized less toxic and biocompatible silver nanoparticles for rapid, highly simple and sensitive, cost-effective detection of lidocaine hydrochloride in velvet antler. To the best of our knowledge, this is the first work done for detection of anesthetic drug, lidocaine hydrochloride in deer antler velvet samples using SLIPSERS.

Overall, this thesis has provided new insights in the field of highly sensitive detection using SLIPSERS and SERS with some minor optimization parameters like laser power, extraction technique. These findings present a reliable method to investigate single molecule regime and opportunity to use for several other unforeseen applications.

7.2. Future Work

Every method on investigation highlights few exciting inventions, advantages but it comes with some shortcomings too which need improvements in future work. This thesis has explored single analyte detection in either simple matrix like water or complex matrices like milk and deer antler velvet, but there is a potential of SLIPSERS substrate to detect an analyte in the presence of other interfering analytes. For example, instead of clean filtered water, we can also try rodenticide detection in wastewater in the presence of nitrate or other anticoagulant rodenticides that gives a broader view of looking optimisation parameters in detail. Due to short of time, this area was not investigated but can be explored in the near future.

Also, few modifications in developing the SLIPS substrate like different lubricating fluid, drying conditions can be worked out to avoid the interferences from the biological matrices.

Another future work is to use SLIPSERS method for disease detection in combination with histological dyes. These dyes are known to enhance the intensity of Raman scattering of laser light dramatically but only if the laser frequency (or wavelength) closely matches the frequency of light absorbed by the dye. This allows the histological stain to sequester bioanalytes and then detect the bioanalytes using enhanced Raman methods.

Finally, SLIPSERS method with little optimisation parameters depending on the analyte matrix can be used to develop a hand-held Raman spectrometer as a sensing platform for real-time applications.

Appendix

I. Python code for calculating Raman cross section.

```
import numpy as np
import matplotlib.pyplot as plt
import os

from cclib.parser import ccopen
from cclib.parser import Gaussian
from cclib.method import Density
from cclib.method import MPA

from cclib.progress import TextProgress
import logging

import pandas as pd

import scipy
from scipy.constants import find, physical_constants

import glob
from glob import glob


import matplotlib.ticker as ticker
import matplotlib.lines as mlines

from scipy.signal import find_peaks

def normalise(spectrum):
    return (spectrum-spectrum.min())/(spectrum.max()-spectrum.min())

def peak_labels(RS,spectrum,axis):
    scaled = normalise(spectrum)
    peaks,_ = find_peaks(scaled)
    for j in peaks:
        axis.annotate('{0:.0f}'.format(float(RS[j])),
                xy=(RS[j], spectrum[j]),
                xycoords='data', xytext=(0, +15), textcoords='offset points',
                fontsize=12,  rotation=90,
                horizontalalignment='center', verticalalignment='bottom',
                arrowprops=dict(arrowstyle="-", connectionstyle="arc3,rad=.0"))
    return peaks

def lorentzian(x,xc,w,A):
    return A/(1+(x/w-xc/w)**2)

get_ipython().run_line_magic('matplotlib', 'notebook')

#prints the current directory.
print(os.getcwd())

#set the directory to the desired directory
#Hint: Right-click in the address bar in File Explorer and copy the address
```

```
os.chdir(r'file location')

#check the current directory.
print(os.getcwd())

ext=('.log','.out','.csv')
for file in [f for f in os.listdir(os.getcwd()) if f.endswith(ext)]:
    print(file)


#Open and parse log file:

filename = "filename"
logfile = ccopen(filename)
data = logfile.parse() # The following lines are log messages

#Obtain desired attribute of parsed output:
print("Number of atoms:",data.natom)
#print("Atom numbers:",data.atomnos)
print('HOMO is MO:',data.homos)


freqs = data.vibfreqs
print("vibrational frequencies:", freqs)
print("Number of modes:",len(freqs))

symms = data.vibsyms
print("Vibrational Symmetries:", symms)

raman = data.vibramans
#print("Raman Activities:", raman)

ir = data.vibirs
print("IR Activities:", ir)

cart_displacements = data.vibdisps
print(cart_displacements.shape)


h = physical_constants['Planck constant']
print('Plancks Constant, h:', h)

c = physical_constants['speed of light in vacuum']
print('Speed of light in vacuum, c', c)

e0 = physical_constants['atomic unit of permittivity']
print('permittivity, e0:',e0)

        kB = physical_constants['Boltzmann constant in inverse meters per kelvin']
        print('Boltzmann, kB:',kB)
        kB_cm = kB[0]/100

        amu = physical_constants['unified atomic mass unit']
        print('amu:',amu)

        Na = physical_constants['Avogadro constant']
        print('Avogadro Constant, Na:',Na)

        nu_in = 10**7/633
        print('nu_in',nu_in)

```

```
        T = 298.15


        F1 = np.pi**2*h[0]/(45*c[0])
        F2 = ((nu_in-freqs)*100)**4/(freqs*100*(1-np.exp(-1*freqs/(kB_cm*T))))
        XS = F1*F2*raman*(1/(amu[0]*10**40))
        XS_cm2 = XS*10**(36)

        # Generate calculated spectra

        wavenumbers = np.linspace(1,4000,3999)
        # the "intensity" will be calculated at each point in wavenumbers

        IR_spec = np.zeros((len(wavenumbers),1))
        for j in range(len(freqs)):
            IR_spec[:,0] += lorentzian(wavenumbers, freqs[j], 7, ir[j])
        IR_spec_max = max(IR_spec)

        Raman = np.zeros((len(wavenumbers),1))
        for j in range(len(freqs)):
            Raman[:,0] += lorentzian(wavenumbers, freqs[j], 7, XS_cm2[j])
        Raman_max = max(Raman)

        print(Raman.shape)
        print(IR_spec_max)
        print(Raman_max)

        fig, ax = plt.subplots(1, figsize=(8,10))

        colors = ['blue','green','red']
        Raman_line = ax.plot(wavenumbers, Raman, color='blue', label = 'Raman')
        ax.set_xlim([0,500])
        ax.set_ylim([0,1.1*Raman_max])
        ax.set_xlabel(r'Wavenumber / cm$^{-1}$', fontsize = 14)
        ax.xaxis.set_major_locator(ticker.MultipleLocator(50))
        ax.xaxis.set_minor_locator(ticker.MultipleLocator(25))
        ax.tick_params(axis='x',which='both',top=False,bottom=True,labelbottom=True, lab
    elsize = 14)
        ax.set_ylabel(r'Raman Cross-Section / $m^2 \; sr^{-1}$')

        lines = []
        line1 = mlines.Line2D([], [], color=Raman_line[0].get_color())
        lines.append(line1)

        ax1 = ax.twinx()

        IR_line = ax1.plot(wavenumbers, IR_spec, color='orange', label = 'IR')
        line2 = mlines.Line2D([], [], color=IR_line[0].get_color())
        lines.append(line2)
        ax1.set_ylim([0,1.1*IR_spec_max])
        ax1.set_ylabel(r'IR intensity /$\: km\; mol^{-1}$')

        plt.legend(lines, ['Raman','IR'], loc='upper right')

        #def peak_labels(RS,spectrum,axis, min_height, threshold, min_dist):

        peaks = peak_labels(wavenumbers,Raman[:,0],ax)
        print('Peak Indices:',peaks)
        peak_labels(wavenumbers,IR_spec[:,0],ax1)


```

```
        fig.savefig(filename[:-4]+'_IR_Raman_Calc.png', dpi=1200)


        print("Raman XS:", XS)
        print("Most intense mode index:",np.argmax(XS)+1)
        print("Most intense mode freq:",freqs[np.argmax(XS)])
        print("Maximum Raman XS (m**2 sr-1):", max(XS))
        vibdata_df = pd.DataFrame({'Freqs / cm-
    1':freqs,'Symm':symms,'Raman Act / A**4 amu-1':raman, 'diff. Raman XS / 10-32 cm**2 sr-
    1':XS_cm2, 'IR activity /  km mol-1':ir})

        vibdata_df.to_csv(filename[:-4]+'.csv',index=False)
        vibdata_df.head()

        writer = pd.ExcelWriter(filename[:-4]+'.xlsx')
        for j in range(len(freqs)):
            df = pd.DataFrame(cart_displacements[j,:,:])
            df.to_excel(writer,'Mode_'+str(j))
        writer.save()

```

II. Formulae used in the notebook for calculating the Raman cross-section from the Gaussian output.

For Raman scattering generated by a vibration with wavenumber, $\tilde{\nu}_p$ and incident radiation with wavenumber, $\tilde{\nu}_{in}$, the Raman scattered photon will have wavenumber, $\left(\tilde{\nu}_{in} - \tilde{\nu}_p\right)$.

The Raman scattering intensity, I, is

$$I = \mathcal{I} \times N \times \frac{d\sigma}{d\omega} \qquad \left[\frac{\mathrm{J}}{\mathrm{s\ sr}}\right]$$

where N is the number of molecules in the scattering volume and $\mathcal{I}$ is the laser intensity (J $\mathrm{m^{-2}s^{-1}}$). The unit sr is the steradian, which is the unit of solid angle. Clearly, the Raman scattering intensity depends on experimental parameters, so the (differential) Raman scattering cross-section, $d\sigma/d\Omega$, is more commonly reported in experimental studies:

$$\frac{d\sigma}{d\Omega} = \frac{I}{\mathcal{I}N} = \frac{\pi^2 h}{45c} \times \frac{\left(\tilde{\nu}_{in} - \tilde{\nu}_p\right)^4}{\tilde{\nu}_p} \times \frac{S'}{1 - \exp\left[-\tilde{\nu}_p / kT\right]} \qquad \left[\frac{\mathrm{m^2}}{\mathrm{sr}}\right]$$

$$k = 0.695\ \mathrm{cm^{-1}\ K^{-1}}$$

The name "cross-section" is apparent from the units, it represents an area of some sort. The Raman cross-section depends on the wavenumber of the scattered radiation, $\tilde{\nu}_p$, and the temperature of the sample (via Boltzmann populations of vibrational excited states which are significant for bands where $\tilde{\nu} \leq 200\ \mathrm{cm^{-1}}$, as $kT \cong 200\ \mathrm{cm^{-1}}$ at room temperature).

III. Python code for line scan processing.

```
import sys
sys.path.insert(0, '../../libs/')
from data_processing.baseline import baseline_als

import numpy as np
import matplotlib.pyplot as plt
from numpy.random import randint
import matplotlib.gridspec as gridspec
import matplotlib.ticker as ticker
from matplotlib import cm

import os
import csv

import scipy.signal  # for removing cosmic spikes

import xlrd
import pandas as pd

import peakutils

from scipy.signal import find_peaks

def normalise(spectrum):
    return (spectrum-spectrum.min())/(spectrum.max()-spectrum.min())

def peak_labels(RS,spectrum,axis,height=None, threshold=None, distance=None):
    scaled = normalise(spectrum)
    peaks,_ = find_peaks(scaled, height=height, threshold=threshold,distance=distance)

    for j in peaks:
        axis.annotate('{0:.0f}'.format(float(RS[j])),
                xy=(RS[j], spectrum[j]),
                xycoords='data', xytext=(0, +15), textcoords='offset points',
                fontsize=12,  rotation=90,
                horizontalalignment='center', verticalalignment='bottom',
                arrowprops=dict(arrowstyle="-", connectionstyle="arc3,rad=.0"))
    return peaks

from sklearn.preprocessing import scale
from sklearn.preprocessing import StandardScaler
from sklearn.decomposition import PCA
from scipy import stats

def scan_PCA(data):
    num_spectra = data.shape[0]
    num_variables = data.shape[1]
    print('Number of Spectra =', num_spectra)
    print('Number of Variables =', num_variables)

    scaled_data = scale(data)

    #Carry out PCA;

```

```
    scores = PCA().fit_transform(scaled_data)
    print('Shape of Scores Matrix:',scores.shape)

    pca = PCA().fit(scaled_data)
    loadings = pca.components_
    print('Shape of Loadings Matrix:',loadings.shape)

    evr = pca.explained_variance_ratio_
    return scores, loadings, evr

get_ipython().run_line_magic('matplotlib', 'notebook')


sheet_names = ['L-3','L-6']

sheet = sheet_names[0]

df_rawdata = pd.read_excel('data.xlsx',sheet_name=sheet, header=None, usecols=range(2,1
026))
array_raw = df_rawdata.values

print('DataFrame Dimensions:',df_rawdata.shape)

num_spectra = df_rawdata.shape[0]

scans_start = [0,200,500,700]
scans_stop = [199,499,699,899]

print('Number of Scans:',len(scans_start))


#Plot the first spectrum to determine the useful pixel range
# set left pixel to zero initially and then edit after viewing plot
# the lam and p parameters should be optimised here too

fig, ax = plt.subplots(1,2, figsize=(10,6))

lp = 150  #leftmost pixel value
rp = 1024 #rightmost pixel value

lam = 300000 #smoothing parameter
p = 0.2 #offset parameter

pixel_domain = np.arange(0,1024)

# make Raman Shift calibration
pix = np.asarray([333,558,647,830])
      RS_points = np.asarray([772,1271,1354,1647])
      nu_0 = 10**(7)/532
      wn = nu_0 + RS_points
      wl = 10**(7)/wn
      (m, c) = np.polyfit(pix, wl, 1)
      regr_params = ["{0:.3f}".format(m),"{0:.3f}".format(c)]
      wl_cal = m*pixel_domain + c
      wn_cal = 10**7/wl_cal
      RS_cal = wn_cal - 10**(7)/532
      print('slope =', regr_params[0], 'intercept =', regr_params[1])

      baseline = baseline_als(array_raw[0,pixel_domain],lam,p)
      corrected = array_raw[0,pixel_domain] - baseline

```

```
        ax[0].plot(RS_cal[lp:],array_raw[0,lp:rp],RS_cal[lp:],baseline[lp:])
        ax[0].set_xlabel('Raman Shift / cm-1')
        ax[1].plot(RS_cal[lp:],corrected[lp:])
        ax[1].set_xlabel('Raman Shift / cm-1')


        # do baseline correction for all spectra


        baselines = np.zeros((num_spectra,len(pixel_domain)))
        baselined = np.zeros((num_spectra,len(pixel_domain)))

        for i in np.arange(num_spectra):
            baselines[i] = baseline_als(array_raw[i,pixel_domain],lam,p)
            baselined[i] = array_raw[i,pixel_domain] - baselines[i]

        spec_err = np.std(baselined)

        df_baselined = pd.DataFrame(baselined)
        df_baselined.to_csv(sheet+"_baselined.csv")

        print('Shape of baselined array is',baselined.shape)


        N_samples=10
        print(['sample'+str(j+1) for j in range(N_samples)])



        '''''
        A simple check for cosmic spikes - compare max. value with
        standard deviation; a small number of cosmics are present if max value
        far exceeds std. dev.
        '''

        print('max value:', baselined.max())
        print('Std. Dev. of baselined:', spec_err)



        # remove cosmics spikes using a mask based on a median filter

        baselined_medfilt = scipy.signal.medfilt(baselined, 5)  # apply median filter to
    dataset
        bad = (np.abs(baselined - baselined_medfilt) / spec_err) > 25.0  # create a mask
    of cosmic spike locations

        cosmic_locations = np.column_stack(np.where(bad))
        print(cosmic_locations.shape)


        print('Number of cosmic spikes:',cosmic_locations.size)

        #[baselined[pixel] for pixel in np.where(bad)]

        print('max value before filter:', baselined.max())

        baselined[bad] = baselined_medfilt[bad] # use the mask to replace the cosmic spi
    kes with their median filtered equivalents

        print('max value after filter:', baselined.max())
```

```
172.
173.       ave_spectrum = np.mean(baselined,axis=0)
174.       ave_baseline = np.mean(baselines,axis=0)
175.
176.
177.       fig, ax = plt.subplots(nrows=1,ncols=len(scans_start)+1, figsize = (12,5))
178.
179.       max_pixels = np.argmax(baselined,axis=1)
180.
181.       num_pix_h = rp - lp
182.       rows = np.linspace(lp,rp,num_pix_h).astype(int)
183.       print(len(rows))
184.
185.
186.       def extents(f):
187.           delta = f[1] - f[0]
188.           return [f[0] - delta/2, f[-1] + delta/2]
189.
190.
191.       for scan in np.arange(len(scans_start)):
192.               line_map = (baselined[scans_start[scan]:scans_stop[scan],lp:])
193.               line_map = np.transpose(line_map)
194.               num_pix_v = scans_stop[scan] - scans_start[scan]
195.               cols = np.linspace(scans_start[scan],scans_stop[scan],num_pix_v).astype(
    int)
196.               spectrum_image = ax[scan].imshow(line_map, cmap = 'magma', aspect='auto'
    , origin = 'lower',extent=extents(cols) + extents(rows))
197.               ax[scan].set_yticks([])
198.               ax[scan].xaxis.set_major_locator(ticker.MultipleLocator(100))
199.               ax[scan].xaxis.set_minor_locator(ticker.MultipleLocator(50))
200.               ax[scan].set_xlabel('Line Scan Position')
201.
202.
203.       ax[0].set_yticks(rows[::200])
204.       ax[0].set_ylabel('Spectral Pixel')
205.       ax[len(scans_start)].plot(ave_spectrum[lp:]/ave_spectrum.max(),RS_cal[lp:])
206.       ax[len(scans_start)].set_ylabel('Raman Shift / cm-1', rotation=270)
207.       ax[len(scans_start)].yaxis.set_label_coords(1.4, 0.5)
208.       ax[len(scans_start)].set_xticks([])
209.       ax[len(scans_start)].set_ylim(RS_cal[lp:].min(),RS_cal[lp:].max())
210.       ax[len(scans_start)].tick_params(axis='y',which='both',right=True,left=False, la
    belleft=False, labelright=True,labelsize = 10, width = 1.0)
211.
212.       plt.tight_layout(h_pad=0.0, w_pad=0.0)
213.
214.       fig.savefig(sheet+'line_scan_maps.png', dpi=600)
215.
216.
217.
218.       fig, ax = plt.subplots(1, figsize=(6,3))
219.
220.       plot_position = [0.15,0.15,0.82,0.70]
221.
222.       ax.plot(RS_cal[lp:],ave_spectrum[lp:]/ave_spectrum.max(),color="None")
223.       ax.set_xlim(RS_cal[lp:].min(),RS_cal[lp:].max())
224.       ax.set_position(plot_position)
225.       ax.set_xlabel(r'Raman Shift / cm-1')
226.
227.       ax1 =ax.twiny()
228.
229.       ax1.plot(pixel_domain[lp:],ave_spectrum[lp:]/ave_spectrum.max(),linewidth=2)
```

```
        ax1.set_xlim(pixel_domain[lp:].min(),pixel_domain[lp:].max())
        ax1.set_xlabel(r'Pixel')
        ax1.set_position(plot_position)
        #ax.set_ylim(0.05,1.2)
          peaks = peak_labels(RS_cal[lp:],ave_spectrum[lp:]/ave_spectrum.max(),ax, 0.05, 0.06,10)
        #print('Peak pixels:',peaks, peaks.shape)

        #fig.savefig(sheet+'_average_spectrum.png' ,dpi=600)
        spectral_points = np.array([334, 556, 648, 711, 768, 811, 830])

        colors = cm.rainbow(np.linspace(0,1,len(spectral_points)))

        for j, point in enumerate(spectral_points):
            ax1.scatter(pixel_domain[point],ave_spectrum[point]/ave_spectrum.max(), s=20, color=colors[j], zorder=20)


        #check 10 randomly selected spectra, baselines and baselined spectra

        fig, ax = plt.subplots(1,2, figsize=(10,6))
        for i in range(10):
            j = randint(1,baselined.shape[0])
            ax[0].plot(RS_cal[lp:],array_raw[j,lp:], RS_cal[lp:], baselines[j,lp:])
            ax[0].set_xlim([RS_cal[lp:].min(),RS_cal[lp:].max()])
            ax[0].set_xlabel('Raman Shift / cm-1')
            ax[1].plot(RS_cal[lp:], baselined[j,lp:])
            ax[1].set_xlim([RS_cal[lp:].min(),RS_cal[lp:].max()])
            ax[1].set_xlabel('Raman Shift / cm-1')



        #create line-scan array

        # Use spectral points identified from average spectrum above or use pixels from peak picking:
        #spectral_points = pixel_index

        line_scan = np.zeros((baselined.shape[0],len(spectral_points)))
        print('Linescan Array Dimensions:',line_scan.shape)

        for i in np.arange(baselined.shape[0]):
            for j,point in enumerate(spectral_points):
                line_scan[i,j] = baselined[i,point]


        fig, ax = plt.subplots(len(scans_start)+1, figsize=(5,7))

        colors = cm.rainbow(np.linspace(0,1,len(spectral_points)))

        ax[0].plot(RS_cal[lp:], ave_spectrum[lp:])
        ax[0].set_yticks([])
        ax[0].set_ylim(ave_spectrum[lp:].min(),1.2*ave_spectrum[lp:].max())
        ax[0].set_xlim(RS_cal[lp:].min(),RS_cal[lp:].max())
        ax[0].set_xlabel('Raman Shift / cm-1')
        for j, point in enumerate(spectral_points):
            ax[0].scatter(RS_cal[point],ave_spectrum[point], s=20, color=colors[j], zorder=20)

```

```
        for j in np.arange(line_scan.shape[1]):
            for i in np.arange(len(scans_start)):
                scan_points = np.arange(scans_stop[i]-scans_start[i])
                ax[i+1].plot(scan_points,line_scan[scans_start[i]:scans_stop[i],j], color=colors[j], label = spectral_points[j])
                ax[i+1].set_yticks([])
                ax[i+1].set_xlabel('Line Scan Position')
                ax[i+1].set_xlim(0,scans_stop[i]-scans_start[i])

        plt.tight_layout(pad=0.0, w_pad=0.0, h_pad=0.4)

        fig.savefig(sheet+'_linescans_stacked.png',dpi=600)



        fig = plt.figure(figsize=(6, 6))

        # gridspec inside gridspec
        # determine number of outer_grid subplots from number of scans

        if len(scans_start)%2==0:
            ncols_outer = int(len(scans_start)/2)
        else:
            ncols_outer = int(len(scans_start)/2+1)

        outer_grid = gridspec.GridSpec(2, ncols_outer, wspace=0.05, hspace=0.05)

        if line_scan.shape[1]%2==0:
            ncols_inner = int(line_scan.shape[1]/2)
        else:
            ncols_inner = int(line_scan.shape[1]/2+1)


        # determine number of inner_grid subplots from number of spectral points
        for i in np.arange(len(scans_start)):
            inner_grid = gridspec.GridSpecFromSubplotSpec(2, ncols_inner, subplot_spec=outer_grid[i], wspace=0.0, hspace=0.0)
            for j in np.arange(line_scan.shape[1]):
                ax = plt.Subplot(fig, inner_grid[j])
                scan_points = np.arange(scans_stop[i]-scans_start[i])
                ax.plot(scan_points,line_scan[scans_start[i]:scans_stop[i],j], color = colors[j])
                ax.set_yticks([])
                ax.set_xticks([])
                fig.add_subplot(ax)

        fig.savefig(sheet+'_linescans_nested.png',dpi=600)



        fig, ax = plt.subplots(nrows=2,ncols=len(scans_start)+1, figsize = (10,5))

        spectra = [baselined,baselines]

        max_pixels = np.argmax(baselined[:,lp:],axis=1)  # finds pixel with maximum intensity for each scan
        print('Shape of truncated spectral array:',baselined[:,lp:].shape)
        print('Shape of maximum intensity pixel array:',len(max_pixels))

        num_pix_h = rp - lp
        rows = np.linspace(lp,rp,num_pix_h).astype(int)
```

```
344.
345.       def extents(f):
346.           delta = f[1] - f[0]
347.           return [f[0] - delta/2, f[-1] + delta/2]
348.
349.
350.       n,_,_ = ax[0,0].hist(max_pixels+lp,bins=len(pixel_domain[lp:]), range=(lp,rp), o
    rientation ='horizontal', color='orange')
351.       ax[0,0].set_ylim([lp,rp])
352.       ax[0,0].set_xlim(0,1.1*n.max())
353.       ax[0,0].invert_xaxis()
354.       #ax[0,0].set_xticks([])
355.       ax[0,0].set_yticks(rows[::200])
356.       ax[0,0].set_ylabel('Spectral Pixel')
357.       ax[0,0].set_xlabel('Frequency / Average Intensity')
358.       ax[0,0].xaxis.set_label_coords(0.5, 1.1)
359.
360.
361.       ax_twin = ax[0,0].twiny()
362.       ax_twin.plot(ave_spectrum[lp:], pixel_domain[lp:])
363.       ax_twin.set_xlim(ave_spectrum[lp:].min(),1.2*ave_spectrum[lp:].max())
364.       ax_twin.invert_xaxis()
365.       ax_twin.set_xticks([])
366.
367.
368.
369.
370.
371.
372.       print(normalise(ave_baseline[lp:]).min(),normalise(ave_baseline[lp:]).max())
373.       ax[1,0].plot(normalise(ave_baseline[lp:]), pixel_domain[lp:])
374.       ax[1,0].set_ylim([lp,rp])
375.       ax[1,0].set_xlim(0,1.2)
376.       ax[1,0].set_xticks([])
377.       ax[1,0].set_yticks([])
378.       ax[1,0].invert_xaxis()
379.       ax[1,0].set_yticks(rows[::200])
380.       ax[1,0].set_ylabel('Spectral Pixel')
381.       ax[1,0].set_xlabel('Average intensity')
382.
383.
384.       for j, spectrum in enumerate(spectra):
385.           for scan in np.arange(len(scans_start)):
386.               line_map = (spectrum[scans_start[scan]:scans_stop[scan],lp:])
387.               line_map = np.transpose(line_map)
388.               num_pix_v = scans_stop[scan] - scans_start[scan]
389.               cols = np.linspace(scans_start[scan],scans_stop[scan],num_pix_v).astype(
    int)
390.               spectrum_image = ax[j,scan+1].imshow(line_map, cmap = 'magma', aspect='a
    uto', origin = 'lower',extent=extents(cols) + extents(rows))
391.               ax[j,scan+1].set_yticks([])
392.               ax[j,scan+1].set_xticks([])
393.               ax[1,scan+1].xaxis.set_major_locator(ticker.MultipleLocator(100))
394.               ax[1,scan+1].xaxis.set_minor_locator(ticker.MultipleLocator(50))
395.               ax[1,scan+1].set_xlabel('Line Scan Position')
396.
397.       plt.tight_layout(h_pad=0.0, w_pad=0.0)
398.
399.       fig.savefig(sheet+'line_scan_maps_plus_baseline.png', dpi=600)
400.
401.
```

```
402.
403.       #find row index of max value for each pixel using argmax along axis=0
404.
405.       fig, ax = plt.subplots(nrows=2,ncols=len(scans_start)+1, figsize = (10,5))
406.
407.       max_pixels = np.argmax(baselined[:,lp:],axis=1)
408.
409.       num_pix_h = rp - lp
410.       rows = np.linspace(lp,rp,num_pix_h).astype(int)
411.
412.       #ax[0,0].plot(ave_spectrum[lp:], pixel_domain[lp:], linewidth = 1)
413.       n,_,_ = ax[0,0].hist(max_pixels+lp,bins=len(pixel_domain),range=(lp,rp), orienta
    tion ='horizontal', color = cm.magma(128))
414.       ax[0,0].set_ylim([lp,rp])
415.       ax[0,0].set_xlim(0,1.2*n.max())
416.       ax[0,0].set_xticks([])
417.       ax[0,0].set_yticks([])
418.       ax[0,0].invert_xaxis()
419.       ax[0,0].set_xlabel('Position Frequency')
420.       #ax[0,0].xaxis.set_label_coords(0.5, 1.1)
421.       ax[0,0].set_yticks(rows[::200])
422.       ax[0,0].set_ylabel('Spectral Pixel')
423.
424.       ax_twin = ax[0,0].twiny()
425.       ax_twin.plot(ave_spectrum[lp:], pixel_domain[lp:])
426.       ax_twin.set_xlim(ave_spectrum[lp:].min(),1.2*ave_spectrum[lp:].max())
427.       ax_twin.invert_xaxis()
428.       ax_twin.set_xticks([])
429.       ax_twin.set_xlabel('Average Intensity')
430.
431.       ax[1,0].axis('off')
432.
433.       for scan in np.arange(len(scans_start)):
434.           line_map = (baselined[scans_start[scan]:scans_stop[scan],lp:])
435.           line_map = np.transpose(line_map)
436.           num_pix_v = scans_stop[scan] - scans_start[scan]
437.           cols = np.linspace(scans_start[scan],scans_stop[scan],num_pix_v).astype(int)

438.           spectrum_image = ax[0,scan+1].imshow(line_map, cmap = 'magma', aspect='auto'
    , origin = 'lower',extent=extents(cols) + extents(rows))
439.           ax[0,scan+1].set_yticks([])
440.           ax[0,scan+1].set_xticks([])
441.           scan_points = np.arange(scans_stop[scan]-scans_start[scan])
442.           max_rows = np.argmax(baselined[scans_start[scan]:scans_stop[scan]],axis=0)
443.           _,_,_ = ax[1,scan+1].hist(max_rows,bins=scan_points, color = cm.magma(128))

444.           ax[1,scan+1].set_xlim(0,len(scan_points))
445.           ax[1,scan+1].set_yticks([])
446.           ax[1,scan+1].set_xticks([])
447.           ax[1,scan+1].invert_yaxis()
448.           ax[0,scan+1].xaxis.set_major_locator(ticker.MultipleLocator(100))
449.           ax[0,scan+1].xaxis.set_minor_locator(ticker.MultipleLocator(50))
450.           ax[0,scan+1].set_xlabel('Line Scan Position')
451.           ax[0,scan+1].xaxis.set_label_coords(0.5, 1.2)
452.           ax[0,scan+1].tick_params(axis='x',which='both',bottom=False,top=True, labelt
    op=True, labelbottom=False,labelsize = 10, width = 1.0)
453.
454.
455.       ax[1,1].set_ylabel('Pixel Frequency', rotation=90)
456.
457.
```

```
458.        plt.tight_layout(h_pad=0.0, w_pad=0.0)
459.
460.        fig.savefig(sheet+'line_scan_maps_plus_pixel_scan_histograms.png', dpi=600)
461.
462.
463.
464.        from collections import Counter
465.
466.        scan_hist = Counter(max_rows)
467.        print('Scan mode and frequency:',scan_hist.most_common(1))  # Returns the highes
    t occurring item
468.        scan_hist_array = np.array(scan_hist.most_common())   # Returns all unique items
     and their counts
469.        df_scan_hist = pd.DataFrame(scan_hist_array)
470.        #df_scan_hist.to_csv(sheet+"_scan_hist.csv", header=False, index=False)
471.
472.        # check that all pixels have been included in the count
473.        print('Sum of pixels from histogram data:',np.sum(scan_hist_array, axis=0)[1])
474.        print(scan_hist_array.shape[0])
475.
476.
477.
478.        pixel_hist = Counter(max_pixels)
479.        print('Pixel mode and frequency:',pixel_hist.most_common(1))  # Returns the high
    est occurring item
480.        pixel_hist_array = np.array(pixel_hist.most_common())   # Returns all unique ite
    ms and their counts
481.        df_pixel_hist = pd.DataFrame(pixel_hist_array)
482.        #df_pixel_hist.to_csv(sheet+"_pixel_hist.csv", header=False, index=False)
483.
484.        # check that all scans have been included in the count
485.        print('Sum of scans from histogram data:',np.sum(pixel_hist_array, axis=0)[1])

486.
487.
488.
489.        from collections import Counter
490.
491.        for scan in np.arange(len(scans_start)):
492.            fig, ax = plt.subplots(nrows=1,ncols=2, figsize = (12,6))
493.
494.            max_pixels = np.argmax(baselined[scans_start[scan]:scans_stop[scan]],axis=1)

495.            pixel_hist = Counter(max_pixels)
496.            print('Scan_'+str(scan)+' Pixel mode and frequency:',pixel_hist.most_common(
    1))  # Returns the highest occurring item
497.            pixel_hist_array = np.array(pixel_hist.most_common())   # Returns all unique
     items and their counts
498.            df_pixel_hist = pd.DataFrame(pixel_hist_array)
499.            df_pixel_hist.to_csv(sheet+"_scan_"+str(scan)+"_pixel_hist.csv", header=Fals
    e, index=False)
500.            print('Sum of scans from histogram data:',np.sum(pixel_hist_array, axis=0)[1
    ]) # check that all scans have been included in the count
501.
502.            pixel_points = np.arange(1,pixel_hist_array.shape[0]+1)
503.            ax[0].scatter(pixel_points, pixel_hist_array[:,1],zorder=20)
504.            ax[0].bar(pixel_points, pixel_hist_array[:,1])
505.            ax[0].set_title(sheet+"_scan_"+str(scan)+" maximum pixel distribution")
506.            ax[0].set_ylabel(r'frequency', fontsize=14)
507.
508.            a, m = 0.2, 4.
```

```
            fit_pixel_hist = a*m**a / pixel_points**(a+1)
            ax[0].plot(pixel_points, max(pixel_hist_array[:,1])*fit_pixel_hist/max(fit_p
    ixel_hist), linewidth=2, color='r')


            max_scans = np.argmax(baselined[scans_start[scan]:scans_stop[scan]],axis=0)

            scan_hist = Counter(max_scans)
            print('Scan_'+str(scan)+' Scan mode and frequency:',scan_hist.most_common(1)
    )  # Returns the highest occurring item
            scan_hist_array = np.array(scan_hist.most_common())   # Returns all unique i
    tems and their counts
            df_scan_hist = pd.DataFrame(scan_hist_array)
            df_scan_hist.to_csv(sheet+"_scan_"+str(scan)+"_scan_hist.csv", header=False,
     index=False)
            print('Sum of pixels from histogram data:',np.sum(scan_hist_array, axis=0)[1
    ]) # check that all pixels have been included in the count

            scan_points = np.arange(1,scan_hist_array.shape[0]+1)
            ax[1].scatter(scan_points,scan_hist_array[:,1],zorder=20)
            ax[1].set_title(sheet+"_scan_"+str(scan)+" maximum scan distribution")
            ax[1].bar(scan_points, scan_hist_array[:,1])

            fit_scan_hist = a*m**a / scan_points**(a+1)
            ax[1].plot(scan_points, max(scan_hist_array[:,1])*fit_scan_hist/max(fit_scan
    _hist), linewidth=2, color='r')

            plt.tight_layout(h_pad=0.0, w_pad=0.0)
            fig.savefig(sheet+'scan_'+str(scan)+'_max_distributions.png', dpi=600)



        # PCA output
        # PCA is run on each scan using the scan_PCA function

        fig, ax = plt.subplots(4,len(scans_start), figsize = (7,7))

        n_comps=9
        components = np.arange(n_comps)

        PC_x = 3
        PC_y = 4
        PC_z = 5

        for scan in np.arange(len(scans_start)):
            num_scan_points = scans_stop[scan] - scans_start[scan]
            scan_numbers = np.linspace(scans_start[scan],scans_stop[scan],num_scan_point
    s).astype(int)
            colors = cm.rainbow(np.linspace(0,1,num_scan_points))

            scores, loadings, evr = scan_PCA(baselined[scans_start[scan]:scans_stop[scan
    ],lp:rp])
            ave_scan = np.mean(array_raw[scans_start[scan]:scans_stop[scan],lp:rp],axis=
    0)

            ax[0,scan].plot(components, 100*evr[:n_comps], "o-", color='orange', lw=3)
            ax[0,scan].bar(components, 100*evr[:n_comps])
            ax[0,scan].set_xticks([])
            ax[0,scan].set_yticks([])
            scores_x = scores[:,PC_x-1]
            scores_y = scores[:,PC_y-1]
```

```
560.
561.            ax[1,scan].scatter(scores_x, scores_y, s=5, color = colors, label=None, alph
    a=0.8)
562.            ax[1,scan].set_xticks([])
563.            ax[1,scan].set_yticks([])
564.
565.            for j, point in enumerate(scan_numbers):
566.                ax[1,scan].annotate('{0:.0f}'.format(scan_numbers[j]),
567.                        xy=(scores_x[j], scores_y[j]),
568.                        xycoords='data', xytext=(+4, +4), textcoords='offset points',
569.                        fontsize=10, clip_on = True,
570.                        horizontalalignment='center', verticalalignment='bottom',
571.                        arrowprops=dict(arrowstyle="-
    ", connectionstyle="arc3,rad=.0"))
572.
573.            ax[2,scan].scatter(scores_x, scores_y, s=5, color = colors, zorder=20)
574.            ax[2,scan].set_xlim(-10,30)
575.            ax[2,scan].set_xlim(-10,10)
576.            ax[2,scan].set_xticks([])
577.            ax[2,scan].set_yticks([])
578.
579.            for j, point in enumerate(scan_numbers):
580.                ax[2,scan].annotate('{0:.0f}'.format(scan_numbers[j]),
581.                        xy=(scores_x[j], scores_y[j]),
582.                        xycoords='data', xytext=(0, +12), textcoords='offset points',
583.                        fontsize=6,  rotation=90, clip_on=True,
584.                        horizontalalignment='center', verticalalignment='bottom',
585.                        arrowprops=dict(arrowstyle="-
    ", connectionstyle="arc3,rad=.0"))
586.
587.            ax[3,scan].plot(RS_cal[lp:],-1*loadings[PC_x-1,:]/loadings[PC_x-
    1,:].max())
588.            ax[3,scan].set_xticks([400,800,1200,1600,2000])
589.            ax[3,scan].set_xlabel('Raman Shift/cm-1')
590.            ax[3,scan].set_yticks([])
591.            ax_twin = ax[3,scan].twinx()
592.            ax_twin.plot(RS_cal[lp:],ave_scan/ave_scan.max(), color='orange')
593.            ax_twin.set_yticks([])
594.
595.        plt.tight_layout(h_pad=0.0, w_pad=0.0)
596.
597.        fig.savefig(sheet+'PCA_output.png', dpi=600)
```

MASSEY UNIVERSITY
GRADUATE RESEARCH SCHOOL

STATEMENT OF CONTRIBUTION
DOCTORATE WITH PUBLICATIONS/MANUSCRIPTS

We, the candidate and the candidate's Primary Supervisor, certify that all co-authors have consented to their work being included in the thesis and they have accepted the candidate's contribution as indicated below in the *Statement of Originality*.

Name of candidate:	Megha Mehta
Name/title of Primary Supervisor:	Dr. Mark R. Waterland
Name of Research Output and full reference:	
Proceedings of SPIE,Highly sensitive surface-enhanced Raman scattering detection of brodifacoum and 1080 rodenticide in milk. Nanoimaging and Nanospectroscopy VI, 2018. International Society for Optics and Photonics, 1072618.	
In which Chapter is the Manuscript /Published work:	Chapter - 5
Please indicate:	
• The percentage of the manuscript/Published Work that was contributed by the candidate:	100%
and	
• Describe the contribution that the candidate has made to the Manuscript/Published Work:	
Candidate carried out experimental work, analysed the data and wrote the manuscript.	
For manuscripts intended for publication please indicate target journal:	
Chemosphere or Journal of Raman Spectroscopy	
Candidate's Signature:	Megha Mehta Digitally signed by Megha Mehta Date: 2019.02.25 12:34:43 +13'00'
Date:	25-02-2019
Primary Supervisor's Signature:	Mark Waterland Digitally signed by Mark Waterland Date: 2019.02.25 14:05:12 +13'00'
Date:	25-02-2019

(This form should appear at the end of each thesis chapter/section/appendix submitted as a manuscript/ publication or collected as an appendix at the end of the thesis)